ROLE OF SURFACE ENHANCED RAMAN SPECTROSCOPY IN THE ANALYSIS OF BIOMARKERS

VÁCLAV RANC

From basic substrates to advanced targeted analysis of biomolecules

May 2019 – The first release

Václav Ranc: *Role of Surface Enhanced Raman Spectroscopy in the Analysis of Biomarkers,* From basic substrates to advanced targeted analysis of biomolecules, © May 2019

There are only two tragedies in life:
one is not getting what one wants, and the other is getting it.

— Oscar Wilde

Dedicated to all the people, who supported my researcher and stood
by my side in all difficult situations.

ABSTRACT

Within the frame of gaining a deeper understanding on structure, chemical composition and properties of cells, tissues and similar samples, relevant from a bio-medicinal perspective, many chemical and physical methods have been developed and applied in recent years. However, considerable knowledge gap involving distribution, quantity and relationships of target compounds in the sample structure still persist. Combination of molecular spectroscopy and optical microscopy has tackled this issue in a non-invasive way; discovery of surface enhanced Raman scattering remarkably broaden its potential and allowed an analysis of until that point unthinkable compounds at ultra-low concentration levels. Following text briefly describes fundamental principles of Raman spectroscopy, shows the most interesting results, achieved by the author within past ten years, and draft its further ways of research and development.

In the history of science,
we often find that the study of some natural phenomenon
has been the starting point in the development of a new branch of knowledge.

C. V. Raman

ACKNOWLEDGEMENTS

This thesis would have remained a dream had it not been for my mentor Prof. Radek Zbořil, Ph.D. I would like to thank also to my coworkers and my family for a constant support.

CONTENTS

LIST OF FIGURES

ACRONYMS

SERS Surface enhanced Raman spectroscopy

CCD Charge-coupled device

RRS Resonance Raman scattering

CARS Coherent anti-Stokes Raman spectroscopy

FT Fourier transformation

RSD Relative standard deviation

STD Standard deviation

CTC Circulating tumor cell

PC Prostate cancer

GESR Graphene enhanced Raman spectroscopy

PSA Prostate spectific antigen

PSMA Prostate specific membrane antigen

CCD Charge coupled device

PCA Principal component analysis

CMC Carboxymethyl chitosan

CSF Cerebrospinal fluid

PJI Prostetic joint infection

PC Prostate cancer

cy Cyanine

POC Point of care

PREABMLE

We are witnessing a technological upheaval which represents a strong incentive for the shaping of modern society. Technical solutions have been developed that have been unimaginable for the previous generation and which significantly influence the quality of life. Social transformation plans are designed as a result of rapid technological development, which seeks to predict the relationship of new technologies, in particular, digitization, to the future form of society and technology to use it profoundly. The skilled observer is able to witness both, fast and slowly coming changes taken place in many, nearly all, fields of human industries. This works aims at the development of methods applicable in biology and medicine, some of them, particularly in medical diagnosis. The course of events in this field can be considered as two-directional. One part of the ongoing research targets development of new analytical methodologies able to analyze even lower concentrations of biomarkers in more complex samples or to detect newly discovered ones. The other part is aimed at strategies applicable to a "point of care, (POC)" operational mode. This movement includes low-cost devices designated for developing countries, and open public use, and smart devices with additionally higher selectivity, specificity or simplicity to operate. However, both research directions have at least one conjunctive motivation, this is to improve the patients' lives for an acceptable price. Due to these aims, analytical techniques, including electrochemistry, mass spectrometry, chromatography, spectroscopy, and others are undergoing significant progress. Raman spectroscopy is standing still on the edge of the real clinical application, even thou a high number of published scientific results, describing its utilization in the analysis of thousands of biomarkers, cells, pathogens, tissues, has already proved its capabilities. During my work with this unique technique, I have recognized two factors, which are efficiently blocking its further utilization in commerce clinical applications, and as a point of care device. First, the robustness of the developed methods is still under acceptable limits, and second, the costs of the necessary equipment are high, compared to other POC techniques. Both issues need to be solved sufficiently, and they will be, eventually. New nanomaterials with exciting properties in surface enhanced Raman spectroscopy (SERS) are being developed on an everyday basis, and new CCD detectors and semiconductor lasers allow to minimize the price down to new lows. Following text describes a way I have gone through the development of analytical methods applicable in an analysis of physiologically active compounds, cells, and bacteria using Raman spectroscopy.

Part I

THEORY CONCERNING RAMAN SPECTROSCOPY

1 INTRODUCTION TO RAMAN SPECTROSCOPY

1.1 HISTORICAL BACKGROUND AND CONSEQUENCES

The genesis of the Raman spectroscopy befallen in the first quarter of the 20th century, when the scattering of monochromatic light, accompanied by a change of frequency was predicted by Adolf Smékal, and partially observed by Capmton for radiation in the X-Ray spectral region.[1, 2] However, the real story begins with a scientist named Raman and his trip through the Mediterranean Sea, where he was struck by the deep blue opalescence of the seawater.[3] Previously, Lord Rayleigh had described the blue color of the sky by a scattering of sunlight by molecules constituting the gaseous atmosphere, and hypothesized that the color of the sea water is caused by a reflection of the sky.[4] Later, Raman showed that the deep blue color is caused by a scattering of light on the molecules of water. This is where his study of the light scattering begun. While studying the scattering of light in various liquids in 1923, Ramanathan, one of the Raman's student, observed a new and entirely unexpected phenomenon. When sunlight, filtered through a violet glass, passed through the liquid, the scattered rays contained wavelengths not previously present in the incident light. The experiment was performed with two complementary filters, and its design provided a clear proof that the scattering transformed the violet light into green. Ramanathan named the phenomenon "weak fluorescence." The same phenomenon was later observed also in experiments, where light scattering was studied in over sixty liquids. Interestingly, Raman's student Krishnan observed another important effect. The new radiation was polarized, in contrast to fluorescence, which is without polarization. Raman and Krishnan further proceeded with more experiments and discovered that the new scattered radiation is separated from the rest unmodified scattered light by a dark space. By this observation, the discovery of this new effect was complete, and it was later named after Raman.[5] The line spectrum, corresponding to the newly discovered radiation, was observed for the first time on the 8th February 1928. Later, after the discovery, Raman and Krishnan carried out further experiments and recognized that: I) each compound has a characteristic Raman spectrum, II) for a given compound the difference in frequency between Raman lines and the exciting line is constant, III) the new lines are sharp and usually observed in pairs. The observed range of frequency shifts is in the range from units of cm^{-1} to 3800 cm^{-1}, and frequencies correspond to oscillations of chemically bond atoms of

the observed molecule. It can be stated that the universality of Raman effect, the straightforwardness of the experimental technique, and simplicity of the resulting spectra mark this effect as a promising tool for the solution of various problems in many branches of science and technology. Since 1928, many modifications and improvements of the experimental design have been proposed and realized. [1] One of the most limiting experimental problems of Raman spectroscopy is the low intensity of inelastic scattering and high intensity of Rayleigh scattering. This fact has posed many restrictions, and have been a cause of extensive development in the instrumentation since the beginning to present. Early development was lead in the way of new radiation sources, including mercury lamp, Toronto arc lamp, and others, where a breakthrough has been achieved with a discovery of LASER in 1960. [6] During the 1970s, most Raman instrumentation used Ar^+, Kr^+, He-Ne, Cadmium or Ruby lasers. Following the demonstration of FT-Raman spectroscopy in 1968, the use of Nd: YAG laser operating at 1064 nm has been generalized as a standard to minimize effects of fluorescence.[7] Progressive development in the field of optoelectronics led to new semiconductor lasers operating at various frequencies; even tunable lasers are available nowadays. The next recognized challenge, worth to investigate, was a difficulty to measure at short Raman shifts due to a presence of Rayleigh scattering. This problem has been partially solved by an application of advanced optical filters, including volume Bragg gratings, edge filters, etc. These optical systems can decrease the level of Rayleigh scattering for 100 or more orders of magnitude even at very short Raman shifts in the units of wave-numbers. Since the discovery of Raman scattering, many experimental techniques based on this phenomenon, have been developed. First resonance Raman spectra were reported in 1953 by Shorigin. [8] Resonance Raman spectroscopy gained on popularity (since) then, especially among scientists working with biological samples, where sensitivity and fluorescence present considerable problems. Next to stokes lines, also utilization of anti-stokes lines was studied and several techniques were developed, with coherent anti stokes Raman spectroscopy (CARS) as a prominent example. CARS allows acquiring high resolution spectra, not limited by the used Raman spectrometer, but only by the line width of the laser. In 1966, it was found out that the intensity of Raman spectra does not depend on the sample volume, and it should be essentially constant for large-volume samples as well as for ultra-small samples.[9] The size of the sample is thus limited only by a diffraction limit and thus by an optical path, including number aperture of the objective, and laser wavelength. Micro-Raman spectrometers then found a stable place

1 Inelastic scattering was analogically observed in the same time era by two Russian scientists L. I. Mandelstamov a G. S. Lansbergov and mathematically described by two Austrian/Czech scientists: Georg Placzek and Adolf Gustav Stephan Smékal. Georg Placzek was the only Czech scientist working on the project Manhattan.

not only in research laboratories, but also in industry. Its potential was further extended by an incorporation of confocal optical designs. However, one of the most critical moment in the history of Raman spectroscopy was a discovery of surface enhanced Raman scattering (SERS). It was first observed on pyridine deposited on a rough surface of the silver electrode by Fleishamn in 1974, and described few years later. [10] The SERS allows to increase the Raman cross section of molecules adsorbed on a plasmonic material several orders of magnitude. Even a detection of as single molecule, deposited on the surface of a single silver nanoparticle was described in 1977 be Kneipp.[11] Numbers of publications, where SERS is applied, exponentially increased since its discovery. Nowadays (February 2019), more than 16 000 publications can be found on the Web of knowledge. It can be thus postulated, that Raman spectroscopy has experienced a great development and explosive penetration into many fields of human activities since 1928, and its position is still growing.

1.2 BASIC PRINCIPLES

According to the traditional perspective of the life creation, the light was separated on the first day. Not too late after, our forebearers gained an appetite for knowledge, which was never lost. The interaction of radiation with a medium results in several processes occurring with various probabilities. For the most part, transmission or reflection takes place. However, a small fraction of the incoming radiation is scattered due to inhomogeneities inside the medium. These can be divided to elastic (e.g., due to crystal dislocations) or dynamic inelastic, such as atomic vibrations, where a change in the wavelength is observed. Only an extremely small portion of the radiation is scattered inelastically. Several light scattering effects, providing structural information are known and understand, and Raman spectroscopy is a technique based on these effects. Today - in 2019, more than 25 types of Raman spectroscopies were described and used. The principal ones include Rayleigh scattering, Raman scattering, hyper-Rayleigh scattering, hyper-Raman scattering, coherent anti-Stokes Raman scattering, coherent Stokes Raman scattering, and stimulated Raman to gain or loss spectroscopy. Raman spectroscopy is a powerful spectral technique based on the evaluation of the inelastically scattered radiation, produced by the interaction of the incident radiation with atomic vibrations. When a radiation (electromagnetic wave) is applied on a molecular system, the electron and nuclei respond by moving in opposite directions, in a respect to the Coulobm's law. The weak electric field induces a dipole moment, which is linearly proportional to the applied electric field, where the proportionality is labeled as polarizability. The intensity of the scattered radiation corresponds to the square of the magnitude of the oscillating dipole moment. To

simplify the description of basic principles behind Raman scattering, infinite crystalline medium at finite temperature will be considered as medium. The normal modes of the vibrations of atoms in the medium are described by virtual quasiparticles, phonons.[12–14]
The medium displacement $\chi(\mathbf{r},t)$, where $\mathbf{r}$ is a position and t time is a sum of random motions described by wave vectors q, and frequency ω_q, described by the equation (1).

$$X(\mathbf{r},t) = \sum_q [X(\mathbf{q},\omega_q)e^{i(\mathbf{q}.\mathbf{r}-\omega_q t)} + X^*(\mathbf{q},t)e^{-i(\mathbf{q}.\mathbf{r}-\omega_q t)}] \quad (1)$$

Atomic displacements have a considerable influence on the change of susceptibility tensor $\overrightarrow{\chi}$ of the irradiated medium. Due to a nature of the displacements, compared to the lattice parameter, only the first order Taylor expansion will be considered (please see the equation (2)):

$$\overrightarrow{\chi} \simeq \overrightarrow{\chi}_0 + (\partial\overrightarrow{\chi}/\partial X)_{x=0}X(\mathbf{r},t) \quad (2)$$

The polarization $\mathbf{P}$ at the position $\mathbf{r}$ and time t is given by the equation (3):

$$\mathbf{P}(\mathbf{r},t) = \varepsilon_0\overrightarrow{\chi}(\omega 1)E_I(\mathbf{r},t) \quad (3)$$

, where $E_1(\mathbf{r},t)$ is the electric field at the position $\mathbf{r}$ at the time t. It is strictly correlated with the excitation radiation, defined by a momentum k_1, and angle frequency ω_1, described by the equation (4):

$$E_I(\mathbf{r},t) = E_I e^{i(k_1.\mathbf{r}-\omega_1 t)} + E_I^* e^{i(k_1.\mathbf{r}-\omega_1 t)} \quad (4)$$

The combination of the four mentioned equations 1-4 leads to an observation that the polarization of the medium is composed of three parts: one with a same phase as the incident radiation, and two are results of the interaction of the incident radiation with a medium susceptibility. This represents the inelastically scattered radiation, and it has two terms:

1. one with a wave vector k_1-q and frequency $\omega_S = \omega_1 - \omega_q$ (Stokes);
2. the other k_1+q and frequency $\omega_{AS} = \omega_1 + \omega_q$ (anti-Stokes).

The nomenclature is originated from the following postulate. According to a Stokes' law applicable in fluorescence related processes, the frequency of fluorescent light must be smaller or equal to that of the exciting radiation, and anti-Stokes lines are those that contradict it. This nomenclature has also been adopted for the Raman effect, albeit its fundamental differences. Conservation of the wave vector as well as the frequency must be fulfilled in every scattering process. However, all scattering processes have in common that, in contrary

to direct absorption processes, the energy of an incident photon does not have to be equal to the energy of the difference between two discrete energy levels. The intensity of the scattering is considerably increased, when the energy of the incident photon gets close to the energy corresponding to a transition of the ground electronic state of the material system to excited electronic state. When the energy levels are equal, the system is considered as resonant and the intensity of the scattered light is increased up to ten times, compared to non-resonant conditions. This phenomenon is labeled as resonant Raman spectroscopy (RRS). Raman scattering is according to its nature incoherent, and as a result the intensity of scattering strictly correlates with the number of non-interacting molecules. Importantly, Raman scattering is independent of the bulk structure of the material system. The explanation of Raman scattering describes the occurrence of inelastic scattering in a three event process, show in the figure 1.

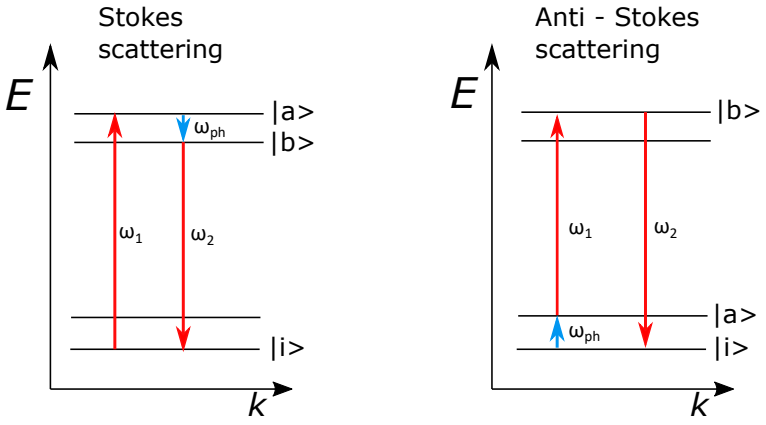

Figure 1: Description of the Stokes and anti-Stokes scattering

1. An electron in its initial state |i> is excited by an incoming photon with an angle frequency ω_1 to an excited state |a>
2. The electron decays to a state |b> after interacting with a phonon of energy ω_{ph}
3. The electron returns to its initial state by emitting a photon of a lower energy ω_2

For anti-Stokes scattering, the initial electronic state of the interacting system is an excited state. The population of atoms in excited states is according to a Bolzman's distribution given by a temperature, where the population increases correspondingly with the increased values. The ratio of intensities of bands corresponding to Stokes and anti-Stokes vibrations is consequently given by the equation (5):

$$\frac{I_{Anti-Stokes}}{I_{Stokes}} = \frac{(\omega_1 + \omega_{ph})^4 e^{-h\omega_{ph}/kT}}{(\omega_1 - \omega_{ph})^4} \tag{5}$$

However, number of excited states is significantly lower compared to ground states and the probability of anti-Stokes scattering is thus considerably lower, compared to Stokes. As a consequence of the state distribution, temperature of the measured medium can be calculated from the ratio of intensities of Stokes and anti-Stokes signals.

1.3 INSTRUMENTATION

Previous chapter covered fundamental aspects of the Raman scattering. In order to measure the inelastically scattered light, each part of the Raman spectrometer has to be carefully tuned to maximize the photon transmission and separation. The Raman spectrometer, including original construction by Raman, consists of the light source, monochromator or interferometer and detector. The following part will discuss particular components in the light of their construction design and its effect on resulting Raman spectra.

The selection of a light source has two fundamental aspects: radiation power, and monochromaticity. The intensity of the radiation is essential for the scattered light to be strong enough to be observed. At the beginnings of journey, sunlight together with mercury vapor lamps were used. The mercury vapor lamp has several strong emission bands localized at 253.7, 365.4, 404.7, 435.8, 561.1, and 578.0 nm. First, large number of emission bands strictly requires a usage of a filter to select only one wavelength. Otherwise, each emission band will produce its own partially overlapping Raman spectrum and the resulting spectral data will be extremely difficult to evaluate, and consequently interpret. Second, the emission bands have relatively large widths, which is initially convoluted into the obtained Raman spectrum, and heartlessly reflected in broad Raman bands. On the other hand, localization of the emission bands, produced by the Mercury vapor lamp, is beneficial for Raman spectroscopy, because these bands are located in the region from UV to visible green light, and the intensity of the scattered light increases with a four power of the frequency. Modern spectrometers use almost exclusively lasers. The reason is a) high amplitude if the emitted radiation and b) radiation is monochromatic. Moreover, the emitted light is polarized, which gives an opportunity for the determination of the depolarization ratio. Nowadays, gas lasers together with semiconductor lasers are frequently used. From the family of gas lasers, argon with an emission at 514 and 488 nm are the most popular.

Modern Raman spectroscopy recognizes two approaches: a) dispersive Raman spectrometers and b) interferometric Raman spectrometers. In contrary to infrared spectroscopy, where interferometric approach is now the almost the only one generally used, dispersive Raman spectrometers still have considerable advantages over spectrometers based on interferometers. First, dispersive Raman spectrometers

are significantly more sensitive, usually by a factor of ten to a hundred, which gives an option to use lasers of lower powers, leading to a lower sample destruction. Second, dispersive systems are less affected by noise, which indicates lower limits of detection. One of the great challenges in Raman spectroscopy is without any dount an efficient removal of Rayleigh signal. Earlier construction designs were based on a set of extra-large double or triple monochromators with focal lengths up to one meter and high resolution. This allowed to measure the Raman signal close to the Rayleigh band. Example of a double monochomator was installed in the earlier Raman models. Triple monochromators were based on several stages with simultaneously rotated gratings, with McPherson McTripple LE as an illustrative example. Nowadays, holographic notch filters with a high optical density up to 6^8, and bandwidth 100 cm^{-1} are commonly applied. The only disadvantage of the notch filers is in their basic principle. Each light source (wavelength) needs to be equipped by its own filter. The great success of interferometric technique in infrared spectroscopy naturally led to a penetration of this approach also to the Raman spectroscopy. The FT-Raman instruments are usually equipped with ND:YAG lasers operating in the near IR region (commonly 1064 nm), and powers in the range of lower units of Watts. Diode laser are becoming very popular due to their interesting benefit / prize ratio.
The FT-Raman spectrometers are usually equipped with Indium Gallium Arsenide (InGaAs) detector, with Germanium detector or with both in the ideal scenario. The InGaAs detector offers great performance for routine measurements and for samples, where higher laser powers can be used. on the other hand, Germanium detector offers better performance for the analysis of compounds with low Raman activity. Dispersive Raman spectrometers are usually equipped with CCD detectors.[15]
Importantly, in FT-Raman spectroscopy, spectral noise has two sources: the dark noise, and the short noise. The dark noise is given by the detector itself, and is always constant. The short nose is given by the photon flux, collected by the detector, and is influenced by the intensity of Raman scattering, the optical throughput of the system and quantum efficiency of the detector.[16–18]
Empirical formula for a total noise with a given sample and experimental conditions is given by the equation (6):

$$N^2 = N_{dark}^2 + \alpha S \tag{6}$$

where α is a proportionality constant and S stands for the peak intensity. The signal to noise (S/N) ratio is than given by the equation (7):

$$S/N = \sqrt[2]{\frac{S^2}{N_{dark}^2} + \frac{S}{\alpha}} \tag{7}$$

The equation 7 shows that a one single constant cannot be used to characterize the S/N performance of the particular instrument. High signal levels are more affected by a short noise, and S/N is thus proportional to the square root of signal intensity. In this case, the detector with the highest quantum efficiency will the wise choice. On the other hand, low signal levels will be less affected by the short noise and dark noise will be thus dominative.

2

FURTHER DEVELOPMENT OF RAMAN SPECTROSCOPY AND CASE STUDIES

2.1 SURFACE ENHANCED RAMAN SPECTROSCOPY

Surface enhanced Raman spectroscopy (SERS) is considered as one of the most important milestones in the development of Raman spectroscopy. The effect was discovered, albeit not recognized, in 1974 by Fleishmann.[10] He observed an intense Raman scattering from pyridine anchored on a silver electrode, previously roughened to increase its surface area and thus a number of adsorbed molecules. The original Fleishmann's intention was to develop an analytical platform able to monitor electrochemical reaction directly using Raman spectroscopy *in situ*. Jeanmaire, Van Duyne, Albrecht, and Creighton observed that the signal amplification of such amplitude could not be caused solely by an increase of adsorbed molecules.[19, 20]. Jeanmarie with Van Duyne hypothesized mechanism based on the electric field enhancement, and Albrecht with Creighton proposed a mechanism based on resonance Raman effect utilizing interaction of metal with adsorbed molecules. The signal enhancement was large, completely unexpected, difficult do understand in that time and had a great practical applicability. Since its discovery, research of SERS accelerated tremendously, and its applications penetrated into many areas of mankind activities. Nowadays, two involved mechanisms describing the Raman signal amplification are taken in account: electromagnetic and chemical enhancement.
The electromagnetic mechanism can be described on an example of a metal sphere in external electromagnetic field. The metal spherical particle has a diameter much smaller than the wavelength of the incident radiation, and it can be thus stated that the electric field is uniform across its surface. The relation between the electric field induced on the surface and external field can be described by the following equation (8).

$$E_{induced} = \frac{[\epsilon_1(\omega) - \epsilon_2]}{\epsilon_1(\omega) + 2\epsilon_2} E_{laser}, \tag{8}$$

where $\epsilon_1(\omega)$ is a complex, frequency-dependent dielectric function of the metal spherical nanoparticle, and ϵ_2 is the relative permittivity of the ambient phase. Interestingly, this function has a resonance at frequency $Re(\epsilon_1) = -2\epsilon_2$. As a result, excitation of the surface plasmon, localized on the metallic sphere, considerably increases the local filed exposed on the adsorbed molecule via the antenna effect. This model suitably describes the most of the experimental observations. Similar

approach can be applied also on nanomaterials of various morphology or shape. The selection of the material used for the SERS substrate depends strongly on its plasmonic properties. Noble metals are used frequently due to the fact that their resonance conditions is satisfied at the visible wavelengths of excitation radiation, commonly used in Raman spectroscopy. Other metals can be possibly applied similarly. However, due to a different localization of the resonance, excitation radiation will have to be shifted adequately. The difference between frequency of incident and scattered radiations leads to an important fact: both fields can be nearly resonant with the surface plasmon only for small frequency shifts. This consecutively leads to the decrease of the intensity observed for higher-frequency vibration bands. The surface plasmon is excited by the incident radiation or the Raman field; never both. The decrease of the enhancement can be described by the equation (9):

$$G = [r/(r+d)]^{12} \tag{9}$$

This equation is applicable for spherical nanoparticles with a diameter r, where the distance of the molecule from the surface is given by d. The effect is even lower for a molecular monolayer. Above mentioned equation 9 indicates the longer effects of the enhancements for nanomaterials with larger radius. The amplification of the Raman signal due to the chemical mechanism is 10^4 - 10^8

Some studies suggest that the electromagnetic effect in not the only reason for the large Raman signal enhancement, and that there has to be a second effect. This effect should operate independently on the electromagnetic mechanism. Based on its principles, electromagnetic enhancement should be a non-selective process applied on all molecules adsorbed on a particular nanomaterial. Interestingly, signal amplification of carbon monoxide and nitrogen differ more than 200x, measured at same experimental conditions. This result cannot be interpreted only by the electromagnetic mechanism. However, this dissonance can be explained by a) resonance Raman mechanism, where the electronic states of the adsorbed molecules are shifted and broadened as a result if their interactions with the surface or b) a fact that new electronic states are created as a result of the chemisorption. These states further serve as resonant intermediates in Raman scattering. The chemical mechanism is better described in a work by Lombardi, where a charge transfer theory of surface enhanced Raman spectroscopy was introduced. [21]. The theory includes both interactions: adsorbed molecule-metallic nanoparticle, as well as metallic nanoparticle-adsorbed molecule. The amplification of the Raman signal due to the chemical mechanism is 10 - 10^2.

Deeper understanding of a role of physiological processes remains of great importance for a medicinal diagnosis and following therapeutic measures. Therefore, analytical procedures, which will allow fast, target-specific detection of target molecules with ultra-low limits of detection, are required. Next to generally accepted methods, surface enhanced Raman spectroscopy has gained considerable attention during the last twenty years. This effect is attributed mainly to the high sensitivity of Raman spectroscopy gained through a SERS effect on plasmonic nanostructures, and its high molecular specificity. SERS is nowadays being applied to analyze various biomolecules, to characterize their interactions with a surface of metallic nanomaterials, to analyze drugs and metabolites in complex clinical samples, to study cells, bacteria or histological tissues, to study diseases, especially their effect on a molecular composition of analyzed samples. In general, two types of analytical approaches are available for SERS based applications, namely: label-free detection and indirect approaches based on Raman tags. The selection between label-free and label based approach relies strongly on the analyzed molecular target and sample complexity. The label-free approach is usually favored due to its simplicity. SERS approaches based on tags are applied in scenarios, where ultra-high sensitivity is needed, analyte itself has only a limited Raman activity or if the analyte is present in a very complex matrix, and a requirement for its sensitive analysis exists. In this approach, analyte, sensor or both are labeled using Raman tags with activity in resonance Raman spectroscopy Molecules from a family of Cyanines, Rhodamine-6g, Tamra, ROX, HEX, FAM, TET or similar compounds are beneficially used. The presence of analyte is then exposed generally by a change in the spectral intensity of the Raman tag. An increase is observed in cases, where an analyte or its counterparts such as hybridization probe or antibody were labeled. A decrease is characteristic for several approaches including hairpin DNA-based analysis or aggregation based SERS procedures. A label-free approach is preferred due to its straightforward principle. Interaction of the analyte, or set of analytes, with a surface of the metal nanostructure, are being evaluated instantly in the obtained SERS spectra. Commonly, nanostructures used in SERS-based applications, including clinical, biological, and medicinal, contain at least four segments: 1. substrate composed of noble metallic nanomaterial with a suitable SERS activity. Substrates are usually composed of silver, gold, or copper metals, frequently combined in complex nanocomposites; nowadays, also non-metallic nanostructures, including graphene are being studied, 2. Raman tag, 3. coating with various polymers, such as polydopamine, silica, polystyrene and other, to increase a biocompatibility and overall stability, 4. molecular selec-

Surface enhanced resonance Raman spectroscopy is an excitation laser wavelength dependent process, please see chapter 2.1 for more details.

tor with a sufficient selectivity to target analytes. The only essential part is the part one, and all other components are applied optionally, and beneficially. The biomolecule is usually defined as any molecule produced by a living system. In the light of chemical composition, biomolecules are composed mainly of carbon, nitrogen, hydrogen, sulfur, phosphor, and oxygen. These atoms consecutively form small biomolecules, which can tend to form larger biopolymers, including nucleic acids, proteins, oligosaccharides.

2.2.1 *Analysis of nucleic acids*

Nucleic acids are essential biocomponents and their detection presents one of the most demanding analytical tasks. Label-free detection of nucleic acids using surface enhanced Raman spectroscopy usually employed silver-based nanomaterial, including silver nanoparticles, layers, and 3D nanostructures.[22–30] Wei and Wu demonstrated a SERS method for an analysis of Lambda-DNA using silver nanoparticles with an average size of 100nm.[23] Raman spectra were acquired using a laser operating at 514 nm, and DNA was analyzed at concentrations down to 250 $ng.mL^{-1}$. Wei and Wu also demonstrated an effect of the DNA concentration of the resulting Raman spectrum, which was ascribed to different coil states of the nucleic acid. Silver nanoparticles offer high amplification factors, however, the robustness of the developed methods is lowered by a complication in a reproducible synthesis of the nanomaterial and unequal conditions during sample measurements. Several approaches showing improved strategies have been presented. Lei et al. introduced a method for an in-situ preparation of silver nanomaterial through a photo-reduction of silver ions supported by laser irradiation and demonstrated higher repeatability of the measured analytical signal and similar amplification factors.[31] Furthermore, Gao showed a method for detection of DNA using silver nanoparticles, where a presence of DNA mediated their size.[32] The DNA-mediated silver nanoparticle growth led to a significant decrease of the limit of detection (down to 10^{-10} $Mol.L^{-1}$), compared to similar approaches. Girel presented a novel nanomaterial for DNA analysis, based on silvered porous silicon, prepared by an electrochemical anodic etching of highly doped n-type silicon wafer.[29] Their method allowed analyzing DNA at limits of detection down to 1 $mg.mL^{-1}$. However, reproducibility of measurements was still at levels comparable to more classical approaches utilizing silver nanoparticles.
A typical Raman spectrum of samples containing DNA and proteins is shown in the figure 2. The DNA spectrum contains spectral bands characteristic for particular bases (labeled using one letter symbols), and the phosphate backbone (labeled as bb). Figure 2 c, and d, contains also bands characteristic for proteins, which will be more dis-

cussed in the following chapter. New approaches towards a DNA

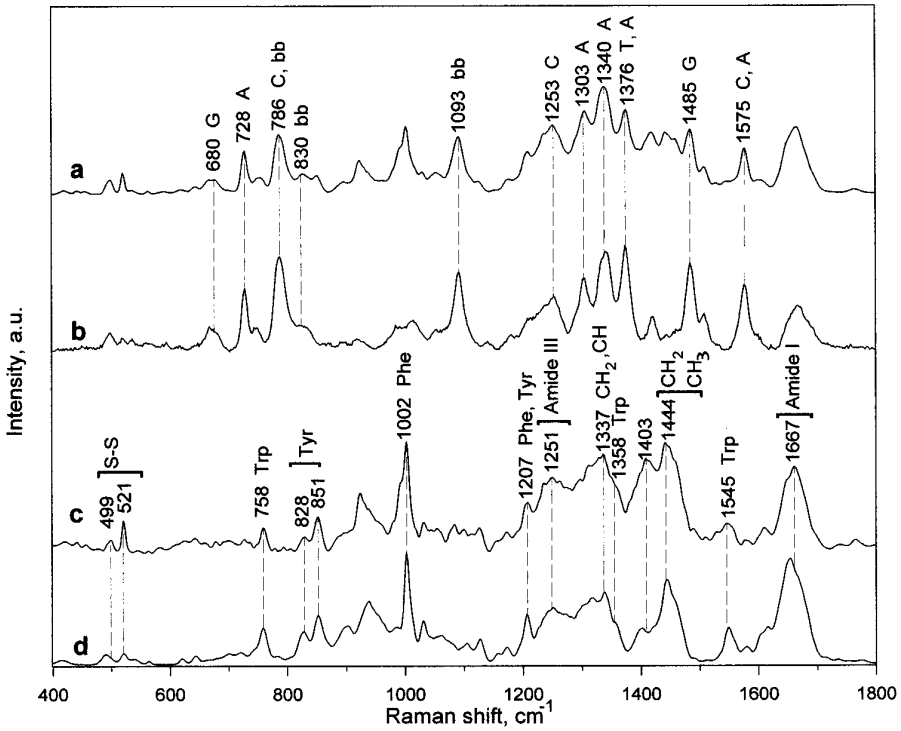

Figure 2: Raman spectra of 68 kDa DNA (a, b) and together with proteins (c,d).This figure was obtained from Fleury *et al.*[33]

detection employs noble metal-free substrates. Illustrative examples are methods based on carbon-based nanomaterials[34], aluminum nanocrystals[35]. Tian introduces a method based on aluminum with sizes in the range 2-4 nm with a thin oxide surface layer.[35] The purpose of the oxide layer, previously used in Raman spectroscopy labeled as "shell-isolated nanoparticle-enhanced Raman spectroscopy; Shiners", lies in its ability to bind various organic molecules and consequently improve their limits of detection.[36]. Eventhou the relatively lower amplification factors of Al nanoparticles, compared to silver or gold (10^5 vs 10^7), the limit of detection was determined to 2 micromoles of DNA. Example of a method for analysis of DNA, based on carbon nanotubes, particularly single-walled carbon nanotubes with Cu nanoparticles (SWCNTCuNPs) is described in the method by Zhou.[34] Zhou applied the method on the analysis of ctDNA in cancer tissues and blood with limits of detection 0.3 fmol.

2.2.2 *Analysis of proteins*

Analysis of proteins using SERS presents one of the most critical tasks. Changes in concentration levels and structure of many proteins can be caused by genetic alterations and can indicate a presence of a disease. Precise knowledge of these two parameters is thus essential

not only in medicinal diagnosis but can be extremely helpful in the monitoring of the follow-up treatment. Next, to immunochemical approaches, where ELIZA and RIA dominate[37], analysis of proteins is also performed using Mass spectrometry, commonly hyphenated with liquid chromatography[38, 39], electrophoresis in all its variants, as mentioned, e.g., by Chetwynd[40], Dawod[41] or Rubin[42], or even gas chromatography [43], and other techniques. The position of molecular spectroscopy within the spectrum of the commonly used techniques gained on importance over the last twenty years. This trend can be assigned to the rapid development of SERS and Raman imaging, which opened utterly new options. This trend will potentially continue and will drive a need for the quantitative interpretation of protein spectra.

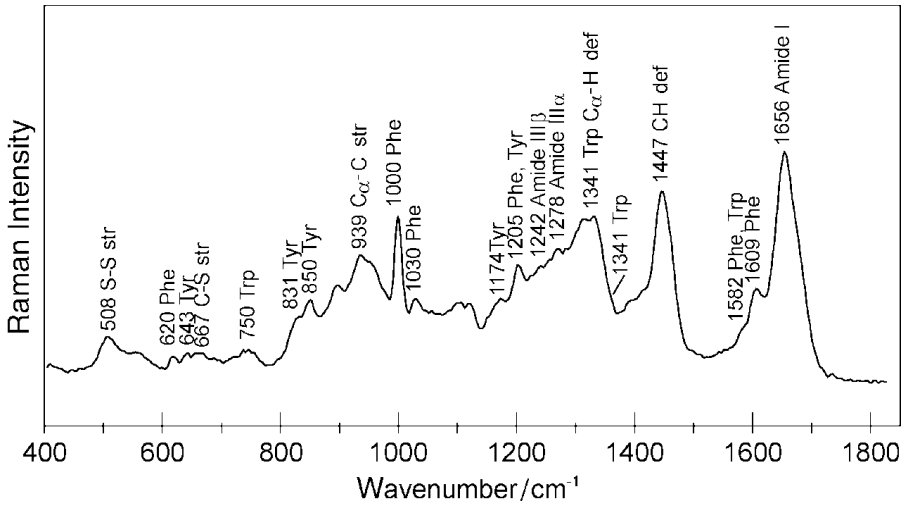

Figure 3: A typical Raman spectrum of proteins, obtained by the analysis of human serum protein. this figure was obtained from Tuma *et al.*[44]

Because proteins are often large polypeptides, consisting of hundreds of amino acids, their Raman spectra contain a complex set of overlapping bands. Nonetheless, structural features, including aromatic amino acids and polypeptide chain usually present firm dominant peaks. Illustrative protein Raman spectrum is shown in the figure 3. The sharp spectral band located at 1656 cm^{-1} is labeled as Amide I and corresponds to the sum of coupled modes of the polypeptide backbone. The significant contribution towards its intensity comes from C=O stretching of the peptide carbonyl groups. The spectral band presented at 1242 cm^{-1} is another example of prominent bands. The band comes from C-N stretching and N-H bending vibrations. Importantly, the position of the band strongly depends on the protein secondary and tertiary structure, and on the interactions between peptide groups due to an ability of carbonyl groups act as acceptors of hydrogen bonds within the ordered structure.
The application potential of SERS-based methods will be demonstrated

on several examples. Bizzari et al. described a method for the analysis of thrombin using surface functionalized gold nanoparticles able to recognize the aromatic moiety of the target protein selectively.[45] The limits of detection were in subpicomolar. Fabris et al. demonstrated an improved selectivity of SERS methods in a protein analysis on silver nanoparticles functionalized using aptamers.[46] Their method allowed to selectively analyze thrombin in a heterogenic protein mixture with a limit of detection 100 pmol.L^{-1}. The limit of detection was further considerably decreased by Heck, who published a method for synthesis of silver nano lenses composed of silver nanoparticles bonded using DNA-origami.[47] A single molecule of streptavidin was anchored on the interface on the synthesized nanostructure, where the signal amplification is highest, and the molecule was successfully detected by SERS. Many attempts have been rendered to improve the plasmonic properties of applied nanomaterials to achieve lower limits of detection, increase the method selectivity or overall robustness. These attempts can be according to their interests divided into three groups: i) tuning of the nanoparticle shape ii) composition of the nanomaterial and formation of hybrids/nanocomposites and iii) functionalization of the nanomaterial, particularly on surface. Importantly, many applications are base on nanosensors with functional improvements involving more than one approach. Nowadays, the "sandwich methodology" is usually employed in the analysis of proteins using SERS, analogically as described in classical immunochemical approaches. However, the signal is provided by Raman labels from the list as mentioned above. The approach was successfully applied in numerous SERS-based methods, including diagnosis of immunodeficiency [48], prostate cancer [49–51], breast cancer[52–55], Zika[56, 57], or even doping control[58].

Thrombin (coagulation factor IIa.) is a serine endopeptidase that hydrolyzes peptide and ester bonds at the carboxylic side of Arginine.

2.2.3 *Analysis of cells*

Importantly, an appearance of the Raman signal of selected protein(s) or nucleic acids (usually miRNA is being utilized for this purpose), in the analyzed sample can also indicate a presence of particular bacteria. Importantly, there exist many SERS methods for detection of bacterial infection, which are based on this presumption. Jarvis et al. demonstrated, in one of the first applications of SERS, a discrimination of bacteria using silver nanoparticles in 2004.[59] The discrimination was based on discriminant function analysis and hierarchical cluster analysis of Raman spectra obtained by the analysis of bacterial samples. Similar data was used by Harz et al., who studied a role of experimental conditions of the cell cultivation on the resulting Raman spectra.[60] This study was followed by Zeiri, who described a role of laser wavelength and chemical protocols used to prepare gold and silver nanoparticles.[61] Later in 2007, Naja demon-

strated a method for analysis of bacteria based on surface-anchored polyclonal antibodies.[62] The method development can be divided into several pathways according to their partially overlapping aims. These usually include at least: i) multiplexing, ii) automatization iii) lower limits of detection iv) detection of particular targets such as diagnosis of specific disease, and detection of a selected contamination. One of the first approaches towards method automatization was demonstrated by Knauer et al. in 2010.[63] Their work aimed at the detection of bacterial cells using lab on chip devices. Kang's study from 2010, named "Patterned Multiplex Pathogen DNA Detection by Au Particle-on-Wire SERS Sensor," opened a door to a multiplexed analysis of bacteria with possible application in medicinal diagnosis.[64] Since then, many works on analysis of bacteria using SERS have been described. Yang et al., have recently described a method for the detection of bacterial infections, namely Escherichia Colli and using $Ag@TiO_2$ nanofibers with the lowest detection limit near to 10^{-9} $mol.L^{-1}$. Similarly, Zhang demonstrated a work for discrimination of Escherichia coli Dh5 and DE3. The work is based on the utilization of plasmonic Ag cylindrical networks. Interesting application has been proposed by Catala et al.[65], who developed an aptamer-based method for a detection of Staphylococcus aureus in human fluids using a microfluidic device.

Part II

RESULTS

3

ILLUSTRATIVE EXAMPLES OF OBTAINED RESULTS

This chapter contains results from the following scientific papers:

1. Prucek, R. et al. Re-crystallization of silver nanoparticles in a highly concentrated NaCl environment—a new substrate for surface enhanced IR-visible Raman spectroscopy. CrystEngComm 13, 2242 (2011).

2. Ranc, V. et al. Quantification of purine basis in their mixtures at femtomolar concentration levels using FT-SERS. JOURNAL OF RAMAN SPECTROSCOPY 43, 971–976 (2012).

3. Prucek, R. et al. Reproducible discrimination between Gram positive and Gram negative bacteria using surface enhanced Raman spectroscopy with infrared excitation. The Analyst 137, 2866 (2012).

4. Ranc, V., Srovnal, J., Kvítek, L. & Hajduch, M. Discrimination of circulating tumor cells of breast cancer and colorectal cancer from normal human mononuclear cells using Raman spectroscopy. The Analyst 138, 5983 (2013).

5. Ranc, V. et al. Magnetically Assisted Surface-Enhanced Raman Scattering Selective Determination of Dopamine in an Artificial Cerebrospinal Fluid and a Mouse Striatum Using Fe 3 O 4 /Ag Nanocomposite. Analytical Chemistry 86, 2939–2946 (2014).

6. Balzerova, A., Fargasova, A., Markova, Z., Ranc, V. & Zboril, R. Magnetically Assisted Surface Enhanced Raman Spectroscopy (MA-SERS) for Label-Free Determination of Human Immunoglobulin G (IgG) in Blood Using Fe 3 O 4 @Ag Nanocomposite. Analytical Chemistry 86, 11107–11114 (2014).

7. Chaloupková, Z. et al. Label-free determination of prostate specific membrane antigen in human whole blood at nanomolar levels by magnetically assisted surface enhanced Raman spectroscopy. Analytica Chimica Acta 997, 44–51 (2018).

8. Fargašová, A. et al. Detection of Prosthetic Joint Infection Based on Magnetically Assisted Surface Enhanced Raman Spectroscopy. Analytical Chemistry 89, 6598–6607 (2017).

9. Balzerova, A., Opletalova, A., Ranc, V. & Zboril, R. Multiplex competitive analysis of HER2 and EpCAM cancer markers in whole human blood using Fe2O3@Ag nanocomposite. Appl. Mater. Today 13, 166–173 (2018).

10. Ranc, V., Žižka, R., Chaloupková, Z., Ševčík, J. & Zbořil, R. Imaging of growth factors on a human tooth root canal by surface-enhanced Raman spectroscopy. Analytical and Bioanalytical Chemistry (2018).

More information can be found in the Appendix, section A.

3.1 RE-CRYSTALLIZATION OF SILVER NANOPARTICLES IN A HIGHLY CONCENTRATED NACL ENVIRONMENT - A NEW SUBSTRATE FOR SURFACE ENHANCED IR-VISIBLE RAMAN SPECTROSCOPY

One of the first steps to a successful development of SERS based methodology is a successful synthesis of a SERS-active substrate. Key parameters influencing the resulting Raman signal amplification include the size of used nanoparticles, their composition, and morphology. Two of the most common materials are silver and gold with their own advantages and disadvantages. Commonly used approaches towards a bottom-up synthesis of silver nanoparticles from the silver nitrate lead to nanomaterials with sizes ranging from few to tens of nanometers and respective surface plasmons in the range from 300 to 500 nm. These values do not represent an optimal situation, especially in light of commonly used excitation lasers. There is, therefore, a great demand for new approaches applicable in a synthesis or activation of as-synthesized nanomaterials for use with lasers of higher wavelengths. The activation of silver nanoparticles commonly contains an addition of chloride ions, which leads to the aggregation of particles into bigger clusters with considerably shifted frequencies of their surface plasmons towards higher wavelengths. The final concentration of sodium chloride in the final step ranges from 0.1 - 10 mM.

Here we have developed new activation method based on the ad-

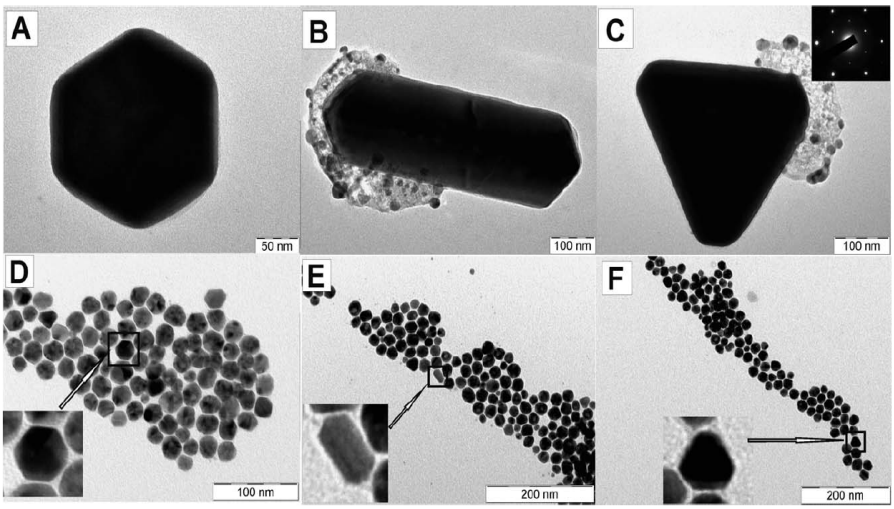

Figure 4: TEM images taken 15 min after the addition of the 4 M NaCl solution exhibiting recrystallized Ag particles with various morphology.[66]

dition of highly concentrated NaCl solutions with a final concentration of NaCl of 400 mM. The addition of such highly concentrated solutions leads to a re-crystallization of present silver nanoparticles to bigger crystals with sizes up to 400 nm. The effect was also com-

pared with the addition of NaBr and NaI at same concentration levels. However there was no re-crystallization observed for these two ions. The primary silver nanoparticles were synthesized by a reduction of the $[Ag(NH_3)_2]^+$ complex cation by maltose, as previously described by Panacek.[67] Silver NPs obtained in this way are nearly monodispersed with an average particle size of 28 nm (determined by the DLS and electron microscopy). The as-prepared nanoparticles were subjected to the activation, directly monitored using TEM, DLS, and UV/Vis. The figure 4 A-C shows various morphological classes of Ag crystals formed fifteen minutes after the initialization of the activation process using 4M NaCl. Figure 4 D and F shows particles of similar morphology found in a non-activated as-prepared nanomaterial. The measurement of a dynamic light scattering was performed

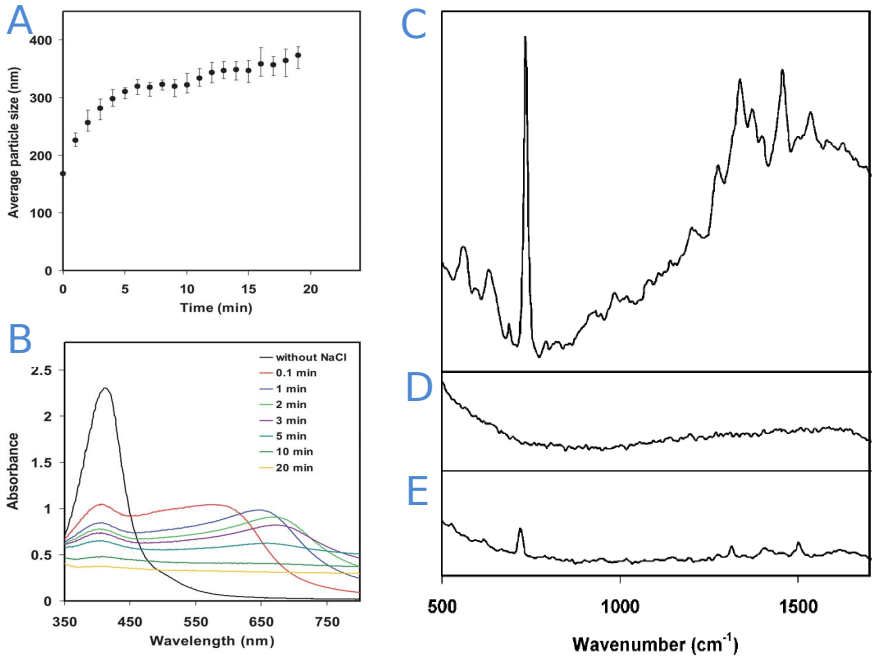

Figure 5: A-B: Time dependence of average size of obtained silver nanoparticles (A) and the respective UV-Vis absorption spectra (B) acquired in the first 20 min after the addition of the NaCl solution (the final concentration of 400 mM). C-E: Raman spectra of adenine measured using the developed activation procedure (C), with as-prepared Ag nanoparticles (B) and without SERS (E).[66]

twelve times in order to acquire enough data for a following statistical evaluation. Measured data are plotted in the figure 5 A, where error bars represent standard deviations calculated from the repeated experiments. It can be seen that the size increased to 200 nm almost immediately after the addition of 4M NaCl to the colloid and then increased gradually up to 400 nm during the first 20 minutes. Similar results were obtained from the measurements of UV/Vis spectra, plotted in the figure 5B. It can be seen that the initial absorption max-

imum for untreated Ag colloid (size 28 nm) was present at 410 nm. The addition of sodium chloride led to a rapid shift of the band towards higher wavelengths, which can be assigned to a crystal growth. The absorption maximum shifted to 680 nm approximately 3 minutes after the addition of NaCl, and its intensity attenuated in the next following minutes. This phenomenon is characteristic for Ag nanocrystals with sizes over 200 nm. Application potential of this activation process was evaluated on a detection of adenine using surface enhanced Raman spectroscopy. Resulting spectra are shown in the figure 5. Spectrum A presents Raman signal of adenine acquired using the developed activation procedure. Spectrum B was obtained by the analysis of adenine (c = 5 $\mu mol.L^{-1}$) using as-prepared silver nanoparticles with a size of 28 nm. Trace C represents a Raman spectrum of adenine (c = 0.1M) measured without SERS. It can be seen that 28 nm Ag nanoparticles do not amplify the Raman signal and amplification factor obtained by the developed activation is in hundreds of thousands (calculated according to the methodology described by Le Ru.[68]

Flowing can be stated in order to summarize this chapter. Here developed approach leads to a re-crystallization of present silver nanoparticles into nanocrystals with longitudinal sizes up to 400 nm. The combination of the size and crystal morphology induces a formation of the surface plasmon with properties applicable in SERS on instruments equipped not only with lasers operating at blue or green wavelengths but also near-IR lasers. This property thus opens new possibilities for SERS in this spectral area.

3.2 QUANTIFICATION OF PURINE BASIS IN THEIR MIXTURES AT FEMTOMOLAR CONCENTRATION LEVELS USING FT-SERS

Purine nucleotides are frequently involved in many cellular functions not only as essential components of nucleic acids, including DNA and RNA, but also as sources of energy, enzyme co-factors in many metabolic pathways, and as components of signal transduction. Alteration of their physiological levels is related to many severe diseases, such as Lesch–Nyhan syndrome and adenosine deaminase deficiency. [69] The Lesch-Nyhan syndrome is a relatively rare monogenic disorder transmitted in the X-linked recessive fashion, causing a high risk of developing gout due to the overproduction of uric acid. All patients are logically male, suffering from a delayed growth and puberty, and some of them develop also shrunken testicles or testicular atrophy. Precise and accurate monitoring of purine basis in clinical samples thus presents an important task, usually performed using chromatographic or electrophoretic approaches.[70, 71] However, Raman spectroscopy, especially in its modality, labeled as surface enhanced Raman spectroscopy, could present an interesting alternative with considerable benefits in shorter analytical runs, lower limits of detection or simplicity of developed methodologies. The utilization of surface enhanced Raman spectroscopy could in this particular case allow to achieve ultra-low limits of detection, due to a nitrogen-containing structure of analytes. It is worth mentioning that the majority of SERS applications uses silver or gold nanoparticles or their nanocomposites as a substrate; however, only a small portion of works describes the influence of particle size, sample pH or of the reduction agent on the method performance.

First, Raman spectra of particular bases were measured using 28 nm silver nanoparticles, synthesized by a reduction of the silver containing amino complex by maltose. Obtained spectral data, shown in the figure 6A indicate several considerable differences, also in the region of the most intense bands, assignable to a C=N vibration mode in the purine ring (630-730 cm^{-1}). The band is located at 735 cm^{-1} for adenine, 730 cm^{-1} for hypoxanthine and 660 cm^{-1} for xanthine, respectively. These differences were later used for a differentiation of purines and their quantification in mixtures. However, more in-detail study of experimental parameters had been performed before the method was developed. First, the influence of a size of nanoparticles on obtained amplification factors was evaluated. Three types of reduction agents, namely maltose, glucose, and sodium citrate were employed and three sizes of the particles were prepared and tested in SERS. As a reference, galactose was applied, however, its use provided extremely low SERS signals and it has not been thus further studied. Reduction of the silver ions by maltose led to spherical nanoparticles with an average size of 28 nm, reduction by a sodium

citrate led to spherical nanoparticles with an average size of 58 nm, and finally, application of glucose led to spherical particles with an average size 44 nm. The highest SERS amplification factors were observed in experiments, where glucose was used as a reduction agent, as shown in the figure 6B. Application of glucose led to 225 % increase of the signal intensity compared to maltose, and 152 % compared to citrate. In the next step, effect of the sample pH was studied. Samples containing adenine, with a pH adjusted to 3, 7, and 10 were prepared and measured. Figure 6C shows that acidic sample provided spectral signals with the lowest intensity, compared to neutral and basic samples. This phenomenon is among other factors given by the pK values of the purine bases and zeta potential on the silver nanoparticles, which influence the interaction between surface of the silver nanoparticles and analytes.

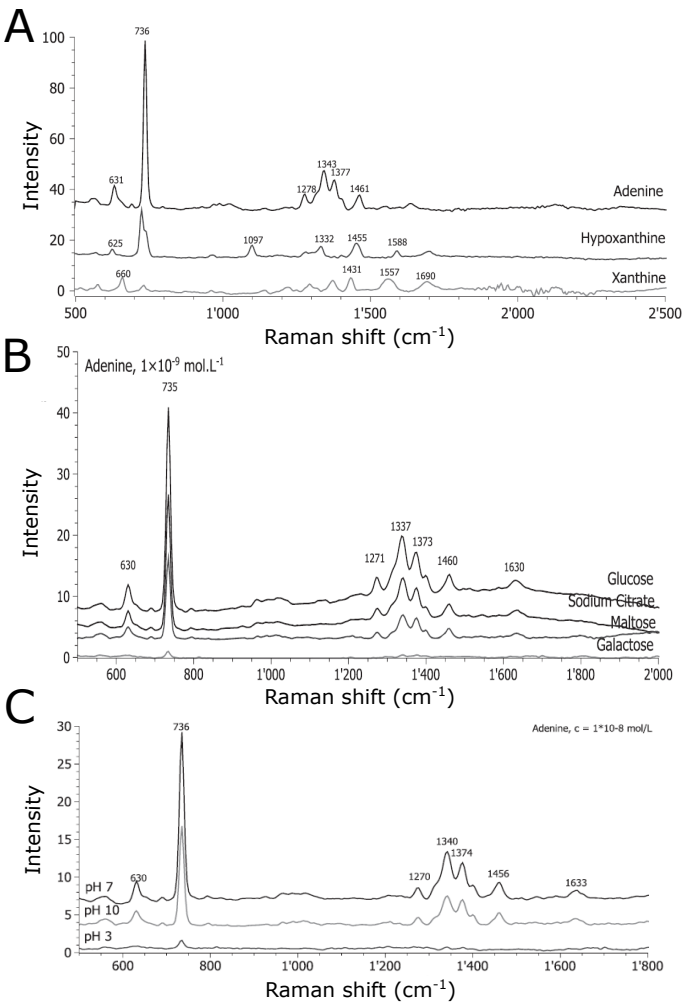

Figure 6: A:SERS spectra of adenine, hypoxanthine and xanthine measured at the concentration level $1_{x10}{}^{-13}$ mol.L^{-1}, B: SERS spectra of adenine measured using nanoparticles prepared by a reduction of silver nitrate using various reduction agents, as shown in the figure.[72]

Next, calibration experiments were performed under experimental conditions tuned in the previous step, namely using silver nanoparticles prepared by a reduction of silver containing amino complex using glucose. Eight-point calibration curves in the range from $1x10^{-15}$ to $1x10^{-11}$ mol.L^{-1} were prepared and measured for each purine base. Data processing led to coefficients of determination, ranging from 0.92 for hypoxanthine to 0.99 for adenine. Limits of detection (LODs) were calculated directly from the spectral data, based on the signal-noise ratio of the spectral band assigned to C=N vibrations in the purine ring (spectral range 630 – 740 cm^{-1}).Limit of detection for adenine was determined to $1x10^{-15}$ mol.L^{-1}, for xanthine $2x10^{-15}$ mol.L^{-1}, and finally for hypoxanthine $1x10^{-14}$ mol.L^{-1}. Consequently, the stability of nanoparticles was evaluated on the measurement of adenine using as-prepared nanoparticles for 10 consequent days. It was found out that the signal of the measured spectra decreases down to 25 % of its original intensity in this time frame. Similar data were observed for all three nanomaterials.
The last step of the presented research describes a determination of the concentration levels of all three purine basis in their mixtures. Analysis was based on the analogous approaches to ones used in the calibration model design. Samples containing all three analytes, present at the selected concentration levels, were measured. There was also a new calibration model constructed, based on the mixed samples containing all three targets. The concentration range was from $1x10^{-15}$ to $1x10^{-10}$ mol.L^{-1}. Spectral markers (bands) were identified for each target. The selection criteria were based on two requirements: first, the selected spectral band has to be unique for a target compound and second, this band has to be intense enough for quantification purposes at femtomolar concentration levels. For adenine, band at 735 cm^{-1} was used, for hypoxanthine, band at 1097 cm^{-1} was used and for xanthine, band at 660 cm^{-1} was selected. Based on these parameters, calibration curves for each analyte were measured. Calibrations were linear in the whole ranges for all three compounds. Finally, three samples containing 10^{-13} mol.L^{-1} of each target compound were analyzed. The results were obtained with RSD values < 5 %.

Here, we have developed a new methodology for analysis of purine bases, namely adenine, xanthine and hypoxanthine, at femtomolar concentration levels. The approach is based on a combination of surface enhanced Raman spectroscopy and silver nanoparticles prepared by a reduction of silver containing amino complex by glucose. Several experimental parameters, including effect of a size of silver nanoparticles, and pH were studied.

3.3 Reproducible discrimination between Gram-positive and Gram-negative bacteria using surface enhanced Raman spectroscopy with infrared excitation

Fast and reliable detection of bacteria strains during an ongoing bacterial infection presents the first step necessary for its following treatment. Generally applied methods frequently include overnight cultivation (time-consuming), appropriate reagents (often expensive), and the plans are usually complex and require extended and specialized training (expensive, need for human resources). It is thus necessary to develop new, fast and straightforward approaches utilizable in reliable detection of bacteria. Molecular spectroscopy, particularly Raman microscopy, presents an interesting alternative to generally applied methodologies. One of the most imitating drawbacks of Raman spectroscopy originates from its low sensitivity. This limitation was considerably overcome by a discovery of surface enhanced Raman scattering (SERS). This effect lowers reachable limits of detection down to a single molecule analysis through a resonant electromagnetic field amplification.[47, 73] Implementation of SERS to the method development allowed a broadening of the Raman application potential into the analysis of microorganisms.[59, 61, 65, 74–76] Interestingly, The most of the works describing utilization of Raman microscopy in a detection of bacteria uses excitation lasers operating in the UV/VIS range, namely from 240 to 850 nm. However, utilization of excitation lasers with lower frequencies can be advantageous especially due to the lowered probability of a background fluorescence; it is often present, when green excitation lasers are used.

We have demonstrated application potential of the newly developed approach for a SERS detection of nucleic bases and adenine in the previous two works. The approach is based on the utilization of silver nanoparticles with the mean size of 28 nm and narrow distribution, with a stability better than two years and applicability in both, visible and near IR region of laser excitation wavelengths. The activation procedure, including the addition of a high amount of sodium chloride (total concentration 400 mmol.L^{-1}) leads to a re-crystallization of the nanoparticles to crystallites with sizes up to 400 nm. Process was evaluated using UV/Vis spectroscopy and can be observed from the resulting spectra shown on the figure 7A, where the addition of sodium chloride leads to a decrease of the absorption band present at 400 nm and formation of new broad bands at higher wavelengths above 600 nm. Here, the recrystallized particles, together with NIR excitation, were employed for a SERS study with the aim to discriminate between Gram-positive (*Enterococcus faecalis* and *Streptococcus pyogenes*) and Gram-negative (*Acinetobacter baumannii* and *Klebsiella pneumoniae*) bacterial lysates. First, SERS spectra of all four bacteria were measured, processed and evaluated. The signal processing con-

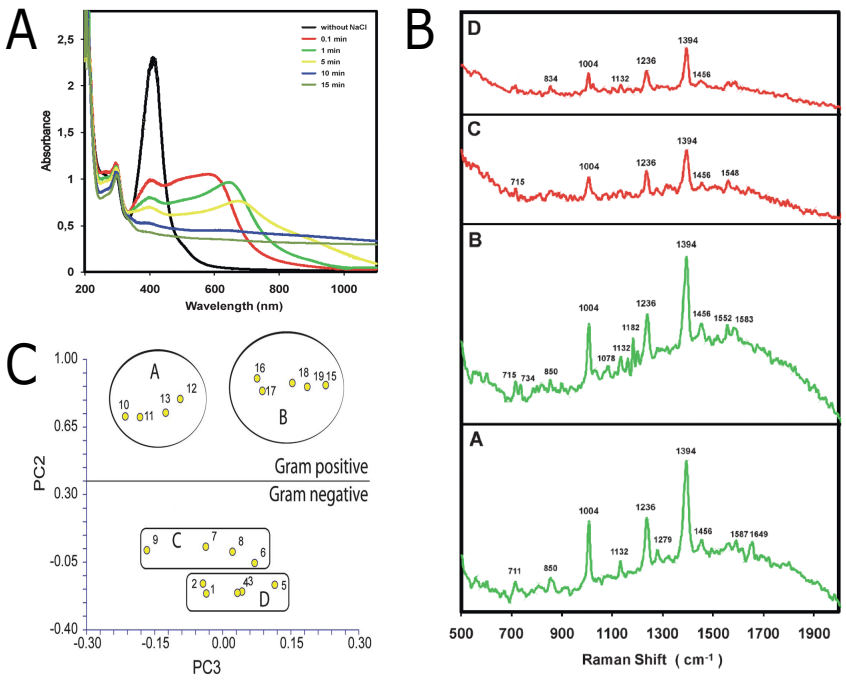

Figure 7: A: The time dependence of UV/Vis absorption spectra recorded over Fifteen minutes after the addition of sodium chloride solution to an Ag nanoparticles dispersion (final concentration of chlorides equal to 400 mM). B: Representative SERS spectra of bacterial lysates: (A) *Enterococcus faecalis*, CCM 4224, (B) *Streptococcus pyogenes*, (C) *Acinetobacter baumannii*, and (BD) *Klebsiella pneumoniae*. C: Cluster analysis of given Gram-positive and Gram-negative Bacteria. A stand for *Enterococcus faecalis*, CCM 4224, B for *Streptococcus pyogenes*, C for *Acinetobacter baumannii* and finally D for *Klebsiella pneumoniae*. N = 5, statistically outlying points were removed from the respective spectral data. [77]

sisted of the background corrections and data smoothing. The signal background was corrected by a subtraction of the previously fitted 3rd order polynomial functions, which were identified as a source of the signal bias, according to a methodology previously described e.g. by Schulze [78]. Data smoothing was processed using Sawitzky-Golay algorithms as proposed e.g. by Hui [79]. The obtained spectra can be seen on the 7B. SERS spectra contain bands of proteins, including Amide I (@1650cm^{-1}, section A), Amide II (@1550 cm^{-1}, all spectra), bands of phenylalanine (@1004 cm^{-1}, all spectra) or peptidoglycans. Importantly, peptidoglycans represent approximately 80 % of the dry mass of Gram-positive bacteria and around 20 % of the dry mass of Gram-negative bacteria. This could thus represent the stage, where above mentioned genera differ significantly, and can be possibly differentiated. Based on this hypothesis, the measured spectral data were subjected to a cluster analysis (performed in the R statistical environment, using Ward's cluster method), where Gram-positive

and Gram negative cultures were evaluated. Figure 7C shows the results of this analysis, and the Gram-positive bacteria, *Enterococcus faecalis* and *Streptococcus pyogenes* form two separate clusters (A and B, respectively). Gram-negative bacteria, C: *Acinetobacter baumannii* and D: *Klebsiella pneumoniae* form also two clusters, noticeably separated from the Gram-positive bacteria.

Here we have demonstrated an application of previously developed methodology for the SERS substrate based on re-crystalized silver nanoparticles in a discrimination of Gram-positive and Gram-negative bacteria. The approach is based on a statistical analysis of the measured SERS spectra in the R statistical environment and allows discriminating between bacteria within few minutes. Compared to a more classical immunochemical approaches, which require enough time for staining, here developed methodology presents an interesting alternative.

3.4 DISCRIMINATION OF CIRCULATING TUMOR CELLS OF BREAST CANCER AND COLORECTAL CANCER FROM NORMAL HUMAN MONONUCLEAR CELLS USING RAMAN SPECTROSCOPY

Cancer is one of the most killing diseases, and a development of methodologies able to diagnose it at its early stage is crucial. Circulating tumor cells present a potential diagnostic marker; their analysis enables an interesting prognosis and diagnostic choices complementary to generally used diagnostic techniques. Based on its importance, the analysis of cells is a scientific aim of many research and clinical institutes. However, it still presents a considerable challenge worth to pursuit, particularly due to a small incidence of the cells in clinical samples (usually units per milliliter), and their similarities to healthy epithelial cells. Here we used Raman microscopy to improve current possibilities in the study of circulating tumor cells and their further differentiation. One of important aspects of the cell Raman imaging is immobilization of the sample (cells) on a suitable substrate, including calcium fluoride, silicon wafer, glass, etc. Many protocols have been described already; however, there is no evidence describing a suitability of one over another regarding the analysis of circulating tumor cells. We have thus focused our attention on the study of three, the most frequently used, fixating protocol on the ability of spectral analysis, performed on the measured data, to discriminate between cancer and healthy cells. Namely, breast (BT 549) and colorectal (HCT116) circulating tumor cell lines and human mononuclear cells were prepared using methanol, paraformaldehyde, and drying-out fixating protocols, and obtained data were studied and evaluated in the light of the method ability to discriminate between the different cell lines. Firstly, representative Raman spectra of the cells were measured. Breast cancer cells (BT 549), colorectal circulating tumor cells (HCT 116), and human mononuclear cells (PBMC) were prepared using a cytospinning technique with 40.000 cells per one sample of the size of 1 x 1 mm using three fixating protocols, namely: drying out (label: dried), methanol (label: methanol) and paraformaldehyde (label: para). The representative spectra are shown in the figure 8A - C. Various differences in a surface composition of the measured cells, caused by a distorted protein expressions between healthy and cancer cells, and between different types of cancers, are projected into considerable differences in the obtained spectral data. Figure 8A shows measured variations in the spectral data obtained on BT 549 cells prepared using different fixating protocols. The observed considerable effect is originated from the ability of methanol or paraformaldehyde to selectively remove some compounds, based on their hydrophobicity, including proteins or lipids, from the cell walls. The effects of the various fixation protocols on the Raman imaging of cell lines were studied also by Hobro [80], Read [81], Kuzmin [82], Konorov [83], and others [84,

85] - similar effects were observed and discussed. More details about a cell analysis can be found in the section 2.2.3.

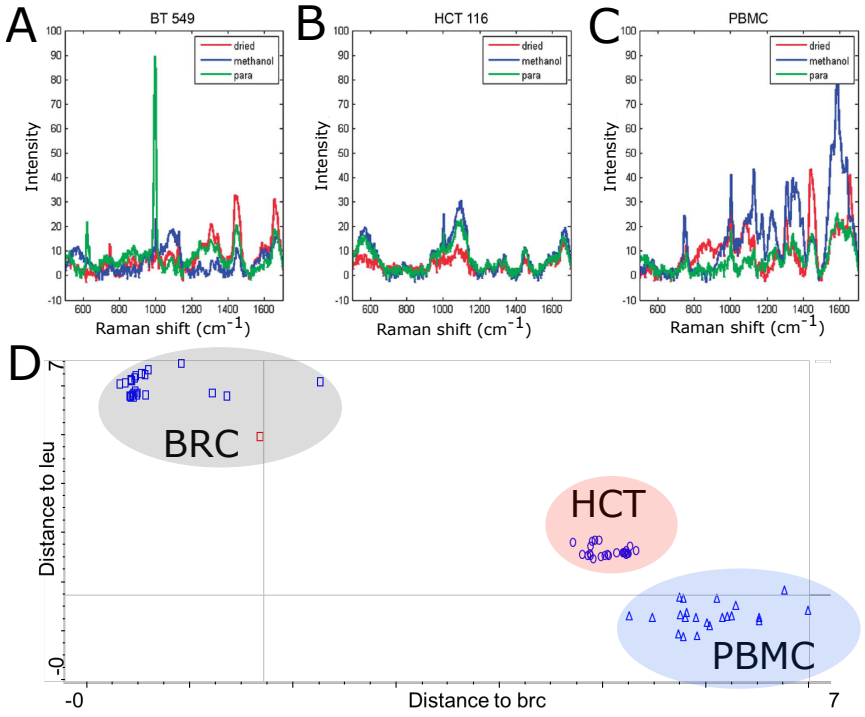

Figure 8: A - C: Spectral characterization of the cell lines acquired on samples with three different protocols of fixation, including dried out samples, methanol, and paraformaldehyde fixation; D: Graphical expression of the principal component analysis of data obtained by evaluation of dried out samples. Cells of the same cell line are centered in respective clusters, where the distance between the clusters represents the level of discrimination (Mahalanobis distance).[86]

However, due to a high complementarity of the measured data, summed up spectral data, belonging to all three tested protocols, offer a more complete picture illustrating a chemical composition of the measured surfaces. It can be seen that all data contain spectral bands at comparable positions, but of different intensities. The use of methanol and paraformaldehyde logically increases bands assigned to membrane proteins found at the following wavelengths: Amide I (1655 cm^{-1}) Amide II (1586 cm^{-1} and 1559 cm^{-1}), protein band (1441 cm^{-1}) as well as PO^{2-} vibration, located at (1244 cm^{-1}). Band of carbohydrates at 1171 cm^{-1} and glycogen at 1014 cm^{-1} can be also found among the strong spectral bands. Similar data were obtained also for the colorectal circulating tumor cells (HCT 115, figure 8B), and human normal mononuclear cells (PBMC, figure 8C). In the next stage, differences between all three tested samples were statistically evaluated using principal component analysis (PCA, calculated using R

statistical environment), performed on all measured data. The results of this analysis are shown in the Figure 8D for the drying out sample fixation method. Data obtained from dried out samples indicate that the method has the potential to differentiate among cancer cell lines and normal human lymphocytes (PBMC) as well as differentiating the HCT 116 and BT 549 cell lines. Experimental data points are concentrated in clusters with a considerable distance between them. BT 549 is represented by a relatively large data cluster, compared to mononuclear cells (PBMC) and HCT 116 cells. Mononclear cells were separated too, but with a smaller Mahalanobis distance from the HCT 116 cells, given by their surface similarities.

Here, we have demonstrated the crucial effect of the applied fixation protocol on the measured Raman spectra of circulating tumor cells, namely breast cancer (BT 549) and colorectal cancer (HCT 116), and human monomuclear cells (PBMC). Fixation using a drying out based process, and methanol and paraformaldehyde based protocols were compared and discussed. Achieved results indicate that all three evaluated cell lines can be discriminated at a significant statistical level using principal component analysis performed on previously normalized data. Here presented results open new possibilities towards a development of methodologies with future applicability in a detection of circulating tumor cells in clinical samples using Raman spectroscopy.

3.5 MAGNETICALLY ASSISTED SURFACE-ENHANCED RAMAN SCATTERING SELECTIVE DETERMINATION OF DOPAMINE IN AN ARTIFICIAL CEREBROSPINAL FLUID AND A MOUSE STRIATUM USING Fe_3O_4/AG NANOCOMPOSITE

Dopamine is a neurotransmitter, which works as a key modulator of learning and motivation. This dual functionality presents an important scientific question: how can target cells distinguish between a signal to learn, and a signal to move? [87] Generally echoed hypothesis involves slow and fast dopamine fluctuations; some studies shown that the signal can be transmitted in sub-second time scales.[88, 89] There is thus a considerable need for a rapid and accurate analytical methodologies able to determinate dopamine levels in the brain. Next to electrochemical approaches[90], with their own critical disadvantages, micro-dialysis with a mass spectrometric detection plays a crucial role.[91, 92]
However, there are two judgmental points worth addressing to get a more precise monitoring of dopamine levels over the signal transmission. These related key points are the time scale of the concentration change, which needs to be achieved, and ultra-low concentration of dopamine in cerebrospinal fluid. Even more, the increase of the sample volume, and thus absolute amount of extracted dopamine, leads to a worsening of the time resolution. Surface enhanced Raman spectroscopy is, due to its low limits of detection, an interesting alternative to mass spectrometry or electrochemistry. Needed sample volume is in units of micro-liters and achieved limits of detection are frequently in nanomolar concentration ranges. However, lowered selectivity of the SERS-based methods, caused by the non-existence of a selective binding of the analyte, which is in this case driven only by the affinity of particulate compounds to silver or gold nanoparticles, limits the method potential in many applications. Surface functionalization is one of the generally applied approaches towards a better selectivity of SERS. The scientific challenge could be then recognized in the development of a suitable methodology, which will allow to separate the formed system nanoparticle-analyte from the rest of the sample. One of the methods can be based on nanocomposite containing magnetic and silver nanoparticles, functionalized by a working selector, which can be separated from the sample by a use of external magnetic force.

The concept of this work is based on Fe_3O_4@Ag nanocomposite, where silver and magnetite nanoparticles are bind covalently with a help of a linker - carboxymethyl chitosan (CMC). The selectivity to dopamine is achieved through a surface functionalzation of the nanocomposite with a low molecular selector, Fe-NTA (iron-nitrilotriacetic acid). The first step of the method development included Raman characteriza-

tion of the nanomaterial, together with a trial of the method potential to detect dopamine. Raman spectrum of the synthesized sensor (Fe_3O_4@Ag@Fe-NTA) present in the aqueous environment can be seen in the figure 9C, label "Blank." It is shown that the initial sensor produces only a low Raman signal with several spectral bands in the region from 500 to 1800 cm_{-1}, assignable to a part of the CMC-Fe-NTA complex (700 cm_{-1}) and its heat-initiated degradation products (1390 - 1650 cm_{-1}) Next, the influence of the artificial cerebrospinal fluid on the sensor behavior was studied. The synthesized nanosensor was magnetically separated from the aqueous dispersion and put into a prepared artificial cerebrospinal fluid (aCSF). The obtained Raman spectra showed a mild suppression of the signal of Fe-NTA, which was contemplated due to the high salinity of the new environment and consequently, affected polarity of the present CMC-Fe-NTA complex. Importantly, spectra of aCSF containing 50, and 500 fmol.L_{-1} concentrations of dopamine show strong signals. Spectra were compared with previously measured Raman spectra of the one mol.L_{-1} aqueous solution of domanine and available literature [93], and finally assigned to this compound.
Next, calibration samples with dopamine in the concentration range from 10 - 5000 fmol.L_{-1} were measured and evaluated. The achieved coefficient of determination was 0.99, and calculated limit of detection (evaluation of the band at 1046 cm^{-1}, based on the IUPAC methodology) was 4.99 fmol.L_{-1} In order to further evaluate the method parameters, two model samples containing 50 and 500 fmol.L_{-1} dopamine were used in the study of intra-day and inter-day errors of measurements. Both relative standard deviations were lower than 25 % (21, and 25 %, respectively), which is comparable to values usually achieved by broadly used analytical techniques, including mass spectrometry and electrochemistry. Finally, three real samples of a mice striatum were measured. The dopamine was determined using a standard addition method to minimize the influence of matrix effects and sample inhomogeneities. Measured spectra are shown in the figure 9D and E. Dopamine was determined using the intensity of spectral band present are 1046 cm^{-1}. All measured values were compared to data obtained using HPLC, and the differences between measured values are < 20% (RSD).

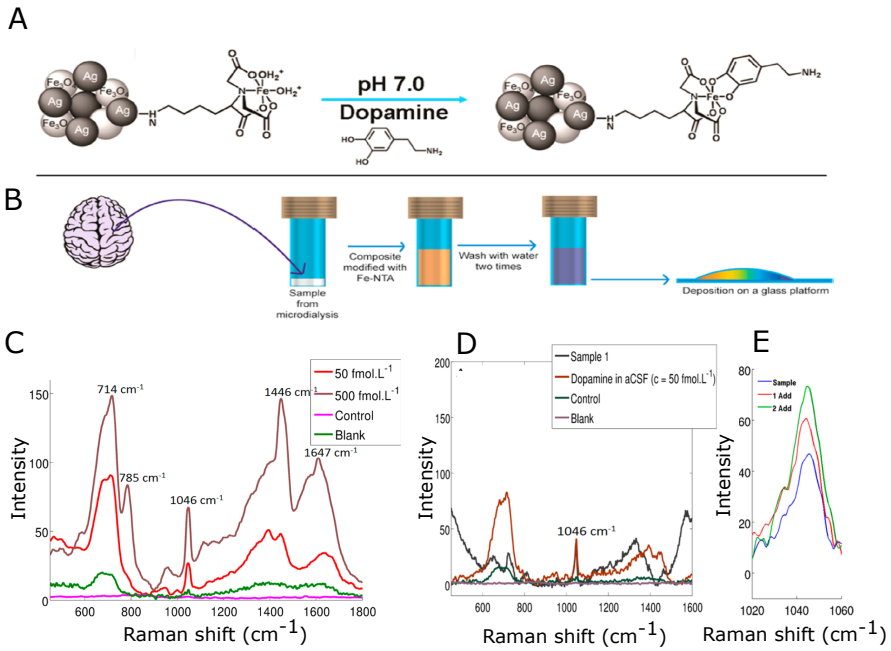

Figure 9: (A) Schematic representation of selective dopamine binding on the Fe_2O_3@Ag@Fe-NTA nanocomposite. (B) General scheme of the analysis. (C) SERS spectra of dopamine analyzed in artificial cerebrospinal fluid (aCSF) at a concentration level of 50 and 500 fmol·L $^{-1}$. The spectra of control and blank samples are included for better transparency. The control sample was measured with m@cmCH@Ag@Fe-NTA and aCSF, the blank sample only with m@cmCH@Ag@Fe-NTA nanocomposite. (D) SERS spectra of dopamine analyzed in mice striatum. The panel displays analysis of dopamine at a concentration level of 50 fmol.L^{-1} and analysis of control and blank samples for a better transparency. (E) Raman spectrum focused on the band at 1046 cm^{-1}(selected as a dopamine marker) before and after two additions of dopamine standard.[94]

The developed methodology based on the combination of the surface functionalized Fe_3O_4@Ag nanocomposite, and magnetically assisted surface enhanced Raman spectroscopy allows to determine an important neurotransmitter, dopamine, at ultra low concentration levels (LOD = 5 fmol.L^{-1}) both, in artificial cerebrospinal fluid, and directly in a brain tissue, where the method was tested on mouse striatum. The quantification of dopamine is based on the standard addition method that allows to minimize effects of the complex matrix. Obtained results were successfully compared to data achieved using liquid chromatography hyphenated with mass spectrometry.

3.6 Magnetically-assisted surface enhanced Raman spectroscopy (MA-SERS) for label-free determination of human immunoglobulin G (IgG) in blood using Fe_3O_4@Ag nanocomposite

Immunoglobulins are produced as a response to immunogens by B-Cells, and are the most abundant proteins in the blood. It has been demonstrated that immunoglobulins play a key role in defensive mechanisms against viruses or bacteria. Five classes, namely A, G, M, E and D, with various specific functions were described. [95] Importantly, Immunoglobulin G (IgG) is the most common type of antibody, and its protection is based on a "remembering" to which bacteria/viruses the organism was exposed before. The physiological level of IgG in the blood is from 7 - 15 $g.L^{-1}$. Symptoms of the IgG deficiency include sinus infections and other respiratory , digestive tract, and ear infections, pneumonia, bronchitis, and others. The levels of IgG can be tested in saliva, cerebrospinal fluid; however, blood test is the most common procedure. The classic analytical approaches are immunomethods, such as enzyme-linked immunosorbent assay (ELISA). [96, 97] Molecular spectroscopy, particularly a previously described MA-SERS approach, could be an interesting and advantageous alternative. The main expected benefits can be in ultra-low limits of determination and short times per analytical run.
The first task in the development work-flow (as demonstrated in the figure 10A) was to synthesize and characterize the nanosensor, composed of the Fe_3O_4@Ag nanocomposite, surface functionalized by streptavidin and consequently, by a biotinylated Anti-IgG. Briefly, the synthesis contains seven successive steps covering the synthesis of magnetic nanoparticles, their modification using carboxymethyl chitosan(CMC), reduction of the silver nanoparticles and follow up functionalization by streptavidin, via a formation of amide bonds through activated carboxyl groups (present on CMC), and finally by the attachment of biotinylated anti-IgG. Each step of the synthesis was monitored by a measured infrared spectra and ζ-potentials, which are summarized in the figure 10B. It is shown that the synthesis is accompanied by the change of values from negative (-46.2 mV) to positive (0.7 mV). The cause of the alteration is in the suppression of the originally negative charge of the present pristine silver nanoparticles by positively charred proteins (streptavidin, anti-Igg). The final nanosenor was also evaluated using transmission electron microscopy with illustrative results shown on the figure 10C. The silver nanoparticles are represented by a green sphere of a diameter approximately 28 nm, and the Fe_3O_4 nanoparticles functionalized using CMC are shown as red spheres with sizes ranging around ten nanometers.

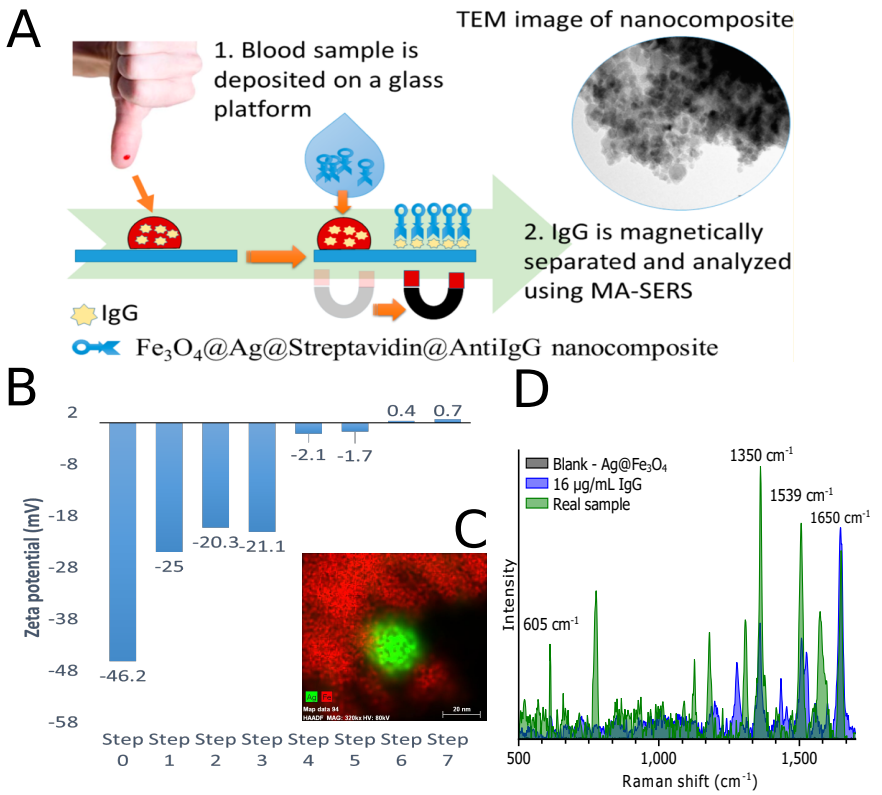

Figure 10: A:General scheme of the analysis, B: Changes of the ζ-potential measured along the 7-step synthesis of the sensor, C: TEM image of the synthesized nanosenor, D: Raman spectra obtained by the analysis of model and real samples.[98]

The purpose of the prepared nanosensor to analyze IgG using SERS as a detection method was evaluated on the set of experiments, including a measurement of blank samples containing only the bare Fe_2O_3@Ag nanosenor, and samples containing human IgG present at various concentration levels. The spectra in the figure 10D show a higher complexity of the analytical signal, which contain many spectral bands assignable to particular amino acids in the protein sequences, and to characteristic amide bands presented in the range 1100 - 1600 cm^{-1} The quantification of the IgG in the samples cannot be thus based only on the evaluation of the absolute intensity of any present spectral bands, and more complex approach was thereby developed. It was demonstrated that a pattern of the previously described protein bands depends upon the concentration of the IgG in the measured sample as a result of the interaction between IgG and anti-IgG. The determination of IgG was thus based on the evaluation of the ratio of spectral bands present at 1539, and 1650 cm^{-1}, previously normalized to the intensity of a band present at 609 cm^{-1} (ethylamine) as a reference. This way of calculation allows to minimize the negative effect of the signal heterogeneity, and allows to measure the analytical signal with RSD < 5 % for intra-day, and < 15 % for inter-

day determination of IgG in the model sample. The analysis of IgG in the human whole blood was performed according to the previously tuned conditions. The example of the obtained spectra is shown on the figure 10D (green trace). When compared with the model sample (blue trace), the spectrum contains additional spectral bands, which could be originated in non-specific interactions of the nanosenor with sample constituents; however, these effects do not influence the determination of the IgG levels, which was performed using the standard addition method. The RSD of the five consecutive analyses was lower than 5 %.

Here we have developed a new methodology for a determination of immunoglobulin G in the human whole blood samples using a finger prick method. This method is based on a combination of Fe_2O_3@Ag nanocomposite, functionalized using streptavidin and biotinylated anti-IgG, and magnetically assisted surface enhanced Raman spectroscopy. The method allows to analyze the IgG from 600 $fg.mL^{-1}$, and allows to determine IgG in the whole human blood, where the sample does not considerably exceed a volume of few microliters.

3.7 DETECTION OF PROSTHETIC JOINT INFECTION BASED ON MAGNETICALLY ASSISTED SURFACE ENHANCED RAMAN SPECTROSCOPY

Joint replacement significantly improves a quality of life for many people each year.[99] Successful surgery helps to relieve pain, and at least partially restores movement capabilities. These surgeries are usually performed without complications; however, a considerable number of them is later accompanied by prosthetic joint infection (PJI), which require additional treatment.[100] Several sources have reported an increasing trend in the incidence of PJI, where it increased from 2 % to 2.18 % from 2001 to 2009.[101, 102] Next to the health-related issues, PJI is also challenging from the economic perspective. The overall cost to treat PJI in the US was 266 million USD in 2009 alone. [102]

The currently used method to diagnose PJI is based on the Koch's culturing and consecutive colony counting, which is often expensive, and involve several difficult steps with many possible errors. Molecular spectroscopy plays in this field only a marginal role, albeit it's previously demonstrated advantages. One of the perspective techniques is surface enhanced Raman spectroscopy, particularly its variant MA-SERS employing magnetic nanocomposite functionalized by respective antibodies selective to bio markers present on the bacterial surface of the most common sources of PJI, including staphylococcus aureus and streptococcus pyogenes.

The presented work is based on a combination of MA-SERS and magnetic nanobeads with streptavidin anchored on its surface. The nanomaterial, labeled as MNP@Step, was easily functionalized by biotinylated antibodies against Staphylococcus aureus and Streptococcus pyogenes, as two the most common sources of PJI, and by silver nanoparticles to provide the amplification of Raman signal through a SERS effect. The two utilized antibodies were selective to protein A, characteristic for *Staphylococcus Aureus*, and group-A *streptococci* polysaccharide, characteristic for *Streptococcus Pyogenes*. The synthesis was evaluated using infrared spectra and ζ-potentials, measured at each step in analogy with the previous study. The ζ-potential of bare magnetic nanoparticles was negative (-22.3 mV). The functionalization by streptavidin led to the increase towards more positive values (9.63 mV), and final anchoring of anti-IgA led to a further increase to 10.4 mV. This considerable increase indicated a successful synthesis of the sensor. The as-prepared sensor, together with anchored streptavidin and antibodies (anti-IgA), was accordingly characterized using Raman spectroscopy with results shown in the figure 11A. The black trace (label: MNP/Ag) represents a Raman spectrum obtained by a measurement of the bare magnetic MNP/Ag nanocomposite composed of the initial magnetic nanoparticles functionalized using silver

nanoparticles prepared according to a procedure described in the Section 3.1. The Raman signal includes several weak bands at positions assignable to carboxyl groups incorporating a polymer, presented on the surface of the nanomaterial. Importantly, the here present spectral bands are not interfering with a signal of magnetic nanomaterial functionalized by streptavidin (blue trace), and by a biotinylated anti-IgA (green trace). Both functionalized nanomaterials provide spectra with characteristic protein spectral bands (Amide bands I, II and III) and signals characteristic for particular amino acids. Despite of the similarities between the spectra, considerable differences can be still identified. The here presented detection of bacterial infection is based on the altered ratio of spectral bands found at 1391, and 1558 cm^{-1}, caused by protein-protein, particularly antibody-antigen, interactions; visualized by gray lines in the figure 11A. The red trace in the figure corresponds to a signal obtained by a measurement of the model sample containing a lysate of staphylococcus aureus (labeled as STAU). It can be seen that the ratio of the spectral bands changed from 13.31 (blank sample - bare sensor) to 0.36. Similar results we obtained also for streptococcus pyogenes(labeled as STPY), where the ration changed from 19.71 (blank sample - bare sensor) to 0.48. This clearly indicates an interaction between the lysate, and the functionalized biosensor. The next step of the method development

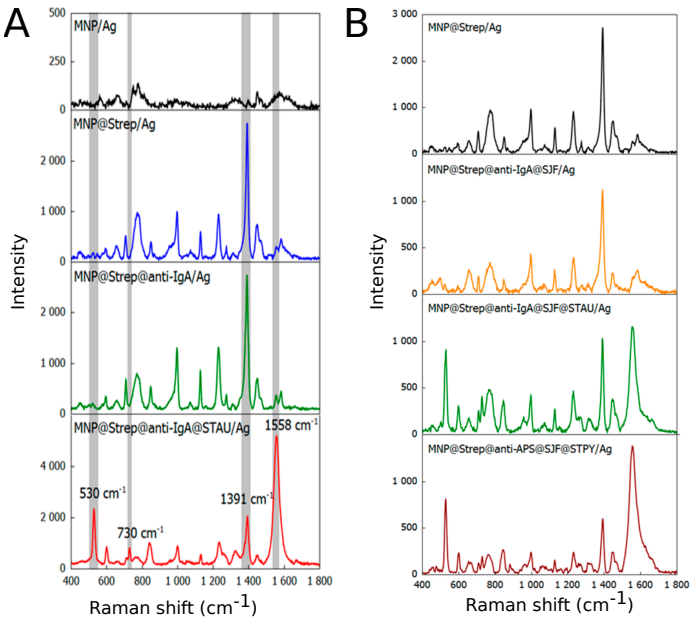

Figure 11: A:SERS spectra obtained by a measurement of model samples containing STPY and STAU, B: SERS spectra obtained by a measurement of STAU and STPY in the sterile knee joint fluid.[103]

was a study of the sensor performance in real samples, represented by a sterile knee joint fluid. Obtained results are in a good analogy with model samples. Resulting spectra are shown in the figure 11B,

where the alteration of the intensity of spectral bands present at 1391, and 1558 cm^{-1} can be observed. The black trace with intense protein bands corresponds to a bare magnetic nanocomposite functionalized by streptavidin (MNP@Strep/Ag) Its functionalized modality with an anchored anti-IgA antibody is represented by a yellow trace, where a moderate change in the protein band ratio can be already observed. The spectral differences were further intensified by an introduction of lysates containing STAU and STPY, as shown as green (STAU) and red (STPY) traces. Next, limits of detection for STPY and STAU were determined by a lowering of the concentration of particular lysates in knee joint fluid (described by CFU numbers) until a point, where a statistically significant change of the protein band ratio can be still observed. The method gives positive results for concentrations of STAU and STPY from 3 x 10^8 $CFU.mL^{-1}$ Next, a possibility to measure both bacteria in a mixture was studied. Samples containing STAU and STPY in ratios 1:9, and 9:1 were measured; protein band rations were calculated and further evaluated by a cluster analysis (Ward's method). Statistically significant differences were observed, and it was estimated that the assay is selective for both pathogens, although one is present in a very small amount compared to the other one. Finally, real samples obtained from four patients (labeled as A, B, C and D) were measured and statistically evaluated. Similar results were obtained also in this scenario.

Aspiration of the knee joint fluid is an integral part of the re-operation due to a possible presence of prosthetic joint infection, and is frequently performed as a standard procedure during a routine check. The possible infection is usually diagnosed by a performed culturing test, which is time consuming and could lead to false negative results. Here we have developed a new procedure based on the magnetically assisted surface enhanced Rama spectroscopy utilizing magnetic nanocomposite, functionalized by antibodies selective to *Staphylococcus Aureus* and *Streptococcus Pyogenes* as two the most frequent sources of PJI. The method allows to selectively, and simultaneously detect both bacteria in the real patient's samples, which is demonstrated on the measured data. Calculated limit of detection is 3 x 10^8 $CFU.mL^{-1}$ for both bacteria.

3.8 LABEL-FREE DETERMINATION OF PROSTATE SPECIFIC MEMBRANE ANTIGEN IN HUMAN WHOLE BLOOD AT NANOMOLAR LEVELS BY MAGNETICALLY ASSISTED SURFACE ENHANCED RAMAN SPECTROSCOPY

Prostate cancer (PC) belongs among the most common male malignancy, and represents a second-leading cause of dead among men.[104] Surgery, chemotherapy, cryosurgery or hormonal therapy are the most common approaches to therapy. [105] Regarding its diagnosis, many antigens have been identified, tested and evaluated. One of the most promising is prostate specific antigen (PSA), which is now commonly used. However, next to many advantages, many disadvantages, limiting its current use exist. One of the biggest drawbacks of PSA in the role of the PC marker lies in its limited selectivity, where elevated levels could, next to a PC, indite also benign hyperplasia or infection.[106] Other antigens are therefore needed. Prostate specific membrane antigen (PSMA) is one of the potential candidates. PSMA is a Type 2 trans-membrane glycosylated protein, and belongs to the group of zinc-dependent exopeptidases. PSMA is considerably overexpressed in all types of cancerous tissues and its expression is related to a disease progression.[107]
Its detection methods are based on the utilization of antibodies, aptamers, peptides or prostate-specific small molecules (e.g. N-acetyl-L-aspartyl-L-glutamate, NAAG). However, there is still a strong need for a simple, fast and reliable methodology, able to detect PSMA in complex clinical samples.
The here presented approach is based on the magnetically assisted surface enhanced Raman spectroscopy utilizing Fe_3O_4@Anti-GCPII@Ag nanocomposite according to procedure shown in the figure 12A. The anti-GCPII compound is a low-molecular-weight GCPII inhibitor used in this scenario as the iBody. The functionality of the sensor was first evaluated using surface enhanced Raman spectroscopy on a set of standard solutions containing PSMA. The obtained SERS spectra are shown in the figure 12B, where the red trace (label: Blank sample) represents a spectrum obtained by the analysis of the raw Fe_3O_4@Anti-GCPII@Ag nanocomposite, and the green spectrum (label: Standard of PSMA) stands for the results obtained by the measurement of the model sample containing 10 ng.L^{-1} PSMA. The spectrum of the blank sample contains weak Raman signals assignable to a structure of the anchored selector. SERS spectrum obtained by the analysis of the model sample contain strong spectral bands, characteristic for proteins. These vibrations include strong spectral bands present at 678, 728, 955, 1235 (Amide II), 1335, 1450, 1577, 1670 (Amide I), and 1790 cm^{-1}. The here presented approach is based on the evaluation of the spectral band at 1335 cm^{-1}. The 6-point calibration curve, covering a concentration range from 5 to 200 ng.mL^{-1} PSMA was prepared and

measured. The resulting data show a good correlation between the concentration of PSMA and intensity of the above mentioned spectral band with R^2=0.985, LOD = 0.48 ng.mL^{-1} (calculated from the S/N ratio). Next, the repeatability of the method was evaluated on

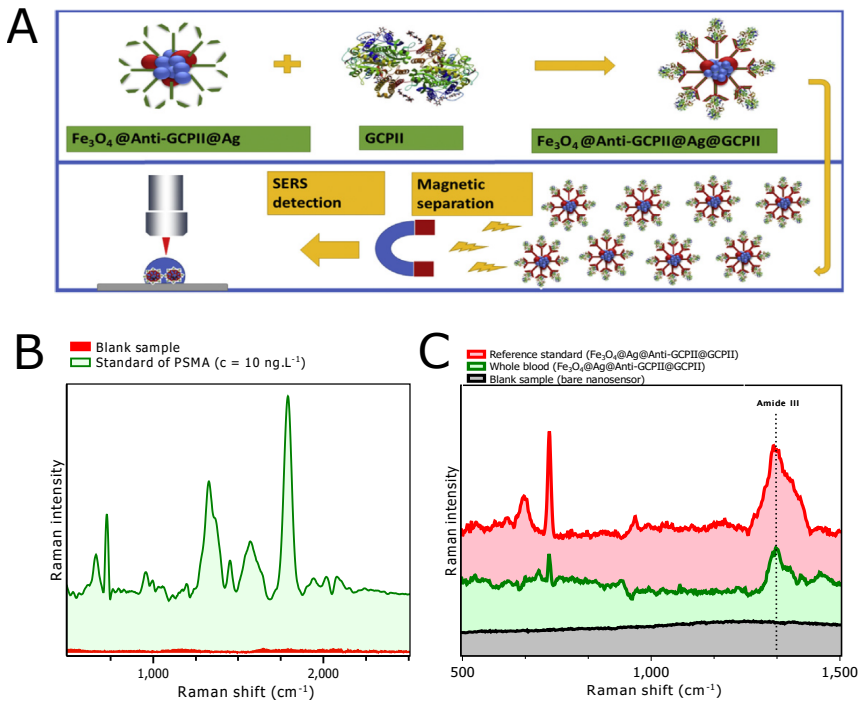

Figure 12: A:preparation of the sensor, general scheme of the analysis; B: SERS spectra obtained by the analysis of model sample; C: SERS spectra obtained by the analysis of real samples (whole human blood).[108]

the set of five measured samples; variability of the intensity of the three most abundant bands in the spectrum do not exceed seven percent. The method performance was evaluated on a set of real whole blood samples, obtained from two human volunteers. Representative SERS spectrum, obtained by the analysis of these samples, is shown in the figure 12C - green trace. Importantly, spectra obtained by the measurement of reference (red trace) and blank samples (black trace) were added for a better description. The similarities between the reference and real samples indicate a good ability of the sensor to isolate PSMA from the real samples; only few minor peaks originated from the non-specific interactions were identified. The up-to now obtained results indicated a good ability of the methodology to detect PSMA. Finally, the method ability to quantify concentrations levels of PSMA in real samples was studied on a framework of the standard addition approach. The PSMA levels were determined in five real samples based on three standard additions of PSMA, and the results (1 - 7 ng.mL^{-1}) are in a good agreement with levels previously reported for

a healthy population.

Here we have developed a new methodology applicable in the analysis of PSMA in human whole blood samples. The method is based on magnetically assisted surface enhanced Raman spectroscopy, and magnetic Fe_3O_4@anti-GCPII@Ag nanocomposite composed of iron oxide and silver nanoparticles functionalized using GCPII (PSMA) inhibitor in the role of the low-molecular-weight selector for PSMA. Spectral analysis, performed on the Raman spectra of model samples, uncovered a presence of bands characteristic for proteins, the quantitative analysis was based on the Amide band located at 1335 cm^{-1}. The method is able to detect PSMA at ultra-trace concentrations (LOD < 500 $pg.mL^{-1}$) with a signal repeatability seven percent. Further, the method potential was evaluated on the quantitative analysis of PSMA in a real samples, where a good agreement with previously reported values was achieved. The reliability and simplicity of this method suggest its potential as an advantageous alternative to generally applied analytical procedures.

3.9 MULTIPLEX COMPETITIVE ANALYSIS OF HER2 AND EPCAM CANCER MARKERS IN WHOLE HUMAN BLOOD USING Fe_2O_3@AG NANOCOMPOSITE

Metastatic disease is responsible for more than ninety percent of all cancer deaths.[109, 110] The key importance of circulating tumor cells in a formation of metastases has been proposed by Ashworth in 1869.[111] Since then, many studies describing a detection of CTCs, their treatment or describing their mechanisms of action have been reported. Nowadays, their identification and molecular characterization in cancer patients stays a scientific challenge, which resolution is a key to unprecedented insights into the metastatic process. The sample (expressed in 7.5 mL blood) of healthy patients do not contain more than 2 CTCs. On contrary, cancer patients had from 0 to almost 24.000 cells, and 36 % of specimen contain more than 2 CTCs.[112] The number depends on a particular cancer, and highest incidences were found in prostate, ovary and breast carcinomas. However, expeditious progress on this field had been slowed down until recent times due to a non-existence of suitable analytical methods able to detect CTCs with an adequate confidence, as the detection of CTCs can be compared to a proverbial 'needle in a haystack'. Recently developed approaches include immnomagnetic separation, filtration, centrifugation, flow cytometry, nucleic acid based methods, microfluidics, and others.[113–115] Major, and common problem of these techniques is their reliability. New and better methods able to detect CTCs are thus being researched and developed. Surface enhanced Raman spectroscopy presents a method with a great potential. Its ability to detect CTCs has been already demonstrated on interesting methods, however, their limits of detection and selectivity were still limiting factors for its broader application.[116, 117]

Analysis of cancer markers presents an important task not only in a diagnosis, but also in a treatment and monitoring of a progression. Human epidermal growth factor receptor 2 (Her2) is associated with breast, lung, and ovarian cancer, and is overexpressed in almost 25 % cases. Epithelial cell adhesion molecule (EpCAM) can be linked to human adenocarcinomas and squamouscell carcinomas or also breast, ovarian, and colon carcinomas. Multiplex detection of these two markers can considerably improve the reliability of follow-up diagnosis. The here presented method is based on a competitive approach similar to processes found in immunology. The analyte (Her2, EpCam) is detected via a decrease of the analytical signal of the labeled reference standard — which logically provides the highest signal, when there is no analyte present in the sample. General approach of the analysis is shown in the figure 13A. This approach potentially offers a simultaneous detection of both analytes in a single analytical run. First, the as-prepared Fe_2O_3@anti-EpCAM@Amti-

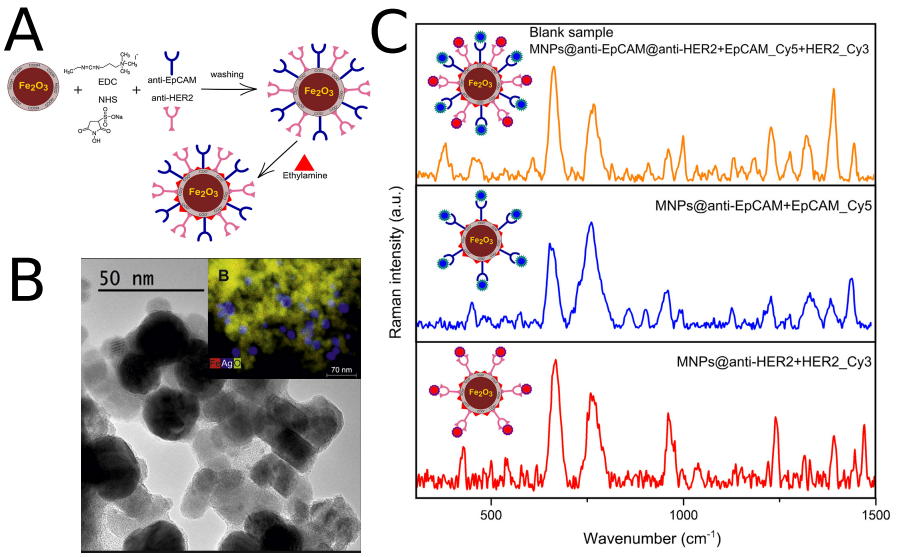

Figure 13: A: General scheme of the analysis; B: microscopy images of the nanosensor, insert shows results of the EDX analysis: yellow - magnetic Fe_2O_3 nanoparticles, blue - silver nanoparticles; C: Raman spectra obtained by the analysis of model samples.[118]

Her2 nanosensor was characterized using electron microscopy with results displayed in the figure 13B. It is shown that spherical silver nanoparticles (black) have an average diameter of 28 nm, and are surrounded by a considerably smaller spherical iron oxide nanoparticles. Analogical results were obtained also by a performed elemental analysis (insert B), where silver nanoparticles are shown in blue color, and iron oxide nanomaterial is shown in red/yellow colors. Next to a microscopy, the nanomaterial has been also characterized using infrared spectroscopy, x-ray diffraction, and ζ-potential. Maghemite (gama-Fe_2O_3) and silver were identified as the only crystalline phases. Infrared spectra indicated a successful anchoring of antibodies, based on a presence of characteristic protein bands, including Amide I (–CO–NH) and Amide II (–CO–NH–)at 1570 and 1650 cm^{-1}, respectively. Anchoring of the proteins is also supported by a measured ζ-potential, which considerably changed from -22.3 mV for the bare magnetic nanoparticles to 9 mV for a fully functionalized nano-system. In the next step, the Fe_2O_3@anti-EpCAM@Amti-Her2 nanosensor was characterized using Raman spectroscopy. As mentioned above, the multiplex analysis was based on a competition approach between tagged and naturally occurring analytes. The labeled variant of Her2 was Her2-Cy3, and analogically, EpCAM-Cy5 for EpCAM. Raman spectroscopy was employed in a study of the interaction between the sensor and tagged analytes. Obtained spectra are shown in the figure 13C, where yellow trace represents a spectrum of a model sample containing the sensor and both tagged antigens, namely Her2-Cy3, and EpCAM-Cy5. Analogically, blue and red

spectra represent the analysis of Her2, and EpCAM, respectively. All three spectra contain characteristic protein bands, including Amide III (1240 cm^{-1}), and characteristic signals of both cyanins: Cy3 (373 cm^{-1}) and Cy5 (475 cm^{-1}). Importantly, addition of both analytes into the measured sample caused a significant decrease of in the intensity of both tags. Moreover, Raman signals of both tags were normalized to the intensity of a spectral band present at 660 cm^{-1} (characteristic to tyrosine) in order to achieve a better repeatability and reliability. The comparison of ratios allowed to minimize an effect of non-specific spectral differences between both, technical and biological replicates. This procedure allowed to detect both analytes at a common limit of detection 4.9 $ng.L^{-1}$.
Finally, the method was tested on a set of real samples (whole human blood), ten from two human volunteers were collected and analyzed five times to perform a statistical evaluation. Student's t-tests were performed to determine the significance of differences of average intensity ratios for signals of particular tags (Cy3 and Cy5) between blank and spiked blood samples (c = 5 $ng.L^{-1}$ of both analytes). The average calculated p-values per sample were 0.0093 for HER2 and 0.0016 for EpCAM.

Generally used analytical approaches aimed on an analysis of cancer markers in clinical samples are commonly based on a detection of fluorescence. These methods are able to detect proteins at ultra-low concentrations; however, high risk of autofluorescence and photobleaching can not be neglected, and mark them difficult to apply them globally. Here presented magnetic nanosensor for the multiplex detection of Her2 and EpCAM could be an interesting alternative. The developed sensor enables simultaneous analysis of these two important tumor markers at <5 $ng.L^{-1}$ limits of detection even in a relatively complex blood samples.
The benefit of such an approach is in a possible exploration of Her2 and EpCAM on a surface of circulating tumor cells. This step is planned in the follow-up research.

3.10 IMAGING OF GROWTH FACTORS ON A HUMAN TOOTH ROOT CANAL BY SURFACE-ENHANCED RAMAN SPECTROSCOPY

Endodontic treatment of immature permanent tooth with necrotic pulp is one of the most challenging treatment options in endodontics.[119] The standard approach is a root canal treatment, which involves complete removal of the necrotic pulp, chemo-mechanical preparation of root canal walls and obturation; however, the prognosis of conventionally treated immature teeth is quite low and leads to a loss of the teeth before adulthood of the patient.[120] All disadvantages of conventional root canal treatment can be solved by particular regenerative treatment modalities. Although it has been proved *in vitro* that isolated stem cells of dental origin are able to form pulp-like tissue with deposition of tubular dentin, if they are transplanted in a suitable carrier system, this cell-based approach is affected by several problems. As an alternative option, cell-free approach of regenerative treatment seems to be feasible treatment modality as proved by recent reports.[121] This approach relies on intracanal delivery of scaffold which is rich on growth factors and can contain stem cells or is able to attract such cells residing in the periapical region. Very important step is also conditioning of dentin surface, because extracellular matrix of dentin is rich on growth factors, which were embedded during dentinogenesis into the collagen template as it mineralizes. The growth factors of extracellular dentinal matrix, which are assumed to play the most significant role in pulp-dentin regeneration are transforming growth factor-beta1 (TGF-beta1), bone morphogenetic protein-2(BMP-2) and basic fibroblast growth factor (bFGF). Here presented approach employing surface enhanced Raman spectroscopy allows to simultaneously visualize above mentioned growth factors directly on a dentin surface.

Here presented approach is based on a functionalized Fe_3O_4@Ag nanocomposite with covalently anchored antibodies tagged using Raman tags, namely Cy3, Cy5, and Cy7. First, the as-prepared nanomaterial was evaluated using electron microscopy - results show a presence of silver nanoparticles with size around 30 nm, and clusters of iron oxide nanoparticles of size around 10 nm. The synthesis of the nanosenor was next to electron microscopy and Raman techniques monitored also using a measured ζ-potential in analogy with previous reports. Obtained values increased from -42 mV for a Fe_3O_4@Ag nanocomposite to 2 mV for nanocomposite functionalized using tagged antibodies. This considerable change can detonate a successful binding of the tagged antibodies on the surface of nanocomposite. Raman spectroscopy measurements, performed at particular steps of the synthesis, show a successful tagging of all there antibodies, namely anti-TGF-β1, AntibBMP-2, and AntibFGF using Cy3, Cy5, and Cy7. Next, interaction of the nanomaterial was evaluated on a

physiological sample (dentin surface) using fluorescence microscopy to i) study optical properties of the nanosenor, and ii) evaluate a distribution of the sensor over the dentin surface. Results show that all three sensors can be visualized with a suitable signal intensity and that the dentin surface apparently contains places with localized growth factors.

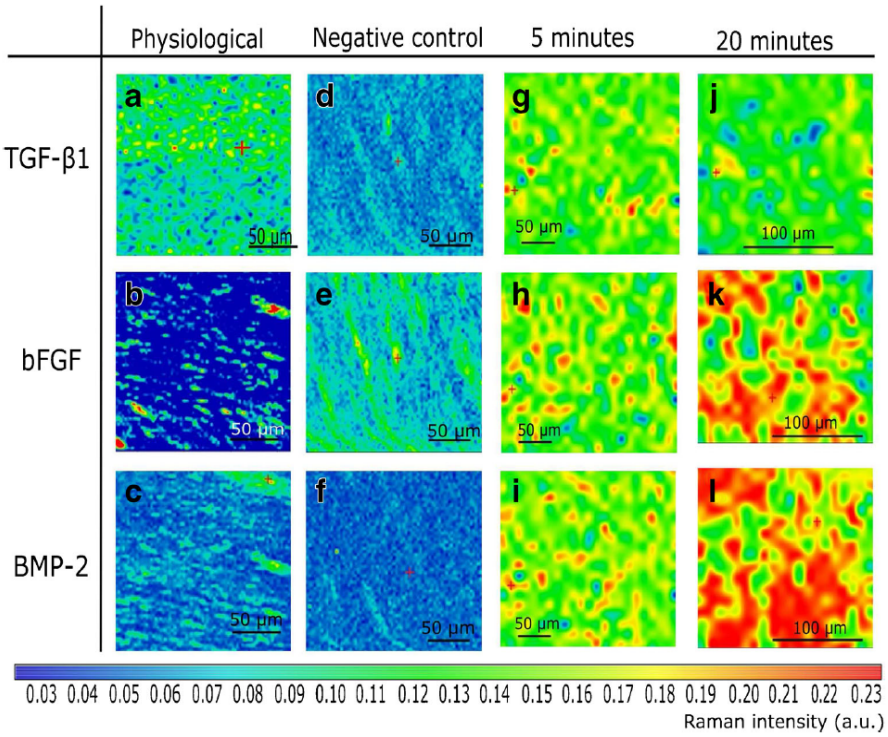

Figure 14: SERS spectral maps obtained by the analysis of selected samples of dentin. Physiological sample was obtained without any treatment. Negative control represents a sample with a smear layer, which efficiently blocks the sample surface, and 5 and 20 minutes samples were obtained by a treatment of dentin using EDTA for 5 or 20 minutes, respectively.[122]

Finally, the prepared nanosensor was tested in the imaging of these growth factors on the surface of dentin treated using EDTA for various time intervals, namely 5, and 20 minutes. For a comparison, physiological sample (without any treatment) and negative control (dentin with a smear layer blocking the surface) were also analyzed. Obtained results are shown in the figure 14. Parts a - c show a distribution of growth factors TGF-β1, bFGF, and BMP-2 on a surface of the physiological sample. It can be seen that the first named is present at relatively higher amounts. Analysis of the negative control (parts d-f) displays a considerable decrease in the intensities belonging to all three tags. The five-minutes treatment using EDTA (parts g - i) led to an increase of abundances of all there factors over values found in the physiological sample, and twenty-minutes treatment (parts j - l)

led to a further increase of the SERS intensity; with one exception, the TGF-β1. This growth factor was probably washed out by the excess of EDTA, as described in the previous works by Zeng *et al.*.[123]

4

CONCLUSIONS

Discovery of the surface enhanced Raman scattering changed the perception of the Raman spectroscopy not only from the perspective of ultra-trace analysis but It also allowed to markedly increase an achievable lateral resolution of Raman imaging through tip-enhanced Raman spectroscopy. The presented thesis briefly describes fundamental aspects of Raman effect, together with a surface enhanced Raman scattering. Further chapters describe the important application of Raman spectroscopy in the analysis of biomolecules, including proteins, nucleic acids, and analysis of cells. Application potential of Raman spectroscopy, surface enhanced Raman spectroscopy, and magnetically assisted surface enhanced Raman spectroscopy to analyze various physiologically active compounds is further demonstrated in the next chapter, where ten author's papers are discussed and summarized.

First, the method for a synthesis of silver nanoparticles, and their activation for SERS is described. Follwing works describe the utilization of abovementioned nanomaterials in the analysis of selected bases and discrimination of bacteria. Further, Raman modality, namely magnetically assisted surface enhanced Raman spectroscopy, is described and demonstrated on the analysis of dopamine, human IgG, and cancer biomarkers. Finally, the localization of growth factors on human dentin is shown. One of the main advantages of MA-SERS is given by two analytical parameters: increased selectivity to target molecules - compared to basic SERS methods based on bare nanoparticles, and lower limits of detection - compared with the same. Both important properties are basally given by two wired factors: i) presence of anchored selectors (antibodies) on the surface of the Fe_3O_4@Ag nanocomposite, and ii) possibility to magnetically separate the nanomaterial from the complex sample simply by an application of external magnetic force.

Developed methods present an interesting alternative to generally used approaches, including immunochemical methods, separation techniques, or electrochemical methods, and present a possible future perspective of analytical methods applicable not only in medicinal diagnosis, but also in other aspects of human activities.

Part III

OUTLOOK

5

OUTLOOK ON THE FUTURE APPLICATIONS OF RAMAN SPECTROSCOPY

The research in the field of a modern biology and medicine partially depends on results obtained using the state of the art analytical instruments, deeper understanding of physiological processes frequently relies on the ability to reliably detect or quantify particular compounds present in a complex matrix, or to evaluate a whole profile of related compounds such as proteins, lipids, amino acids or nucleic acids. Development of modern instruments and development of new analytical methods thus presents a task with a high importance. Position of Raman spectroscopy in this area considerably improved with a discovery of surface enhanced Raman scattering, and with a development of Raman microscopy, as a combination of optical microscopy and Raman spectroscopy. This work had an important aim - to provide the information about results, which can be obtained by a combination of available options and demonstrate various possibilities of Raman spectroscopy. The first part briefly describes an introduction to the Raman spectroscopy, following part reports on achieved results.

Raman microscopy and surface enhanced Raman spectroscopy are standing at the beginning of their journeys. At least this can be prospectively presumed in the light of recent developments and future trends. Rapid development on the field of nanotechnologies produces novel nanomaterials endowed with interesting plasmon properties with an incredible cadence. Utilization of these structures in Raman spectroscopy decrease achievable limits of detection, improve selectivity or specificity, increase a reliability of finally developed analytical protocols. Recent discovery of graphene and graphene enhanced Raman spectroscopy, followed by discoveries of other perspective 2D nanomaterials, including hematene, silicene or black phosphorus, opened door to more advanced Raman substrates with multimodal properties. One example could be drug or gene delivery, combined with a simultaneously performed targeted imaging of their biological distribution. Recent developments on the field of core-shell nanaparticles or hybrid nanostructures allow to precisely control properties of the present surface plasmon and thus efficiently increase the amplification of resulting Raman signal. Last but not least, research on the field of metal organic frameworks or covalent organic frameworks allows introducing novel Raman substrates with better tuned properties. The future will tell.

BIBLIOGRAPHY

(1) Compton, A. H. *Physical Review* **1923**, *21*, 483–502.

(2) Smekal, A. *Naturwissenschaften* **1923**, *43*, 873.

(3) Krishnan, R. S.; Shankar, R. K. *Journal of Raman Spectroscopy* **1981**, *10*, 1–8.

(4) Selter, K. P.; Kunze, H. J. *Physics Letters A* **1978**, *68*, 57–58.

(5) Raman, C.; Krishnan, R. S. *Nature* **1928**, *121*, 501.

(6) Maiman, T. H. *Nature* **1960**, *187*, 493–494.

(7) Hirschfeld, T.; Chase, B. *Applied Spectroscopy* **1986**, *40*, 133–137.

(8) Shorigin, P. *Dokl. Akad. Nauk SSSR* **1953**, *87*, 201.

(9) Delhaye, M; Migeon, M. *C.R. Acad. Sci. Paris* **1966**, *262*, 1513.

(10) Fleishmann, M; Hendra, P. J.; McQuillan, A. J. *Chemical Physics Letters* **1974**, *26*, 4.

(11) Kneipp, K.; Wang, Y.; Kneipp, H.; Perelman, L. T.; Itzkan, I.; Dasari, R.; Feld, M. S. *Physical Review Letters* **1997**, *78*, 1667–1670.

(12) *Practical Raman Spectroscopy*; Gardiner, D. J., Graves, P. R., Eds.; Springer-Verlag: Berlin Heidelberg, 1989.

(13) Long, D. A., *The Raman effect: a unified treatment of the theory of Raman scattering by molecules*; Wiley: Chichester ; New York, 2002; 597 pp.

(14) Szymanski, H. A., *Raman Spectroscopy: Theory and Practice*; Springer US: 1967.

(15) Byrne, H. J.; Knief, P.; Keating, M. E.; Bonnier, F. *Chemical Society Reviews* **2016**, *45*, 1865–1878.

(16) Dyer, S.; Hardin, D. *Applied Spectroscopy* **1985**, *39*, 655–662.

(17) Everall, N.; Howard, J. *Applied Spectroscopy* **1989**, *43*, 778–781.

(18) Olsson, N.; Hegarty, J. *Journal of Lightwave Technology* **1986**, *4*, 396–399.

(19) Albrecht, M.; Creighton, J. *Journal of the American Chemical Society* **1977**, *99*, 5215–5217.

(20) Jeanmaire, D.; Vanduyne, R. *Journal of Electroanalytical Chemistry* **1977**, *84*, 1–20.

(21) Lombardi, J.; Birke, R.; Lu, T.; Xu, J. *Journal of Chemical Physics* **1986**, *84*, 4174–4180.

(22) Rao, S.; Raj, S.; Balint, S.; Bardina Fons, C.; Campoy, S.; Llagostera, M.; Petrov, D. *Applied Physics Letters* **2010**, *96*, 213701.

(23) Wei, H.; Xu, H. *Applied Physics a-Materials Science & Processing* **2007**, *89*, 273–275.

(24) Muntean, C. M.; Leopold, N.; Halmagyi, A.; Valimareanu, S. *Journal of Raman Spectroscopy* **2011**, *42*, 1925–1931.

(25) Muntean, C. M.; Bratu, I.; Leopold, N.; Purcaru, M. A. P. *Spectroscopy-Biomedical Applications* **2011**, *26*, 59–68.

(26) Muntean, C. M.; Bratu, I.; Leopold, N. *Spectroscopy-Biomedical Applications* **2011**, *26*, 245–254.

(27) Shi, M.; Zheng, J.; Liu, C.; Tan, G.; Qing, Z.; Yang, S.; Yang, J.; Tan, Y.; Yang, R. *Biosensors & Bioelectronics* **2016**, *77*, 673–680.

(28) Torres-Nunez, A.; Faulds, K.; Graham, D.; Alvarez-Puebla, R. A.; Guerrini, L. *Analyst* **2016**, *141*, 5170–5180.

(29) Girel, K.; Yantcevich, E.; Arzumanyan, G.; Doroshkevich, N.; Bandarenka, H. *Physica Status Solidi a-Applications and Materials Science* **2016**, *213*, 2911–2915.

(30) McArdle, H.; Spain, E.; Keyes, T. E.; Stallings, R. L.; Brennan-Fournet, M.; Forster, R. J. *Electrochemistry Communications* **2017**, *79*, 23–27.

(31) Lei, W.; Hai-Chao, L.; Hai-Feng, Z.; Yu, S.; Hao-Ran, X.; Ming, L.; Chun-Hua, Y.; Wen-Zhao, L.; Zheng-Qiang, L. *Chinese Journal of Analytical Chemistry* **2011**, *39*, 1159–1165.

(32) Gao, F.; Lei, J.; Ju, H. *Analytical Chemistry* **2013**, *85*, 11788–11793.

(33) Fleury, F.; Ianoul, A.; Kryukov, E.; Sukhanova, A.; Kudelina, I.; Wynne-Jones, A.; Bronstein, I. B.; Maizieres, M.; Berjot, M.; Dodson, G. G.; Wilkinson, A. J.; Holden, J. A.; Feofanov, A. V.; Alix, A. J. P.; Jardillier, J.-C.; Nabiev, I. *Biochemistry* **1998**, *37*, 14630–14642.

(34) Zhou, Q.; Zheng, J.; Qing, Z.; Zheng, M.; Yang, J.; Yang, S.; Ying, L.; Yang, R. *Analytical Chemistry* **2016**, *88*, 4759–4765.

(35) Tian, S.; Neumann, O.; McClain, M. J.; Yang, X.; Zhou, L.; Zhang, C.; Nordlander, P.; Halas, N. J. *Nano Letters* **2017**, *17*, 5071–5077.

(36) Ye, L.-P.; Hu, J.; Liang, L.; Zhang, C.-y. *Chemical Communications* **2014**, *50*, 11883–11886.

(37) Zlatanova, J. *Molecular and Cellular Biochemistry* **1990**, *92*, 1–22.

(38) Wu, Y.; Engen, J. R. *Analyst* **2004**, *129*, 290–296.

(39) Baldwin, M. A., *Peptides and Proteins Studied Using Mass Spectrometry*; Lindon, J. C., Tranter, G. E., Koppenaal, D. W., Eds.; Academic Press Ltd-Elsevier Science Ltd: London, 2017.

(40) Chetwynd, A. J.; Guggenheim, E. J.; Briffa, S. M.; Thorn, J. A.; Lynch, I.; Valsami-Jones, E. *Nanomaterials* **2018**, *8*, 99.

(41) Dawod, M.; Arvin, N. E.; Kennedy, R. T. *Analyst* **2017**, *142*, 1847–1866.

(42) Rubin, R.; Leonardi, C. *Methods in Enzymology* **1983**, *96*, 184–192.

(43) Stack, M. *Journal of Gas Chromatography* **1967**, *5*, 22–&.

(44) Tuma, R. *Journal of Raman Spectroscopy* **2005**, *36*, 307–319.

(45) Bizzarri, A. R.; Cannistraro, S. *Nanomedicine-Nanotechnology Biology and Medicine* **2007**, *3*, 306–310.

(46) Fabris, L.; Dante, M.; Nguyen, T.-Q.; Tok, J. B.-H.; Bazan, G. C. *Advanced Functional Materials* **2008**, *18*, 2518–2525.

(47) Heck, C.; Kanehira, Y.; Kneipp, J.; Bald, I. *Angewandte Chemie-International Edition* **2018**, *57*, 7444–7447.

(48) Gu, X.; Yan, Y.; Jiang, G.; Adkins, J.; Shi, J.; Jiang, G.; Tian, S. *Analytical and Bioanalytical Chemistry* **2014**, *406*, 1885–1894.

(49) Cheng, Z.; Choi, N.; Wang, R.; Lee, S.; Moon, K. C.; Yoon, S.-Y.; Chen, L.; Choo, J. *Acs Nano* **2017**, *11*, 4926–4933.

(50) Damborska, D.; Bertok, T.; Dosekova, E.; Holazova, A.; Lorencova, L.; Kasak, P.; Tkac, J. *Microchimica Acta* **2017**, *184*, 3049–3067.

(51) Zhou, L.; Liu, Y.; Wang, F.; Jia, Z.; Zhou, J.; Jiang, T.; Petti, L.; Chen, Y.; Xiong, Q.; Wang, X. *Talanta* **2018**, *188*, 238–244.

(52) Pal, S.; Harmsen, S.; Oseledchyk, A.; Hsu, H.-T.; Kircher, M. F. *Advanced Functional Materials* **2017**, *27*, 1606632.

(53) Yarbakht, M.; Nikkhah, M.; Moshaii, A.; Weber, K.; Matthaeus, C.; Cialla-May, D.; Popp, J. *Talanta* **2018**, *186*, 44–52.

(54) Zhang, Y.; Yang, P.; Muharnmed, M. A. H.; Alsaiari, S. K.; Moosa, B.; Almalik, A.; Kumar, A.; Ringe, E.; Khashab, N. M. *Acs Applied Materials & Interfaces* **2017**, *9*, 37597–37605.

(55) Zheng, Z.; Wu, L.; Li, L.; Zong, S.; Wang, Z.; Cui, Y. *Talanta* **2018**, *188*, 507–515.

(56) Camacho, S. A.; Sobral-Filho, R. G.; Aoki, P. H. B.; Constantino, C. J. L.; Brolo, A. G. *Acs Sensors* **2018**, *3*, 587–594.

(57) Sanchez-Purra, M.; Carre-Camps, M.; de Puig, H.; Bosch, I.; Gehrke, L.; Hamad-Schifferli, K. *Acs Infectious Diseases* **2017**, *3*, 767–776.

(58) Gjergjizi, B.; Cogun, F.; Yildirim, E.; Eryilmaz, M.; Selbes, Y.; Saglam, N.; Tamer, U. *Sensors and Actuators B-Chemical* **2018**, *269*, 314–321.

(59) Jarvis, R. M.; Goodacre, R. *Analytical Chemistry* **2004**, *76*, 40–47.

(60) Harz, M.; Rosch, P.; Peschke, K. D.; Ronneberger, O.; Burkhardt, H.; Popp, J. *Analyst* **2005**, *130*, 1543–1550.

(61) Zeiri, L.; Efrima, S. *Journal of Raman Spectroscopy* **2005**, *36*, 667–675.

(62) Naja, G.; Bouvrette, P.; Hrapovic, S.; Luong, J. H. T. *Analyst* **2007**, *132*, 679–686.

(63) Knauer, M.; Ivleva, N. P.; Liu, X.; Niessner, R.; Haisch, C. *Analytical Chemistry* **2010**, *82*, 2766–2772.

(64) Kang, T.; Yoo, S. M.; Yoon, I.; Lee, S. Y.; Kim, B. *Nano Letters* **2010**, *10*, 1189–1193.

(65) Catala, C.; Mir-Simon, B.; Feng, X.; Cardozo, C.; Pazos-Perez, N.; Pazos, E.; Gomez-de Pedro, S.; Guerrini, L.; Soriano, A.; Vila, J.; Marco, F.; Garcia-Rico, E.; Alvarez-Puebla, R. A. *Advanced Materials Technologies* **2016**, *1*, 1600163.

(66) Prucek, R.; Panáček, A.; Fargašová, A.; Ranc, V.; Mašek, V.; Kvítek, L.; Zbořil, R. *CrystEngComm* **2011**, *13*, 2242.

(67) Panacek, A.; Kvitek, L.; Prucek, R.; Kolar, M.; Vecerova, R.; Pizurova, N.; Sharma, V. K.; Nevecna, T.; Zboril, R. *Journal of Physical Chemistry B* **2006**, *110*, 16248–16253.

(68) Le Ru, E. C.; Etchegoin, P. G.; Grand, J.; Felidj, N.; Aubard, J.; Levi, G. *Journal of Physical Chemistry C* **2007**, *111*, 16076–16079.

(69) Bell, S.; Kolobova, I.; Crapper, L.; Ernst, C. *Molecular Syndromology* **2016**, *7*, 302–311.

(70) Ohdoi, C.; Nyhan, W. L.; Kuhara, T. *Journal of Chromatography B-Analytical Technologies in the Biomedical and Life Sciences* **2003**, *792*, 123–130.

(71) Guan, Y. Q.; Chu, Q. C.; Ye, J. N. *Analytical and Bioanalytical Chemistry* **2004**, *380*, 913–917.

(72) Ranc, V.; Hruzikova, J.; Maitner, K.; Prucek, R.; Milde, D.; Kvitek, L. *JOURNAL OF RAMAN SPECTROSCOPY* **2012**, *43*, 971–976.

(73) Sharma, B.; Frontiera, R. R.; Henry, A.-I.; Ringe, E.; Van Duyne, R. P. *Materials Today* **2012**, *15*, 16–25.

(74) Dina, N. E.; Zhou, H.; Colnita, A.; Leopold, N.; Szoke-Nagy, T.; Coman, C.; Haisch, C. *Analyst* **2017**, *142*, 1782–1789.

(75) Boardman, A. K.; Wong, W. S.; Premasiri, W. R.; Ziegler, L. D.; Lee, J. C.; Miljkovic, M.; Klapperich, C. M.; Sharon, A.; Sauer-Budge, A. F. *Analytical Chemistry* **2016**, *88*, 8026–8035.

(76) Lin, C.-C.; Lin, C.-Y.; Kao, C.-J.; Hung, C.-H. *Sensors and Actuators B-Chemical* **2017**, *241*, 513–521.

(77) Prucek, R.; Ranc, V.; Kvítek, L.; Panáček, A.; Zbořil, R.; Kolář, M. *The Analyst* **2012**, *137*, 2866.

(78) Schulze, G.; Jirasek, A.; Yu, M. M. L.; Lim, A.; Turner, R. F. B.; Blades, M. W. *Applied Spectroscopy* **2005**, *59*, 545–574.

(79) Hui, C.; Guo-chang, J.; Jing-lin, Y.; Yong-quan, W. *Spectroscopy and Spectral Analysis* **2007**, *27*, 1148–1151.

(80) Hobro, A. J.; Smith, N. I. *Vibrational Spectroscopy* **2017**, *91*, 31–45.

(81) Read, D. S.; Whiteley, A. S. *Journal of Microbiological Methods* **2015**, *109*, 79–83.

(82) Kuzmin, A. N.; Pliss, A.; Prasad, P. N. *Analytical Chemistry* **2014**, *86*, 10909–10916.

(83) Konorov, S. O.; Schulze, H. G.; Caron, N. J.; Piret, J. M.; Blades, M. W.; Turner, R. F. B. *Journal of Raman Spectroscopy* **2011**, *42*, 576–579.

(84) Draux, F.; Gobinet, C.; Sule-Suso, J.; Trussardi, A.; Manfait, M.; Jeannesson, P.; Sockalingum, G. D. *Analytical and Bioanalytical Chemistry* **2010**, *397*, 2727–2737.

(85) Meade, A. D.; Clarke, C.; Draux, F.; Sockalingum, G. D.; Manfait, M.; Lyng, F. M.; Byrne, H. J. *Analytical and Bioanalytical Chemistry* **2010**, *396*, 1781–1791.

(86) Ranc, V.; Srovnal, J.; Kvítek, L.; Hajduch, M. *The Analyst* **2013**, *138*, 5983.

(87) Berke, J. D. *Nature Neuroscience* **2018**, *21*, 787–793.

(88) Lohani, S.; Martig, A. K.; Underhill, S. M.; DeFrancesco, A.; Roberts, M. J.; Rinaman, L.; Amara, S.; Moghaddam, B. *Neuropsychopharmacology* **2018**, *43*, 2083–2092.

(89) Wickham, R. J.; Park, J.; Nunes, E. J.; Addy, N. A. *Jove-Journal of Visualized Experiments* **2015**, e52468.

(90) Kishida, K. T.; Sandberg, S. G.; Lohrenz, T.; Comair, Y. G.; Saez, I.; Phillips, P. E. M.; Montague, P. R. *Plos One* **2011**, *6*, e23291.

(91) Kim, M.; Kim, D. H.; Lee, Y. S.; Jang, C.-G.; Yang, C. H.; Lee, S. *Forensic Toxicology* **2017**, *35*, 66–76.

(92) Wei, N.; Zhao, X.-E.; Zhu, S.; He, Y.; Zheng, L.; Chen, G.; You, J.; Liu, S.; Liu, Z. *Talanta* **2016**, *161*, 253–264.

(93) Kneipp, K.; Wang, Y.; Dasari, R.; Feld, M. *Spectrochimica Acta Part a-Molecular and Biomolecular Spectroscopy* **1995**, *51*, 481–487.

(94) Ranc, V.; Markova, Z.; Hajduch, M.; Prucek, R.; Kvitek, L.; Kaslik, J.; Safarova, K.; Zboril, R. *Analytical Chemistry* **2014**, *86*, 2939–2946.

(95) Fahey, J. *Journal of the American Medical Association* **1965**, *194*, 71–&.

(96) Tissot, J.; Spertini, F. *Journal of Chromatography A* **1995**, *698*, 225–250.

(97) Gapper, L. W.; Copestake, D. E. J.; Otter, D. E.; Indyk, H. E. *Analytical and Bioanalytical Chemistry* **2007**, *389*, 93–109.

(98) Balzerova, A.; Fargasova, A.; Markova, Z.; Ranc, V.; Zboril, R. *Analytical Chemistry* **2014**, *86*, 11107–11114.

(99) Lewallen, L. W.; Kremers, H. M.; Lahr, B. D.; Mabry, T. M.; Steckelberg, J. M.; Berry, D. J.; Hanssen, A. D.; Berbari, E. F.; Osmon, D. R. *Infection Control and Hospital Epidemiology* **2014**, *35*, 1323–1329.

(100) Tande, A. J.; Patel, R. *Clinical Microbiology Reviews* **2014**, *27*, 302–345.

(101) Dale, H.; Fenstad, A. M.; Hallan, G.; Havelin, L. I.; Furnes, O.; Overgaard, S.; Pedersen, A. B.; Karrholm, J.; Garellick, G.; Pulkkinen, P.; Eskelinen, A.; Makela, K.; Engesaeter, L. B. *Acta Orthopaedica* **2012**, *83*, 449–458.

(102) Kurtz, S. M.; Lau, E.; Watson, H.; Schmier, J. K.; Parvizi, J. *The Journal of Arthroplasty* **2012**, *27*, 61–65.e1.

(103) Fargašová, A.; Balzerová, A.; Prucek, R.; Sedláková, M. H.; Bogdanová, K.; Gallo, J.; Kolář, M.; Ranc, V.; Zbořil, R. *Analytical Chemistry* **2017**, *89*, 6598–6607.

(104) Schatten, H. In *Cell & Molecular Biology of Prostate Cancer: Updates, Insights and New Frontiers*, Schatten, H., Ed.; Springer International Publishing Ag: Cham, 2018; Vol. 1095, pp 1–14.

(105) Carlsson, S.; Vickers, A. J.; Roobol, M.; Eastham, J.; Scardino, P.; Lilja, H.; Hugosson, J. *Journal of Clinical Oncology* **2012**, *30*, 2581–2584.

(106) Lorente, J. A.; Arango, O.; Bielsa, O.; Cortadellas, R.; Gelabert-Mas, A. *International Journal of Biological Markers* **2002**, *17*, 84–89.

(107) Jiang, Y.; Michael, C. W. *Modern Pathology* **2016**, *29*, 104A–104A.

(108) Chaloupková, Z.; Balzerová, A.; Bařinková, J.; Medříková, Z.; Šácha, P.; Beneš, P.; Ranc, V.; Konvalinka, J.; Zbořil, R. *Analytica Chimica Acta* **2018**, *997*, 44–51.

(109) Wittekind, C.; Neid, M. *Oncology* **2005**, *69 Suppl 1*, 14–16.

(110) Tellez-Gabriel, M.; Cochonneau, D.; Cade, M.; Jubelin, C.; Heymann, M.-F.; Heymann, D. *Cancers* **2019**, *11*, 19.

(111) Ashworth, T. *Aust Med J* **1869**, *14*, 146–149.

(112) Allard, W. J.; Matera, J.; Miller, M. C.; Repollet, M.; Connelly, M. C.; Rao, C.; Tibbe, A. G. J.; Uhr, J. W.; Terstappen, L. W.M. M. *Clinical Cancer Research: An Official Journal of the American Association for Cancer Research* **2004**, *10*, 6897–6904.

(113) Zou, D.; Cui, D. *Cancer Biology & Medicine* **2018**, *15*, 335–353.

(114) Khetani, S.; Mohammadi, M.; Nezhad, A. S. *Biotechnology and Bioengineering* **2018**, *115*, 2504–2529.

(115) Wu, T.; Cheng, B.; Fu, L. *Molecular Pharmacology* **2017**, *92*, 232–239.

(116) Zhang, Y.; Mi, X.; Tan, X.; Xiang, R. *Theranostics* **2019**, *9*, 491–525.

(117) Ferhan, A. R.; Jackman, J. A.; Park, J. H.; Cho, N.-J.; Kim, D.-H. *Advanced Drug Delivery Reviews* **2018**, *125*, 48–77.

(118) Balzerova, A.; Opletalova, A.; Ranc, V.; Zboril, R. *Applied Materials Today* **2018**, *13*, 166–173.

(119) Wigler, R.; Kaufman, A. Y.; Lin, S.; Steinbock, N.; Hazan-Molina, H.; Torneck, C. D. *Journal of Endodontics* **2013**, *39*, 319–326.

(120) Nosrat, A.; Homayounfar, N.; Oloomi, K. *Journal of Endodontics* **2012**, *38*, 1428–1434.

(121) Smith, A.; Scheven, B.; Takahashi, Y.; Ferracane, J.; Shelton, R.; Cooper, P. *Archives of Oral Biology* **2012**, *57*, 109–121.

(122) Ranc, V.; Žižka, R.; Chaloupková, Z.; Ševčík, J.; Zbořil, R. *Analytical and Bioanalytical Chemistry* **2018**.

(123) Zeng, Q.; Nguyen, S.; Zhang, H.; Chebrolu, H. P.; Alzebdeh, D.; Badi, M. A.; Kim, J. R.; Ling, J.; Yang, M. *Journal of Endodontics* **2016**, *42*, 1760–1766.

DECLARATION

I declare that this thesis was composed by myself, that the work contained herein is my own except where explicitly stated otherwise in the text, and that this work has not been submitted for any other processional qualification. Parts of this work have been published, as declared in the section 3.

Olomouc, May 2019

Václav Ranc

Václav Ranc

Václav Ranc

Digitally signed by Václav Ranc
Date: 2019.05.07 10:09:52 +02'00'

Part IV

APPENDIX

A

ATTACHED ARTICLES

CrystEngComm

Cite this: *CrystEngComm*, 2011, **13**, 2242

www.rsc.org/crystengcomm

PAPER

Re-crystallization of silver nanoparticles in a highly concentrated NaCl environment—a new substrate for surface enhanced IR-visible Raman spectroscopy†

Robert Prucek,*[a] Aleš Panáček,[a] Ariana Fargašová,[a] Václav Ranc,[b] Vlastimil Mašek,[c] Libor Kvítek[a] and Radek Zbořil*[a]

Received 26th October 2010, Accepted 24th November 2010
DOI: 10.1039/c0ce00776e

The common approach of silver nanoparticles activation for surface enhanced Raman spectroscopy often exploits an addition of chloride ions, generally at low concentrations of about 0.1–10 mM in the final dispersion. For the first time, we report the applicability of a highly concentrated NaCl solution (final concentration of 400 mM) for the SERS activation of silver nanoparticles (~30 nm). Microscopic, optical and particle size distribution measurements reveal the rapid and reproducible re-crystallization of the primary silver nanoparticles to one-order larger crystallites (~400 nm) already after 15 min after NaCl addition. The crystal growth mechanism is discussed with respect to the proved essential role of oxygen in the reaction system. The specific action of chloride ions is demonstrated through a comparison with NaBr and NaI solutions of the identical concentrations, which do not induce the analogous crystallization process. The recrystallized silver particles are efficient in an enhancement of the Raman signal not only for visible (488 nm) but also for near infrared laser excitation (1064 nm) as illustrated with the representative spectra of adenine.

Introduction

Fleischmann's 1974 discovery of Surface Enhanced Raman Scattering (SERS) on a silver electrode,[1] and especially its re-discovery on colloidal silver particles in 1977 by Creighton,[2] started the extensive development of a new and very sensitive analytical method[3–7] enabling to detect molecules in the concentration range from pico- to femtomols.[8] High enhancements of SERS even allowed the detection of individual molecules adsorbed on a single silver particle.[9–12] Some studies have shown that the highest value of enhancement is achieved only on the silver particles of a certain size which are referred to as 'hot particles'. The optimal size of these hot particles depends on the wavelength of the laser used for excitation and ranges from approximately 70 nm to 200 nm for excitation wavelengths between 488 and 647 nm.[13] For the commonly used argon laser with a wavelength of 514.5 nm, the 'hot particle size' is reported from 80 to 100 nm.[8,14] For a use of lasers with an excitation wavelength in the red region ($\lambda = 785$ nm), and especially in the NIR region ($\lambda = 1064$ nm), we can assume that the highest enhancement of the Raman signal would be achieved with particles of around 400 nm in diameter. Nevertheless, the preparation of such large particles represents a hard task from the synthetic viewpoint. Moreover, particles of these dimensions are unstable and usually settle within a few hours. Silver nanoparticles (Ag NPs) of 20–30 nm in sizes can be stable for several months or years, even without any extra stabilization. However, these small particles themselves usually do not provide enhancement of the Raman signal. For this purpose, they must be activated for example by the addition of some inorganic ions.[7,15–18] The most frequently used activation agents of the silver nanoparticles prepared by the common reduction procedures[2,19,20] include halide ions, particularly chlorides.[21–24] However, the mechanism of the activation has not yet been fully explained.[25–29] One possible explanation is based on the formation of silver particle aggregates.[29] Recently, it has been shown that a very strong increase in the Raman signal is achieved in nanocrystal junction sites between two nanoparticles.[30–32]

In this work, we report a simple and reproducible method for the activation of monodispersed Ag NPs by introducing the concentrated NaCl solution (resulting concentration of 400 mM) into the Ag NP dispersion. It is worth mentioning that the effect of as-high concentrations of chloride ions, which is one to three orders higher than commonly mentioned in the literature, have

[a]*Regional Centre of Advanced Technologies and Materials, Department of Physical Chemistry, Faculty of Science, Palacky University, 17 Listopadu 1192/12, 771 46 Olomouc, Czech Republic. E-mail: zboril@prfnw.upol.cz; robert.prucek@upol.cz; Fax: +420 585 634 761; Tel: +420 585 634 427*
[b]*Department of Analytical Chemistry, Faculty of Science, Palacky University, 17 Listopadu 12, Olomouc, 771 46, Czech Republic*
[c]*Department of Pharmacology, Faculty of Medicine and Dentistry, Palacky University, Hněvotínská 3, Olomouc, 775 15, Czech Republic*

† Electronic supplementary information (ESI) available: Additional UV-vis absorption spectra, DLS measurement data, TEM images, XRD and SAED patterns. See DOI: 10.1039/c0ce00776e

not been studied yet. In almost all cases when chloride ions were used for the SERS activation, the final concentration of chlorides ranged from 0.1 mM to 20 mM.[20,21,24–27] As a principal result, the high concentration of chloride ions induces a rapid re-crystallization (in only a few minutes) of the primary Ag NPs to crystallites of around 400 nm, which convey reproducible Raman enhancement both for the visible and near infrared excitation.

Experimental

Preparation of the silver nanoparticles

Ag NPs, with a diameter of approximately 28 nm, were synthesized by a reduction of the complex $[Ag(NH_3)_2]^+$ cation with D-maltose. The initial concentrations of the reaction components were 10^{-3} M and 10^{-2} M for $AgNO_3$ and the reducing sugar, respectively. The concentration of the ammonia used was 5×10^{-3} M. Sodium hydroxide solution was added to the reaction system to adjust the value of pH at 11.5 ± 0.1, as well as to achieve a reaction time of 3–4 min. The as-prepared aqueous dispersion of the silver NPs was used for the subsequent experiments without any additional modifications. All the measurements were performed at the laboratory temperature (20 °C).

The specific Ag NPs treatment procedure for DLS and UV-vis, was as follows: The amount of 0.2 mL of the stock solution of Ag NPs was diluted by 0.7 mL of deionised water and then 0.1 mL of the 4 M NaCl solution was added. After adding chloride ions to the diluted dispersion of Ag NPs, the solution was quickly mixed and immediately (within several seconds), the measurements began. For the purpose of SERS measurements, 0.2 mL of the stock solution of Ag NPs was diluted with 0.7 mL of deionised water. Then, 0.1 mL of 4 M NaCl was quickly added to the diluted dispersion of Ag NPs and the solution was shaken. Next, an appropriate amount of 10^{-3} M solution of adenine was added, the solution was shaken again, and the Raman spectrum was collected.

Materials and chemicals

Silver nitrate (99.9%, Safina), ammonia (25% (w/w) aqueous solution, p.a., Lachema), sodium hydroxide (p.a., Lachema), sodium chloride/bromide/iodide (p.a., Sigma-Aldrich) and D(+)-maltose monohydrate (p.a., Riedel-de Haën) were used for the preparation of silver NPs without any further purification.

Instrumentation

The size of the well-dispersed silver NPs as well as the size of the agglomerates formed during the re-crystallization process was determined by a dynamic light scattering method (DLS) using a Zeta Plus analyzer (Brookhaven, USA). TEM observations of the silver NPs were performed with a JEM 2010 (Jeol, Japan) electron microscope at 160 kV of the acceleration voltage. SEM images were collected using a SU 6600 (Hitachi, Japan) at an accelerating voltage of 10 kV. UV-vis absorption spectra of the silver NP dispersions were acquired by using a Specord S 600 (Analytic Jena AG, Germany) spectrophotometer. Experiments concerning the usage of Raman spectrometry were performed using an FT-IR spectrometer (Nicolet FT-IR 6700, USA) with a Raman accessory (NXR FT-Nicolet module, USA) equipped with a liquid nitrogen-cooled germanium detector. An FT-Raman was equipped with an argon laser with a wavelength of 1064 nm (near infrared), laser power incident onto a sample was 300 mW, 256 scans were obtained for each measurement and data were averaged. Spectra were measured in the range from 200 to 2000 cm^{-1}. Raman experiments concerning visible excitation were performed at laboratory temperature on a Jobin-Yvon T 64 000 (Jobin-Yvon, France) spectrometer equipped with a liquid nitrogen-cooled CCD detector. The argon laser (Coherent Innova 90C FreD, Coherent Inc., $\lambda = 488$ nm) was used for the excitation. Spectra were registered in the range from 600 to 2000 cm^{-1} with 1 cm^{-1} resolution and 10 s scan time; 10 accumulations were made. The laser light power incident onto a sample was 100 mW.

Results and discussion

The primary Ag NPs were synthesised by a reduction of the complex $[Ag(NH_3)_2]^+$ cation with D-maltose.[33] Silver NPs obtained in this way are nearly monodispersed with an average particle size of 28 nm (as determined by the Dynamic Light Scattering method—DLS). With regard to the use of these Ag NPs in practical applications including SERS measurements, their time stability is an important practical aspect. Thus, the time stability of Ag NPs stored in a dark flask at the laboratory temperature was monitored by measuring their average size (DLS) and absorption spectra. During a period of 600 days, the average particle size remains constant (28.4 ± 0.8 nm) as proved by DLS data (inset in Fig. S1)† and by measuring the absorption spectra that were unchanged during the mentioned period of time (Fig. S1).† However, an application of these NPs (without further treatment) in SERS is not particularly effective, as these NPs usually do not provide any significant enhancement of the Raman signal.

The process of silver particle activation by a highly concentrated NaCl solution was monitored by measuring the average particle size (using the DLS method) and by recording the UV-vis absorption spectra. The experiments were repeated twelve times in order to verify the reproducibility (see error bars, Fig. 1A). The particle size was averaged out after every minute of the measurement and the resulting values for the final concentration of Cl^- equal to 400 mM are shown in Fig. 1A. The representative absorption spectra demonstrating the change in the average size of Ag NPs are depicted in Fig. 1B. Immediately after the addition of NaCl solution to Ag NPs, there was a considerable change in the colour of the dispersion of Ag NPs with corresponding changes in its absorption spectrum. The colour of the dispersion changes immediately from yellow to violet. 20 s after the addition of sodium chloride solution, the colour of the dispersion becomes grey. The original absorption peak with the maximum at 410 nm, corresponding to the surface plasmon of the original nanoparticles, was considerably suppressed, while at the same time, the secondary peak with the maximum at 570 nm has emerged. The secondary peak with the similar maximum was previously reported for Ag particles with dimensions of 100–110 nm.[34,35] After the first minute following the addition of chloride ions, there was a further decrease in the absorption maximum at 410 nm and a shift of the secondary absorption maximum to 650 nm, which moved to 680 nm over the next two minutes. This shift in the position of the secondary

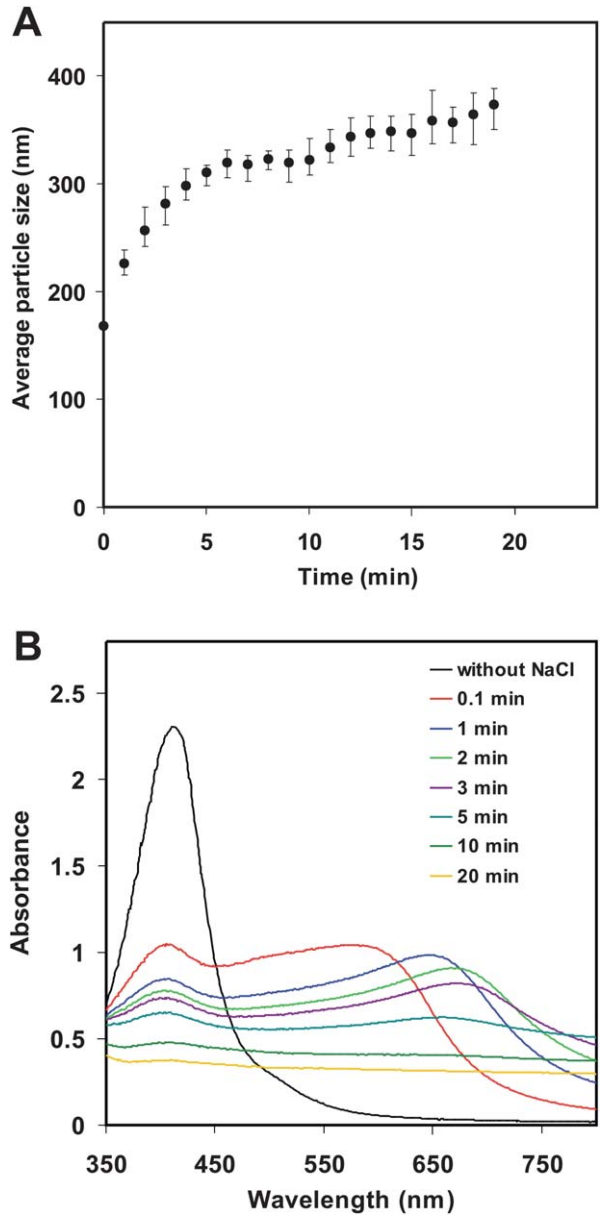

Fig. 1 Time dependence of average size of Ag NPs (A) and the representative UV-vis absorption spectra (B) recorded during 20 min after the addition of the NaCl solution (the final concentration of 400 mM).

absorption peak can be considered as a confirmation of the gradual increase in the average size of Ag particles. After the 5th minute, the absorption spectra already had a very flat course without any pronounced maximum, which is characteristic of Ag particles with dimensions of about 200 nm and larger.[35]

In order to explore the re-crystallization process including changes in the size and morphology of Ag NPs after NaCl addition, several representative samples were analysed by TEM. Fig. 2A shows the primary non-activated particles included in the stock solution of Ag NPs without the presence of any chloride anions. The average particle size (24 nm) determined by TEM is in a good accordance with the value determined by the DLS method (28 nm). From TEM measurements, the average particle size was determined by the image analysis performed for two independent images containing 50 nanoparticles in minimum in the window. Other samples were taken at the time of 30 s, 2 min, and 15 min after the addition of NaCl solution. In these cases, the samples were diluted by the tenfold amount of deionised water before spreading on a copper grid coated with a carbon layer, due to the suppression of the reaction that could be in progress further (in case of non-dilution). After 30 s, TEM image revealed considerable amount of silver nanoparticles with the size of equal to or below 25 nm (~90%) (Fig. 2B). However, a certain number of particles (~10%) had dimensions ranging from 50 to 100 nm (inset in Fig. 2B). In the sample taken 2 min after the addition of NaCl solution, the presence of Ag particles with a size of around 150 nm was observed, and the particles of dimensions of around 25 nm were almost not present (Fig. 2C). After 15 min, the large Ag particles with the size of around 400 nm were found in the dispersion (Fig. 2D), while any smaller particles and/or their aggregates were not detected. Approximately 20% of the Ag NPs were present in the form of well-defined crystalline shapes, such as hexagonal (Fig. 3A), rod-like (Fig. 3B), and triangular (Fig. 3C). The miscellaneous morphologies of recrystallized particles are probably related to the presence of particles with different shapes already present in the original dispersion (Fig. 3D, 3E, 3F). The single-crystal character and typical cubic structure of these recrystallized silver particles were confirmed by the selected area electron diffraction (inset in Fig. 3C). The chemical composition of transformed large silver particles was also confirmed by XRD measurement (Fig. S2).† The process of re-crystallization of silver nanoparticles induced by 400 mM NaCl was investigated at different reaction temperatures. These experiments were monitored *via* time-dependent UV-vis absorption measurements (Fig. S3).† The time changes in absorbance were accelerated/decelerated by increasing/decreasing the reaction temperature. The absorption spectrum obtained after 10 min since the addition of NaCl solution at a reaction temperature of 20 °C was almost the same as that recorded after 2 min since the addition of NaCl solution at a reaction temperature of 60 °C. TEM images of the sample taken after 20 s at this temperature revealed particles with sizes between 10 nm and 70 nm (Fig. S4A).† After 2 min since the addition of NaCl solution, the fully recrystallized large silver particles (~350 nm) were observed (Fig. S4B).† The obtained data confirm the reductive deposition along dissolution-re-growth mechanism as there are no TEM indications of the particle aggregation neither at 20 °C nor at 60 °C. TEM images reveal the intermediate presence of silver crystallites with a rather broad size distribution (Fig. 2B and Fig. S4A).† Just the simultaneous presence of smaller and larger crystals compared to the original particles is a strong evidence for dissolution-re-growth mechanism. The particle re-growth is finished as soon as all dissolved silver is consumed. This is supported by temperature-dependent observations when the final size of silver particles is almost the same independently on the temperature (compare Fig. 2D and Fig. S4B)† although the rate of crystal growth is evidently higher with increasing temperature (see Fig. S3).†

To get a deeper insight into the mechanism of the silver crystal growth induced by a highly concentrated NaCl solution, we performed similar experiments with NaBr and NaI solutions of the same final concentrations (400 mM). In all cases, the yellow colouring changed to the grey colour within several seconds. However, this colour change, implying for a disappearance of the

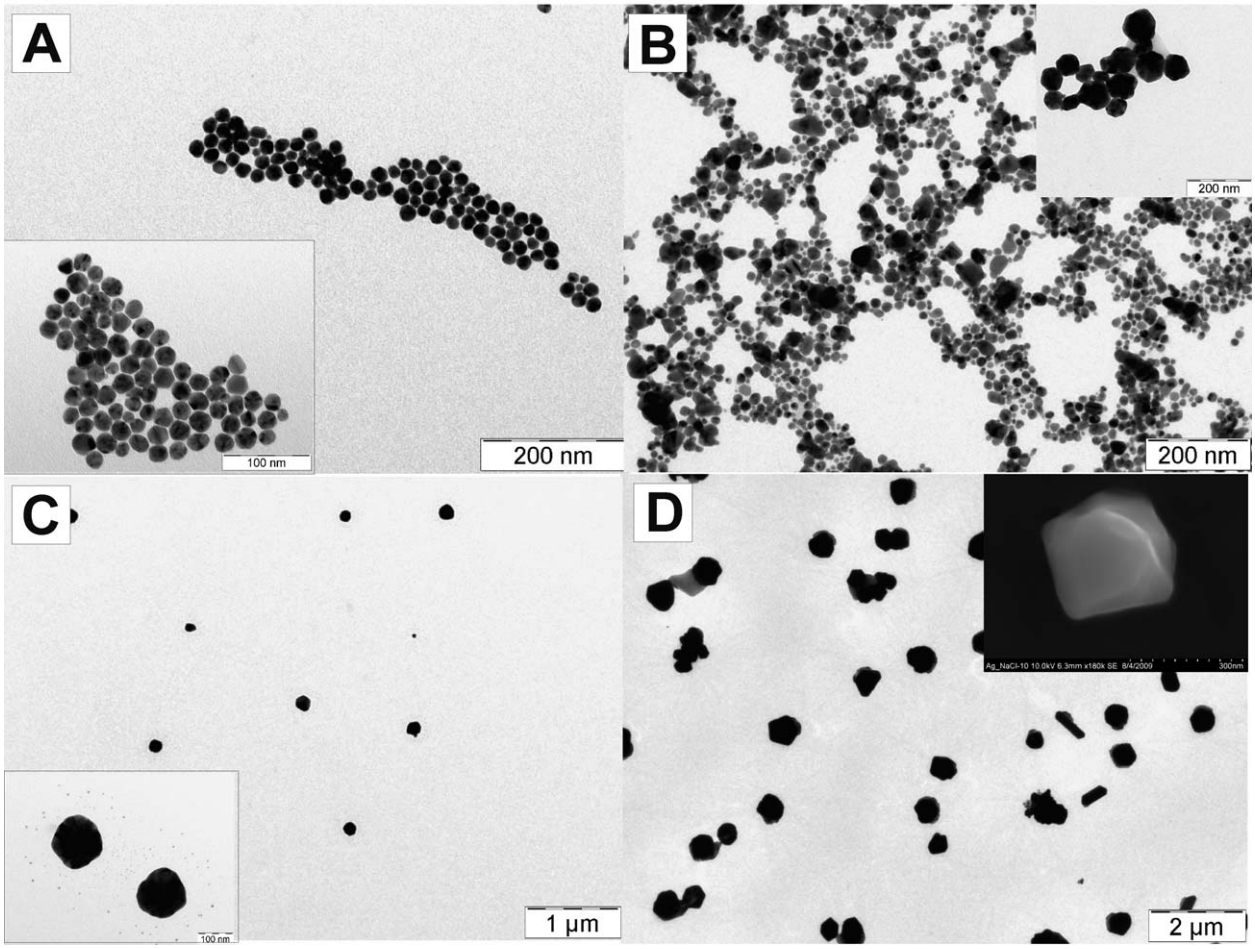

Fig. 2 TEM images of primary non-activated Ag NPs (A) and those formed by gradual crystallization after 30 s (B), 2 min (C), and 15 min (D) since the addition of the 4 M NaCl solution. The inset in D demonstrates the final 400 nm-sized single crystal imaged by SEM, while other insets show TEM images evidencing for gradual crystal growth.

original well-dispersed nanoparticles, is not due to the re-crystallization of silver nanoparticles as observed after the NaCl addition. In the case of NaBr and NaI additions, the primary dissolution followed by a secondary precipitation of silver halogenides are competitive processes, which were proved by detailed TEM (Fig. 4) and UV-vis measurements (Fig. S5).† TEM images of the objects formed after NaBr (NaI) addition revealed presence of aggregates (particles) with the sizes of several tens to hundreds of nanometres (Fig. 4A and 4C). These objects were, after the radiation by electrons in the transmission electron microscope, subjects to partial (Fig. 4B) or almost total destruction (Fig. 4D). This might be a proof of the formation of a certain amount of AgBr (in the case of NaBr addition) or even prevailing amount of AgI (in the case of NaI addition). The chemical compositions were confirmed by the selected area electron diffraction (Fig. S6A and S6B).† The different action of iodide ions in comparison with chloride ions is also reflected in the obtained absorption spectra (see representative spectra after iodide addition in Fig. S5B)† when almost zero absorbance, between wavelengths of 500–900 nm, registered after 20 min since the NaI addition, gives further support for an absence of metallic nanoparticles in the system. Evidently, the highly concentrated solutions of bromides and iodides are not applicable for activation of silver nanoparticle dispersion due to the precipitation of silver halogenides. It is well known that halide anions can serve as a precipitant of Ag^+ ions at a low concentration and a complexing agent at a high concentration of halides. The halide ions can react with the silver atoms and dissociate them from the surface of Ag particles. This phenomenon is known as the oxidative etching process.[36–38] Henglein *et al.*[39] have reported that oxidative etching of silver particles is accelerated through the presence of complexing agents. They observed that ligands that coordinated more strongly with silver induced the oxidative etching at much faster rates. The suggested mechanism underlying this phenomenon was that the silver atoms on the surface are coordinated by halide ions and this action is accompanied with a simultaneous pick-up of the electrons by oxygen. Under such conditions, the varying behaviour of Br^- and I^- ions compared to Cl^- is therefore given by significantly higher stability constants of AgX_2^- complexes with Br^- and I^- ions ($\beta_1 = 3.23$, $\beta_2 = 5.15$ for $AgCl_2^-$, $\beta_1 = 4.68$, $\beta_2 = 7.70$ for $AgBr_2^-$, $\beta_1 = 6.58$, $\beta_2 = 11.7$ for AgI_2^-). In the case of bromides and iodides, etched Ag^+ ions are more firmly tied up into a respective complex compound and the subsequent recrystallisation of particles proceeds with a greater difficulty (Br^-) or almost not at all (I^-). In summary, it can be concluded that chloride ions in

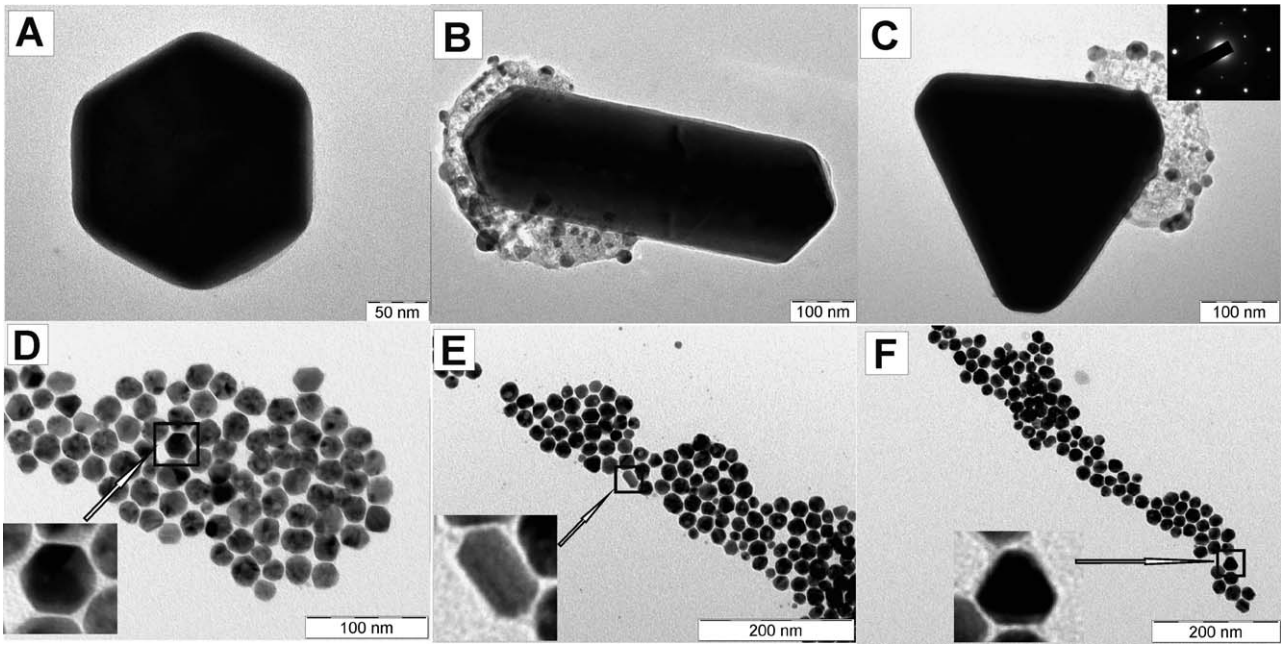

Fig. 3 TEM images taken 15 min after the addition of the 4 M NaCl solution exhibiting recrystallized Ag particles with various morphologies (A, B, C), and images of primary non-activated Ag NPs of the same crystal shapes (D, E, F).

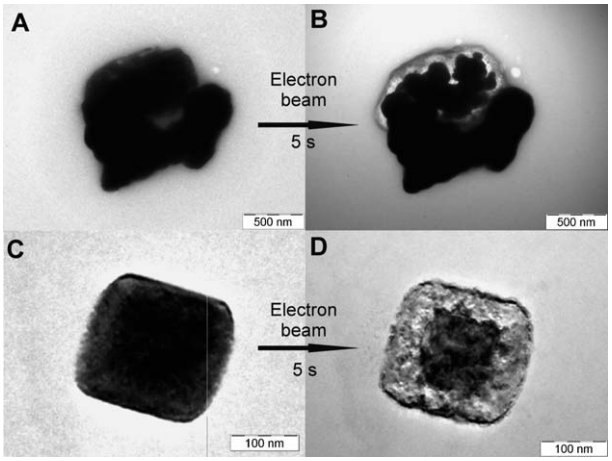

Fig. 4 TEM images demonstrating the electron beam induced transformation of particles formed after 15 min since the addition of the NaBr (A, B) and NaI (C, D).

a high concentration provide the optimal means for controlled re-crystallization of Ag NPs, while the solutions containing bromides, iodides and nitrate in the same concentrations are not able to induce the same activation effect.

In order to examine the role of oxygen in the chloride induced re-crystallization of Ag NPs, the dissolved oxygen was removed by bubbling argon in the solutions used. The sample was taken 15 min after the addition of NaCl solution and the transmission electron microscopy revealed large globular objects ranging from 2 to 3 μm in size (Fig. 5A). When these objects were explored in a high resolution mode, it was found out that they are composed of Ag NPs with dimensions of around 20 nm, which are well seen mainly on the aggregate surface (Fig. 5B). We can certainly conclude that, in the absence of oxygen, the aggregation of the primary Ag NPs occurs as a predominant process, while their re-crystallization is suppressed. The question is how oxygen acts in this oxidative etching process. Xia *et al.*[40] have studied the similar phenomenon after the addition of chloride ions in the polyol synthesis of Ag NPs. In the presence of oxygen, they observed enhanced oxidation and preferential etching of twinned particles, leaving the single-crystals to grow. When this reaction was performed without the presence of oxygen, there was no oxidation to compete with the polyol reduction, and multiply twinned particles grew quickly into long nanowires.

The original Ag NPs (~30 nm), as well as the recrystallized Ag particles transformed after the addition of NaCl (~400 nm) were tested for application in surface enhanced Raman spectroscopy with adenine as an model analyte. SERS measurements were performed for the two excitation laser wavelengths (1064 nm and 488 nm). The final concentrations of adenine were 2.5×10^{-5} M ($\lambda = 1064$ nm) and 5×10^{-6} M ($\lambda = 488$ nm). Fig. 6A shows the typical SER spectrum of adenine recorded using the recrystallized Ag particles for the excitation wavelength of 1064 nm. When the diluted dispersion of the original Ag NPs (28 nm) without NaCl activation was used, no spectrum of adenine was registered (Fig. 6B). For the evaluation of enhancement, the Raman spectrum of adenine alone (concentration of 0.1 M) was measured without the presence of Ag NPs (Fig. 6C).

The enhancement of the Raman signal was monitored depending on the period of time that elapsed since the addition of the NaCl solution to the diluted dispersion of original Ag NPs (Fig. 6D). For an excitation wavelength of 1064 nm, the enhancement reached maximum between the 12th and the 16th minute. The increase in the enhancement during the first 12 min can be explained by an increase in the particle size caused by the re-crystallization process. After the mentioned time elapsed since the addition of sodium chloride, the particle size reached a value of around 400 nm, which is in good agreement with the

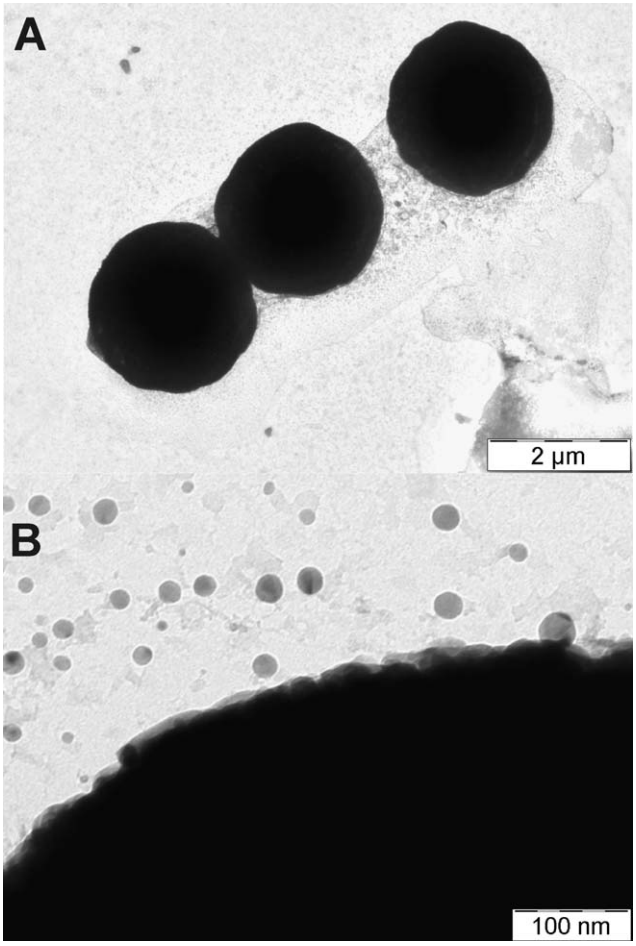

Fig. 5 TEM images of Ag aggregates obtained after the addition of NaCl (400 mM) using oxygen-free solutions (A). Detail of nanoparticles on the aggregate surface and in its near surrounding (B).

prediction of optimal size of silver particles based on previously published results regarding the dependence of enhancement of the Raman signal on the particle size for the given excitation wavelength.[13] In the case of excitation at 488 nm, a considerable enhancement was achieved within two minutes after the addition of the NaCl solution. The size of Ag particles reached approximately 150 nm at this moment (Fig. 2C). Surprisingly, the enhancement grew further with the increasing particle size. This fact can be probably connected to the irregular surface of most Ag particles providing active sites for the enhancement and consequent investigation of this phenomena is under progress. Generally, it is well-known that chloride anions, in low concentrations (about 10 mM),[20,21,24–27] induce the aggregation process and the junctions among silver nanoparticles (tens of nanometres) represent the active sites for the Raman signal enhancement. However, data presented in this work indicate that chloride ions (in high concentrations of about 400 mM) cause the formation of large silver particles (hundreds of nanometres), which are very efficient for the Raman signal enhancement.[13]

Accordingly, the presence of transformed Ag particles with dimensions of around 400 nm induced by 400 mM chloride ions is necessary for application in the NIR region. In summary, the mentioned facts would be of primary importance for the practical

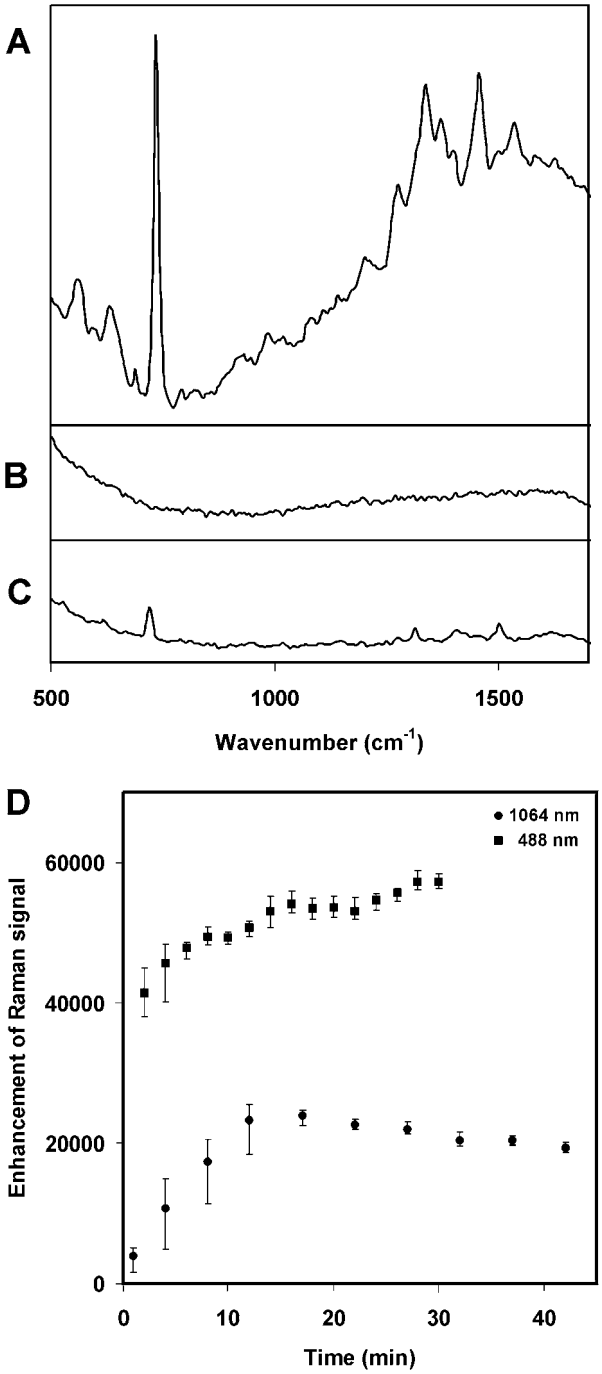

Fig. 6 Surface enhanced Raman spectrum of adenine in the presence of silver particles transformed by chloride ions (A). Raman spectrum of adenine in the presence of primary non-activated Ag NPs with (B). Raman spectrum of adenine in deionised water (C). All spectra were taken for an excitation wavelength of 1064 nm. Time dependence of enhancement of Raman signal of adenine after the addition of chloride ions for the excitation wavelengths of 1064 nm and 488 nm (D). The enhancement factor was determined by comparing the intensities of the most intensive peak in spectrum at 734 cm^{-1}.

use of the developed re-crystallization procedure in the surface enhanced NIR-visible Raman spectroscopy. It is worth to mention that when NaBr and NaI were used for the transformation of Ag NPs, no enhancement of the Raman signal of adenine was

recorded. This is in accordance with the above mentioned fact that application of Br^- and I^- anions in such high concentrations results in a formation of large amount of AgBr or AgI particles.

Conclusions

We described the simple and reproducible procedure how to activate silver nanoparticles (~30 nm) for an efficient application in the surface enhanced Raman spectroscopy. By adding the concentrated solution of chloride ions, we induced a rapid re-crystallization process towards larger silver crystals (~400 nm) providing a considerable enhancement of Raman signal with excitation in the near infrared region. This simple way to obtain SERS substrate possesses a great application potential in the analytical practice.

Acknowledgements

The authors gratefully acknowledge the support by the Operational Program Research and Development for Innovations - European Social Fund (project no. CZ.1.05/2.1.00/03.0058 of the Ministry of Education, Youth and Sports of the Czech Republic). This work has been supported by the Ministry of Education, Youth and Sports of the Czech Republic (project no. MSM6198959218, MSM6198959223, and 1M6198959201) and Czech Science Foundation (Project No. GAP304/10/1316).

References

1 M. Fleischmann, P. J. Hendra and A. J. McQuillan, *Chem. Phys. Lett.*, 1974, **26**, 163.
2 J. A. Creighton, C. G. Blatchford and M. G. Albrecht, *J. Chem. Soc., Faraday Trans. 2*, 1979, **75**, 790.
3 W. Xu, J. X. Zhang, L. D. Zhang, X. Y. Hu and X. L. Cao, *J. Nanosci. Nanotechnol.*, 2009, **9**, 4812.
4 J. Kneipp, H. Kneipp, A. Rajadurai, R. W. Redmond and K. Kneipp, *J. Raman Spectrosc.*, 2009, **40**, 1.
5 D. G. Thompson, A. Enright, K. Faulds, W. E. Smith and D. Graham, *Anal. Chem.*, 2008, **80**, 2805.
6 J. Kneipp; H. Kneipp; K. Kneipp., Surface-Enhanced Raman Spectroscopy-Based Optical Labels Deliver Chemical Information from Live Cells. In *New Approaches in Biomedical Spectroscopy*, Kneipp, K; Aroca, R; Kneipp, H; Wen trupByrne, E., ed. 2007; Vol. 963, pp 186.
7 C. Y. Wu, W. Y. Lo, C. R. Chiu and T. S. Yang, *J. Raman Spectrosc.*, 2006, **37**, 799.
8 K. Kneipp, Y. Wang, R. R. Dasari and M. S. Feld, *Appl. Spectrosc.*, 1995, **49**, 780.
9 S. M. Nie and S. R. Emery, *Science*, 1997, **275**, 1102.
10 K. Kneipp, Y. Wang, H. Kneipp, L. T. Perelman, I. Itzkan, R. Dasari and M. S. Feld, *Phys. Rev. Lett.*, 1997, **78**, 1667.
11 J. Kneipp, H. Kneipp and K. Kneipp, *Chem. Soc. Rev.*, 2008, **37**, 1052.
12 L. Brus, *Abstracts of Papers of the American Chemical Society*, 2001, **221**, 112.
13 S. R. Emory, W. E. Haskins and S. M. Nie, *J. Am. Chem. Soc.*, 1998, **120**, 8009.
14 R. L. Garrell, *Anal. Chem.*, 1989, **61**, 401A.
15 S. E. J. Bell and N. M. S. Sirimuthu, *J. Phys. Chem. A*, 2005, **109**, 7405.
16 N. R. Yaffe and E. W. Blanch, *Vib. Spectrosc.*, 2008, **48**, 196.
17 M. V. Canamares, J. V. Garcia-Ramos, S. Sanchez-Cortes, M. Castillejo and M. Oujja, *J. Colloid Interface Sci.*, 2008, **326**, 103.
18 Z. Jurasekova, J. V. Garcia-Ramos, C. Domingo and S. Sanchez-Cortes, *J. Raman Spectrosc.*, 2006, **37**, 1239.
19 P. C. Lee and D. Meisel, *J. Phys. Chem.*, 1982, **86**, 3391.
20 N. Leopold and B. Lendl, *J. Phys. Chem. B*, 2003, **107**, 5723.
21 A. M. Michaels, M. Nirmal and L. E. Brus, *J. Am. Chem. Soc.*, 1999, **121**, 9932.
22 Y. Maruyama and M. Futamata, *J. Raman Spectrosc.*, 2005, **36**, 581.
23 X. Q. Zou and S. J. Dong, *J. Phys. Chem. B*, 2006, **110**, 21545.
24 W. N. Leng, H. Y. Woo, D. Vak, G. C. Bazan and A. M. Kelley, *J. Raman Spectrosc.*, 2006, **37**, 132.
25 P. X. Zhang, Y. Fang, W. N. Wang, D. H. Ni and S. Y. Fu, *J. Raman Spectrosc.*, 1990, **21**, 127.
26 M. Campbell, S. Lecomte and W. E. Smith, *J. Raman Spectrosc.*, 1999, **30**, 37.
27 W. E. Doering and S. M. Nie, *J. Phys. Chem. B*, 2002, **106**, 311.
28 H. Bengter, C. Tengroth and S. P. Jacobsson, *J. Raman Spectrosc.*, 2005, **36**, 1015.
29 A. Otto, A. Bruckbauer and Y. X. Chen, *J. Mol. Struct.*, 2003, **661–662**, 501.
30 T. Dadosh, J. Sperling, G. W. Bryant, R. Breslow, T. Shegai, M. Dyshel, G. Haran and I. Bar-Joseph, *ACS Nano*, 2009, **3**(7), 1988.
31 W. Y. Li, P. H. C. Camargo, X. M. Lu and Y. N. Xia, *Nano Lett.*, 2009, **9**(1), 485.
32 L. Brus, *Acc. Chem. Res.*, 2008, **41**(12), 1742.
33 A. Panacek, L. Kvitek, R. Prucek, M. Kolar, R. Vecerova, N. Pizurova, V. K. Sharma, T. Nevecna and R. Zboril, *J. Phys. Chem. B*, 2006, **110**, 16248.
34 T. Jensen, L. Kelly, A. Lazarides and G. C. Schatz, *J. Cluster Sci.*, 1999, **10**, 295.
35 S. Schneider, P. Halbig, H. Grau and U. Nickel, *Photochem. Photobiol.*, 1994, **60**, 605.
36 S. H. Im, Y. T. Lee, B. Wiley and Y. N. Xia, *Angew. Chem., Int. Ed.*, 2005, **44**, 2154.
37 C. M. Cobley, M. Rycenga, F. Zhou, Z. Y. Li and Y. N. Xia, *Angew. Chem., Int. Ed.*, 2009, **48**, 4824.
38 J. Yang, Q. B. Zhang, J. Y. Lee and H. P. Too, *J. Colloid Interface Sci.*, 2007, **308**, 157.
39 A. Henglein, T. Linnert and P. Mulvaney, *Berichte Der Bunsen-Gesellschaft-Physical Chemistry Chemical Physics*, 1990, **94**, 1449.
40 B. Wiley, T. Herricks, Y. G. Sun and Y. N. Xia, *Nano Lett.*, 2004, **4**, 2057.

Research Article

Journal of RAMAN SPECTROSCOPY

Received: 12 July 2011 Revised: 27 October 2011 Accepted: 30 October 2011 Published online in Wiley Online Library: 22 December 2011

(wileyonlinelibrary.com) DOI 10.1002/jrs.3124

Quantification of purine basis in their mixtures at femto-molar concentration levels using FT-SERS

Vaclav Ranc,[a]* Jana Hruzikova,[b] Kamil Maitner,[b] Robert Prucek,[c] David Milde[b] and Libor Kvítek[c]

Surface-enhanced Raman scattering spectroscopy represents one of the unique techniques for studying nanoscale objects, and its distinctive properties can be used in the process of further analysis. The careful evaluation of the particular influence of selected key-role experimental parameters (e.g. pH value of measured sample mixture, size and distribution of used nanoparticles) and the influence of reduction agent used in the process of formation of desired nanoparticle objects presents an important task in the further study of surface-enhanced Raman scattering effect. A broad study of these experimental parameters was performed in this paper. The main aim of the presented work was to a demonstrate an application potential of selected experimental conditions in the determination of three purine bases: adenine, xanthine, and hypoxanthine. The resulting limits of detection are at femtomolar concentration levels for all three studied compounds. Copyright © 2011 John Wiley & Sons, Ltd.

Keywords: FT-SERS; adenine; hypoxanthine; xanthine; Raman spectrometry; nucleotides; nanoparticle

Introduction

Nanoscale objects, e.g. nanoparticles, can be studied using distinctive approaches and by many different more common or even uncommon procedures. Common techniques used for the study of physical and optical properties usually comprise scanning electron microscopy,[1] transmission electron microscopy,[1–3] dynamic light scattering microscopy,[4] or by, especially in last few years, the very popular atomic force microscopy.[5] These techniques present a possibility to rapidly and easily characterize some of the key physical parameters of nanoparticles, e.g. their effective cross-section, density, surface characteristics or optical characteristics, respectively. Surface-enhanced Raman scattering (SERS) spectroscopy presents an interesting alternative substantially in the study of selected chemical properties of given nanoparticles at defined conditions.

Besides this assignment, SERS can also be employed in the study of various analytes of interest using nanoparticles as mediators for those actions. Signal enhancement using nanoparticles was described in detail, e.g. in the review by Smith *et al.*[6]

The study of experimental conditions is one of the key aspects of development of many methods utilizing SERS spectroscopy. The pH effect on surface charge and the resulting SERS spectra has been investigated using numerous chemical compounds, such as thiol molecules,[7–11] imidazole,[12] purine derivatives,[13] cytosine and uracil,[14] pyridines and acridines,[15,16] isonicotinic acid,[17–19] mercaptones,[20] humic substances,[21] lysozyme pigments,[22] dyes,[23] pesticides,[24,25] vitamins,[26] food additives,[27] nucleic acids,[28] amino acids,[29–32] proteins,[31,33–35] ligands,[36] lipids and lipolysis,[37–39] and drug components.[26,40–43] There even exist some studies on bacteria[44,45] that have investigated the pH effect.

The effect of nanoparticles cross-sections and size distributions has been also evaluated, e.g. in the work by Mahmoud and Badr,[46] where silver nanoparticles with various definite sizes were used. His investigation led to the important finding of nanoparticle size influence on the obtained enhancement factor and possible red shift. Another important work was performed by Glaspell *et al.*,[47] where nanoparticles in the range from 5 to 50 nm were studied, or by Nie *et al.*,[48] where single metal nanoparticles were evaluated. SERS effect was performed on Rhodamine 6 G. Link *et al.*[49] also investigated the influence of the size of nanoparticles used for SERS experiments; temperature dependency was also investigated in this work. It was shown that not only nanoparticle size plays an essential role but also the temperature of the measured solution has a significant effect on the resulting enhancement factor obtained by SERS measurements.

Detection or a respective determination of nucleotides, nucleosides or their free bases present one of the continuously increasing important analytical tasks especially in the field of biochemistry, medicine, and related branches.[50,51] Nucleic acids constituents present in the body fluids, tissues or cells can be products of nucleic acid catabolism, enzymatic degradation of tissues or unhealthy dietary habits.[52,53] Alternation of tracked concentration levels of these compounds can also indicate some substantial deviances of activities of selected catabolic, anabolic or interconversion enzymes. Nucleic acid constituents can thus in some cases present effective markers of various diseases that cause alternations in the purine and pyrimidine metabolic pathways.

* *Correspondence to: Vaclav Ranc, Department of Physiology, Faculty of Medicine University of Fribourg, Chemin du Musee 5, 1700 Fribourg, Switzerland. E-mail: vaclan.ranc@unifr.ch*

a *Department of Physiology, Faculty of Medicine, University of Fribourg, Chemin du Musee 5, Fribourg, CH1700, Switzerland*

b *Department of Analytical Chemistry, Faculty of Science, Palacky University Olomouc, 17. Listopadu 12, Olomouc, CZ77146, Czech Republic*

c *Regional Centre of Advanced Technologies and Materials, Department of Physical Chemistry, Faculty of Science, Palacky University, Slechtitelu 11, 78371, Olomouc, Czech Republic*

Analytical tasks dealing with an identification or determination of nucleic acids constituents are in most cases performed using capillary electrophoresis (e.g. Refs [54–60]), capillary electrochromatography[55] or high performance liquid chromatography (HPLC, e.g. Refs [61–65]). These techniques offer high sample throughput connected with automation and robustness, and are financially efficient. One of the main problems of these techniques lies in their comparably higher detection limits.

Sheng *et al*. published a method for the determination of selected purine basis using RP-HPLC using real-time SERS spectroscopy.[66] This method was based on the use of a separation technique (RP-HPLC) to separate target compounds and then, afterwards, SERS was used in an on-line detection technique. Analyzed concentration levels for target compounds were very good; they were in units of nmols per liter. This pilot work on an on-line approach introduced a possibility of using alternative analytical procedures (SERS) as detection systems. Development of methods targeted on the determination of selected analytes using SERS approaches present an interesting alternative to commonly used detection techniques but also have some significant limitations that have to be taken into account.

Du *et al*. developed a method based on SERS for the determination of melamine[67] and it can be seen that the limit of detection is in the order of hundreds of micrograms per liter. However, the experimental design presents a complicated step and also the analysis of real samples presents a limitation. Quantification of target analytes using SERS has also been discussed, e.g. in the works by Barber *et al*.,[68] Cai *et al*.,[69] Creighton,[70,71] Lindgren and Larsson,[72,73] and Xu *et al*.[72,73]

Koglin *et al*. described a method for the analysis of nucleic acid bases based on SERS effect established on the use of silver colloids.[74,75] This work brought interesting results but the method, in its original setup, was not able to quantify an amount of respective compounds.

The main aim of this work is to develop an easy to use and effective method for the determination of selected bases: adenine, xanthine and hypoxanthine (for details see the Fig. 1).

Experimental

Apparatus

All spectroscopic experiments were performed using a Fourier transformation infrared spectroscopy instrument Nicolet 6700 with NXR accessory (Thermo – Electron, USA). The instrument was equipped with a germanium detector cooled by a liquid nitrogen and Raman laser (NdYAG) with wavelength of 1064 nm. Laser power was set to 100 mW (on sample) and the aperture was set to 150 (fully opened). The setting of experimental parameters was performed using a standard solution of adenine ($c = 1*10^{-6}$ mol/L) and all the relevant experimental parameters (laser power, aperture, gain, optical velocity) were set to obtain the most intense and time independent SERS spectroscopy signal. All experiments were repeated five times if not stated otherwise.

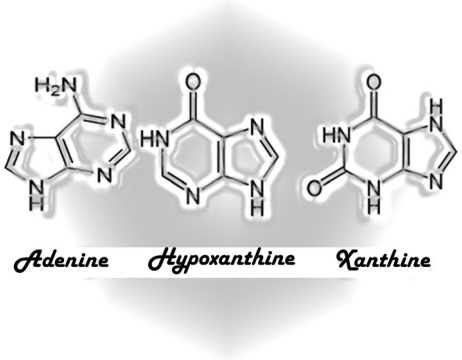

Figure 1. Schemes of analyzed compounds.

Chemicals

Adenine, xanthine, hypoxanthine, glucose, sodium citrate, and maltose (all pro analysis grade) were purchased from Sigma-Aldrich (San Jose, MA, USA). Silver nitrate, hydrochloric acid (36%), ammonium hydroxide (24%), and triethylamine (all pro analysis grade) were purchased from Fluka (part of Sigma-Aldrich, San Jose, USA). The water used was obtained from a Milli-Q water processing device (Millipore, USA) with conductivity less than 18 μS.

Preparation of standard solutions

Standard solutions of adenine, xanthine, and hypoxanthine were prepared by a precise and accurate weighting of 1 mg of the corresponding base standard. The standard was dissolved in 1 ml of deionized water giving concentration level of 1 mg/mL. This solution mixture was diluted to desired concentration levels defined by calibration range.

Preparation of nanoparticles

Nanoparticles were synthesized using a modified procedure described by Kvitek *et al*., [76] Soukupova *et al*.,[77] and Prucek *et al*.[78] This procedure is based on the reduction of silver salt (silver nitrate is usually used) by a selected reduction agent (e.g. reduction sugar, sodium citrate, etc.) in a basic environment. This work uses silver nitrate (concentration 1 mg/mL), where the silver is reduced using glucose ($c = 10$ mg/mL), maltose ($c = 10$ mg/mL) or citrate ($c = 10$ mg/mL). The basic environment resulted from the addition of ammonium hydroxide (0.1% v/v, pH = 10). Formed silver nanoparticles were stabilized using the addition of triethylamine ($c = 10$ mmol/L).

Preparation of working solutions

Working solution mixtures were prepared as follows. Precisely 200 μL of nanoparticles solution (60 ppm) was added to 690 μL of deionized water. Then, 100 μL of sodium chloride solution ($c = 100$ mmol) was added and the mixture was vortexed. Finally, 10 μL of analyte at corresponding concentration level was added. This solution was measured immediately.

Results and discussion

The study of selected experimental parameters

First, SERS spectra for all respective compounds, namely xanthine, hypoxanthine, and adenine, were measured at the concentration level 1×10^{-13} mol·L^{-1}. The results can be seen in Fig. 2. It is clear that the resulting SERS spectra differ and regions that are unique for selected compounds can be easily found.

Second, selected experimental parameters were taken into account. It is clear that the reduction agent used has a strong

Journal of RAMAN SPECTROSCOPY

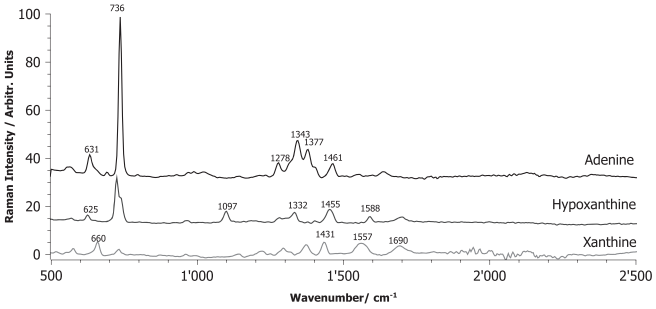

Figure 2. SERS spectra of adenine, hypoxanthine and xanthine measured at the concentration level 1×10^{-13} mol·L^{-1}.

influence on the resulting nanoparticle size and thus also on a significant number of the physical parameters by which the particle is defined. The main purpose of this work was to develop a SERS method for the analysis of selected nucleotides; thus, the influence of particle size on the resulting Raman peak areas has been evaluated. The obtained results are summarized in Table 1. It can be seen that the particle size (evaluated using dynamic light scattering microscopy) plays a significant role in the process of SERS spectroscopy measurements. Spectra obtained using glucose, maltose, and sodium citrate as reduction agents are shown in Fig. 3. It can also be seen that the use of sodium citrate and glucose led to similar results in contrast with the use of maltose that led to worse enhancement factors, outspread to this particular system and analytes. Another important parameter of the given nanoparticles is their stability in time. This factor was studied in the range of 10 days. Prepared nanoparticles were stored in the dark and at laboratory temperature for a given time and repeatedly used for SERS experiments (once every 2 days). The signal stability was studied. It was observed that the Raman signal decreases with time in the case of all selected silver nanoparticles. The study was based on the analysis of adenine ($c=1\times10^{-8}$ mol/L). After a week of use, the signal was at half of its initial value in all cases of used reduction agents. Obtained data are shown in Fig. 4. A significant decrease of Raman intensity in time can be seen for all prepared types of nanoparticles (maltose, glucose, and sodium citrate were used as reduction agents). According to this situation, nanoparticles were prepared every working day from this point.

Table 1. Summary of the obtained experimental values. The highest peaks in the corresponding spectra were evaluated. The average particle side (*d*) was obtained by dynamic light scattering microscopy

Reduction agent	Glucose, d = 44 nm		Citrate, d = 58 nm		Maltose d = 28 nm	
	AVG	**STD**	**AVG**	**STD**	**AVG**	**STD**
Hypoxanthine, peak area at 730 cm^{-1}						
PH 7	47.62	2.62	9.04	9.04	31.92	3.79
PH 10	40.85	2.48	14.41	3.86	18.48	5.12
Xanthine, peak at 660 cm^{-1}						
PH 7	65.44	1.48	20.54	3.46	17.11	2.67
PH 10	57.51	0.66	12.61	1.62	8.78	3.16
Adenine, peak at 736 cm^{-1}						
PH 7	199.49	9.75	115.45	12.39	180.59	3.16
PH 10	171.78	15.85	112.74	21.55	121.44	75.69

AVG, average of 5 experimental values; STD, standard deviation.

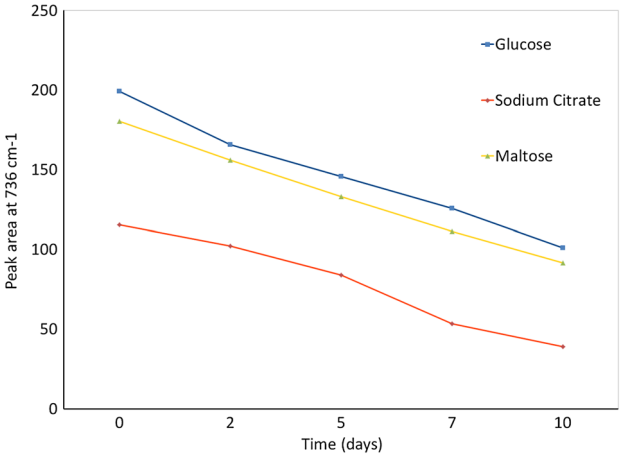

Figure 3. Dependency of selected Raman peak areas for respective compounds on time, $n=5$. Standard deviation of respective measurements is given by an error bar.

The third important parameter that was taken in account in this particular study is the influence of pH value of the measured sample mixtures. The influence of pH plays an important role in the case of proteolytic analytes, but has also some partial and not insignificant influence in other cases. It has been demonstrated that the state of a given analyte proteolytic balance influences the resulting SERS spectra mainly because a current proteolytic form of analyte, which is given by a pH value of environment, determines the method of its adsorption on silver nanoparticles.[79] The study of the influence of pH value was performed using three different pH values of sample mixtures, pH =3, 7, and 10. The value pH = 3 was obtained by the addition of hydrochloric acid ($c=50$ mmol/L), pH 7 was a native pH of the initial solution and pH 10 was obtained by the addition of ammonium hydroxide ($c=20$ mmol/L). For an illustration, Fig. 5 shows the analysis of adenine ($c=1\times10^{-8}$ mol/L) at different pH values. Similar results were obtained for xanthine and hypoxanthine (data not shown). It was demonstrated that the addition of hydrochloric acid leads to a suppression of SERS signal. According to our best knowledge, the basic principles of SERS effect are still unknown but it can be seen that a shift of proteolytic balance can significantly influence a desired Raman spectrum. One of the possible causes can be the presence of positive charge on the heterogeneous nitrogen atom by which an analyte is adsorbed on a silver nanocomposite. On the other hand, higher pH values led to a significant increase of Raman signal, which supports our theory.

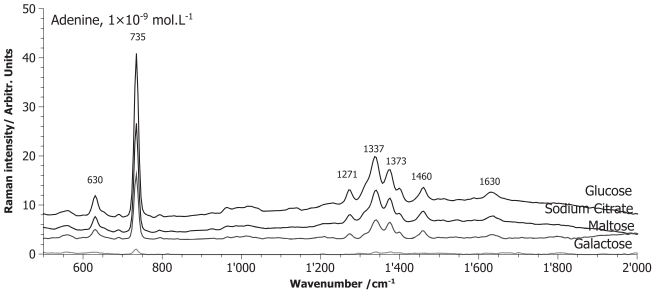

Figure 4. SERS spectra of adenine obtained for experiments where various reduction agents were used during the preparation of concrete nanoparticles.

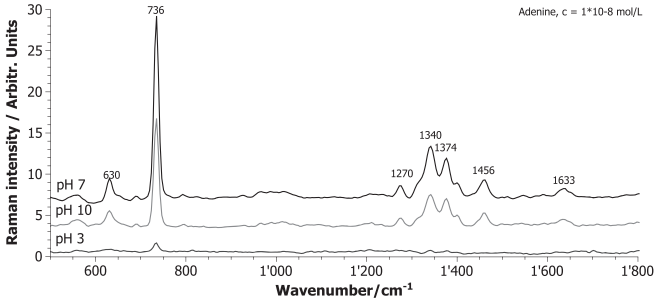

Figure 5. Influence of pH value of analyzed sample mixture on corresponding SERS spectra.

Table 2. Summary of the obtained results of the calibration experiment. Calibration is based in a linear model ($y = Ax + B$)

Calibration; $y = Ax + B$						LOD
	A (mg/L)	STD	B (mg/L)	STD	R^2	mol/L
Xantine	0.82	0.01	3.44	0.21	0.99	2×10^{-15}
Hypoxantine	1.82	0.02	213.74	1.25	0.92	1×10^{-14}
Adenine	2.82	0.01	0.04	0.01	0.99	1×10^{-15}

STD, standard deviation.

According to the results that were obtained during the study of experimental conditions, final conditions were selected and consequently used in the study of calibration parameters. The highest intensity of respective SERS signal was obtained with glucose as reduction agent of silver nitrate. Particles prepared using the mentioned reduction agent embodies suitable properties concerning the Raman enhancement factors and their stability in time. The best results were obtained using a pH value at pH = 7.

All obtained experimental values are summarized in the Table 1. The influence of selected experimental parameters, i.e. pH and reduction agent, was evaluated using peak area of the highest peak in the corresponding Raman spectrum. For adenine, the peak at 735 cm^{-1} was selected. This peak corresponds to a vibration of the C = N bond in the purine ring. For hHypoxanthine, the peak that corresponds to a similar vibration was selected. It was located at 730 cm^{-1}. In the case of xanthine, the peak at 660 cm^{-1} was selected. This peak was interpreted as the C = N vibration on the pyrimidine ring.

Calibration model design and evaluation

The quantitative analysis was based on the evaluation of SERS spectroscopic data. For each target analyte, the highest peak in the corresponding spectrum was selected and taken into account. Its known that this approach is valid only in the narrow concentration rang and thus only a narrow interval of concentration levels was used.[80] This limited validity is given mainly because of the concurrent adsorption of ballast species on the nanoparticle surface and by their limited surface (higher limit), and on the other side of the range there can be found serious problems with excitation laser incoherence and instrumental noise. However, it is possible to obtain qualification information using SERS experiments by a careful selection of experimental conditions and using defined and highly restricted concentration range. In an agreement with the mentioned possibilities, every evaluated spectrum was compared with the corresponding spectrum obtained by the analysis of a blank solution (working solution without an addition of analyte). In this way, the target peak in the analyte spectrum was compared with a corresponding peak in the blank spectrum and these two peaks were abstracted. The obtained reduced peak area was afterwards used for further evaluation. Every calibration level was measured five times if not stated otherwise.

Calibration levels for target compounds (adenine, xanthine, and hypoxanthine) were selected in the concentration range from 1×10^{-15} mol/L to 1×10^{-8} mol/L in ordered intervals (eight calibration levels). However, the linearity of calibration curves was obtained only in the lower part of this interval. For adenine, the linearity of the calibration curve was obtained in the range from 1×10^{-15} to 1×10^{-11} mol/L; for hypoxanthine and xanthine, this interval was from 1×10^{-14} to 1×10^{-10} mol/L, respectively.

The curvature of the calibration curves at higher concentration levels could be caused, e.g. by concurrent adsorption processes on the limited surface of nanoparticles described above.

The limits of detection (LOD) were calculated from the obtained spectra. Measured data were compared with corresponding blank spectra and after subtraction, LOD was calculated from the highest peak in the given reduced spectrum using an approach that is based on the signal-to-noise ratio. The summary of the obtained results can be seen in the Table 2.

Analysis of model mixtures

The analysis of model mixtures was based on the similar approaches that have been used in the calibration model design. Samples containing all three target compounds on the selected concentration levels were measured. These concentration levels were selected according to the results that were obtained in the process of calibration model development. For all three target compounds (adenine, xanthine, and hypoxanthine), these levels were 1×10^{-12} and 1×10^{-13} mol/L of the respective target compound. A new mixture calibration model has also been constructed. This calibration model was based on the analysis of the mixture containing all three targets: xanthine, hypoxanthine, and adenine. The calibration range was selected from 1×10^{-15} to 1×10^{-10} mol/L. For each target compound, its unique peak was found. The selection criteria for these peaks were based on two prerequisites: first, the selected peak has to be unique for a target compound and second, this peak has to be intense enough for quantification purposes at femtomolar concentration levels. For adenine, the peak at 735 cm^{-1} was used; for hypoxanthine, the peak at 1097 cm^{-1} was used; and for xanthine, the peak at 660 cm^{-1} was selected. On the basis of these principles, calibration curves for each target compound were constructed. Calibrations were linear in the whole selected ranges for all three compounds. The spectrum obtained by the analysis of the sample containing 1×10^{-12} mol/L of target compounds can be seen in the Fig. 6. Two model samples containing 1×10^{-12} and 1×10^{-11} mol/L of all target compounds were prepared to test the calibration. Results obtained by the analysis of these model samples are given in the Table 3. It can be seen that the analysis of sample mixtures brought some difficulties that were reflected in a relatively lower obtained correlation coefficients (compared with an analysis of standards), but the method is suitable for a screening analysis of selected compounds in the mixture on very low concentration levels.

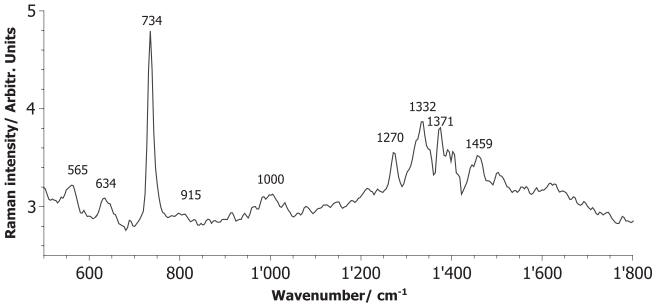

Figure 6. SERS spectrum of the mixture of target analytes: adenine, hypoxanthine, and xanthine, $c = 1 \times 10^{-12}$ mol/L.

Table 3. The summary of results obtained by an analysis of model sample mixtures, RSD stands for relative standard deviantion.

	Sample A [mol/L] 10^{-13}	RSD [%]	Difference [mol/L] 10^{-13}	Sample B [mol/L] 10^{-13}	RSD [%]	Difference [mol/L] 10^{-12}
Adenine	9.5	4.5	0.5	98	5.1	2
Xanthine	7.2	5.5	2.8	105	5.2	5
Hypoxanthine	14.9	4.8	4.9	108	4.8	8

Concluding remarks

A method for the analysis of model sample mixtures of selected nucleotides was developed. This method is based on the use of SERS spectroscopy with Fourier transformation. Adenine, hypoxanthine, and xanthine were selected as model analytes. The obtained limits of detection are in the units of femtomols for adenine and xanthine and in tens of femtomols for hypoxanthine. By the analysis of model sample mixtures containing all three selected compounds, it was shown that the obtained RSD is on average 5% (from 4.5% to 5.5%) for both selected model samples.

Acknowledgements

The authors gratefully acknowledge the support of the Operational Program Research and Development for Innovations - European Regional Development Fund (Project No. CZ.1.05/2.1.00/03.0058 of the Ministry of Education, Youth and Sports of the Czech Republic).

References

[1] E. D. Cabanillas, M. S. Granovsky, M. J. Ratner, *Acta Microsc.* **2010**, *19*(2), 190–195.
[2] P. Fredrickx, D. Helary, D. Schryvers, E. Darque-Ceretti, *Appl Phys a-Mater* **2004**, *79*(2), 283–288.
[3] T. J. Bromwich, D. G. Bucknall, B. Warot, A. K. Petford-Long, C. A. Ross, *Inst. Phys. Conf. Ser.* **2004**, *21*(179), 95–98.
[4] D. Chicea, *Optoelectron. Adv. Mat.* **2010**, *4*(9), 1310–1315.
[5] S. Kim, F. Shafiei, D. Ratchford, X. Q. Li, *Nanotechnology* **2011**, *22*(11), 1–6.
[6] W. E. Smith, G. McNay, D. Eustace, K. Faulds, D. Graham, *Appl. Spectrosc.* **2011**, *65*(8), 825–837.
[7] R. Langer, C. Wang, N. T Flynn, *Adv. Mater.* **2004**, *16*(13), 1074–1079.
[8] G. N. R. Tripathi, M. Clements, *J. Phys. Chem. B* **2003**, *107*(40), 11125–11132.
[9] Q. J. Meng, W. W. Zhang, X. M. Ren, H. F. Li, C. S. Lu, C. J. Hu, H. Z. Zhu, *J Colloid Interf Sci* **2002**, *255*(1), 150–157.
[10] R. L. Garrell, C. A. Szafranski, W. Tanner, P. E. Laibinis, *Langmuir* **1998**, *14*(13), 3580–3589.
[11] A. T. Hubbard, J. Y. Gui, *J Chim Phys Pcb* **1991**, *88*(7–8), 1547–1590.
[12] W. S. Yang, J. Guan, L. Jiang, J. Li, *J. Phys. Chem. C* **2008**, *112*(9), 3267–3271.
[13] J. G. Duguid, V. A. Bloomfield, J. M. Benevides, G. J. Thomas, *Biophys. J.* **1995**, *69*(6), 2623–2641.
[14] G. R. Loppnow, B. E. Billinghurst, S. A. Oladepo, *J. Phys. Chem. B* **2009**, *113*(20), 7392–7397.
[15] G. Levi, J. Pantigny, J. P. Marsault, J. Aubard, *J. Raman Spectrosc.* **1993**, *24*(11), 745–752.
[16] S. T. Oh, K. Kim, M. S. Kim, *J Phys Chem-Us* **1991**, *95*(22), 8844–8849.
[17] Y. Fang, R. Wen, *J Colloid Interf Sci* **2005**, *292*(2), 469–475.
[18] S. M. Park, K. Kim, M. S. Kim, *J. Mol. Struct.* **1995**, *344*(3), 195–203.
[19] S. M. Park, K. Kim, M. S. Kim, *J. Mol. Struct.* **1994**, *328*, 169–178.
[20] I. M. Weidinger, M. Sezer, J. J. Feng, H. K. Ly, Y. F. Shen, T. Nakanishi, U. Kuhlmann, P. Hildebrandt, H. Mohwald, *Phys. Chem. Chem. Phys.* **2010**, *12*(33), 9822–9829.
[21] M. M. Campos-Vallette, P. Leyton, I. Cordova, P. A. Lizama-Vergara, J. S. Gomez-Jeria, A. E. Aliaga, E. Clavijo, J. V. Garcia-Ramos, S. Sanchez-Cortes, *Vib. Spectrosc.* **2008**, *46*(2), 77–81.
[22] M. Breitman, S. Ruiz-Moreno, R. Perez-Pueyo, *J. Cult. Herit.* **2003**, *4*, 314s-316s.
[23] Z. L. Zhang, D. H. Chang, Y. J. Mo, *Spectroscopy-Us* **2011**, *26*(6), 38–42.
[24] S. Li, F. Y. Ji, D. N. Yu, G. M. Zhou, Q. A. He, *Acta Chim Sin.* **2010**, *68*(16), 1616–1622.
[25] J. S. Kang, S. Y. Hwang, C. J. Lee, M. S. Lee, *B Kor Chem Soc* **2002**, *23*(11), 1604–1610.
[26] S. C. Pinzaru, I. Pavel, N. Leopold, W. Kiefer, *J. Raman Spectrosc.* **2004**, *35*(5), 338–346.
[27] E. Podstawka, M. Swiatlowska, E. Borowiec, L. M. Proniewicz, *J. Raman Spectrosc.* **2007**, *38*(3), 356–363.
[28] S. Sanchezcortes, J. V. Garciaramos, *J. Mol. Struct.* **1992**, *274*, 33–45.
[29] G. M. Zhou, D. N. Yu, S. Li, D. C. Yang, *Acta Chim Sin.* **2007**, *65*(7), 640–644.
[30] W. Z. Ke, J. Z. Wu, *Spectrosc Spect Anal* **2004**, *24*(5), 551–553.
[31] X. M. Dou, Y. M. Jung, H. Yamamoto, S. Doi, Y. Ozaki, *Appl. Spectrosc.* **1999**, *53*(2), 133–138.
[32] H. Lee, M. S. Kim, S. W. Suh, *J. Raman Spectrosc.* **1991**, *22*(2), 91–96.
[33] M. Iosin, V. Canpean, S. Astilean, *J Photoch Photobio A* **2011**, *217*(2–3), 395–401.
[34] P. Leyton, P. A. Lizama-Vergara, M. M. Campos-Vallette, M. I. Becker, E. Clavijo, I. C. Reyes, M. Vera, C. A. Jerez, *J. Chil. Chem. Soc.* **2005**, *50*(4), 725–730.
[35] R. P. Van Duyne, L. A. Dick, A. J. Haes, *J. Phys. Chem. B* **2000**, *104*(49), 11752–11762.
[36] D. M. Zhang, S. M. Ansar, R. Haputhanthri, B. Edmonds, D. Liu, L. Y. Yu, A. Sygula, *J. Phys. Chem. C* **2011**, *115*(3), 653–660.
[37] S. H. Oh, K. C. Bantz, A. F. Meyer, N. J. Wittenberg, H. Im, O. Kurtulus, S. H. Lee, N. C. Lindquist, C. L. Haynes, *Phys. Chem. Chem. Phys.* **2011**, *13*(24), 11551–11567.
[38] M. D. Morris, M. K. Weldon, *Appl. Spectrosc.* **2000**, *54*(1), 20–23.
[39] M. D. Morris, M. K. Weldon, V. R. Zhelyaskov, *Appl. Spectrosc.* **1998**, *52*(2), 265–269.
[40] S. Sanchez-Cortes, I. Izquierdo-Lorenzo, J. V. Garcia-Ramos, *Langmuir* **2010**, *26*(18), 14663–14670.
[41] S. Farquharson, A. D. Gift, C. Shende, P. Maksymiuk, F. E. Inscore, J. Murran, *Vib. Spectrosc.* **2005**, *38*(1–2), 79–84.
[42] S. Sanchez-Cortes, L. Rivas, A. Murza, J. V. Garcia-Ramos, *Vib. Spectrosc.* **2001**, *25*(1), 19–28.
[43] S. Farquharson, Y. H. Lee, *Biochem. Biomol. Sen.* **2000**, *4200*, 89–95.
[44] T. Smith-Palmer, M. Kazanci, J. P. Schulte, C. Douglas, P. Fratzl, D. Pink, *Appl. Spectrosc.* **2009**, *63*(2), 214–223.
[45] Y. R. Chen, Y. L. Liu, X. W. Nou, K. L. Chao, *Appl. Spectrosc.* **2007**, *61*(8), 824–831.
[46] M. A. Mahmoud, Y. Badr, *J. Mol. Struct.* **2005**, *749*(1–3), 187–192.
[47] G. P. Glaspell, C. Zuo, P. W. Jagodzinski, *Abstr Pap Am Chem S* **2001**, *221*, U279-U279.
[48] E. Sr, W. E. Haskins, S. M. Nie, *J. Am. Chem. Soc.* **1998**, *120*(31), 8009–8010.
[49] S. Link, L. Slaughter, W. S. Chang, *J. Phys. Chem. Lett.* **2011**, *2*(16), 2015–2023.
[50] G. M. Blackburn, Nucleic acids in chemistry and biology, (3rd ed.), RSC Pub., Cambridge, UK, **2006**; p xxxi, p. 470
[51] Nucleosides, nucleotides & nucleic acids. In Marcel Dekker, Monticello, N.Y., **2000**; p v.

[52] P. Illes, H. Zimmermann, Nucleotides and their receptors in the nervous system. (1st ed.), Elsevier Science, Amsterdam; New York, **1999**; p xvi, p. 432
[53] L. Belardinelli, A. Pelleg, Adenosine and adenine nucleotides: from molecular biology to integrative physiology, Kluwer Academic Publishers, Boston, **1995**; p xix, p. 543
[54] B. Vester, H. Doessing, *Molecules* **2011**, *16*(6), 4511–4526.
[55] S. P. Li, X. J. Chen, F. Q. Yang, Y. T. Wang, *Electrophoresis* **2010**, *31*(13), 2092–2105.
[56] A. E. Barron, C. P. Fredlake, D. G. Hert, E. R. Mardis, *Electrophoresis* **2006**, *27*(19), 3689–3702.
[57] J. F. Van Bocxlaer, A. V. Willems, D. L. Deforce, C. H. Van Peteghem, *Electrophoresis* **2005**, *26*(7–8), 1221–1253.
[58] E. Bayer, A. von Brocke, G. Nicholson, *Electrophoresis* **2001**, *22*(7), 1251–1266.
[59] A. Harsch, C. L. Andrews, P. Vouros, *J. Chromatogr. A* **1999**, *856*(1–2), 515–526.
[60] N. W. Smith, M. B. Evans, *J Pharmaceut Biomed* **1994**, *12*(5), 579–611.
[61] F. Toldra, L. Mora, A. S. Hernandez-Cazares, M. C. Aristoy, M. Reig, *Food Anal Method* **2011**, *4*(1), 121–129.
[62] A. Kohen, K. A. Markham, *Curr. Anal. Chem.* **2006**, *2*(4), 379–388.
[63] M. O'Regan, *Neurol. Res.* **2005**, *27*(2), 175–181.
[64] W. F. Smyth, *Trac-Trend Anal Chem* **1999**, *18*(5), 335–346.
[65] B. J. Smith, M. R. Wales, M. J. Perry, *Appl Biochem Biotech* **1993**, *41*(3), 189–218.
[66] R. S. Sheng, F. Ni, T. M. Cotton, *Anal. Chem.* **1991**, *63*(5), 437–442.
[67] X. B. Du, H. Y. Chu, Y. W. Huang, Y. P. Zhao, *Appl. Spectrosc.* **2010**, *64*(7), 781–785.
[68] T. E. Barber, M. S. List, J. W. Haas, E. A. Wachter, *Appl. Spectrosc.* **1994**, *48*(11), 1423–1427.
[69] W. B. Cai, X. K. Xue, S. J. Huo, Y. G. Yan, J. Y. Wang, J. L. Yao, *Acta Chim Sin.* **2007**, *65*(15), 1437–1442.
[70] J. A. Creighton, *Surf. Sci.* **1983**, *124*(1), 209–219.
[71] J. A. Creighton, *Surf. Sci.* **1986**, *173*(2–3), 665–672.
[72] J. Lindgren, M. Larsson, *J. Raman Spectrosc.* **2005**, *36*(5), 394–399.
[73] H. X. Xu, E. J. Bjerneld,J. Aizpurua, P. Apell, L. Gunnarsson, S. Petronis, B. Kasemo, C. Larsson, F. Hook, M. Kall, *Nanoparticles and Nanostructured Surfaces: Novel Reporters with Biological Applications* **2001**, *2* (15), 35–42.
[74] E. Koglin, J. M. Sequaris, J. C. Fritz, P. Valenta, *J. Mol. Struct.* **1984**, *114*(MAR), 219–223.
[75] E. Koglin, J. M. Sequaris, P. Valenta, *J. Mol. Struct.* **1982**, *79*(1–4), 185–189.
[76] L. Kvitek, R. Prucek, A. Panacek, J. Soukupova, M Vanickova, Nanocon 2009, *Conference Proceedings* **2009**, 74–82.
[77] J. Soukupova, L. Kvitek, A. Panacek, T. Nevecna, R. Zboril, *Mater. Chem. Phys.* **2008**, *111*(1), 77–81.
[78] R. Prucek, A. Panacek, A. Fargasova, V. Ranc, V. Masek, L. Kvitek, R. Zboril, *CrystEngComm* **2011**, *13*(7), 2242–2248.
[79] X. M. Dou, Y. M. Jung, Z. Q. Cao, Y. Ozaki, *Appl. Spectrosc.* **1999**, *53*(11), 1440–1447.
[80] P. D. O'Neal, G. L. Cote, M. Motamedi, J. Chen, W. C. Lin, *J. Biomed. Opt.* **2003**, *8*(1), 33–39.

Analyst

Cite this: *Analyst*, 2012, **137**, 2866

www.rsc.org/analyst

PAPER

Reproducible discrimination between Gram-positive and Gram-negative bacteria using surface enhanced Raman spectroscopy with infrared excitation

Robert Prucek,*[a] Václav Ranc,†[b] Libor Kvítek,[a] Aleš Panáček,[a] Radek Zbořil[a] and Milan Kolář[c]

Received 28th December 2011, Accepted 24th April 2012
DOI: 10.1039/c2an16310a

The on time diagnostics of bacterial diseases is one of the essential steps in the foregoing treatment of such pathogens. Here we sought to present an easy to use and robust method for the discrimination between Gram-positive (*Enterococcus faecalis* and *Streptococcus pyogenes*) and Gram-negative (*Acinetobacter baumannii* and *Klebsiella pneumoniae*) bacterial genera based on surface enhanced Raman scattering (SERS) spectroscopy. The robustness of our approach lies in the novel method for the production of the SER substrate based on silver nanoparticles and their subsequent re-crystallization in solutions containing high concentrations of chloride ions. The method presented here could be an interesting alternative both to commonly used histochemical approaches and commercial SERS substrates.

Introduction

The targeted and effective therapy of bacterial diseases demands a utilization of rapid methods of identification of such pathogens, however many of the classical techniques, developed over the past years are time-consuming and often require additional resources, from financial to human.[1] These conventional immunohistochemical techniques often involve the overnight culture of bacteria in a suitable growth medium to grow colonies large enough for detection, and usually require advanced medical personnel trained in bacteriology.[1–3] Therefore, the development of rapid, accurate, and preferably automated methods for the identification of microorganisms is highly demanding. Ideal methods for rapid microbial characterization include those that require minimal sample volume, permit automated analysis with negligible reagent costs, and allow a rapid sample characterization. Optical spectroscopies such as vibrational spectroscopy, fluorescence, and photoluminescence are promising analytical tools in this field. In comparison to fluorescence and luminescence methods, vibrational spectroscopy is able to provide specific chemical information on the analyte. Typical vibrational spectroscopy (IR or FT-IR spectroscopy) is not optimal for biological samples due to the absorption of IR photons by ever-present water molecules. On the contrary, Raman spectroscopy is better suited to application in aqueous environment. However, the Raman effect is particularly weak and analyses require long collection times and high laser power even for highly concentrated samples. This drawback can be overcome by the exploitation of surface enhanced Raman spectroscopy (SERS) which has become an increasingly relevant analytical tool that enables the detection of analytes in pico- to femtomol concentrations.[4–9] Considerable enhancements in SERS have allowed the detection of individual molecules adsorbed on a single silver particle.[10–13]

SERS has been utilized for the study of various bacteria, *e.g.*, *Bacillus cereus*, *Bacillus subtilis*, *Bacillus anthracis Sterne*, *Bacillus thuringiensis*, *Salmonella typhimurium*,[14–20] *Bacillus megaterium*,[21–23] *Pseudomonas aeruginosa*,[18,21,24] *Staphylococcus cohnii*,[23,25] *Listeria monocytogenes*,[26,27] *Helicobacter pylori*,[28] *Shigella sonnei*, *Proteus vulgaris*, *Erwinia amylovara*,[29,30] *Escherichia coli*,[23,27,31–36] *Staphylococcus aureus*,[37,38] and *Shewanella oneidensis*.[39]

Measurements of the above-mentioned bacteria were performed using instruments with various excitations, mainly in the UV/Vis region (between 244 nm and 830 nm) and using various (mainly based on Ag and Au nanoparticles) substrates. It is worth mentioning that for SERS instruments equipped with red lasers (780 nm, 830 nm), gold particles or arrays and aggregates of gold particles are commonly used.[14–34] Utilization of NIR (≥800 nm) excitation can be more advantageous for biological samples to avoid most of the background fluorescence. In these cases, for example, a substrate based on 80 nm Au nanoparticles is involved.[15,33,40] Accordingly, for different laser wavelength, miscellaneous substrates must be applied. This may be problematic when interpreting and comparing the spectra as the resulting SER spectrum depends on the excitation wavelength.[33,41] Although hundreds of papers are published annually

[a]*Regional Centre of Advanced Technologies and Materials, Department of Physical Chemistry, Faculty of Science, Palacky University, Slechtitelu 11, 783 71 Olomouc, Czech Republic. E-mail: robert.prucek@upol.cz; Fax: +420 58563 4761; Tel: +420 58563 4427*
[b]*Department of Analytical Chemistry, Faculty of Science, Palacky University, 17 Listopadu 12, 771 46 Olomouc, Czech Republic*
[c]*Department of Microbiology, Faculty of Medicine and Dentistry, Palacky University, Hnevotinska 3, 775 15 Olomouc, Czech Republic*
† Current address: Visual Cognition Laboratory, Department of Physiology, University of Fribourg, Chemin du Musee 5, CH 1700 Fribourg, Switzerland.

referring to the applicability of this method for the detection of a growing number of analytes, there are only a few commercial SERS substrates. Recently, we presented a simple, easy-to-use, and reproducible technique for obtaining a SERS substrate based on the re-crystallization of silver nanoparticles (NPs) which is applicable both for visible (488 nm) and near infrared (1064 nm) excitation wavelengths.[42]

In this work, we used this technique for a rapid identification and discrimination of selected biologically relevant Gram-positive (*Enterococcus faecalis* and *Streptococcus pyogenes*) and Gram-negative (*Acinetobacter baumannii* and *Klebsiella pneumoniae*) bacterial lysates.

Experimental

Preparation and activation of silver nanoparticles

Ag NPs, with a diameter of approximately 28 nm, were synthesized by a reduction of the complex $[Ag(NH_3)_2]^+$ cation with D-maltose.[42] The initial concentrations of the reaction components were 10^{-3} mol·L^{-1} and 10^{-2} mol·L^{-1} for $AgNO_3$ and maltose, respectively. The concentration of used ammonia was 5×10^{-3} mol·L^{-1}. Sodium hydroxide solution was added to the reaction system to adjust the value of the pH to 11.5 ± 0.1, as well as to achieve a reaction time of 3–4 minutes. All chemicals were purchased from Sigma-Aldrich and used as received. The as-prepared aqueous dispersion of silver NPs was used for the subsequent experiments without any additional modifications. All the measurements were performed at the laboratory temperature (20 °C).

The specific treatment procedure for SERS measurements was as follows: 0.2 mL of the stock dispersion of Ag NPs was diluted with 0.7 mL of deionised water and then 0.1 mL of 4 M NaCl solution was added. After adding chloride ions to the diluted dispersion of Ag NPs, the solution was quickly mixed and finally, an amount of 0.05 mL of bacterial lysate was added. Lysates of bacterial cells were de-frosted immediately before measurement with the FT-Raman instrument. The Raman spectra were recorded 10 min after incubation.

Preparation of bacterial lysates

Bacterial lysates were prepared using 24 hour cultures of the standard reference strain of *Enterococcus faecalis* CCM 4224 (from the Czech Collection of Microorganisms (CCM), Faculty of Science, Masaryk University Brno), *Streptococcus pyogenes*, *Klebsiella pneumoniae*, and *Acinetobacter baumannii* were obtained from the Teaching Hospital Olomouc, Czech Republic. All tested microorganisms were stored in cryotubes (ITEST plus, Czech Republic) at −80 °C. Well isolated colonies of the above-mentioned bacteria were transferred to 5 mL of Mueller Hinton Broth (Becton Dickinson, France) so that the resulting density was equivalent to the 0.5 McFarland turbidity standard. Each strain was separately inoculated into Mueller Hinton Broth. Subsequently, the broths were placed in a thermostat for 4 hours at 37 °C. Following incubation, the broths were centrifuged at 2000 rpm for 10 min. The supernatant was removed and the bacterial pellet was resuspended in 1 mL of distilled water. The suspension was frozen at −72 °C for 10 min and then thawed completely in a water bath at 37 °C. This step was repeated 10 times. The obtained bacterial lysate was diluted with distilled water using a densitometer to 2×10^5 lysed bacteria per mL.

Instrumentation

The size of the silver particles was determined by a dynamic light scattering method (DLS) using a Zeta Plus analyzer (Brookhaven, USA). TEM observations of the silver NPs were performed with a JEM 2010 (Jeol, Japan) electron microscope operating at an acceleration voltage of 160 kV. UV/Vis absorption spectra of silver NP dispersions were acquired by using Specord S 600 (Analytic Jena AG, Germany) and Lambda 35 (Perkin Elmer) spectrophotometers. Experiments concerning the usage of Raman spectrometry were performed using an FT-IR spectrometer (Nicolet FT-IR 6700, USA) with a Raman accessory (NXR FT-Nicolet module, USA) equipped with a liquid nitrogen-cooled germanium detector. An FT-Raman was equipped with an Nd:YAG laser with a wavelength of 1064 nm, 512 scans for each measurement were acquired and averaged, laser power incident onto a sample was 300 mW. Spectra were measured in the range from 500 to 2000 cm^{-1}.

Results and discussion

Recently, we have introduced an activation procedure for the purposes of SERS based on the re-crystallization of Ag NPs. The advantages of this procedure include its reproducibility, robustness, and possibility of application for both visible and near infrared excitation.[42]

The primarily prepared Ag NPs are nearly monodispersed with an average particle size of about 25 nm and exhibit long-term stability (~2 years). It is known that an application of such small NPs without further treatment is not usually effective for SERS as these NPs usually do not provide any significant enhancement of the Raman signal. The generally used procedures of Ag NPs activation for SERS use an addition of inorganic (especially chloride) ions, generally at low concentrations of about 0.1–10 mM. In our approach, here, we used very high final concentrations of chlorides (400 mM). Such a large amount of chloride ions induces the rapid recrystallization of primary Ag NPs to crystallites with sizes of around 400 nm.[42] The recrystallization process of Ag NPs proceeds within 15 minutes and can be monitored visually or more precisely by recording the UV/Vis absorption spectra (Fig. 1).

We employed the recrystallized particles together with NIR excitation for SERS of a selection of an important population of Gram-positive (*Enterococcus faecalis* and *Streptococcus pyogenes*) and Gram-negative (*Acinetobacter baumannii* and *Klebsiella pneumoniae*) bacterial lysates with the aim of distinguishing between these bacterial genera. Typical recorded SER spectra of these bacteria after subtracting the blank (activated silver particles without addition of bacterial lysate) are shown in Fig. 2. Several identical bands for Gram-positive and Gram-negative bacteria can be identified from the measured spectra. It is worth noting that from a bio-molecular point of view, bacterial lysates are a very complex "cocktail" containing proteins, saccharrides, DNA, RNA, *etc.* However, a substantial part of this mixture contains peptidoglycans consisting of *N*-acetylglucosamine, *N*-acetylmuramic acid, and some amino acids (mainly alanine and

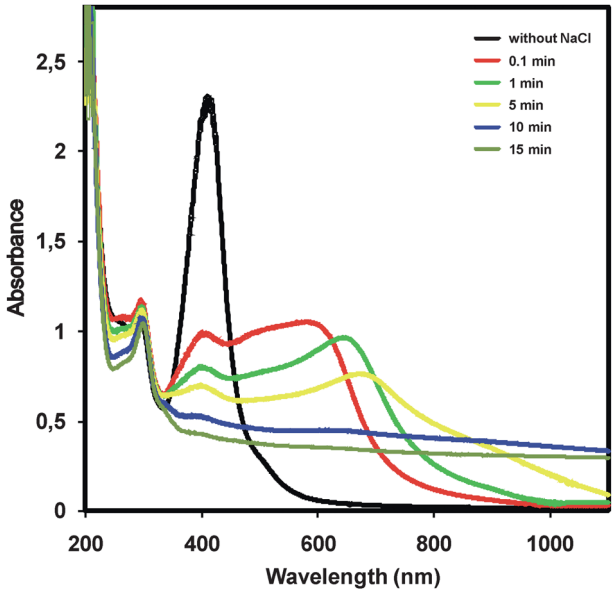

Fig. 1 The time dependence of UV/Vis absorption spectra recorded over 15 minutes after the addition of NaCl solution to a Ag NP dispersion (final concentration of chlorides equal to 400 mM).

glutamic acid). Peptidoglycans represent about 80% of the dry mass of Gram-positive bacteria and around 20% of the dry mass of Gram-negative bacteria. Just the most intensive bands may be assigned to the above mentioned compounds (Table 1).

Only the positions of these main bands cannot be used for discriminating between Gram-positive and Gram-negative bacterial lysates. For the purposes of discrimination, a comparison of the absolute intensity of the main absorption bands could be applied only when the constant amount of bacteria in the analyzed samples is guaranteed. Fortunately, some peaks are present only in the spectra of Gram-positive and other ones in the spectra of Gram-negative bacterial lysates. These regions are observed at about 700 cm^{-1}, 1200 cm^{-1}, and 1600 cm^{-1}. For the verification of the reproducibility of this activation procedure for bacterial analysis and for verification of the possibility of distinguishing between the mentioned Gram-positive and Gram-negative bacterial genera, several samples of lysates from each type of bacteria were analyzed separately after 10 minutes of incubation with activated silver particles. Firstly, each spectrum obtained by an analysis of every respective lysate was evaluated.

The data analysis was not based on the direct comparison of a few discrete peaks but on a comparison of the whole spectra. Measured spectra were subjected to a statistical evaluation using the *R* statistical environment (open-source data processing tool, Vienna, Austria). Firstly, before the main data evaluation was carried out, normalization of all the obtained datasets was performed. It was based on a mathematical comparison of each respective experimental point with its baseline level given by a measurement of the blank sample (sample mixture without an addition of bacteria lysates). Regarding the data reproducibility, in Fig. 3, we show as an example the measured data for *Enterococcus faecalis*. It is clear that the spectra are very close to each other and statistical evaluation confirms this finding. The reproducibility of the obtained data was investigated on each of two repetitive spectra for all the particular bacteria (8

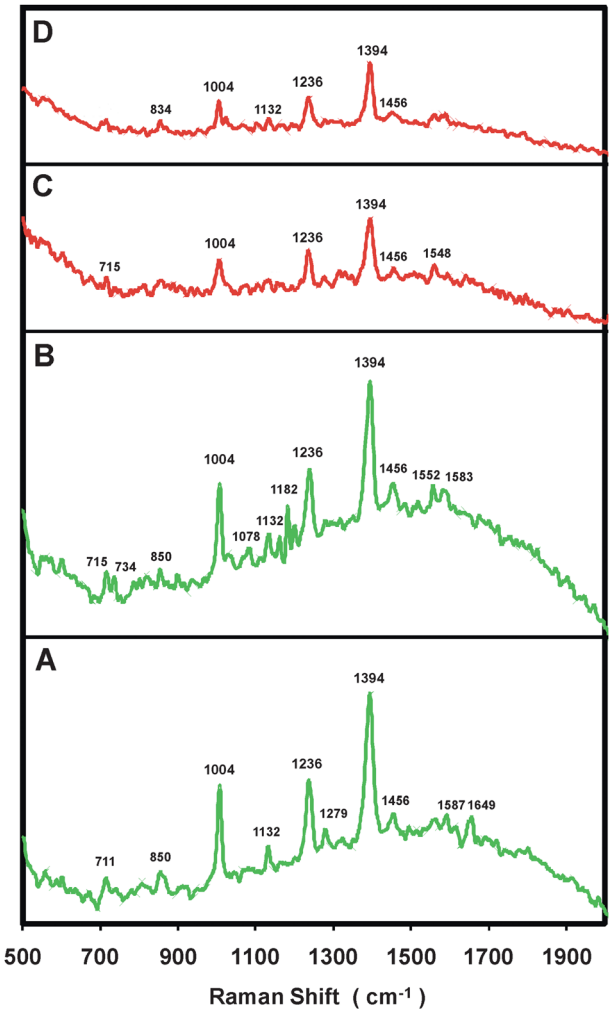

Fig. 2 Representative SERS spectra of bacterial lysates: (A) *Enterococcus faecalis*, CCM 4224, (B) *Streptococcus pyogenes*, (C) *Acinetobacter baumannii*, and (D) *Klebsiella pneumoniae*.

measurements per one bacterial population), and no statistical difference (paired *t*-test, $p < 0.05$) was found. The reproducibility of the measurements is further expressed by the calculated mean RSD values of all the evaluated peak areas found in the spectra. Total relative standard deviances are summarized in Table 2 and vary from 0.21% for *Streptococcus pyogenes* to 1.34% for *Klebsiella pneumoniae*. Secondly, the obtained datasets (full spectral range), were subjected to a cluster analysis, where Gram-positive (*Enterococcus faecalis* and *Streptococcus pyogenes*) and Gram-negative (*Acinetobacter baumannii* and *Klebsiella pneumoniae*) cultures were evaluated. Fig. 4 shows the results of this analysis, and it can be seen that the Gram-positive bacteria, *Enterococcus faecalis* and *Streptococcus pyogenes* form two distinct clusters (A and B, respectively), and thus can be further distinguished. Gram-negative bacteria, C: *Acinetobacter baumannii* and D: *Klebsiella pneumoniae* form also two clusters, considerably distinguished from Gram-positive bacteria.

The use of cluster analysis presents an alternative approach for bacterial characterization, and compared to the evaluation of particular peaks, presented in the spectra, this approach fully evaluates the whole spectral range and thus more objectively

Table 1 Assignment of SERS bands

Enterococcus faecalis	*Streptococcus pyogenes*	*Acinetobacter baumanii*	*Klebsiella pneumoniae*	Band assignment
711	715			
	734			Ring breathing (adenine)
850	850		854	ν(CNC) alanine, symm stretch CON
1004	1004	1004	1004	CC ring breathing (polysaccharide)
	1078			
1132	1132	1132	1132	ν(COC), ring breathing
	1182			Amide III
1236	1236	1236	1236	Amide III
1279		1263	1263	
1394	1394	1394	1394	$\nu(CO_2)$ (α-aminoacids
1456	1456	1456	1456	COH (oligosaccharides)
1556	1552			*N*-Acetyl related bands
1587	1583			δ(NH) and ν(CN) amide II
1649				ν(C=O) amide I

compares data between individual spectra while keeping the whole procedure as simple as possible.

Conclusions

Herein is presented a robust, rapid and easy to use methodological approach, based on SERS, which enables the characterization of pathogenic microorganisms. The method consists of a simple technique for the reproducible fabrication of a SERS substrate, and a straightforward evaluation of the obtained data. Its applicability was demonstrated by the successful discrimination between Gram-positive (*Enterococcus faecalis* and *Streptococcus pyogenes*) and Gram-negative (*Acinetobacter baumannii* and *Klebsiella pneumoniae*) bacteria. Compared to

Table 2 Total relative standard deviances determined by evaluation of all peak areas in the spectra of the selected bacteria

Enterococcus faecalis	*Streptococcus pyogenes*	*Acinetobacter baumannii*	*Klebsiella pneumoniae*
0.23%	0.21%	0.76%	1.35%

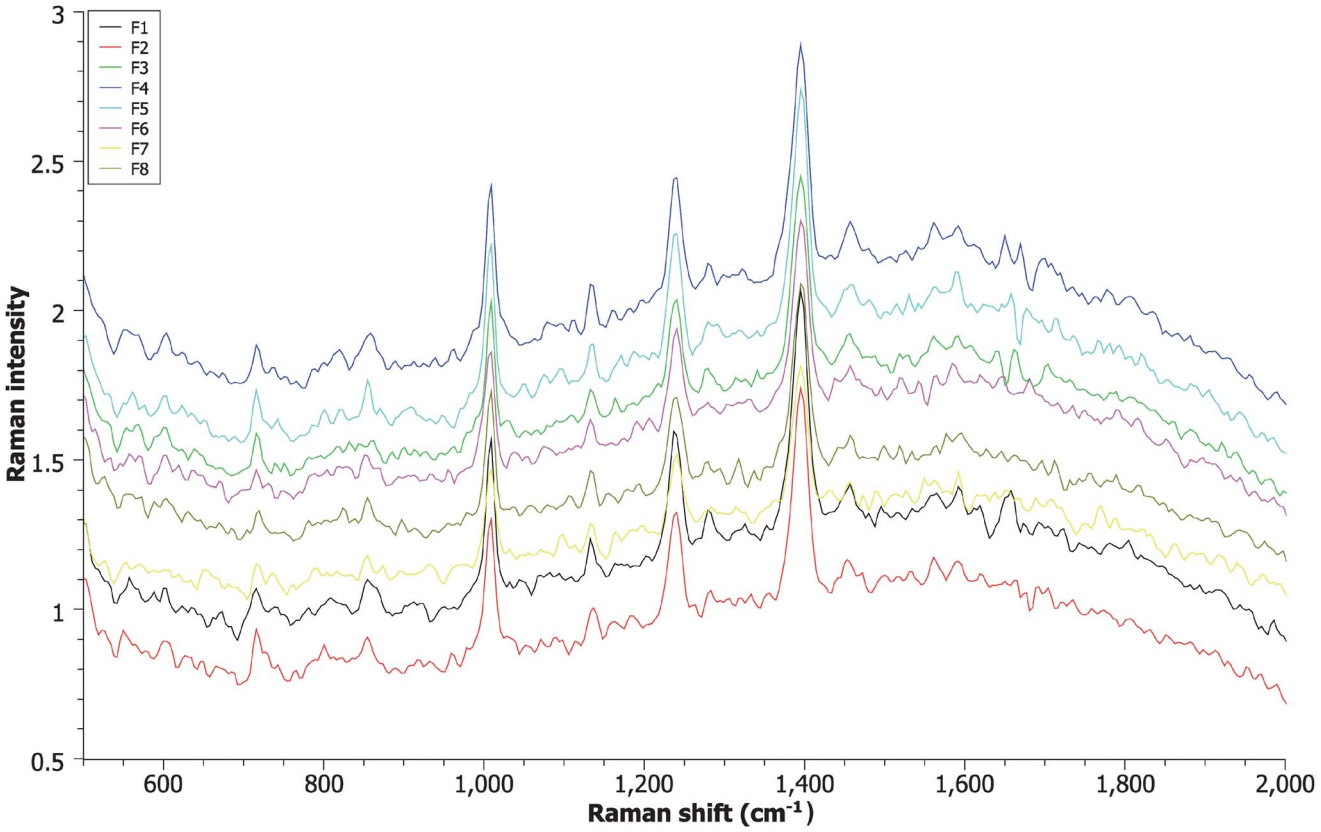

Fig. 3 SERS spectra of *Enterococcus faecalis*, CCM 4224. Measurements were repeated 8 times (F1–F8).

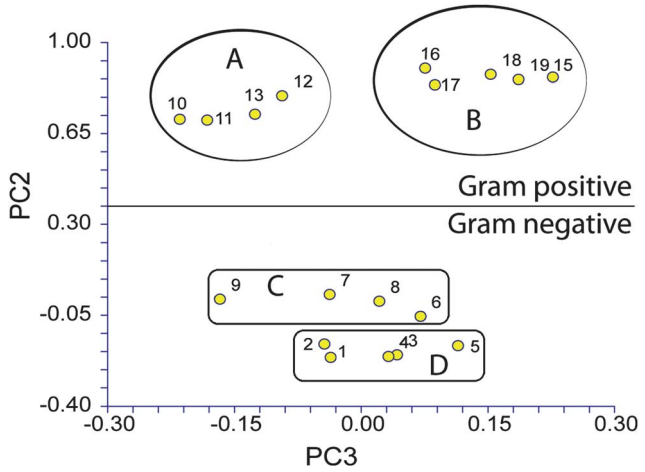

Fig. 4 Cluster analysis of given Gram-positive and Gram-negative bacteria. A stands for *Enterococcus faecalis*, CCM 4224, B for *Streptococcus pyogenes*, C for *Acinetobacter baumannii* and finally D for *Klebsiella pneumoniae*. $N = 5$, statistically outlaying points were removed from the respective datasets.

classical histochemical methods, usually employed in this field, which are based on the staining of a previously grown bacterial population, the method presented here is an interesting alternative with clearly defined potential.

Acknowledgements

The authors gratefully acknowledge the support from the Operational Program Research and Development for Innovations – European Social Fund (Project no. CZ.1.05/2.1.00/03.0058) and the Operational Program Education for Competitiveness-European Social Fund (CZ.1.07/2.3.00/20.0056) of the Ministry of Education, Youth and Sports of the Czech Republic. This work has also been supported by the Czech Science Foundation (Project no. GAP304/10/1316) and by the Student Project PrF_2012_028 of Palacky University.

Notes and references

1 J. C. Pommerville and I. E. Alcamo, *Alcamo's Fundamentals of Microbiology*, Jones and Bartlett Publishers, Sudbury, Mass., 9th edn, 2011.
2 A. G. Johnson, R. J. Ziegler and L. Hawley, *Microbiology and Immunology*, Lippincott Williams & Wilkins, Philadelphia, 5th edn, 2010.
3 W. W. C. Topley, G. S. Wilson, A. A. Miles and M. T. Parker, *Topley and Wilson's Principles of Bacteriology, Virology and Immunity*, Williams & Wilkins, Baltimore, 7th edn, 1983.
4 W. Xu, J. X. Zhang, L. D. Zhang, X. Y. Hu and X. L. Cao, *J. Nanosci. Nanotechnol.*, 2009, **9**, 4812.
5 J. Kneipp, H. Kneipp, A. Rajadurai, R. W. Redmond and K. Kneipp, *J. Raman Spectrosc.*, 2009, **40**, 1.
6 D. G. Thompson, A. Enright, K. Faulds, W. E. Smith and D. Graham, *Anal. Chem.*, 2008, **80**, 2805.
7 J. Kneipp, H. Kneipp and K. Kneipp, Surface-Enhanced Raman Spectroscopy-Based Optical Labels Deliver Chemical Information from Live Cells, in *New Approaches in Biomedical Spectroscopy*, ed. K. Kneipp, R. Aroca, H. Kneipp and E. Wen trupByrne, 2007, vol. 963, p 186.
8 C. Y. Wu, W. Y. Lo, C. R. Chiu and T. S. Yang, *J. Raman Spectrosc.*, 2006, **37**, 799.
9 K. Kneipp, Y. Wang, R. R. Dasari and M. S. Feld, *Appl. Spectrosc.*, 1995, **49**, 780.
10 S. M. Nie and S. R. Emory, *Science*, 1997, **275**, 1102.
11 K. Kneipp, Y. Wang, H. Kneipp, L. T. Perelman, I. Itzkan, R. Dasari and M. S. Feld, *Phys. Rev. Lett.*, 1997, **78**, 1667.
12 J. Kneipp, H. Kneipp and K. Kneipp, *Chem. Soc. Rev.*, 2008, **37**, 1052.
13 L. Brus, *Abstracts of Papers of the American Chemical Society*, 2001, vol. 221, 112–PHYS.
14 F. Yan and T. Vo-Dinh, *Sens. Actuators, B*, 2007, **121**, 61.
15 W. R. Premasiri, D. T. Moir, M. S. Klempner, N. Krieger, G. Jones and L. D. Ziegler, *J. Phys. Chem. B*, 2005, **109**, 312.
16 A. Sengupta, M. L. Laucks and E. J. Davis, *Appl. Spectrosc.*, 2005, **59**, 1016.
17 H. Y. Chu, Y. W. Huang and Y. P. Zhao, *Appl. Spectrosc.*, 2008, **62**, 922.
18 T. Smith-Palmer, C. Douglas and P. Fredericks, *Vib. Spectrosc.*, 2010, **53**, 103.
19 J. Guicheteau, S. Christesen, D. Emge and A. Tripathi, *J. Raman Spectrosc.*, 2010, **41**, 1632.
20 Y. L. Wang, K. Lee and J. Irudayaraj, *J. Phys. Chem. C*, 2010, **114**, 16122.
21 L. Zeiri, B. V. Bronk, Y. Shabtai, J. Czege and S. Efrima, *Colloids Surf., A*, 2002, **208**, 357.
22 M. Culha, A. Adiguzel, M. M. Yazici, M. Kahraman, F. Sahin and M. Gulluce, *Appl. Spectrosc.*, 2008, **62**, 1226.
23 M. Kahraman, K. Keseroglu and M. Culha, *Appl. Spectrosc.*, 2011, **65**, 500.
24 M. L. Laucks, A. Sengupta, K. Junge, E. J. Davis and B. D. Swanson, *Appl. Spectrosc.*, 2005, **59**, 1222.
25 M. Kahraman, M. M. Yazici, F. Sahin and M. Culha, *Langmuir*, 2008, **24**, 894.
26 Y. L. Liu, Y. R. Chen, X. W. Nou and K. L. Chao, *Appl. Spectrosc.*, 2007, **61**, 824.
27 C. Fan, Z. Q. Hu, A. Mustapha and M. S. Lin, *Appl. Microbiol. Biotechnol.*, 2011, **92**, 1053.
28 H. Kudo, T. Itoh, T. Kashiwagi, M. Ishikawa, H. Takeuchi and H. Ukeda, *J. Photochem. Photobiol., A*, 2011, **221**, 181.
29 D. Cam, K. Keseroglu, M. Kahraman, F. Sahin and M. Culha, *J. Raman Spectrosc.*, 2010, **41**, 484.
30 M. Culha, M. Kahraman, D. Cam, I. Sayin and K. Keseroglu, *Surf. Interface Anal.*, 2010, **42**, 462.
31 A. Sengupta, M. Mujacic and E. J. Davis, *Anal. Bioanal. Chem.*, 2006, **386**, 1379.
32 R. M. Jarvis and R. Goodacre, *Anal. Chem.*, 2004, **76**, 40.
33 L. Zeiri and S. Efrima, *J. Raman Spectrosc.*, 2005, **36**, 667.
34 A. Sengupta, N. Brar and E. J. Davis, *J. Colloid Interface Sci.*, 2007, **309**, 36.
35 A. Walter, A. Marz, W. Schumacher, P. Rosch and J. Popp, *Lab Chip*, 2011, **11**, 1013.
36 E. Kastanos, K. Hadjigeorgiou, A. Kyriakides and C. Pitris, in *Plasmonics in Biology and Medicine Viii*, ed. T. VoDinh and J. R. Lakowicz, 2011, vol. 7911.
37 M. Potara, E. Jakab, A. Damert, O. Popescu, V. Canpean and S. Astilean, *Nanotechnology*, 2011, **22**, 135101.
38 J. Y. Zhang, J. Do, W. R. Premasiri, L. D. Ziegler and C. M. Klapperich, *Lab Chip*, 2010, **10**, 3265.
39 X. Yang, C. Gu, F. Qian, Y. Li and J. Z. Zhang, *Anal. Chem.*, 2011, **83**, 5888.
40 H. W. Cheng, S. Y. Huan, H. L. Wu, G. L. Shen and R. Q. Yu, *Anal. Chem.*, 2009, **81**, 9902.
41 S. Efrima and L. Zeiri, *J. Raman Spectrosc.*, 2009, **40**, 277.
42 R. Prucek, A. Panáček, A. Fargašová, V. Ranc, V. Mašek, L. Kvítek and R. Zbořil, *CrystEngComm*, 2011, **13**, 2242.

Analyst

RSC Publishing

PAPER

View Article Online
View Journal | View Issue

Cite this: *Analyst*, 2013, **138**, 5983

Discrimination of circulating tumor cells of breast cancer and colorectal cancer from normal human mononuclear cells using Raman spectroscopy

Václav Ranc,*[a] Josef Srovnal,[b] Libor Kvítek[a] and Marian Hajduch[b]

Circulating tumor cells present an important marker of the progress of several cancer diseases including breast and colorectal cancer, and enables an interesting prognosis and diagnostic options that can complement convenient diagnostic techniques based on several imaging methods. Based on its relevance, the analysis of such kinds of cells is within the scope of many research and clinical institutes; however, it still presents a difficult task. Here we used a state-of-the-art micro-Raman microscopic technique to enhance possibilities in the study of circulating tumor cells and their further differentiation. As cytospins present a convenient form of sample collection and preparation, we used this form of sampling as the initial point. Raman presents a non-destructive form of sample analysis and thus the samples can be further used for a method validation. We have considered the influence of fixation methods of the cells, where we found out that the ability of Raman spectroscopy to differentiate between three cell lines strictly depends upon the sample preparation method used. Namely breast (BT 549) and colorectal (HCT 116) circulating tumor cell lines and human mononuclear cells were compared. Methanol and paraformaldehyde methods of fixation were compared to simple drying out of the sample. It has been shown that drying out of the cells enables the best performance to be obtained in cell differentiation and this is demonstrated by the use of principal component analysis, where all three given cell lines were differentiated with a high level of confidence. Next, the cells were also scanned using 1 μm spatial resolution. The acquired data were visualized using both chemigrams and hierarchical clustering analysis.

Received 26th April 2013
Accepted 24th July 2013

DOI: 10.1039/c3an00855j

www.rsc.org/analyst

1 Introduction

Cancer represents one of the most serious diseases in the world, and a development of methods able to diagnose its early stages is thus very demanding. Among different types of cancer, breast, non-small cell lung cancer and colorectal cancer represent the most dangerous types.[1] It is worth mentioning that breast cancer incidence is increasing at 1.5% per annum and represents almost 20% of all cancer types in woman and is the commonest cause of cancer death for women.[2] Colorectal cancer (CRC) presents a serious public health problem: it is the second leading cause of cancer mortality in the modern world, next to a lung cancer. Each year there are nearly one million new cases of CRC diagnosed worldwide and half a million deaths.[3] Nowadays, the tumor staging is mainly focused on local tumor extension, metastatic lymph node involvement, and evidence of overt distant metastasis obtained by imaging technologies such as PET scan, MRI, CT, mammography and others.[4] However, the sensitivity of mentioned staging procedures is very limited and the detection of early tumor cell dissemination as a key event in tumor progression can thus be problematic. Many research teams have therefore aimed their research scope at the development of sensitive assays allowing the specific detection of single tumor cells. An emerging approach to detect metastasis is the analysis of circulating tumor cells (CTCs), which has recently shown promise in filling gaps left by the previously mentioned imaging techniques. CTCs are tumor cells originated in primary tumor sites or metastases, respectively. These cells are circulating in a patient's blood stream and are not usually found in the healthy population.[5] CTCs are usually analyzed using several established procedures including mRNA markers,[6–9] membrane micro filters,[10] flow cytometers,[9,11,12] or by an evaluation of morphology.[13] Recent progress in microfluidic techniques has led to new detection strategies able to detect low volumes of samples and with increased efficiency.[12] Spectroscopic methods based on IR and Raman spectroscopy present an interesting alternative to commonly used techniques and have the strong potential to become used on a more common basis. There have been some pilot works already

[a]*Regional Centre of Advanced Technologies and Materials, Department of Physical Chemistry, Faculty of Science, Palacký University in Olomouc, 17 listopadu 12, 77146 Olomouc, Czech Republic. E-mail: vaclav.ranc@upol.cz*

[b]*Institute of Molecular and Translational Medicine, Faculty of Medicine and Dentistry, Palacky University Olomouc, Hněvotínská 5, 779 00 Olomouc, Czech Republic*

published on the theme of the detection of CTCs, which show its current state and potential.[14–19] For example, Kim *et al.* have shown the potential of SERS biotags in the analysis of cancer cells using composites based on silver with attached antibodies, which were able to detect cancer cells based on their receptors on the cell surface.[20] Noh *et al.* updated this idea with the incorporation of a magnetic core so that the tumor cells could be separated from the presented matrix.[21] Analysis of CTCs presents an interesting field, where only a little research has been performed so far. Neugebauer *et al.* have performed initial pilot studies in the analysis of circulating tumor cells using MicroRaman imaging, where they sought to distinguish between various cells presented in human blood.[15,22] The method was performed in aqueous medium. However, analysis of CTCs on cytospins, where common sample procedures are taken into account has, at present, received little or minor attention. The main advantage lies in the possibility of analyzing cells using non-destructive spectral technique such as Raman spectroscopy, and afterwards validating the results using the classical histochemical approach.

Here we sought to evaluate the potential of Raman spectroscopy in the discrimination of CTCs from normal human lymphocytes and between two cancer cell lines, namely breast cancer (BT 549) and colorectal cancer (HCT 116) cell lines. Our goal was to achieve a suitable level of discrimination on cytospin cell samples, where three different approaches to cell fixation were compared: drying out, methanol and paraformaldehyde, respectively. The importance of a selection of suitable fixation agent has already been proved on cultured exfoliated oral (buccal) mucosa cells and HeLa cells,[23,24] where the basics of spectral cytopathology were also discussed. It was found that fixation does not influence the quality of Raman spectra over time and has no or only a minor effect, compared to changes induced by diseases. However, the influence of different fixation procedures on the quality of spectra has not been described in detail so far, and presents an important aspect which is covered in this work. The analysis described here is based on a commonly used procedure of sample preparation: cytospinning. In his way, prepared samples of cells present a convenient approach and thus their further application in Raman spectroscopy can present a potentially strong alternative source of information, where the samples can be further used in morphological and histochemical studies.

2 Experimental

2.1 Preparation of cells for Raman measurements

The HCT 116 cell line was purchased from Horizon Discovery (Cambridge, UK) and maintained in McCoy's 5A medium with 2 mM glutamine, 100 U mL^{-1} penicillin, 100 mg mL^{-1} streptomycin and 10% fetal calf serum. The BT 549 cell line was purchased from Charles River laboratories (Wilmington, MA, USA) and maintained in DMEM/RPMI 1640 with 5 g L^{-1} glucose, 100 U mL^{-1} penicillin, 100 mg mL^{-1} streptomycin and 10% fetal calf serum. Human mononuclear cells from blood were isolated by an osmotic lysis method using hypotonic lysis buffer (containing 1.55 M NH_4Cl, 0.1 M NH_4HCO_3 and 1 mM EDTA). The mixture of mononuclear cells and BT 549, resp. HCT 116, were prepared at a 1 : 1 ratio in phosphate buffered saline (PBS) and centrifuged at 500 rpm for 5 min in the cytospin chamber on glass slides (Cyto-tek Cytocentrifuge, Sakura, Torrance, CA, USA). Cytospins were dried and then fixed using methanol or paraformaldehyde.

2.2 Apparatus

Raman spectra of the cytospins were acquired using a Thermo Scientific DXR Raman Microscope (Thermo Electron, USA) equipped with laser operating at the 532 nm wavelength. The laser power on sample was set up to 10 mW and the measured range was 40–1800 cm^{-1}. The exposition time was set to 5 s with 3 expositions per spectrum. Sixteen spectra were averaged to obtain one experimental data point. Each chemigram shown of the respective tumor cell was acquired using a spatial resolution of 1 μm. Experimental points are averages of 16 independent scans.

2.3 Data processing

All of the obtained spectra were processed using custom scripts written in Matlab (Version 2012a, Mathworks, USA). Each spectrum was compared with a spectrum of a corresponding blank point (average of 16 measurements of a glass platform), where individual blanks were measured for each platform. Consequently, spectra were smoothed using the Savitsky–Golay algorithm with a convolution coefficient of 5 and vector normalization. Next, normalization of the spectra was performed by the subtraction of individually calculated polynomial functions from each spectrum, where the polynomial function was calculated using a fitting algorithm. This algorithm served as a tool to find a best fitting polynomial function for each respective evaluated spectrum.

2.4 Acquisition of the chemigrams

Firstly, samples of defined cells of cancer cell lines were scanned over using a micro stage Raman accessory. Firstly, 10 spectra of each cell were obtained. Scanning parameters were then set accordingly to obtained results. Consequently, one cell of each population was scanned using high-resolution mode (total spatial resolution was set to 1 μm). Chemigrams were plotted using Atlus software (Thermo Electron, USA) and ENVI (version 5.0, Excelis visualization solution, USA).

2.5 Spectral image processing

Firstly, data obtained by the spectral characterization of each cell at 1 μm spatial resolution were vector normalized and the spectrum of a blank spot was subtracted from each data point. Data were then truncated to the 450–1800 cm^{-1} region and were transferred to statistical imaging software ENVI (version 5.0, Excelis visualization solution, USA) for further data mining, where hierarchical clustering and main data imaging were performed. The hierarchical cluster analysis was performed by means of finding the best number of clusters, where 3–11 were

tested. Finally, 4 clusters were selected as the most suitable and corresponding imaging was performed.

2.6 Principal component analysis

Previously normalized and smoothed spectra were processed using analysis of the principal components in TQ Analyst software (Thermo Electron, USA). The spectra were truncated to regions holding the information and analysis was processed in the region from 450 to 1800 cm^{-1}.

3 Results and discussion

First, glasses with prepared cytospins (size of 1000 × 1000 μm), containing 40 000 cells were preliminarily scanned over using a low-resolution image processing mode with a spatial resolution of 100 μm; the obtained results were used for the optimization of sample processing, laser adjustments and set up of the optics. Afterwards, 240 scans were acquired randomly over the population of the cells. Representative spectra are shown in Fig. 1; they are averages of all acquired scans over each cell line prepared using three described fixation approaches, namely: dried out sample, methanol and paraformaldehyde fixation.

It can be seen that there are considerable spectral differences among the different cell lines. These differences probably originate in nuances between the surfaces of the evaluated cells, and this part is measured in our experimental design. The differences between surface compositions of diverse cell lines observed here can be caused by a distorted expression of many proteins and overall chemical changes on the cell surface. These changes are causally projected to variability in a chemical composition of such surfaces that have been previously described, *e.g.* in the works of refs 25–28, where mainly carbohydrates and proteins were taken in account. In Fig. 1, it can be seen that various fixation protocols lead to considerable differences in the measured spectra; however, these averaged spectra contain complementary information. It can be seen that all spectra contain similar bands, but of considerably different intensities. The use of methanol and paraformaldehyde increases bands corresponding to membrane proteins projected at the following wavelengths: Amide I (1655 cm^{-1}), Amide II (1586 cm^{-1} and 1559 cm^{-1}), protein band (1441 cm^{-1}) as well as $\nu_{as}PO_2^-$ (1244 cm^{-1}). Among the strong bands can also be found band of carbohydrates at 1171 cm^{-1} and glycogen at 1014 cm^{-1}. The explanation can lie in the fact that the use of methanol as a fixation agent is washing out most of the membrane lipids and thus is removing one of the key points of difference between the cell lines.[29] On the other hand, information regarding protein composition remains strong and the overall sample matrix is simplified. A similar effect can be induced by the use of paraformaldehyde.[30] It is worth mentioning that the spectral differences among data acquired on the same cell line are lower than 10% (measured as relative standard deviance, RSD, between spectral points).

Differences between all three tested samples were statistically evaluated using principal component analysis (PCA), performed on all measured data. The results of such analysis are shown in the upper image of Fig. 2 for the drying out sample fixation method, and in the bottom images of Fig. 2 for methanol and paraformaldehyde, respectively.

Data obtained from dried out samples indicate that the method has the potential to differentiate among cancer cell lines and normal human lymphocytes (PBMC, △) as well as differentiating the HCT 116 (○) and BT 549 (□) cell lines, because the experimental data points are centered in clusters with a considerable distance between them. BT 549 represents a case with a relatively high degree of difference, compared to mononuclear cells (PBMC) and HCT 116 cells. This fact can be interpreted by considerable changes in expression rates of many proteins on the cell surface. Moreover, differences in different gene expressions are also reflected in the morphology of such cells. Leucocytes were separated from the other two clusters, too, but with a smaller separation factor from the HCT 116 cells, given by their surface similarities. On the other hand, data from methanol and paraformaldehyde fixation gave moderately

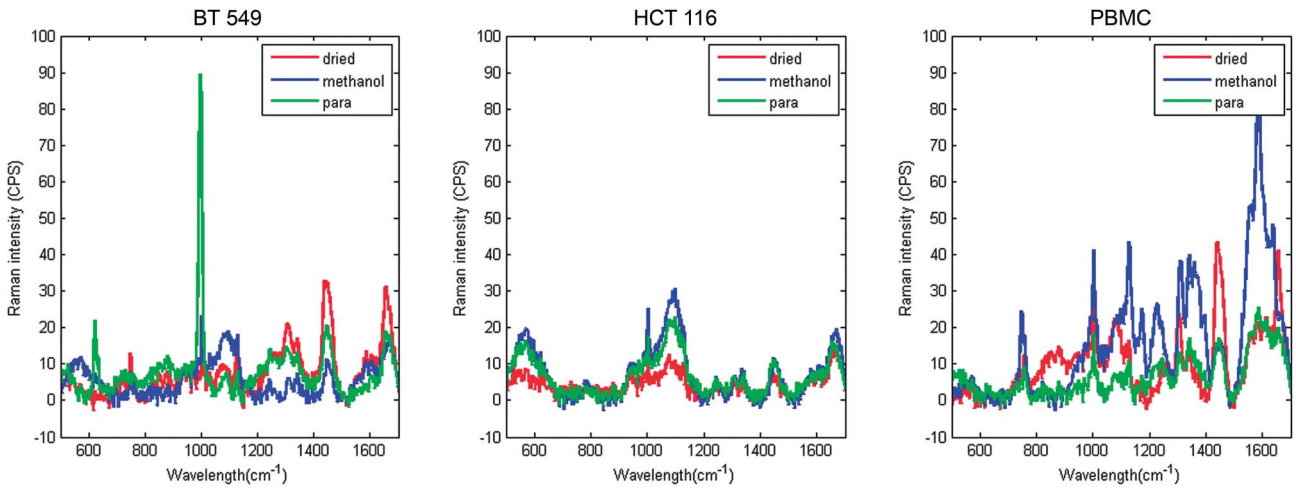

Fig. 1 Spectral characterization of the cell lines acquired on samples with three different protocols of fixation, including dried out samples (—), methanol (—) and paraformaldehyde (—) fixation.

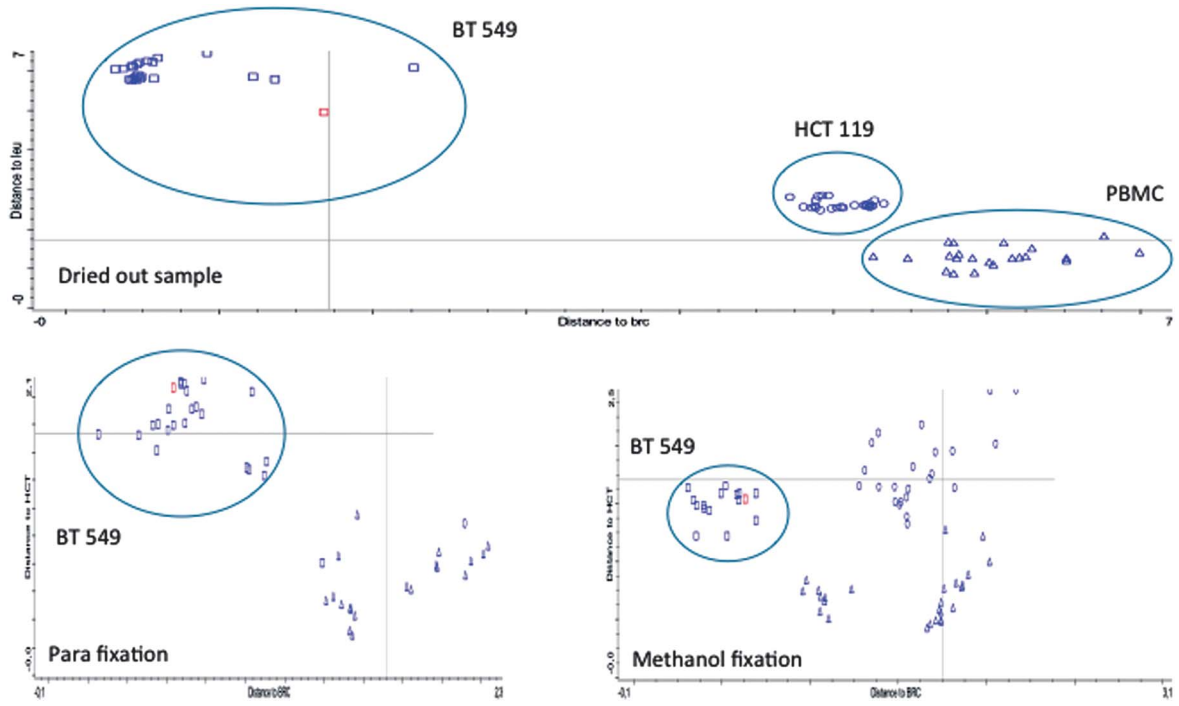

Fig. 2 Graphical expression of the principal component analysis of data obtained by evaluation of dried out samples (upper image) and methanol and para-formaldehyde fixation (bottom images). Cells of the same cell line are centered in respective clusters, where the distance between the clusters represents the level of discrimination (Mahalanobis distance).

worse results, although it is still possible to differentiate these cell lines from PBMC; however, it is not possible to differentiate cancer cell lines any further as can be seen in the bottom images of Fig. 2. This can be caused by the absence of membrane lipids, which hold important information. The overall amount of discrimination can be further described using the Mahalanobis distance, which calculates the distances between standards and clusters. Standards obtained by drying out (Fig. 2 upper image), coming from different cell lines, are completely separated and the distance between the classes is from 1 to 2.5. On the other hand, the distance between members of the same class is in orders of tenths.

However, the multiple-point spectral characterization of given samples does not give complete information regarding the cell surface, which could provide advanced information about the cell itself and thus help to understand the substantial differences between different cancer cells. Such a type of surface analysis presents common tasks; however, only on specifically prepared samples. Here we explored a possibility of reading information about the cell surface from the cytospins provided as a common sample preparation technique. In this way prepared samples can be thus further used in histochemical and morphological experiments and provide additional, complementary information. Moreover, cytospins are usually used as a main sample preparation technique in the diagnosis and prognosis of clinical cancer disease and thus the added Raman spectral information can provide valuable added information without any further sample processing. Here, high resolution chemigrams, with a spatial resolution of 1 μm, of each kind of measured cell line, prepared using drying out of the cells were acquired. The number of scans for each spatial point was set to 16, where this amount of experimental points was found to suit a desired level of the signal/noise ratio. The resulting images are shown in Fig. 3.

BT 549 represents the breast cancer circulating cells and HCT 116 stands for the colorectal carcinoma circulating cell line, respectively. The microscopic images (parts C and F) were acquired using a built in microscope with 50× magnification; part of the MicroRaman microscope used. Fig. 3 also shows two sets of visualizations for both cell lines. First column represents chemigrams (parts A and D) of the cells processed using the ENVI visualization software. Images were acquired by the processing of all acquired bands in the range of 400–1750 cm^{-1}, where all acquired data points were taken in account and compared. Differences between the obtained spectra are shown as different shades of grey. It is well known that the cell surface is a very complex and inhomogeneous matrix, which is supported by the results obtained here. The complexity of the cell surface was also evaluated by the visualization of results of hierarchical clustering performed on the obtained spectra (parts B and E). This process allowed a deeper study of the marginal changes in spectral data obtained at different spatial points. The best fitting number of clusters was found out to be four (tested from 2 to 11, data not shown here), based on the comparison and evaluation of the microscopic images and chemigrams obtained in the previous steps with the results of the hierarchical analysis. It can be seen that our processing is able to distinguish between cells and background and is able to

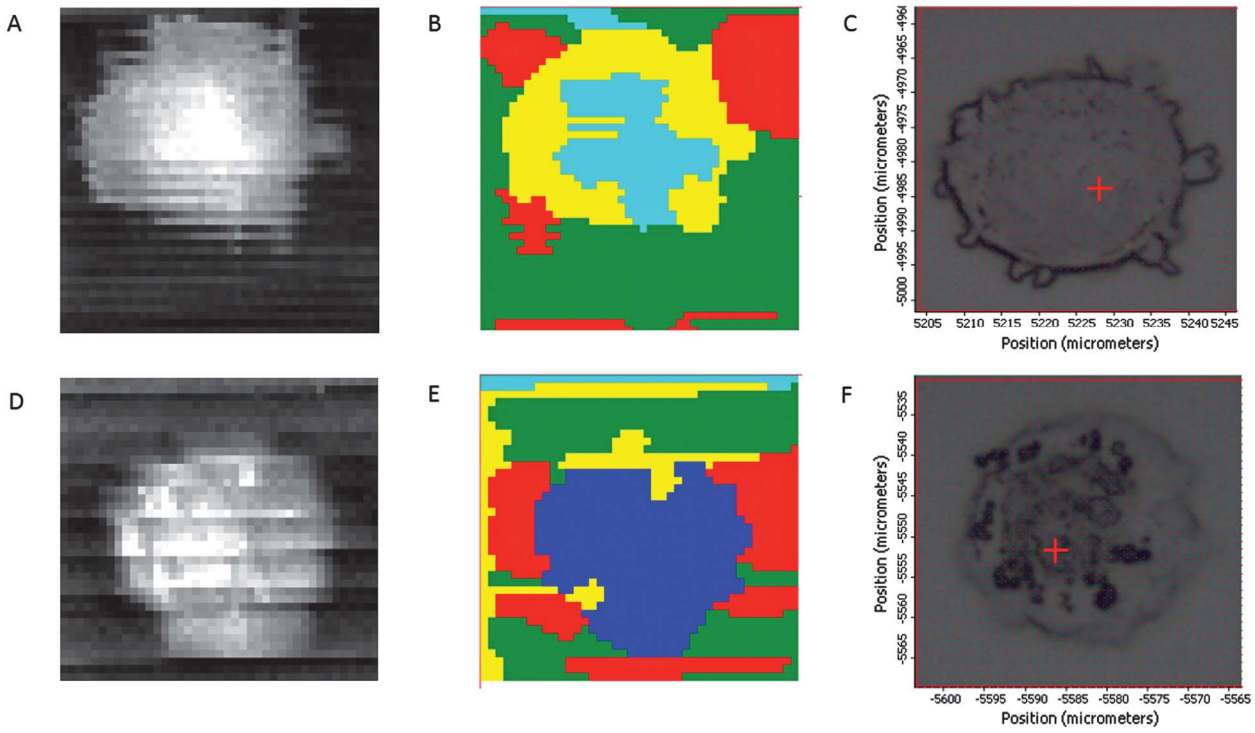

Fig. 3 Visualization of selected cells: (A) represents the chemigram of a BT 549 cell, (B) represents an image given by hierarchical clustering of data obtained on a BT 549 cell, (C) represents an optical microscopic image (50× magnification); (D) is the chemigram of a HCT 116 cell processed similarly to the BT 549 cell, (E) hierarchical image obtained on the HCT cell data, and (F) represents the optical microscopic image of a HCT 116 cell (50× magnification).

process small differences across cell surfaces as well. Set colors present clusters of spectra with a defined level of similarity and on the other hand, difference between colors shows on a spectral difference among clusters. As can be seen in Fig. 3, differentiation between organelles is not possible; however, the information provided by the analysis can be helpful in future method development and statistical data evaluation.

4 Conclusions

The effect of cell fixation approach plays a key role in the evaluation of cells using various optical methods, including Raman and IR spectroscopy. Its effect originates in processes that take place during a fixation and immediately after the fixation is completed. It was found out that the chemical structure of the cells remains unchanged after the fixation is finished and thus they can give comparable spectral information, when measured after a few days or a few years of storage.[23,24] We have evaluated the effect of the cell fixation approaches, namely dried out samples, methanol fixation and paraformaldehyde fixation, on the discrimination of breast circulation cells, colorectal carcinoma circulation tumor cells and human normal lymphocytes. We have found that the cell fixation protocol plays a crucial role in the process of discrimination, where the best results were obtained using the dried out samples. These results indicate that all three evaluated cell lines can be discriminated at a significant statistical level using principal component analysis performed on previously normalized data.

Next, visualization of cells, especially their surfaces, plays a key role in the process of their characterization. We have performed a data visualization using various approaches, namely chemigrams, based on the evaluation of all acquired spectral bands and also visualization based on ahierarchical clustering, where 4 clusters were selected as the best for our experimental data. As a complementary data source, optical microscopic images were also acquired. All three visualization protocols give information about the cells, where chemical visualization also gives results regarding the chemical composition of the cell surface.

Acknowledgements

This work is supported by the Operational Program Research and Development for Innovations – European Regional Development Fund (Project CZ.1.05/2.1.00/03.0058) and by the Technology Agency of Czech Republic (Project no. TA03011368).

References

1 F. E. Bair, National Institutes of Health (U.S.) and National Cancer Institute (U.S.), *Cancer sourcebook: basic information on cancer types, symptoms, diagnostic methods, and treatments, including statistics on cancer occurrences worldwide, and the risks associated with known carcinogens and activities*, Omnigraphics, Detroit, MI, 1991.
2 J. M. Ferrero and M. Namer, *Arch. Anat. Cytol. Pathol.*, 1994, **42**, 198–205.

3 A. Bolocan, D. Ion, D. N. Ciocan and D. N. Paduraru, *Chirurgia*, 2012, **107**, 555–563.
4 C. Alix-Panabieres, H. Schwarzenbach and K. Pantel, *Annu. Rev. Med.*, 2012, **63**, 199–215.
5 D. Wright and M. Unger, *MLO: Med. Lab. Obs.*, 2010, **42**, 6.
6 I. H. Wong, A. T. Chan and P. J. Johnson, *Clin. Cancer Res.*, 2000, **6**, 2183–2188.
7 D. R. Yates, M. Roupret, S. J. Drouin, E. Comperat, S. Ricci, R. Lacave, P. Sebe, G. Cancel-Tassin, M. O. Bitker and O. Cussenot, *Prostate*, 2012, **72**, 1382–1388.
8 R. A. Ghossein and J. Rosai, *Cancer*, 1996, **78**, 10–16.
9 A. M. Gilbey, D. Burnett, R. E. Coleman and I. Holen, *J. Clin. Pathol.*, 2004, **57**, 903–911.
10 S. Zheng, H. Lin, J. Q. Liu, M. Balic, R. Datar, R. J. Cote and Y. C. Tai, *J. Chromatogr., A*, 2007, **1162**, 154–161.
11 C. M. Pitsillides, J. M. Runnels, J. A. Spencer, L. Zhi, M. X. Wu and C. P. Lin, *Cytometry, Part A*, 2011, **79**, 758–765.
12 E. R. Tkaczyk and A. H. Tkaczyk, *Cytometry, Part A*, 2011, **79**, 775–788.
13 S. R. Raper, *Surgery*, 1999, **126**, 827–828.
14 X. Wang, X. Qian, J. J. Beitler, Z. G. Chen, F. R. Khuri, M. M. Lewis, H. J. Shin, S. Nie and D. M. Shin, *Cancer Res.*, 2011, **71**, 1526–1532.
15 U. Neugebauer, T. Bocklitz, J. H. Clement, C. Krafft and J. Popp, *Analyst*, 2010, **135**, 3178–3182.
16 U. Neugebauer, J. H. Clement, T. Bocklitz, C. Krafft and J. Popp, *J. Biophotonics*, 2010, **3**, 579–587.
17 A. S. Biris, E. I. Galanzha, Z. Li, M. Mahmood, Y. Xu and V. P. Zharov, *J. Biomed. Opt.*, 2009, **14**, 021006.
18 M. Y. Sha, H. Xu, M. J. Natan and R. Cromer, *J. Am. Chem. Soc.*, 2008, **130**, 17214–17215.
19 R. Mitra, O. Chao, Y. Urasaki, O. B. Goodman and T. T. Le, *BMC Cancer*, 2012, **12**, 540.
20 J. H. Kim, J. S. Kim, H. Choi, S. M. Lee, B. H. Jun, K. N. Yu, E. Kuk, Y. K. Kim, D. H. Jeong, M. H. Cho and Y. S. Lee, *Anal. Chem.*, 2006, **78**, 6967–6973.
21 M. S. Noh, B. H. Jun, S. Kim, H. Kang, M. A. Woo, A. Minai-Tehrani, J. E. Kim, J. Kim, J. Park, H. T. Lim, S. C. Park, T. Hyeon, Y. K. Kim, D. H. Jeong, Y. S. Lee and M. H. Cho, *Biomaterials*, 2009, **30**, 3915–3925.
22 U. Neugebauer, J. H. Clement, T. Bocklitz, C. Krafft and J. Popp, *J. Biophotonics*, 2010, **3**, 579–587.
23 A. I. Mazur, E. J. Marcsisin, B. Bird, M. Miljkovic and M. Diem, *Anal. Chem.*, 2012, **84**, 8265–8271.
24 A. I. Mazur, E. J. Marcsisin, B. Bird, M. Miljkovic and M. Diem, *Anal. Chem.*, 2012, **84**, 1259–1266.
25 Z. Song, J. Varani and I. J. Goldstein, *Int. J. Cancer*, 1993, **55**, 1029–1035.
26 E. Lang, P. Altevogt and V. Schirrmacher, *Cancer Detect. Prev.*, 1987, **1**, 73–79.
27 M. Fogel, E. Gorelik, S. Segal and M. Feldman, *J. Natl. Cancer Inst.*, 1979, **62**, 585–588.
28 S. Friberg, Jr, J. Molnar and G. I. Pardoe, *J. Natl. Cancer Inst.*, 1974, **52**, 85–93.
29 M. V. Brown, J. E. McDunn, P. R. Gunst, E. M. Smith, M. V. Milburn, D. A. Troyer and K. A. Lawton, *Genome Med.*, 2012, **4**, 33.
30 M. C. Jamur and C. Oliver, *Methods Mol. Biol.*, 2010, **588**, 63–66.

analytical chemistry

Article

pubs.acs.org/ac

Magnetically Assisted Surface-Enhanced Raman Scattering Selective Determination of Dopamine in an Artificial Cerebrospinal Fluid and a Mouse Striatum Using Fe_3O_4/Ag Nanocomposite

Vaclav Ranc,*[,†] Zdenka Markova,[†] Marian Hajduch,[‡] Robert Prucek,[†] Libor Kvitek,[†] Josef Kaslik,[†] Klara Safarova,[†] and Radek Zboril*[,†]

[†] Regional Center of Advanced Technologies and Materials, Department of Physical Chemistry, Faculty of Science, Palacky University Olomouc, 17. listopadu 1192/12, 771 46 Olomouc, Czech Republic

[‡] Institute of Molecular and Translational Medicine, Faculty of Medicine and Dentistry, Palacky University Olomouc, Hněvotínská 5, 779 00 Olomouc, Czech Republic

Supporting Information

ABSTRACT: The dopaminergic neural system is a crucial part of the brain responsible for many of its functions including mood, arousal, and other roles. Dopamine is the key neurotransmitter of this system, and a determination of its level presents a demanding task needed for a deeper understanding of the processes, even pathological, involving this brain part. In this work, we present a method for a fast analysis of dopamine levels in samples of cerebrospinal fluid and mouse striatum. The method is based on a nanocomposite composed of magnetite and silver nanoparticles, whose surface is modified with iron nitriloacetic acid (Fe-NTA)—a dopamine-selective compound. The magnetic properties of this nanocomposite enable simple separation of targeted molecules from a complex matrix while the silver acts as a platform for surface-enhanced Raman scattering (SERS). Silver and magnetite nanoparticles are joined by carboxymethyl chitosan, useful in biological environments and enhancing the sensitivity due to the presence of carboxyl groups. This system reveals a good stability and reproducibility. Moreover, rapid and simple quantitative experiments show an improvement in the detection of dopamine levels in biological assays at low femtomolar concentrations. The comparative data performed with clinical samples of mouse striatum show that the developed magnetic SERS is a strong alternative to conventional high-performance liquid chromatography−mass spectrometry (HPLC−MS) with even several superior aspects including faster and cheaper analysis and no necessity of sample preconcentration or derivatization.

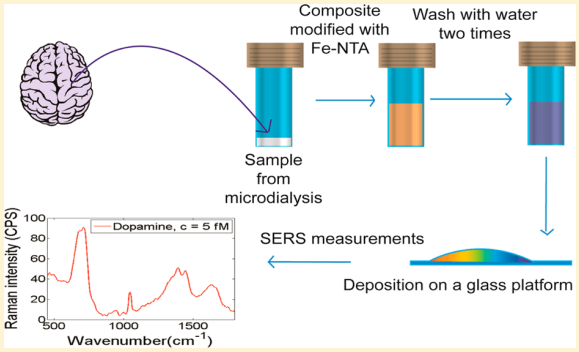

The ability to predictably relate a physiological level of dopamine in selected brain systems to its current state and find a logical correlation in a diagnosis and prognosis present an important task of neurochemistry and neurophysiology. Basal dopamine levels are connected to basic brain functions, where the importance of this particular excitatory neurotransmitter is underlined by its many roles in a brain regulation and modulation.[1] Disturbed concentration levels of this neurochemical had been previously connected to various pathologic states such as Parkinson's or Alzheimer's disease.[2] In the light of these premises, the knowledge of dopamine concentration levels thus plays an important role not only in a treatment of those diseases but also in the study of basic brain functions. Developing methods to determine dopamine levels in various biological matrixes, from cerebrospinal fluid to blood, has a long history. These days, the determination of neurotransmitters is usually performed using electrochemical or mass spectrometric approaches.[3] Regarding dopamine, electrochemical tools are able to determine levels of dopamine in vivo at subnanomolar concentration levels.[4] However, drawbacks of such methods are related to their relatively low selectivity and mechanical properties.[5] Recently, some works have shown that the signal of dopamine can be successfully separated from the matrix using advanced voltametric approaches,[6] where uric acid had been taken as a model system. The ex vivo samples or samples obtained by microdialysis approaches are usually analyzed using chromatographic techniques (mostly high-performance liquid chromatography, HPLC) with electrochemical (ECD) or mass spectrometric (MS) detection.[7] These methods have higher levels of selectivity, compared to direct electrochemical determination; however, the sample preparation can be more complicated and analysis times are longer. Electrochemical determination offers very low limits of detection, usually at nanomolar limits, nonetheless with

Received: September 23, 2013
Accepted: February 20, 2014
Published: February 20, 2014

   dx.doi.org/10.1021/ac500394g | Anal. Chem. 2014, 86, 2939−2946

considerably lower selectivity compared to mass spectrometric approaches. On the other hand, mass spectrometric approaches are limited by higher limits of detection (LOD). These drawbacks have been recently covered by an addition of derivatization steps leading to a decrease of the LODs,[8] however, usually for the price of method reproducibility and reliability. The use of Raman spectroscopy in the analysis of neurotransmitters can be an interesting alternative. Its usage in the analysis of physiological levels of dopamine had not been applicable before the surface-enhanced Raman scattering (SERS) was discovered.[9] The SERS approach offers very interesting limits of detection allowing a detection of single molecules with a relatively high level of selectivity given by the method principle.[10] This technique usually utilizes nanotechnology of nanoparticles (NPs) of noble metals such as silver and gold, respectively.[11] The selectivity of such methods can be further increased using surface modifications of respective nanoparticles, where antibodies are usually used.[12]

Analysis of samples where matrix presents a highly complex system still presents a challenge, and simplification and time efficiency are very demanding properties of newly developed methods. Regarding SERS, the nanoparticles with magnetic properties are one of the available ways.[13] The ability to magnetically separate the target from the complex matrix and detect it using SERS presents a very interesting option and can fill the gap left by the use of chromatographic approaches. The preparation of Fe_3O_4/Ag nanocomposites has been deeply studied, and many preparation procedures have been published.[14] Such nanocomposites have been already applied in the SERS methods, e.g., in the analysis of circulating tumor cells,[15] proteins,[16] or lung cancer.[17]

In this work, we present a new rapid method for the analysis of dopamine levels in artificial cerebrospinal fluid and in a mice striatum. This brain system plays an important role in many behavioral functions including reward and addiction. This method was designed to work with low sample volumes obtained during commonly used extraction procedures. In principle, magnetic nanobeads with bonded silver nanoparticles are used as substrate, which allows easy sample cleanup and foregoing magnetic separation of the target analyte from the unwanted compounds in the matrix (salts, proteins, peptides, sugars, etc.). The surface of the silver particles is covered with dopamine-selective reporter compounds (α,β-nitriloacetic acid and $Fe(NO_3)_2$; Fe-NTA), allowing specific detection of dopamine using SERS after a previous sample cleanup. This method offers multiple advantages for implication and detection such as sample cleanup in an easy way, method selectivity, and ultralow detection limits (femtomolar) for dopamine. High selectivity is achieved via a two-step signal evaluation. First, dopamine is attached preferably to the reporter molecule (Fe-NTA), and second, its structure is confirmed by its characteristic SERS spectrum. This method achieves femtomolar limit of detection using novel magnetic nanocomposite of magnetite and silver nanoparticles with a high amplification factor for dopamine (1×10^{10}). Compared to previously used approaches,[18] where similar silver nanoparticles with Fe-NTA and SERS were used, these methods showed detection limits hundreds of times lower and moreover required an additional potential of sample preconcentration, cleanup, and analysis automation through an introduction of magnetic composite. Compared to more conventional chromatographic approaches, the method presented here has considerably lower analysis times (sample measurement does not exceed 2 min, with a possibility to spot many samples on a glass platform and measure them automatically) and thus allows a more efficient way of analyzing large sets of samples obtained by brain tissue extraction, while keeping a high level of selectivity and robustness. This method is thus potentially applicable in a clinical and diagnostic praxis performed on human or nonhuman models, respectively.

EXPERIMENTAL SECTION

Chemicals. Sodium cyanoborohydride (p.a.), formaldehyde solution (37 wt %, in H_2O, p.a.), formaldehyde-d_2 solution (20 wt % in D_2O, 98 atom % D, p.a.), dopamine (p.a.), α,β-NTA ($N\varepsilon$-(N-(+)-biotinyl-6-aminohexanoyl)-$N\alpha,N\alpha$-bis-(carboxymethyl)-L-lysine, p.a.), $Fe(NO_3)_2$ (p.a.), and NaCl (Puriss) were bought from Sigma-Aldrich (San Jose, U.S.A.). Silver nitrate (p.a.), chitosan of low molecular weight (chitosan LMW, 75−85% deacetylated), 4-nitrobenzaldehyde (p.a.), iron(II) chloride tetrahydrate (p.a.), and iron(III) chloride hexahydrate (p.a.) were bought from Sigma-Aldrich Chemie (Steinheim, Germany). Sodium hydroxide (p.a.), ammonium hydroxide solution (28.0−30.0% NH_3 basis), acetic acid (99.8%), and methanol (p.a.) were obtained from P-LAB, Czech Republic). All chemicals were used without further purification. LC−MS grade acetonitrile and formic acid were purchased from Fisher Scientific (New Jersey, U.S.A.) and Fluka (Wisconsin, U.S.A.), respectively. Pure water was prepared by GenPure system (TKA, Niederelbert, Germany). Siliconized microcentrifuge tubes (2 mL) were purchased from Eppendorf (Hamburg, Germany).

Preparation of m@cmCH@Ag@Fe-NTA Nanocomposites. Magnetic nanocomposites with dopamine-selective reporter compound (Fe-NTA) were prepared according to protocols previously published by Markova et al.[13b] Briefly, Fe_3O_4 nanoparticles were prepared using Massart coprecipitation method.[19] Nanoparticles were afterward modified using *O*-carboxymethyl chitosan in order to increase the solubility and biocompatibility of the nanocomposites via an introduction of carboxyl groups according to protocols described earlier.[19] As-prepared nanoparticles were subjected to a reaction with $AgNO_3$ in order to produce nanocomposite m@cmCH@Ag which was finally modified with Fe-NTA to induce selectivity toward dopamine according to method described by Kayat and Volkan.[18] Presence of residual amine groups was evaluated using protocols described by Bruce and Sen.[22] In detail, the procedure can be found in the Supporting Information, experimental part.

Animals. An inbred strain of black mice (C57BL/6 $n = 3$) was used in the experiments. Animals were housed under constant temperature and humidity with free access to food and water. All procedures with live animals were conducted using protocols approved by a respective veterinary office of the Czech Republic.

Sample Preparation: Standard and Model Samples. The study of experimental parameters is based on the analysis of four sets of samples containing defined concentration of prepared silver−magnetite composites. First, test samples were prepared as follows: dopamine of concentration 1×10^{-8} in distilled water was prepared by a sequential dilution of stock solution of dopamine with a concentration level $c = 1 \times 10^{-3}$ mol·L^{-1}; similar samples were then prepared with considerably lower concentration levels of dopamine: 10, 50, 100, 500, and 1000 fmol·L^{-1}. Second, control samples containing artificial cerebrospinal fluid (aCSF) with physiologically identical

dx.doi.org/10.1021/ac500394g | Anal. Chem. 2014, 86, 2939−2946

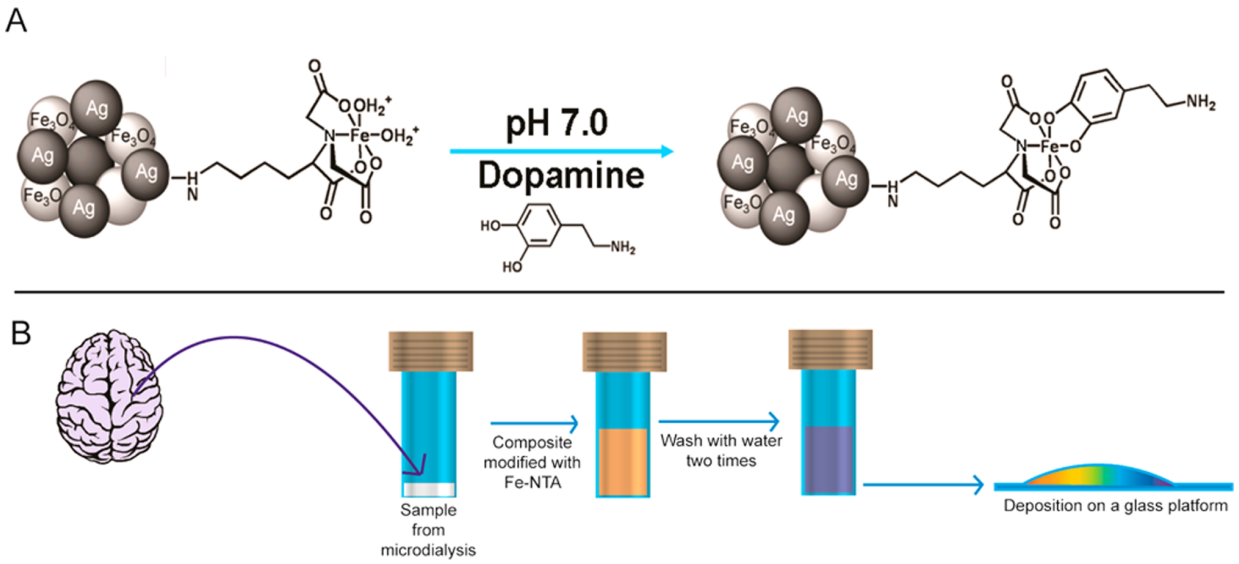

Figure 1. (A) Schematic representation of selective dopamine binding using m@cmCH@Ag@Fe-NTA nanocomposite. (B) Scheme of analysis.

concentrations of salts were prepared. The aCSF was prepared according to well-accepted protocols and contained following concentration of salts and sugars: 124 mM NaCl, 2.5 mM KCl, 2.0 mM $MgSO_4$, 1.25 mM KH_2PO_4, 26 mM $NaHCO_3$, 10 mM glucose, 4 mM sucrose, and 2.5 mM $CaCl_2$.[20] The aCFS was then used as a matrix for a preparation of model samples containing 50 and 500 fmol·L^{-1} of dopamine, reflecting physiological levels.[21] All described samples were treated and analyzed using a protocol described as follows: total volume of 98 μL of a modified composite was mixed with 2 μL of solution containing dopamine, aCSF, or both. Composite was then magnetically separated from the matrix and washed two times in water. Finally, it was redispersed in 10 μL of pure distilled water. From this solution 2 μL were dropped on a glass platform and immediately measured using SERS. The whole scheme of the analysis can be seen in Figure 1.

Sample Preparation: Samples of Brain Tissue Analyzed Using SERS. The male mice of 4−6 weeks old were sacrificed, their brains were dissected, and the striatum parts were carefully extracted. These parts were immediately stored under dark conditions at −80 °C. Brain samples were then subjected to an extraction procedure based on solid−liquid extraction technique and sonication. One milligram of the tissue sample was added to an Eppendorf tube containing 10 μL of acetonitrile/acetic acid (0.98/0.02, v/v) in total. Each sample was homogenized, covered with a tin foil against light, and put into an ultrasonic bath for 15 min. Two microliters of sample extract were mixed with 10 μL of modified composite. It was then magnetically separated, washed two times with distilled water, and redispersed in 10 μL of distilled water. From this solution, 2 μL were dropped on a glass platform and immediately measured using SERS. The scheme of the SERS analysis can be seen in the Figure 1.

Characterization Techniques. Fourier transform infrared (FT-IR) absorption spectra were measured on an FT-IR spectrometer Nicolet iS5 (Thermo Electron, U.S.A.) employing attenuated total reflection (ATR) in a ZnSe crystal, using 64 scans with resolution of 2 cm^{-1}. Air-dried samples were placed directly on a ZnSe crystal. The FT-IR absorption spectra were processed using ATR and baseline corrections.

Transmission electron microscope (TEM) images were obtained using electron microscope JEOL JEM-2010 operating at 160 kV with a point-to-point resolution of 1.9 Å. Energy-dispersive X-ray spectrometry (EDS) measurements were employed on NORAN System 7 X-ray Microanalysis system (Thermo Scientific) combined with a scanning electron microscope Hitachi SU6600 FEG, where for X-ray elemental mapping images, accelerating voltage of 15 kV, working distance 15 mm, and lifetime 4000 s were used. For all microscopic techniques, a drop of a very dilute dispersion was placed on the copper grid with holey carbon film and subsequently allowed to dry at room temperature.

X-ray diffraction (XRD) patterns of all magnetite−polymer−silver composites were recorded on a PANalytical X'Pert PRO diffractometer (iron-filtered CoKα radiation: α = 0.178901 nm, 40 kV, and 30 mA) in Bragg−Brentano geometry, equipped with an ÁCelerator detector, programmable divergence, and diffracted beam antiscatter slits. Magnetically preconcentrated suspensions were dropped on a zero-background single-crystal Si slide, allowed to dry by evaporation at room temperature, and scanned in continuous mode (resolution of 0.017° 2θ, scan speed of 0.008° 2θ/s, 2θ range of 20−105°) under ambient conditions. The SRM640 (Si) and SRM660 (LaB6) commercial standards from NIST were used for the evaluation of line positions and instrumental line broadening, respectively. The acquired patterns were processed (i.e., phase analysis and Rietveld refinement) using X'Pert HighScore Plus software (PANalytical, The Netherlands) and PDF-4+ and ICSD databases (ICSD collection codes are Ag, 52545, and Fe_3O_4, 43001, respectively).

Raman spectra of given samples were acquired on the Thermo Scientific DXR Raman microscope (Thermo Electron, U.S.A.) equipped with a laser operating at 532 nm. The laser power on the sample was set to 10 mW, and the measured range was 400−1800 cm^{-1}. Exposition time was set to 5 s with three expositions per spectrum. Sixteen spectra were averaged to get one experimental data point. Samples were measured as follows: a droplet of volume of 2 μL containing prepared sample mixture (defined in the previous section) was sampled on a glass platform and immediately measured. Regarding the

dx.doi.org/10.1021/ac500394g | Anal. Chem. 2014, 86, 2939−2946

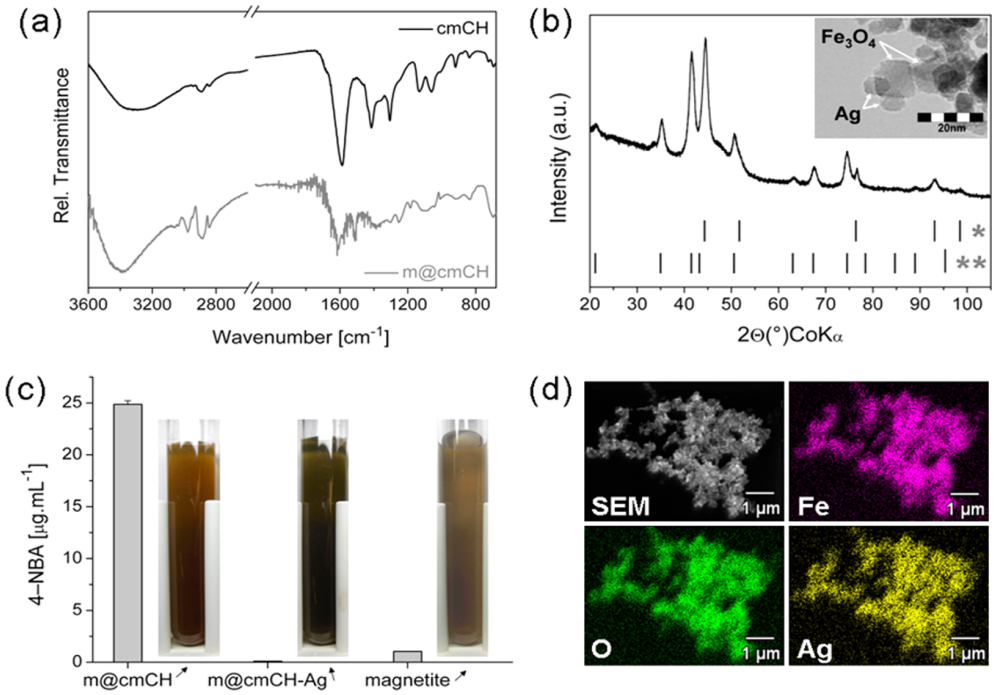

Figure 2. Characterization of prepared m@cmCH hybrid and m@cmCH@Ag composites: (a) FT-IR absorption spectra of cmCH and m@cmCH hybrid. (b) XRD pattern of m@cmCH@Ag nanocomposite (inset: TEM image of the nanocomposite). Theoretical positions of diffraction lines of metallic Ag (*) and magnetite (**) are also shown (ICSD collection codes are Ag, 52545, and Fe_3O_4, 43001, respectively). (c) UV colorimetric analyses of amine groups with 4-nitrobenzaldehyde (4-NBA) performed on m@cmCH hybrid, m@cmCH@Ag composite, and reference (magnetite NPs), respectively, supplemented with relevant photographs of samples. The amount of aldehyde molecules is proportional to the amount of present amine groups. (d) SEM image and X-ray elemental mapping of m@cmCH−Ag nanocomposite.

measurements of calibration curves and repeated analysis of the model and clinical samples, all samples were spotted on the glass platform next to each other (distance = 3 mm) and automatically measured using custom scripts written for the automation software (Macros basic, part of the Omnic 8 suite, Thermo Electron, U.S.A.).

Data Processing. All obtained Raman spectra were processed using custom scripts written in the Matlab (version 2012a, Mathworks, U.S.A.). Each spectrum was compared with a spectrum of corresponding blank point (average of 16 measurements of the currently used glass platform), where individual blanks were measured before each experiment. Consequently, spectra were smoothed using the Savitsky−Golay algorithm with convolution coefficient equal to 5. Next, normalization of the spectra was performed by a subtraction of individually calculated polynomial functions from each spectrum, where the polynomial function was obtained using an in-house written fitting algorithm. This algorithm served as a tool to find a best fitting polynomial function for each respective evaluated spectrum.

RESULTS AND DISCUSSION

Characterization of m@cmCH@Ag Composites. Analysis of dopamine in a cerebrospinal fluid presents a relatively important task given by a function of this neurotransmitter in the brain tissue. Here, we sought to develop an easy to use procedure for the analysis of this compound by SERS using magnetic m@cmCH@Ag composites that can be easily separated from a matrix using magnetic force. First, magnetite−silver nanocomposite was prepared for this application using modified mechanism described earlier by Markova et al.[13b] In this procedure, silver ions are reduced on magnetite surface via amine groups of polymer, which acts also as the stabilizer of magnetic NPs. In this work, *O*-carboxymethyl chitosan (cmCH) was used for surface modification of magnetic NPs. Magnetite@cmCH hybrid (m@cmCH) was prepared by adsorption of cmCH on NPs surface at acidic pH (pH below isoeletric point) where magnetite NPs were positively charged due to the formation of $-FeOH_2^+$ groups.[23]

Infrared spectroscopy was used to determine the absorption of polymer on the NPs surface, and the FT-IR spectra (cmCH and m@cmCH, respectively) are shown in Figure 2a. The characteristic bands of pure cmCH are observed at 3300−3300 (O−H stretch), 2885 (C−H stretch), 1650 (NH_2 deformation), 1600 (N−H bend), 1140 (bridge −O− stretch), 1060 (C−O stretch), and 910 cm^{-1} (pyranose ring). The interpretation of the spectrum was based on previous results published, e.g., by Gao et al.[24] and Chen and Park.[25] Moreover, the peaks of the stretching vibration of asymmetric and symmetric $-COO^-$ groups of cmCH at 1586 and 1415 cm^{-1} are also identifiable in Figure 2a. These characteristic bands are also presented in the spectrum of m@cmCH, although their relative intensities are different. In addition, new peaks occur at 2980, 1260, 1511, and 1200 cm^{-1} in the spectrum of m@cmCH. These peaks can be attributed to a shifted deformation vibration either of OH, COOH, or NH groups upon adsorption on nanoparticles surface.

The m@cmCH hybrid was used for the reduction of silver ions to bind covalently silver nanoparticles. The formed m@cmCH@Ag was characterized by XRD (Figure 2b). In the XRD pattern, we have identified crystalline magnetite and crystalline silver (Figure 2b). The mean X-ray diffraction coherence

dx.doi.org/10.1021/ac500394g | *Anal. Chem.* 2014, 86, 2939−2946

lengths (MCL) calculated from Rietveld refinement analysis of the X-ray powder diffraction pattern for magnetite and silver equals to 10 and 8 nm, respectively. The contents of magnetite and silver phases were found to be 80 and 20 wt %, respectively.

As mentioned above, polymer *O*-carboxymethyl chitosan serves as a linker between magnetite and silver NPs and is essential for both reduction of silver ions and immobilization of silver NPs. However, amine groups can present a potential risk, because of the potentiality of their interaction with the analyte (dopamine) as well causing an increase in the overall limit of detection or leading to unwanted errors in interpretation. Therefore, a UV colorimetric assay that involved reaction of amine with a UV-sensitive reagent (4-nitrobenzaldehyde) was adopted that permitted the accurate, sensitive quantification of surface amine groups. The amount of hydrolyzed 4-nitrobenzaldehyde molecules per milligram of magnetite represents the density of active sites on the composites surface (Figure 2c). From the comparison of m@cmCH hybrid and m@cmCH@Ag nanocomposites, it is clearly seen there is dramatic decrease in free amine groups after silver reduction and immobilization. Moreover, m@cmCH@Ag nanocomposite reveals 10 times lower value (almost undetectable) of immobilized 4-NBA than magnetite NPs without surface modification (magnetite without amine groups on the surface). This difference can be explained as a sorption of 4-NBA with the magnetite surface. These results confirmed that probably all the amine groups on the m@cmCH hybrid are included in the binding of silver nanoparticles and cannot nonspecifically interact during dopamine analysis. Moreover, while all the amine groups are used for binding silver NPs, no change in dispersity of the samples was observed and they reveal excellent colloidal behavior as can be seen from comparison of suspensions before and after silver reduction (see photographs in Figure 2c). Finally, the homogeneous distribution of magnetite and silver NPs over the composite was determined by a scanning electron microscope with energy-dispersive X-ray (SEM/EDX) elemental Fe, O, Ag mapping (Figure 2d).

Analysis of Dopamine Using m@cmCH@Ag@Fe-NTA Nanocomposites. The dopaminergic neuronal system is responsible for many brain functions including cognitive processes[26] and behavior of mammals,[27] among others. Dopamine is also correlated with several diseases, where the most studied are Parkinson's disease,[2b] Alzheimer's,[28] or schizophrenia.[29] The latter correlation was evaluated in NAcc, where the mesolimbic pathway was taken into account. Analysis of this target thus represents a demanding process that can help to uncover a deeper connection between dopamine levels and often pathological states of the brain.

Analysis of dopamine is usually performed using ECD or MS detection, where severe sample pretreatment methods such as solvent evaporation, cryogenic preconcentration, or stable isotopic labeling take place. Here we developed a method for the analysis of dopamine levels using Raman spectroscopy approaches with the utilization of advanced nanocomposites based on Fe_3O_4/Ag. The surface of the particle was modified with Fe-NTA participating as a dopamine-selective molecule. This approach enables an efficient and highly selective target (dopamine) removal from the complex matrix using magnetic force with a consequent determination of its level using SERS methodology. The scheme of the process of analysis can be seen in Figure 1. Silver and magnetite particles were linked together for the first time using carboxymethyl chitosan, which does not contain any free amino groups and thus does not cause any unwanted SERS signal interferences.

The consecutive analytical concept of the new presented approach included several development phases, mainly test samples measurements, quantification experiments, and analysis of model samples. First, test samples containing dopamine were measured. The concentration level of the target was set to $c = 5 \times 10^{-8}$ mol·L^{-1} as an initial point of interest. The SERS spectra were measured using procedures described in the Experimental Section, where a droplet of the washed sample containing dispersion of composite with bonded dopamine was sampled on a glass platform and immediately measured. The resulting spectra are shown in Figure 3. There it can be seen the method

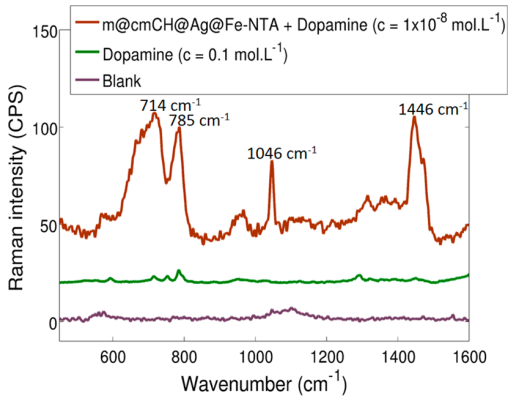

Figure 3. SERS spectra of dopamine, dopamine plus m@cmCH@Ag@Fe-NTA, and blank sample. The concentration level of dopamine was set to 1×10^{-8} mol·L^{-1}. Blank: blank solution containing m@cmCH@Ag@Fe-NTA nanocomposite. Spectrum of dopamine at a concentration level of 1×10^{-1} mol·L^{-1} is added as a reference.

is able to detect the target at this concentration level. Its structure was confirmed using the vibration theory generally used in IR and Raman spectra interpretation. The peak at 1600 cm^{-1} was interpreted as the C═C bond in a phenyl ring, the band at 1446 cm^{-1} was interpreted as C−H bonds presented in the aliphatic chain, the peak at 1046 cm^{-1} was interpreted as the C−N bond, and finally, bands at 785 and 714 cm^{-1} were interpreted as C−H bonds in a phenyl ring. The initial experiment was performed using experimental parameters described in the Experimental Section; nonetheless, their values were tuned to achieve a suitable low limit of detection. The ratio of stock solution of nanocomposite and Fe-NTA was tested from 1:10 to 10:1, where the best results were obtained when 5:1 ratio was selected. For a better transparency, dopamine was measured per se. The signal of the compound was obtained for a final concentration of $c = 1 \times 10^{-1}$ mol·L^{-1}. It can be seen that the signal is moderately weak and dopamine itself cannot be analyzed without the use of the SERS effect. The reached amplification factor (defined, for example, in the work by Li et al.[31]) was 0.952×10^{10}. As the next step, calibration solutions containing 10−5000 fmol·L^{-1} of dopamine were prepared and analyzed; the number of measured replicates was set to five. The band at 1046 cm^{-1} was selected as a quantification marker of dopamine. The parameters of calibration curve can be seen in Table S1 in the Supporting Information. On the basis of the calculated correlation coefficient ($R^2 = 0.996$), it was found out that there exists a linear relationship between the concentration of dopamine and

dx.doi.org/10.1021/ac500394g | *Anal. Chem.* 2014, 86, 2939−2946

intensity of spectral bands interpreted as parts of dopamine structure.

Our focus for model samples was to determine the dopamine levels from microdialysis performed on brain tissue samples. Samples obtained by this procedure are usually highly complex matrixes of salts, small molecules such as neurotransmitters and sugars, and larger molecules such as neuropeptides or even larger proteins, depending on the used dialysis membrane. The volume of the obtained sample is limited to a few microliters, thus complicating the process of analysis by giving only a limited chance to preconcentrate or further purify the sample. Here we sought to mimic the complexity of the matrix by the use of aCSF. The spectra, obtained by measurements of these two solutions, were compared with a measured blank and control solutions (see Figure 4). The blank consisted of target

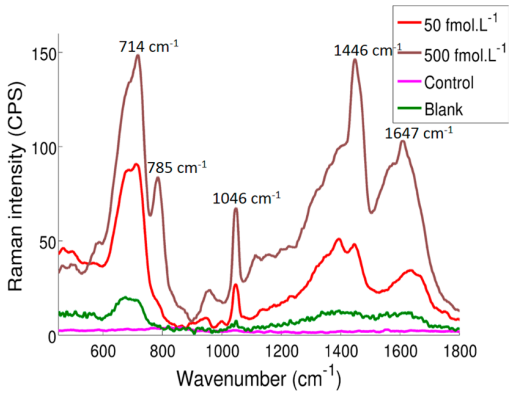

Figure 4. SERS spectra of dopamine analyzed in artificial cerebrospinal fluid (aCSF) at a concentration level of 50 and 500 fmol·L^{-1}. The spectra of the control and blank samples are included for better transparency. The control sample was measured with m@cmCH@Ag@Fe-NTA and aCSF, the blank sample only with m@cmCH@Ag@Fe-NTA nanocomposite.

concentration of m@cmCH@Ag@Fe-NTA in distilled water, without any addition of dopamine or aCSF, respectively. The control sample was obtained by processing 2 μL of aCSF in the same manner as m@cmCH@Ag@Fe-NTA, without addition of dopamine. All samples were processed according to the protocol described in the Experimental Section. Resulting spectra can be seen in Figure 4. Further, dopamine in the model samples was quantified using a previously constructed five-point calibration curve (in the range of 10−5000 fmol·L^{-1}). The samples were measured in batches where number of replicates was set to five. Samples were measured two times per one experimental day (intraday) and again after 5 days (interday). The obtained raw files were subjected to spectral normalization or each measured spectra with the blank solution (defined earlier in the text) measured at the beginning of each batch. Results are summarized in Table S2 in the Supporting Information. It can be seen that the developed method is applicable for the quantification of dopamine at the femtomolar levels. Even though the relative standard deviances are relatively higher compared to a mass spectrometric or electrochemical method, this method presents a great alternative to commonly used analytical techniques in this area of interest. The higher errors are given mainly by the fundamental limits of SERS itself, where any difference between measured spots leads to variations of band abundances. Spectral normalization is thus an essential tool in data processing and can be fully automated. Nonetheless, this method can be successfully used in diagnostic or clinical applications, where the changes between pathological and basal states are high.

The LOD presented here is of several orders lower than LODs obtained with methods using mass spectrometric detection, where derivatization, e.g., using ethyl chloroformate[7e] or dansyl chloride,[30a] were used with respective limits of detections in orders from units of micromolar to tens of picomoles per liter. Derivatization steps could even in some cases present a drawback in the means of lowered method robustness and simplicity; moreover, previous sample cleanup has to be performed using chromatographic approaches. Methods based on electrochemistry stand for a golden standard in neurochemical sciences; however, the selectivity of such methods is usually lowered due to unwanted interferences. The LODs of electrochemical methods are usually in orders of tens of femtomoles per liter,[32] which is comparable to the results presented here.

This analytical procedure was then applied in the analysis of dopamine levels in mice striatum. In total, three biological replicates were analyzed using the modified m@cmCH@Ag@Fe-NTA nanocomposite. Samples were pooled together to minimize biological variability and the obtained amount was divided back into three parts, giving samples 1, 2, and 3, respectively. Each part was weighted, and dopamine was extracted using extraction procedure described in the Experimental Section. In total, 2 μL of each extract was used for the analysis; the obtained spectrum is shown in the Figure 5.

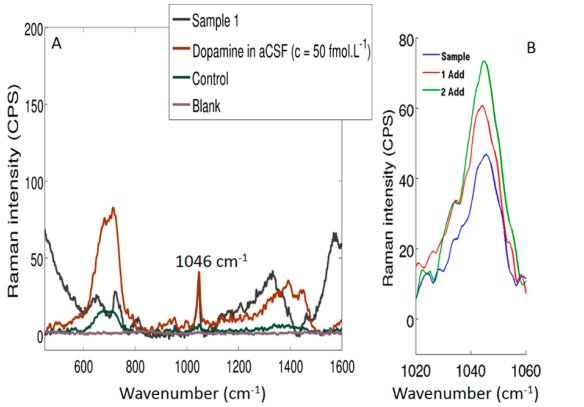

Figure 5. (A) SERS spectra of dopamine analyzed in mice striatum. The panel displays analysis of dopamine at a concentration level of 50 fmol·L^{-1} and analysis of control and blank samples for a better transparency. The model sample (50 fmol·L^{-1} dopamine) was measured with m@cmCH@Ag@Fe-NTA in aCSF, the control sample was measured with m@cmCH@Ag@Fe-NTA and aCSF, and the blank sample only with m@cmCH@Ag@Fe-NTA nanocomposite. (B) Raman spectrum with the band at 1046 cm^{-1} before and after two additions of dopamine standard.

The spectrum includes bands previously interpreted as parts of dopamine−Fe-NTA chemical structure; however, some interferences occurred. This is probably caused by nonspecific interactions of Fe-NTA with interfering molecules. However, interferences can be removed from a further data processing by a careful comparison of spectra obtained by analysis of the dopamine standard and the real sample, as performed in our study. After data preprocessing, including baseline corrections and noise reduction, the band at 1046 cm^{-1} was used for the

dx.doi.org/10.1021/ac500394g | Anal. Chem. 2014, 86, 2939−2946

quantification analysis. Quantification was performed using the standard addition method, where two standard additions of 50 fmol·L^{-1} were used. The resulting spectra are shown in Figure 5B.

To compare the results of the magnetic SERS technique with the conventional approach, the same samples of striatum were analyzed also using HPLC−MS. The samples for HPLC−MS runs were obtained using the same protocols and procedures applied in the SERS analysis and analyzed using modified protocols described earlier by Boersema et al.[8d] In detail, protocols are described in the Supporting Information, experimental part. Results of this comparison are summarized in Supporting Information Table S3. Clearly, the newly developed SERS method gives results with moderately higher relative standard deviations (20% for SERS vs 15% for HPLC−MS); however, it is considerably faster, economically advantageous, and easier to perform. HPLC methods usually require massive standard derivatization and labeling in order to increase their selectivity and sensitivity. Moreover, removal of the labeling and preconcentration steps decreases the LOD and limit of quantitation (LOQ), and thus, very low dopamine levels could be determined with difficulties. Furthermore, samples analyzed using HPLC−MS techniques have to be preconcentrated, e.g., using evaporation or other relevant techniques. All these procedures are time-consuming and may dramatically influence the method performance.

To evaluate the robustness and reproducibility of the new approach, a set of six technical replicates of one clinical sample of mice striatum measured using the same batch of nanocomposite was analyzed (Figure S1, Supporting Information). The replicates were measured in order to evaluate the stability of the signal across different samples of the same origin. The results demonstrate no considerable change among intensities of the target band at 1046 cm^{-1}. More specifically, spectral analysis revealed that the relative standard deviation (RSD) among respective intensities is lower than 5%.

Finally, the stability of the newly developed nanocomposite was evaluated with the use of one batch of the m@cmCH@Ag nanocomposite. We performed analysis of dopamine standard ($c = 1 \times 10^{-8}$ mol·L^{-1}) in the time period of 10 days. Obtained results of the as-prepared sample ($t = 0$) and samples after 3, 7, and 10 days are shown in Figure S2 in the Supporting Information. Evidently, the signal is stable for the period of 10 days without any significant drop in its intensity. Moreover, in this case, the relative standard deviation among measured values is lower than 5%.

CONCLUSIONS

The dopaminergic neuronal system is responsible for many brain functions including cognitive processes,[26] behavior of mammals,[27] etc. Dopamine is also correlated with several diseases, where the most studied are Parkinson's disease,[2b] Alzheimer's,[28] or schizophrenia.[29] The latter correlation was evaluated in NAcc, where the mesolimbic pathway was taken into account. Analysis of this target thus represents a demanding process that can help to uncover a deeper connection between dopamine levels and, in many cases, pathological states of the brain.

In this work, the new magnetite−*O*-carboxymethyl chitosan−silver nanocomposite with Fe-NTA in the role of dopamine-selective compound (m@cmCH@Ag@Fe-NTA) was prepared with the use of the biocompatible polymer *O*-carboxymethyl chitosan that acts as an in situ reducing agent for silver ions. It creates a linker of both magnetite and silver NPs and enables good dispersity of the nanocomposite. Moreover, all amino groups of this polymer are involved in silver NPs binding and do not influence the sorption of unwanted interferences on the polymer. The developed method is able to analyze dopamine at a concentration level from units to thousands of femtomoles using a novel approach of purifying the sample with magnetic separation and consequent detection using SERS.

The analyses of the clinical samples of mice striatum proved that this magnetic SERS approach is a strong alternative to commonly used chromatographic methods with mass spectrometric detection. The key advantages include the simplicity of the proposed protocol and very fast analysis, giving a possibility to automate the process for hundreds of samples (depending on the size of the glass platform and Raman configuration).

The versatility and general applicability of this approach lies mainly in the possible substitution of Fe-NTA for other antibodies as well as for other small-molecular targets using specific compounds that can be used in the analysis of a broad number of physiologically active compounds. An interesting alternative would be to introduce a peptide with specific antibodies for an ex vivo analysis of neuropeptides, playing essential roles in neuromodulation, in various brain systems, where the application of other more conventional techniques can be complicated or is currently impossible.

ASSOCIATED CONTENT

Supporting Information

Description of preparation of magnetite nanoparticles, magnetite−*O*-carboxymethyl chitosan hybrids (m@cmCH), and m@cmCH@Ag nanocomposite, modification protocol of m@cmCH@Ag nanocomposites with dopamine-selective reporter compounds (Fe-NTA), description of mass spectrometric analysis of dopamine levels, preparation of samples for mass spectrometric analysis, calibration curve parameters, levels of dopamine in the two sample models, levels of dopamine in the samples of mouse striatum, and additional SERS spectra. This material is available free of charge via the Internet at http://pubs.acs.org.

AUTHOR INFORMATION

Corresponding Authors

*Phone: +420 585634753. Fax: +420 585634761. E-mail: vaclav.ranc@upol.cz.

*Phone: +420 585634337. Fax: +420 585634761. E-mail: radek.zboril@upol.cz.

Notes

The authors declare no competing financial interest.

ACKNOWLEDGMENTS

The authors thank to Dr. Dalibor Dolezal (Institute of Molecular and Translation Medicine, Palacky University, Olomouc, Czech Republic) for the preparation of clinical samples, Dr. Jason Perman for language corrections, Dr. Dalibor Jančík and Dr. Pavel Tuček for technical assistance, and Dr. Jiří Tuček (all from Regional Centre of Advanced Technologies and Materials, Faculty of Science, Palacky University, Olomouc, Czech Republic) for his valuable comments and corrections of the manuscript. The authors acknowledge the support by the Technology Agency of Czech Republic (project no. TA03011368), Operational Program

Research and Development for Innovations—European Regional Development Fund (project nos. CZ.1.05/2.1.00/03.0058 and CZ.1.05/2.1.00/01.0030 of the Ministry of Education, Youth, and Sports of the Czech Republic), the Operational Program Unconventional Experimental Techniques in Material and Optical research (project no. CZ.1.07/2.3.00/20.0155 of the Ministry of Education, Youth, and Sports of the Czech Republic), and the Operational Program Research and Development for Innovations—KONTAKT II (project no. LH12085) of the Ministry of Education, Youth, and Sports of the Czech Republic.

REFERENCES

(1) (a) Ungerstedt, U.; Herreramarschitz, M.; Zetterstrom, T. *Prog. Brain Res.* **1982**, *55*, 41−49. (b) Svensson, T. H. *Nord. J. Psychiatry* **1998**, *52*, 100−100.

(2) (a) Brooks, D. J. *Ann. N. Y. Acad. Sci.* **2003**, *991*, 22−35. (b) Ribeiro, M. J.; Vidailhet, M.; Loc'h, C.; Samson, Y.; Dupel, C.; Cesaro, P.; Nguyen, J. P.; Hantraye, P.; Remy, P. *Neurology* **2000**, *54*, A113. (c) Ceravolo, R.; Volterrani, D.; Gambaccini, G.; Bernardini, S.; Rossi, C.; Logi, C.; Tognoni, G.; Manca, G.; Mariani, G.; Bonuccelli, U.; Murri, L. *J. Neural. Transm.* **2004**, *111*, 1065−1073.

(3) (a) Nandi, P.; Lunte, S. M. *Anal. Chim. Acta* **2009**, *651*, 1−14. (b) Schltz, K. N.; Kennedy, R. T. *Annu. Rev. Anal. Chem.* **2008**, *1*, 627−661. (c) Tsunoda, M. *Anal. Bioanal. Chem.* **2006**, *386*, 506−514.

(4) (a) White, B. M.; Rubinson, J. F. *ECS Trans.* **2009**, *19*, 103−108. (b) Gao, Z. Q.; Chen, B. S.; Zi, M. X. *Analyst* **1994**, *119*, 459−464. (c) Zachek, M. K.; Takmakov, P.; Park, J.; Wightman, R. M.; McCarty, G. S. *Biosens. Bioelectron.* **2010**, *25*, 1179−1185.

(5) (a) Kovach, P. M.; Ewing, A. G.; Wilson, R. L.; Wightman, R. M. *J. Neurosci. Methods* **1984**, *10*, 215−227. (b) Gonon, F.; Buda, M.; Cespuglio, R.; Jouvet, M.; Pujol, J. F. *Nature* **1980**, *286*, 902−904.

(6) (a) Zen, J. M.; Hsu, C. T.; Hsu, Y. L.; Sue, J. W.; Conte, E. D. *Anal. Chem.* **2004**, *76*, 4251−4255. (b) Bergstrom, B. P.; Cummings, D. R.; Skaggs, T. A. *Neuropharmacology* **2007**, *53*, 967−974.

(7) (a) Wasti, A.; Siddiqui, N. A. *J. Pak. Med. Assoc.* **2010**, *60*, 628−632. (b) Zhao, X. D.; Cao, Y. Q.; Liu, H. H.; Li, F. Q.; You, B. M.; Zhou, X. P. *Brain Res.* **2009**, *1286*, 230−238. (c) Kulkarni, S. K.; Bishnoi, M.; Chopra, K. *Indian J. Exp. Biol.* **2009**, *47*, 91−97. (d) Tsai, L. H.; Cheng, J. T. *Neurosci. Res.* **1995**, *21*, 235−240. (e) Park, J. Y.; Myung, S. W.; Kim, I. S.; Choi, D. K.; Kwon, S. J.; Yoon, S. H. *Biol. Pharm. Bull.* **2013**, *36*, 252−258. (f) Gosetti, F.; Mazzucco, E.; Gennaro, M. C.; Marengo, E. *Anal. Bioanal. Chem.* **2013**, *405*, 907−916. (g) Chan, E. C. Y.; Ho, P. C. *Rapid Commun. Mass Spectrom.* **2000**, *14*, 1959−1964. (h) Moini, M.; Schultz, C. L.; Mahmood, H. *Anal. Chem.* **2003**, *75*, 6282−6287. (i) Rogers, K. L.; Philibert, R. A.; Allen, A. J.; Molitor, J.; Wilson, E. J.; Dutton, G. R. *J. Neurosci. Methods* **1987**, *22*, 173−179.

(8) (a) Song, P.; Mabrouk, O. S.; Hershey, N. D.; Kennedy, R. T. *Anal. Chem.* **2012**, *84*, 412−419. (b) Ji, C. J.; Li, W. L.; Ren, X. D.; El-Kattan, A. F.; Kozak, R.; Fountain, S.; Lepsy, C. *Anal. Chem.* **2008**, *80*, 9195−9203. (c) Kleifeld, O.; Doucet, A.; Prudova, A.; Keller, U. A. D.; Gioia, M.; Kizhakkedathu, J. N.; Overall, C. M. *Nat. Protoc.* **2011**, *6*, 1578−1611. (d) Boersema, P. J.; Raijmakers, R.; Lemeer, S.; Mohammed, S.; Heck, A. J. R. *Nat. Protoc.* **2009**, *4*, 484−494.

(9) (a) Kneipp, K.; Kneipp, H. *Abstr. Pap.—Am. Chem. Soc.* **2011**, 242. (b) Porter, M. D.; Lipert, R. J.; Siperko, L. M.; Wang, G.; Narayanana, R. *Chem. Soc. Rev.* **2008**, *37*, 1001−1011.

(10) (a) An, Q.; Zhang, P.; Li, J. M.; Ma, W. F.; Guo, J.; Hu, J.; Wang, C. C. *Nanoscale* **2012**, *4*, 5210−5216. (b) Lv, B. L.; Xu, Y.; Tian, H.; Wu, D.; Sun, Y. H. *J. Solid State Chem.* **2010**, *183*, 2968−2973. (c) Lutz, B.; Dentinger, C.; Sun, L.; Nguyen, L.; Zhang, J. W.; Chmura, A. J.; Allen, A.; Chan, S.; Knudsen, B. *J. Histochem. Cytochem.* **2008**, *56*, 371−379.

(11) (a) Li, T.; Guo, L. P.; Wang, Z. *Anal. Sci.* **2008**, *24*, 907−910. (b) Sackmann, M.; Bom, S.; Balster, T.; Materny, A. *J. Raman Spectrosc.* **2007**, *38*, 277−282. (c) Ranc, V.; Hruzikova, J.; Maitner, K.; Prucek, R.; Milde, D.; Kvitek, L. *J. Raman Spectrosc.* **2012**, *43*, 971−976. (d) Prucek, R.; Ranc, V.; Kvitek, L.; Panacek, A.; Zboril, R.; Kolar, M. *Analyst* **2012**, *137*, 2866−2870. (e) Ranc, V.; Stanova, A.; Marak, J.; Maier, V.; Sevcik, J.; Kaniansky, D. *J. Chromatogr., A* **2011**, *1218*, 205−210.

(12) (a) Arslanoglu, J.; Zaleski, S.; Loike, J. *Anal. Bioanal. Chem.* **2011**, *399*, 2997−3010. (b) Liu, P.; Liu, R. Y.; Guan, G. J.; Jiang, C. L.; Wang, S. H.; Zhang, Z. P. *Analyst* **2011**, *136*, 4152−4158.

(13) (a) Zhu, M. Y.; Wang, C. J.; Meng, D. H.; Diao, G. W. *J. Mater. Chem. A* **2013**, *1*, 2118−2125. (b) Markova, Z.; Siskova, K.; Filip, J.; Safarova, K.; Prucek, R.; Panacek, A.; Kolar, M.; Zboril, R. *Green Chem.* **2012**, *14*, 2550−2558. (c) Xia, H. Q.; Cui, B.; Zhou, J. H.; Zhang, L. L.; Zhang, J.; Guo, X. H.; Guo, H. L. *Appl. Surf. Sci.* **2011**, *257*, 9397−9402.

(14) (a) Chon, H.; Lim, C.; Ha, S. M.; Ahn, Y.; Lee, E. K.; Chang, S. I.; Seong, G. H.; Choo, J. *Anal. Chem.* **2010**, *82*, 5290−5295. (b) Jun, B. H.; Noh, M. S.; Kim, J.; Kim, G.; Kang, H.; Kim, M. S.; Seo, Y. T.; Baek, J.; Kim, J. H.; Park, J.; Kim, S.; Kim, Y. K.; Hyeon, T.; Cho, M. H.; Jeong, D. H.; Lee, Y. S. *Small* **2010**, *6*, 119−125. (c) Liu, R. Y.; Liu, B. H.; Guan, G. J.; Jiang, C. L.; Zhang, Z. P. *Chem. Commun.* **2012**, *48*, 9421−9423. (d) Zhang, H.; Harpster, M. H.; Park, H.; Johnson, P. A. *Anal. Chem.* **2011**, *83*, 254−260. (e) Kang, H.; Jeong, S.; Park, Y.; Yim, J.; Jun, B.-H.; Kyeong, S.; Yang, J.-K.; Kim, G.; Hong, S.; Lee, L. P.; Kim, J.-H.; Lee, H.-Y.; Jeon, D. H. *Adv. Funct. Mater.* **2013**, *23*, 3719−3727.

(15) Sha, M. Y.; Xu, H. X.; Natan, M. J.; Cromer, R. *J. Am. Chem. Soc.* **2008**, *130*, 17214.

(16) Jun, B. H.; Noh, M. S.; Kim, G.; Kang, H.; Kim, J. H.; Chung, W. J.; Kim, M. S.; Kim, Y. K.; Cho, M. H.; Jeong, D. H.; Lee, Y. S. *Anal. Biochem.* **2009**, *391*, 24−30.

(17) (a) Chon, H.; Lee, S.; Yoon, S. Y.; Chang, S. I.; Lim, D. W.; Choo, J. *Chem. Commun.* **2011**, *47*, 12515−12517. (b) Chon, H.; Lee, S.; Son, S. W.; Oh, C. H.; Choo, J. *Anal. Chem.* **2009**, *81*, 3029−3034.

(18) Kayat, M.; Volkan, M. *Anal. Chem.* **2012**, *84*, 7729−7735.

(19) Shi, Z. L.; Neoh, K. G.; Kang, E. T.; Shuter, B.; Wang, S. C.; Poh, C.; Wan, W. *ACS Appl. Mater. Interfaces* **2009**, *1*, 328−335.

(20) Griffith, H. B. *J. Neurol., Neurosurg. Psychiatry* **1987**, *50*, 646.

(21) Argentiero, V.; Tavolato, B. *J. Neurol.* **1980**, *224*, 53−58.

(22) Bruce, I. J.; Sen, T. *Langmuir* **2005**, *21*, 7029−7035.

(23) Xu, X. Q.; Shen, H.; Xu, J. R.; Xie, M. Q.; Li, X. J. *Appl. Surf. Sci.* **2006**, *253*, 2158−2164.

(24) Gao, L. Z.; Wu, J. M.; Lyle, S.; Zehr, K.; Cao, L. L.; Gao, D. *J. Phys. Chem. C* **2008**, *112*, 17357−17361.

(25) Chen, X. G.; Park, H. J. *Carbohydr. Polym.* **2003**, *53*, 355−359.

(26) (a) Simon, H.; Scatton, B.; Lemoal, M. *Nature* **1980**, *286*, 150−151. (b) Vernaleken, I.; Kumakura, Y.; Buchholz, H. G.; Siessmeier, T.; Bartenstein, P.; Cumming, P.; Grunder, G. *NeuroImage* **2006**, *31*, T172.

(27) Stahle, L.; Ungerstedt, U. *Acta Physiol. Scand.* **1987**, *130*, 533−534.

(28) Mizukawa, K.; Mcgeer, E. G.; Mcgeer, P. L. *Mol. Chem. Neuropathol.* **1993**, *18*, 133−144.

(29) Gray, J. A.; Kumari, V.; Lawrence, N.; Young, A. M. J. *Psychobiology* **1999**, *27*, 225−235.

(30) (a) Nirogi, R.; Komarneni, P.; Kandikere, V.; Boggavarapu, R.; Bhyrapuneni, G.; Benade, V.; Gorentla, S. *J. Chromatogr., B* **2013**, *913*, 41−47. (b) Zheng, X.; Kang, A.; Dai, C.; Liang, Y.; Xie, T.; Xie, L.; Peng, Y.; Wang, G. J.; Hao, H. P. *Anal. Chem.* **2012**, *84*, 10044−10051.

(31) Li, J. W.; Bai, Y.; Mo, Y. J.; Wachter, P. *Spectrosc. Spectral Anal. (Beijing, China)* **2006**, *26*, 463−466.

(32) (a) Jing, F. C.; Chen, H.; Li, C. L. *Biomed. Environ. Sci.* **2007**, *20*, 317−320. (b) Van Gompel, J. J.; Chang, S. Y.; Goerss, S. J.; Kim, I. Y.; Kimble, C.; Bennet, K. E.; Lee, K. H. *Neurosurg. Focus* **2010**, *29*, E6.

analytical chemistry

Article

pubs.acs.org/ac

Magnetically-Assisted Surface Enhanced Raman Spectroscopy (MA-SERS) for Label-Free Determination of Human Immunoglobulin G (IgG) in Blood Using Fe_3O_4@Ag Nanocomposite

Anna Balzerova, Ariana Fargasova, Zdenka Markova, Vaclav Ranc,* and Radek Zboril*

Regional Centre of Advanced Technologies and Materials, Department of Physical Chemistry, Faculty of Science, Palacký University in Olomouc, 17. listopadu 12, CZ-77146, Olomouc, Czech Republic

Supporting Information

ABSTRACT: Development of methods allowing determination of even ultralow levels of immunoglobulins in various clinical samples including whole human blood and plasma is a particular scientific challenge, especially due to many essential discoveries in the fields of immunology and medicine in the past few decades. The determination of IgG is usually performed using an enzymatic approach, followed by colorimetric or fluorimetric detection. However, limitations of these methods relate to their complicated setup and stringent requirements concerning the sample purity. Here, we present a novel approach based on magnetically assisted surface enhanced Raman spectroscopy (MA/SERS), which utilizes a Fe_3O_4@Ag@streptavidin@anti-IgG nanocomposite with strong magnetic properties and an efficient SERS enhancement factor conferred by the Fe_3O_4 particles and silver nanoparticles, respectively. Such a nanocomposite offers the possibility of separating a target efficiently from a complex matrix by simple application of an external magnetic force, followed by direct determination using SERS. High selectivity was achieved by the presence of anti-IgG on the surface of silver nanoparticles coupled with their further inactivation by ethylamine. Compared to many recently developed sandwich methods, application of single nanocomposites showed many advantages, including simplicity of use, direct control of the analytic process, and elimination of errors caused by possible nonspecific interactions. Moreover, incorporation of advanced spectral processing methods led to a considerable decrease in the relative error of determination to below 5%.

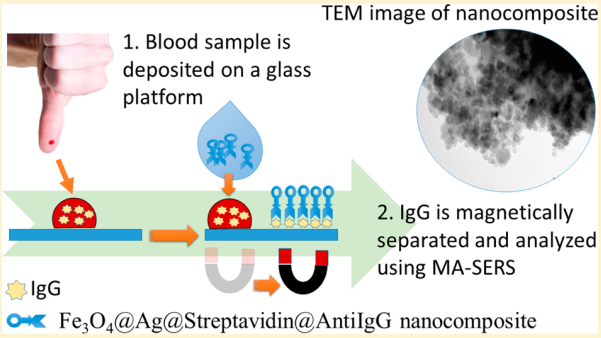

Immunoglobulins (Ig) play an essential role in many defensive mechanisms of organisms against various potentially damaging objects, such as viruses or bacteria. Five classes have been shown to be present in the human circulatory system, namely immunoglobulins A, G, M, E, and D.[1] It is noteworthy that IgG has a considerably smaller effective diameter compared to other immunoglobulins in the above-mentioned classes.[2] It is thus able to enter placenta and defend an unborn organism in its prenatal phase of development. IgG is present in the blood of healthy human adults at concentrations of approximately 10 $g \cdot L^{-1}$, but these levels are usually changed during pathological processes induced by diseases.[3] Therefore, advanced technologies and novel materials have been utilized to improve currently used methods to develop new procedures for determining levels of IgG with superior selectivity, even at ultralow concentrations, in order to decrease sample requirements, particularly the amount.

Classical methods and approaches for measuring IgG concentrations include immunomethods based on spectroscopic detection, such as enzyme-linked immunosorbent assay (ELISA).[4] Several alternatives to ELISA have been developed in order to increase the method accuracy and improve the limit of detection, e.g., fluorescence-based methods.[5] The presence of fluorophore defined by a design of the method can be advantageous for the above-mentioned reasons. However, such approaches may be limited by the modification steps required and by possible photobleaching or autofluorescence. Other well-established methods are based on separation techniques (electrophoresis, liquid chromatography), which are often coupled with mass spectrometry.[6] These techniques possess several advantages, including high sensitivity and robustness. However, they also have some drawbacks regarding the requirements for sample purity and composition.

An alternative technique that can be used for the determination of human IgG is surface enhanced Raman spectroscopy (SERS),[7] which allows detection of various organic, inorganic, and biological compounds at ultralow concentrations, even at the molecular level. Until now, SERS has been successfully applied in many fields, ranging from the enterprise sector, clinical praxis to environmental control, and forensic sciences.[8] Moreover, the application potential of SERS can be further increased by employing magnetic nanomaterials

Received: May 20, 2014
Accepted: September 26, 2014
Published: September 26, 2014

   dx.doi.org/10.1021/ac503347h | *Anal. Chem.* 2014, 86, 11107−11114

for efficient sample separation and preconcentration,[9] an approach referred here as magnetically assisted surface enhanced Raman spectroscopy (MA-SERS). This innovative approach has already been successfully applied for the purification of recombinant biotinylated human sarco-/endoplasmic reticulum Ca^{2+}-ATPase using a magnetic nanomaterial functionalized with avidin.[10] Another important study showed that a magnetic nanocomposite containing silver nanoparticles could be utilized for the detection of a protein−small molecule complex (avidin−biotin) using SERS.[11] MA-SERS has also recently been applied for the determination of dopamine in an artificial cerebrospinal fluid and mouse striatum.[12] Another possibility is to use various magnetic nanomaterials with gold nanoparticles.[13] Drake et al. exploited the magnetic properties of iron oxide nanoparticles to trap and isolate *Staphylococcus aureus* bacteria and then employed active gold nanoparticles (AuNPs) coated with 4-mercaptobenzoic acid for the detection and quantification of the bacteria by SERS.[14] One of the key features of the nanocomposites presented here is the formation of a covalent bond between the magnetic and noble metal nanoparticles. Such a property is useful not only for the analysis of *ex-vivo* samples because of the increased stability of the nanocomposites but also for future applications in *in vivo* experiments, where a stable bond between the magnetic core and surface modified silver/gold nanoparticles is crucial.

To the best of our knowledge, the detection of proteins by SERS-based immunoassay has so far mostly been indirect and required a Raman label to provide a strong Raman signal.[15] An example of such an approach can be seen in the work of Chen et al.[16] They developed an analytical approach for detecting IgG at a very low limit of detection (LOD) of 0.1 $\mu g.mL^{-1}$.[16] Moreover, Song et al. prepared gold nanoparticles labeled with 4-mercaptobenzoic acid and used them as a Raman label for the detection of IgG at a level of 100 $fm.mL^{-1}$.[17] It is worth mentioning that this approach can be enhanced by employing sandwich systems.[18] The magnetic properties of some nanoparticles can be employed to improve the separation of targets from a complex matrix. A common sandwich-type analytical system thus consists of a combination of magnetic and SERS-active substrates. The magnetic substrates are used to efficiently extract a target from a complex matrix by employing a selective bond between an analyte and immunorecognition molecule (previously immobilized on the surface) and applying an external magnetic force. The SERS-active silver or gold nanoparticles are added after purification and selectively attached to the target using the same set of immunorecognition molecules present on the metal surface. Indirect analysis is then performed by measuring the signal of a Raman label present as a linker between the antibody and metal surface of the SERS-active substrate.[17,19] Chon et al. demonstrated the application potential of such an approach for the analysis of IgG.[19b] They developed a method based on SERS and opto-fluidics for the detection. The LOD was between 1 and 10 $ng{\cdot}mL^{-1}$.[19b]

The above-mentioned methods have many advantages, such as ultralow LODs and versatility. However, their simplicity of use is limited by several drawbacks, including the necessity to synthesize two sets of nanoparticles with limited stability, usually complicated experimental design, high risk of false results as a result of nonspecific interactions between particles and nontargeted compounds attracted from a matrix, and inability to monitor the direct bonding of target to a specific antibody. These limitations may explain the relatively low uptake of such methods in other scientific fields.

Here we present a label-free SERS based method for the determination of human IgG using a single nanocomposite. The method utilized a novel magnetic Fe_3O_4@Ag@streptavidin@anti-IgG nanocomposite, which comprised a magnetic core modified by O-carboxymethylchitosan (CM) to covalently attach silver nanoparticles. The silver surface was subsequently modified by streptavidin and finally anti-imunoglobulin G (anti-IgG). The immobilization of anti-IgG via a bond with streptavidin did not influence its total activity, in contrast to the approaches mentioned above, which utilized unspecific direct immobilization on the metal surface. Application of the method is demonstrated for the determination of human IgG in blood samples obtained by the finger prick method. Despite being relatively straightforward, the proposed method showed high accuracy and reliability. Further, the relative standard errors of determination were reduced to below 5% by using a newly developed advanced spectral processing method, which involved background normalization and utilization of two reference spectral points.

MATERIALS AND METHODS

Chemicals. Silver nitrate (p.a.), low molecular weight (LMW) chitosan (75−85% deacetylated), iron(II) chloride tetrahydrate (p.a.) and iron(III) chloride hexahydrate (p.a.), 1-[3-(dimethylamino)propyl]-3-ethylcarbodiimide methiodide (EDC), *N*-hydroxysulfosuccinimide sodium salt (≥98% (HPLC); NHS), IgG from human serum (reagent grade, ≥95% (SDS-PAGE), essentially salt-free, lyophilized powder), antihuman IgG (Fc specific)-biotin antibody produced in rabbit (IgG fraction of antiserum, lyophilized powder), ethylamine (purum, 70% in H_2O), streptavidin from *Streptomyces avidinii* (essentially salt-free, lyophilized powder, ≥13 units/mg protein) and α,ω-bis{2-[(3-carboxy-1-oxopropyl)amino]ethyl}-polyethylene glycol (M_r 2000) (carboxy-PEG) were purchased from Sigma-Aldrich and used without further purification. H_3PO_4 (p.a., 85% w/w) and NaOH (p.a.) were bought from Lach-Ner. Acetic acid (99,8%) and methanol (p.a.) were obtained from P-LAB (Czech Republic).

Preparation of standard solutions and buffers. A phosphate-buffered saline solution (PBS; 10 mM, pH 7.5) was prepared from 100 mM stock solution of H_3PO_4 by fine-tuning its pH value using a highly concentrated solution of NaOH (50%, w/v) under constant stirring. The final concentration was adjusted by addition of a defined volume of water. Stock solutions of 0.2 $mol{\cdot}L^{-1}$ NHS and EDC were prepared in a volume of 10 mL weighing exact amounts of each. Solutions were used immediately after preparation. Stock solutions of all used proteins, namely IgG, anti-IgG and streptavidin, were prepared by dissolving 1 mg of protein in 1 mL of water in an Eppendorf tube. Solutions of proteins were kept in the dark at −20 °C for no longer than 5 days.

Preparation of Fe_3O_4@Ag nanocomposite. Magnetic nanocomposites were prepared according to the process described earlier by Markova et al.[20] Briefly, magnetic nanoparticles were prepared by the Massart coprecipitation method of an aqueous solution of $FeCl_3.6H_2O$ and $FeCl_2.4H_2O$ using sodium hydroxide; 1.5 M NaOH was slowly added to a mixture of $FeCl_3.6H_2O$ and $FeCl_2.4H_2O$ to obtain a pH of 11. The synthesis was carried out at room temperature under constant bubbling of nitrogen to prevent further oxidation of the ferrous ions. After 1 h of stirring, the product was washed

dx.doi.org/10.1021/ac503347h | *Anal. Chem.* 2014, 86, 11107−11114

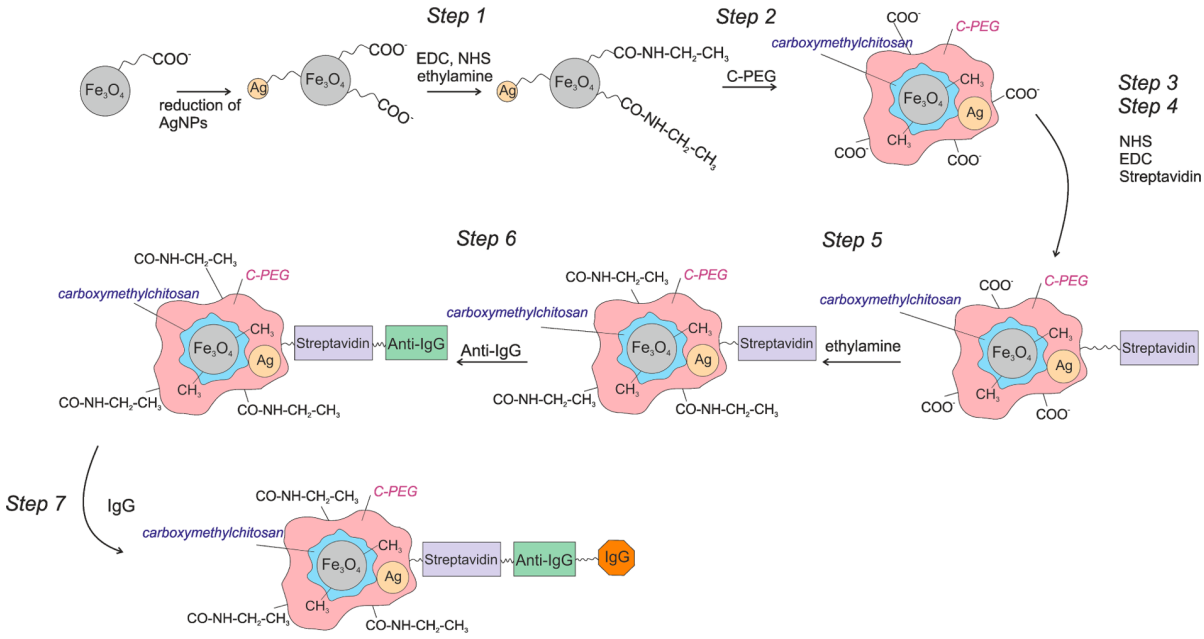

Figure 1. Scheme showing the individual steps in the modification of nanocomposite Fe_3O_4@Ag.

several times with water and separated using simple magnetic decantation. The magnetic nanoparticles generated were used for the preparation of magnetite-O-carboxymethylchitosan hybrids by adsorption of polymer onto the surface of the as-prepared nanoparticles induced by gradually increasing the temperature to 80 °C. Finally, silver nitrate was added to the magnetite-O-carboxymethylchitosan hybrids and silver ions were reduced on the surface of the hybrids by amine groups in the polymer under alkaline conditions and at a temperature of 80 °C. The products were finally washed several times with deionized water and separated using magnetic decantation.

Preparation of Fe_3O_4@Ag@strepavidin@anti-IgG nanocomposite. Immobilization of anti-IgG on the surface of the previously described nanocomposite Fe_3O_4@Ag was carried out according to the steps shown in Figure 1. First, 1 mL of magnetic nanoparticles prepared by the process described above was mixed with 100 μL of EDC and NHS (final concentration of both reagents was set to 20 mM) and stirred for 30 min. Next, ethylamine was added to a final concentration of wt.7%. The nanocomposite was collected by application of an external magnetic field and washed twice with 10 mM PBS buffer. Then, 5 mM carboxy-PEG was added (final concentration 1 mM) to the washed magnetic nanocomposite. After 1 h of stirring at 300 rpm, the magnetic nanocomposite was separated from the reaction mixture by simple application of an external magnetic field and washed with PBS buffer. Next, EDC and NHS (1:1, final concentration 20 mM) were added and the reaction stirred for a further 1 h. The resulting nanocomposite was again magnetically separated and washed with PBS buffer. In the next step, nanocomposite with previously activated carboxylic groups was mixed with streptavidin (0.2 mg·L^{-1}) and stirred for 1 h to form covalent bonds between the free amino ($-NH_2$) groups present in the structure of streptavidin and activated carboxylic groups of the nanocomposite. After the addition of streptavidin, the nanocomposite was magnetically separated and washed with 10 mM PBS buffer. Next, nanocomposite with streptavidin was mixed with biotinylated anti-IgG (final concentration 0.2 mg·L^{-1}) and stirred for 1 h to allow covalent bonds to be formed between between streptavidin and the biotinylated part of the anti-IgG. After washing with PBS buffer, ethylamine at a final concentration of 7% wt. was added to block the rest of the active carboxylic groups.

Analysis of real samples. Human whole blood samples (n = 2) were collected by finger prick method performed according to standard operation procedure UOG-REB, SOP011. A sample of volume V = 2 μL was placed on a glass platform, 10 μL of nanocomposite Fe_3O_4@Ag@streptavidin@anti-IgG was immediately added and the mixture carefully stirred. The nanocomposite was magnetically separated from the blood sample and washed twice with deionized water (20 μL). Finally, the nanocomposite was magnetically separated and analyzed using SERS.

Apparatus. The ζ potentials of the starting material, intermediate and final products were measured using a Zetasizer NanoZS (Malvern, UK). A transmission electron microscope (TEM) (JEM 2010, Jeol, Japan) was used to obtain images of the unmodified magnetic nanocomposite and final nanocomposites. The TEM was operated at a voltage of 160 kV with a point-to-point resolution of 1.9 Å. Raman spectra were collected using a DXR Raman spectroscope (Thermo Scientific, U.S.A.) equipped with a laser operating at a wavelength of 532 nm. The laser power on the sample was set to 2 mW. Each measured Raman spectrum was an average of 32 experimental microscans. The acquisition time was set to 1s. Infrared spectra were acquired using a Nicolet iS5 infrared spectrometer (Thermo Scientific, U.S.A.). A total of 32 scans were measured and averaged for each material. Raman and IR spectra were evaluated using instrument control software (Omnic, version 8, Thermo Scientific, USA) and highs of target spectral bands were statistically evaluated using LibreOffice (version 4.3.0, The Document foundation, Berlin, Germany).

RESULTS AND DISCUSSION

Infrared spectroscopy and ζ- potential measurements were used to monitor changes in the surface characteristics of the as-

dx.doi.org/10.1021/ac503347h | Anal. Chem. 2014, 86, 11107−11114

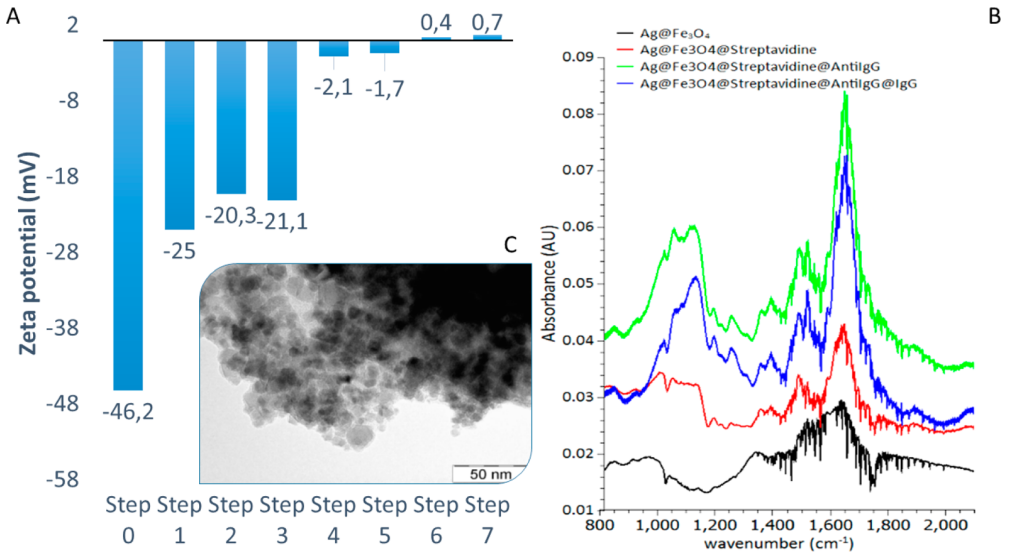

Figure 2. (A) Measured ζ-potentials of the prepared nanocomposite and of the nanocomposites after each step of modification. (B) IR spectra of the bare nanocomposite and modified nanocomposites. (C) TEM image of Fe_3O_4@Ag nanocomposite.

prepared nanocomposite during the surface modification process. Such modifications included adsorption of chemicals on the surface of the nanocomposite, activation of functional groups, and formation of new bonds. Infrared spectra and ζ-potentials measured during the surface modification process are shown in Figure 2. The measured ζ-potential of an unmodified initial nanocomposite (labeled as Step 0) corresponded to a charge −46.2 mV. The nanocomposite was composed of Fe_3O_4 and Ag nanoparticles covalently bonded by O-carboxymethyl-chitosan. This linker was selected because of the presence of free carboxylic groups, which increased the long-term stability of the as-prepared nanocomposite by enhancing its dispersibility in aqueous environments. However, such groups cause relatively high negative surface charge. Therefore, their presence during subsequent surface modification steps had to be minimized to ensure highly selective bonding of streptavidin only to a free surface of silver nanoparticles, while at the same time maximizing the sensitivity of the designed analytical system. The free carboxylic groups were thus removed in the first step by reaction with an aqueous mixture of EDC:NHS, followed by an aqueous solution of ethylamine. The deactivation (Step 1) and blockage (Step 2) of carboxylic groups led to a considerable change of ζ-potential to −20.3 mV. This decrease in negative charge confirmed that the carboxylic groups were successfully activated and efficiently blocked. The residual negative charge was attributed to the bare silver nanoparticles. In the next step (Step 3), free carboxyl groups were generated on the surface of the silver nanoparticles by addition of carboxy-PEG. This step was required for further selective immobilization of streptavidin. The adsorption of carboxy-PEG on the surface of Ag led to a moderate increase of surface charge to −21.1 mV. The difference between the latter value and the initial negative charge (−46.2 mV) was due to different numbers of immobilized functional groups. Activation of the newly created carboxylic groups with an aqueous mixture of EDC and NHS (Step 4) was accompanied by a large decrease in negative charge to a value of −2.1 mV. The following step was performed to immobilize streptavidin on the silver surface (Step 5). Covalent bonds were formed between $-NH_2$ groups of streptavidin and activated carboxyl groups by stirring for 1 h at 100 rpm. Immobilization of streptavidin onto the nanocomposite surface changed the charge only slightly to −1.7 mV. Successful immobilization of streptavidin was confirmed by measuring IR spectra, which showed an increase of bands interpreted as part of the protein structure (1450 and 1650 cm^{-1}). Streptavidin played a key role for binding the biotinylated part of anti-IgG, which was added to the nanocomposite in the next step (Step 6). The formation of a bond between streptavidin and the biotinylated part of anti-IgG was accompanied by changes in the surface charge to 0.4 mV and by changes in the previously mentioned IR bands. Final blockage of the remaining carboxylic groups with ethylamine was confirmed by an additional increase of the ζ-potential to 0.7 mV (Step 7). Moreover, the ability of the analytical system to bind IgG was tested by IR measurements. It was expected that successful binding of IgG would lead to a further change of protein band intensities, as can be seen in Figure 2C. A TEM image of the as-prepared and surface-modified nanocomposite is shown in Figure 2C, where the bright fringes surrounding the silver nanoparticles (shown in gray) can be interpreted as attached protein layers. Additional TEM images acquired at three important stages of the modification are shown in Figure S1A − Figure S01C. It can be seen that the synthesis did not lead to any considerable structural changes. Moreover, the HRTEM images accompanied by a map with the distribution of Ag and Fe_3O_4 nanoparticles in the prepared Fe_3O_4@Ag@Streptavidin@AntiIgG nanocomposite are included in Figure S1D−S1E. The signal stability of the modified nanocomposite is of the highest importance, and several experiments were conducted in order to evaluate its parameters. The as-prepared nanocomposite Fe_3O_4@Ag was prepared at day = 0 and stored for a period of 90 days. Its final modifications (labeled as Fe_3O_4@Ag@Streptavidin@AntiIgG) were prepared at selected instances, namely on days 1, 5, 10, 20, and 90, and their respective Raman spectra were acquired. Average Raman spectra can be seen in Figure S2. The calculated variation of the intensity of the spectral band at 1650 cm^{-1} between measured spectra is lower than 10%. It can be thus stated that the modification is repeatable and resulting Raman spectra comparable.

dx.doi.org/10.1021/ac503347h | *Anal. Chem.* 2014, 86, 11107−11114

The as-prepared Fe_3O_4@Ag@anti-IgG nanocomposite was successively utilized for the determination of levels of one of the most important immunoglobulins, IgG, in human whole blood samples. Based on vibration theory, it was predicted that the specific interaction of IgG with anti-IgG antibody immobilized on the surface of the nanocomposite would lead to a spectral shift of the order of a few wavenumbers or change in intensity of Raman bands corresponding to parts of the binding site of the antibody. To test this hypothesis, standard samples containing 100 ng·L^{-1} of human IgG dissolved in water were analyzed, as well as blank and control samples. The blank sample contained only the pure unmodified nanocomposite Fe_3O_4 dispersed in water, whereas the control sample consisted of an aqueous dispersion of nanocomposite Fe_3O_4@Ag@streptavidin@anti-IgG without addition of IgG. The spectra obtained are shown in Figure 3. The Raman signal of the control sample contained several important spectral bands that were attributed to parts of the protein structure of the designed analytical probe. Spectral bands at 1650, 1539, and 1350 cm^{-1} were interpreted as Amide I, II, and III, respectively. Moreover, the relatively sharp band at 1650 cm^{-1} indicated an α helix type secondary structure. The band at 605 cm^{-1} was interpreted as an Ag−N bond vibration originating from the addition of ethylamine in the first steps of the modification of the Fe_3O_4@Ag nanocomposite, as can be seen from the experiments summarized in Figure S3. Furthermore, its position and intensity were expected to be insensitive to further formation of a bond between anti-IgG covalently attached to the surface of the analytical probe, and IgG in a sample. On the other hand, successful formation of a bond between anti-IgG and IgG was anticipated to change the absolute intensities and, more importantly, the ratio of the spectral bands of Amide I, II, and III, owing to the different structures of these two proteins. Detailed comparison of spectra of the control and model samples revealed that both the position and intensity of the band at 605 cm^{-1} remained unchanged, as predicted, whereas the intensities and ratios of the protein spectral bands differed.

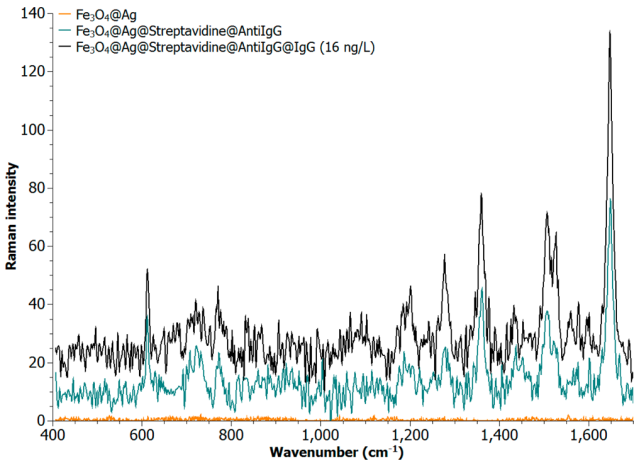

Figure 3. Raman spectra of bare nanocomposite Fe_3O_4@Ag, modified nanocomposite obtained by immobilization of streptavidin and anti-IgG (Fe_3O_4@Ag@streptavidin@anti-IgG), and model sample with a concentration of IgG 16 ng·L^{-1} (labeled as Fe_3O_4@Ag@streptavidin@anti-IgG@IgG).

The selectivity of the here designed method is a very important issue. AntiIgG used in the role of selector has been previously utilized by many authors where a high selectivity of antiIgG toward IgG was successfully demonstrated.[16−18] The overall selectivity of this approach was tested using mouse IgG and BSA; the presence of these proteins did not lead to any significant changes in the observed analytical signal, as can be seen in Figure S4; calculated values of RS were not significantly different from the values obtained for the blank solution. In order to evaluate the method's capabilities for obtaining quantitative information, five calibration samples were prepared. All the calibration samples were measured under the same conditions. The range of concentrations used to construct the calibration curve was selected to comply with demands for methods able to perform ultratrace analysis, and was set from 100 ng·L^{-1} to 500 mg·L^{-1}. Corresponding Raman spectra of the selected standards are shown in Figure 4.

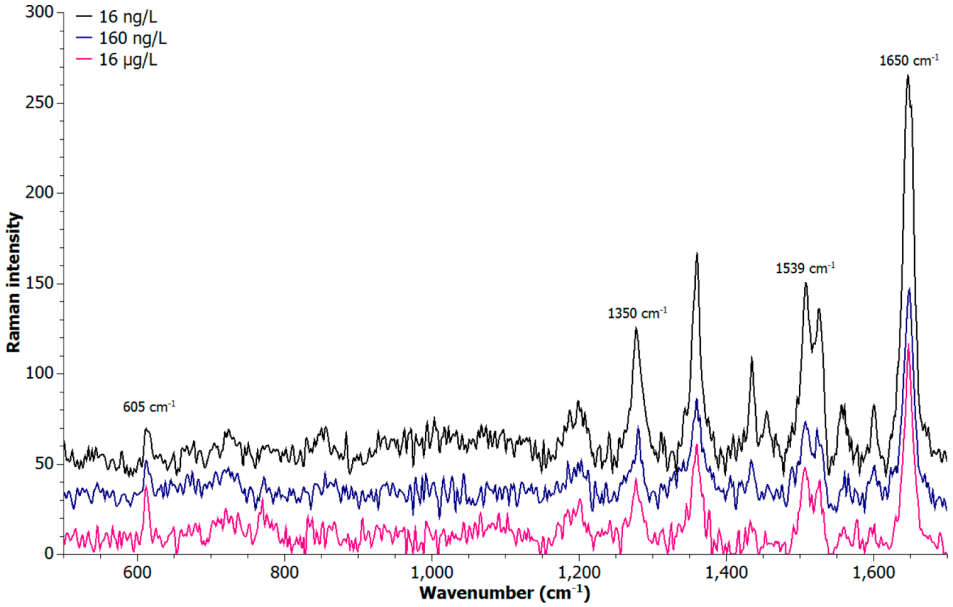

Figure 4. Raman spectra obtained in the presence of model samples containing 16 ng·L^{-1}, 160 ng·L^{-1}, and 16 μg·L^{-1} IgG.

dx.doi.org/10.1021/ac503347h | Anal. Chem. 2014, 86, 11107−11114

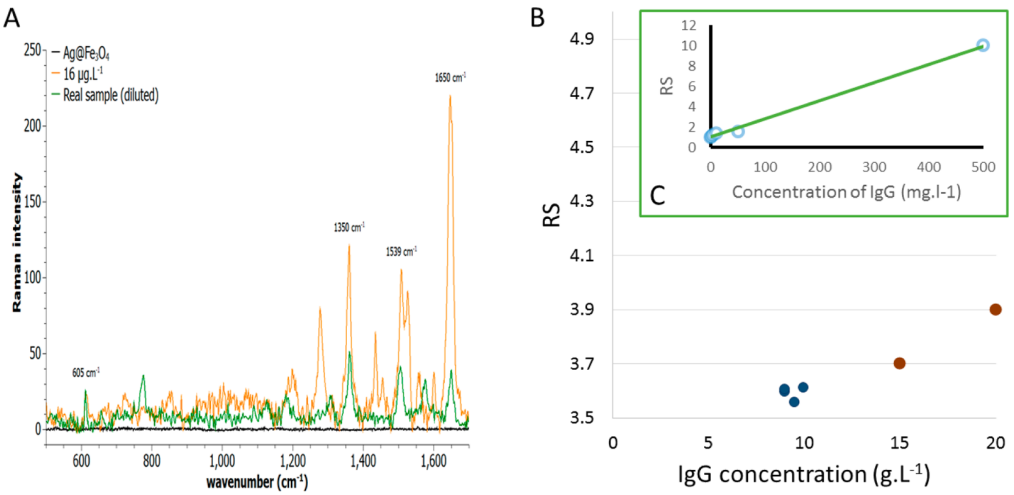

Figure 5. (A) Raman spectrum obtained in the presence of a real sample of whole human blood. For comparison, the Raman spectra of a model sample containing 16 $\mu g \cdot L^{-1}$ IgG and bare nanocomposite are also presented. (B) Concentration determination of analyzed samples. Blue points stand for real samples and brown points show data obtained by standard additions. (C) Calibration curve for a determination of IgG in model samples.

Normalized and baseline-corrected spectra were evaluated and used for a calibration. Presented fluctuations in the spectral data, observed from the instability of the spectral band at 605 cm^{-1}, do not allow a direct determination of the amount of IgG from absolute intensities, as can be seen in Figure 4. However, previous works suggest that protein interactions lead to considerable changes in ratios of selected spectral bands.[8] Quantification of IgG is thus based on a simple equation (eq 1) that allows calculation of the ratio of the intensities of the protein 1539 and 1650 cm^{-1} bands, where the absolute intensities of I1650 and I1539 were previously normalized to the intensity of the reference band at 605 cm^{-1} in order to minimize the unwanted fluctuations in the analytical signal.

$$R = \frac{I_{1539}/I_{605}}{I_{1650}/I_{605}} \quad (1)$$

where I_{1539}, I_{1650}, and I_{605} stand for the intensities of the spectral bands at 1539, 1650, and 605 cm^{-1}, respectively. I_{605} was used as a spectral reference to normalize the whole spectrum in order to minimize system errors originating from changes in the composite constitution, structure, and Raman signal instability. As the data come from separate spectral analyses, values of I_{605} in eq 1 could not be completely eliminated. Moreover, to make the method more robust, a Raman spectrum for a control sample containing only Fe_3O_4@Ag@streptavidin@anti-IgG composite was used as a reference, as shown in eq 2:

$$\mathrm{RS} = \frac{\mathrm{IStd}_{1539}/\mathrm{IStd}_{605}}{\mathrm{IStd}_{1650}/\mathrm{IStd}_{605}} \Big/ \frac{\mathrm{IRef}_{1539}/\mathrm{IRef}_{605}}{\mathrm{IRef}_{1650}/\mathrm{IRef}_{605}} \quad (2)$$

where IS denotes the intensities of the spectral bands obtained by analysis of the samples and, analogously, IRef stands for the spectral intensities of bands in the Raman spectra of the control samples. RS thus describes the degree of change of the protein band ratios between the control and each analyzed sample; the greater the value above one, the higher the amount of IgG present in the sample (control sample; RS = 1). It was found that the ratio showed a linear trend over the whole measured range with a coefficient of determination amounting to 0.98, as can be seen in Figure 5. The calculated limit of detection was 0.6 $ng \cdot L^{-1}$ (calculated from the parameters of the calibrations curve, $S/N = 3$). The limit of detection of most current assays for the analysis of IgG in human blood samples is of the order of tens of $\mu g \cdot L^{-1}$, with a relative standard error of determination of around 20%; this includes serum and whole blood samples. Although those assays are based on similar principles (interaction of the target with a particular antibody), the developed method is capable of detecting human IgG at 1000× lower concentration level and at the same time uses much lower sample volumes. This is due to a superior signal amplification effect achieved by careful selection of the SERS conditions (described in the Materials and Methods). Moreover, 10 measurements were taken on 10 separate days to test the stability of the Raman signal. It was found out that the relative error of *RS* between replicates was lower than 8%. Next, measurements of two model samples were performed to test the method reliability and robustness. Sample A contained 10 $ng \cdot L^{-1}$ IgG and Sample B 100 $ng \cdot L^{-1}$, with differences between the real and experimentally obtained values of around 20% and relative standard deviation, RSD = 5%. The same samples were measured at two different times of day (intraday values) and on three separate days (interday values). It was shown that the relative error was lower than 5% for the intraday experiments and lower than 15% for the interday experiments. This demonstrates the applicability of the described method for the analysis of IgG.

The application potential of the proposed method was further tested with the aim of using it for the analysis of human whole blood samples obtained using the finger prick method (details are given in the experimental part), where sample amount is strictly limited to a few microliters. It should be noted that a design of the described procedure was tuned to minimize nonspecific interactions of the synthesized nanocomposites with nontargeted compounds present in the complex matrix of human blood. However, part of the overall Raman signal may still have originated from nonspecific interactions, and thus the Raman signal had to be properly verified and normalized by careful comparison of the spectra obtained for real and model samples. The experimental analysis was performed according to the procedures previously used in the calibration experiments. Briefly, 2 μL of 100× diluted whole

dx.doi.org/10.1021/ac503347h | *Anal. Chem.* 2014, 86, 11107−11114

blood was collected and deposited on a glass platform. Then, 10 μL of a solution containing prepared Fe_3O_4@Ag@streptavidin@anti-IgG nanocomposite was added and well mixed with the sample. The nanocomposite was washed twice with water using an external magnetic force for separation (in total 10 μL) and analyzed using SERS. To perform a full statistical evaluation, four samples from two patients were collected and analyzed 5 times. A SERS spectrum for the real sample is presented in Figure 5A, showing that all the bands previously attributed to the analytical probe were present; nevertheless, the spectral band interpreted as Amid II is moderately shifted due to a different structure of IgG, compared to antiIgG and Streptavidin. The Raman spectrum of the real sample was thus compared to a respective Raman spectrum of a standard solution of human IgG (initial concentration = 5 g·L^{-1}) in order to demonstrate the origin of the analytical signal. Results are shown in Figure S4, where the same pattern of both spectra is demonstrated.

Further demonstration of the method involved evaluation of the method selectivity. It can be stated that the immunochemical reaction can be considered as very selective, and the impact of such a statement has already been demonstrated. Moreover, the approach used in this analytical method further minimized possible interferences caused by the presence of nontargeted proteins by the applied synergy of magnetic separation and preconcentration with a high selectivity of AntiIgG. Albeit the number of already published papers dealing with the applications of antibodies in the role of selectors was mentioned previously,[15−18] the selectivity of the here described method was further tested on a set of proteins, namely mouse IgG, human IgG, and bovine serum albumin. The results obtained from the performed experiment are shown in Figure S5, where it can be seen that the presence of BSA or mouse IgG did not lead to any considerable changes in the spectra; the calculated value of RS is equal to 1 for the blank solution (without human IgG), 1.05 for BSA (c = 100 mg·L^{-1}), and 1.08 for mouse IgG. Nonetheless, the concentration level of human IgG in real samples was quantified by a standard addition method in order to minimize possible spectral interferences originating from the matrix effects and to achieve a suitable level of accuracy and precision. A defined amount of IgG was thus added to each sample, and the spectral position and intensity of all bands were evaluated and compared to Raman spectra of real samples. The obtained values are shown in Figure 5B, where real samples are labeled as blue points, and two standard additions are labeled as brown points, respectively. Signal stability was evaluated using a set number of technical replicates (N = 5). Obtained Raman spectra of Sample 1 retrieved from patient A are shown in Figure S6. The obtained relative standard deviation between calculated values of RS is lower than 5%. The results of the analysis show that samples from patient A contained 9 g·L^{-1} of IgG, and analogously, samples obtained from patient B contained 10 g·L^{-1} of IgG. It is worth mentioning that the determined amounts of IgG are in good compliance with the levels recorded in a healthy population.[21]

CONCLUSIONS

Current methods for the determination of levels of IgG in humans are mostly based on interactions of antibodies with a target coupled with colorimetric or fluorimetric detection. These methods are usually robust and fast. However, their further development is limited and there is increasing demand for methods able to determine IgG at ultralow concentrations. Here, we report a novel method for the determination of human IgG in whole blood samples. The method utilizes a magnetic Fe_3O_4@Ag nanocomposite, where silver nanoparticles are covalently bonded using carboxymethylchitosan chosen as a physiologically compatible linker. The surface of the as-prepared nanocomposite was modified using streptavidin, followed by anti-IgG. The nanocomposite enabled the development of a robust method for the direct determination of IgG at concentrations from 600 fg.mL^{-1}. The benefit of such an approach is that it can be modified relatively easily in order to analyze many other targets by selecting an appropriate antibody modified by addition of biotin.

ASSOCIATED CONTENT

Supporting Information

TEM images and Raman spectra. This material is available free of charge via the Internet at http://pubs.acs.org.

AUTHOR INFORMATION

Corresponding Authors

*Phone: +420 585634753. Fax: +420 585634761. E-mail address: vaclav.ranc@upol.cz (V.R.).

*Phone: +420 585634337. Fax: +420 585634761. E-mail address: radek.zboril@upol.cz (R.Z.).

Notes

The authors declare no competing financial interest.

ACKNOWLEDGMENTS

The authors gratefully acknowledge support from the Operational Program Research and Development for Innovations—European Social Fund (Project No. CZ.1.05/2.1.00/03.0058), New Technologies UP in Chemistry and Biology (Project No. CZ.1.05/3.1.00/14.0302), and the Research Team of the Regional Centre of Advanced Technologies and Materials with a Focus on Unconventional Experimental Techniques in Materials and Optical Research (RCPTM_FRONT) (Project No. CZ.1.07/2.3.00/20.0155) of the Ministry of Education, Youth and Sports of the Czech Republic. This work has also been supported by the Operational Program Education for Competitiveness—European Social Fund (CZ.1.07/2.3.00/20.0056), an internal grant of Palacky University in Olomouc (PrF_2014032), and the Technology Agency of the Czech Republic (Project No. TA03011368). The authors would like to thank Jana Straska and Klara Cepe for providing HRTEM and EDX data.

REFERENCES

(1) Yap, P. L. *Clinical Applications of Intravenous Immunoglobulin Therapy*; Churchill Livingstone: Edinburgh, New York, 1992; p ix, pp 270.

(2) Shakib, F. *The Human IgG Subclasses: Molecular Analysis of Structure, Function, and Regulation*, 1st ed.; Pergamon Press: Oxford, New York, 1990; p xi, pp 316.

(3) Virella, G. *Medical Immunology*, 6th ed.; Informa Healthcare: New York, 2007; p ix, pp 465.

(4) Dobson, R.; Topping, J.; Giovannoni, G. *J. Med. Virol.* **2013**, *85*, 128−131.

(5) van Eeden, P. E.; Wiese, M. D.; Aulfrey, S.; Hales, B. J.; Stone, S. F.; Brown, S. G. A. *PLoS One* **2011**, *6*, e16741.

(6) de Costa, D.; Broodman, I.; VanDuijn, M. M.; Stingl, C.; Dekker, L. J. M.; Burgers, P. C.; Hoogsteden, H. C.; Smitt, P. A. E. S.; van Klaveren, R. J.; Luider, T. M. *J. Proteome Res.* **2010**, *9*, 2937−2945.

(7) Rodriguez-Lorenzo, L.; Fabris, L.; Alvarez-Puebla, R. A. *Anal. Chim. Acta* **2012**, *745*, 10−23.
(8) (a) McNay, G.; Eustace, D.; Smith, W. E.; Faulds, K.; Graham, D. *Appl. Spectrosc.* **2011**, *65*, 825−837. (b) Mikhonin, A.; Ahmed, Z.; Ianoul, A. *J. Phys. Chem. B* **2004**, *108*, 19020−19028. (c) Sjöberg, B.; Foley, S.; Cardey, B.; Enescu, M. *Spectrochim. Acta, A: Mol. Biomol. Spectrosc.* **2014**, *128*, 300−311. (d) Guerrini, L.; Pazos, E.; Penas, C.; Vázquez, M. E.; Mascareñas, J. L.; Alvarez-Puebla, R. A. *J. Am. Chem. Soc.* **2013**, *135*, 10314−10317. (e) Avci, E.; Culha, M. *Appl. Spectrosc.* **2014**, *68*, 890−899.
(9) Trang, N. T. T.; Thuy, T. T.; Higashimine, K.; Mott, D. M.; Maenosono, S. *Plasmonics* **2013**, *8*, 1177−1184.
(10) Magro, M.; Faralli, A.; Baratella, D.; Bertipaglia, I.; Giannetti, S.; Salviulo, G.; Zboril, R.; Vianello, F. *Langmuir* **2012**, *28*, 15392−15401.
(11) Chen, L.; Hong, W.; Guo, Z.; Sa, Y.; Wang, X.; Jung, Y. M.; Zhao, B. *J. Colloid Interface Sci.* **2012**, *368*, 282−286.
(12) Ranc, V.; Markova, Z.; Hajduch, M.; Prucek, R.; Kvitek, L.; Kaslik, J.; Safarova, K.; Zboril, R. *Anal. Chem.* **2014**, *86*, 2939−2946.
(13) (a) Quaresma, P.; Osorio, I.; Doria, G.; Carvalho, P. A.; Pereira, A.; Langer, J.; Araujo, J. P.; Pastoriza-Santos, I.; Liz-Marzan, L. M.; Franco, R.; Baptista, P. V.; Pereira, E. *RSC Adv.* **2014**, *4*, 3659−3667. (b) Neng, J.; Harpster, M. H.; Wilson, W. C.; Johnson, P. A. *Biosens. Bioelectron.* **2013**, *41*, 316−321.
(14) Drake, P.; Jiang, P. S.; Chang, H. W.; Su, S. C.; Tanha, J.; Tay, L. L.; Chen, P. L.; Lin, Y. J. *Anal. Methods* **2013**, *5*, 4152−4158.
(15) (a) Lin, C.-C.; Yang, Y.-M.; Chen, Y.-F.; Yang, T.-S.; Chang, H.-C. *Biosens. Bioelectron.* **2008**, *24*, 178−183. (b) Chen, J.; Luo, Y.; Liang, Y.; Jiang, J.; Shen, G.; Yu, R. *Anal. Sci.* **2009**, *25*, 347−352. (c) Li, T.; Guo, L.; Wang, Z. *Anal. Sci.* **2008**, *24*, 907−910. (d) Penn, M. A.; Drake, D. M.; Driskell, J. D. *Anal. Chem.* **2013**, *85*, 8609−8617. (e) Chen, J. W.; Lei, Y.; Liu, X. J.; Jiang, J. H.; Shen, G. L.; Yu, R. Q. *Anal. Bioanal. Chem.* **2008**, *392*, 187−193. (f) Han, X. X.; Kitahama, Y.; Tanaka, Y.; Guo, J.; Xu, W. Q.; Zhao, B.; Ozaki, Y. *Anal. Chem.* **2008**, *80*, 6567−6572. (g) Li, T.; Guo, L. P.; Wang, Z. X. *Biosens. Bioelectron.* **2008**, *23*, 1125−1130. (h) Wei, L.; Jin, B.; Dai, S. *J. Phys. Chem. C* **2012**, *116*, 17174−17181. (i) Zengin, A.; Tamer, U.; Caykara, T. *Biomacromolecules* **2013**, *14*, 3001−3009.
(16) Chen, J. W.; Lei, Y.; Liu, X. J.; Jiang, J. H.; Shen, G. L.; Yu, R. Q. *Anal. Bioanal. Chem.* **2008**, *392*, 187−193.
(17) Song, C.; Wang, Z.; Zhang, R.; Yang, J.; Tan, X.; Cui, Y. *Biosens. Bioelectron.* **2009**, *25*, 826−831.
(18) Narayanan, R.; Lipert, R. J.; Porter, M. D. *Anal. Chem.* **2008**, *80*, 2265−2271.
(19) (a) Chen, Y.; Cheng, H.; Tram, K.; Zhang, S.; Zhao, Y.; Han, L.; Chen, Z.; Huan, S. *Analyst* **2013**, *138*, 2624−2631. (b) Chon, H.; Lim, C.; Ha, S.-M.; Ahn, Y.; Lee, E. K.; Chang, S.-I.; Seong, G. H.; Choo, J. *Anal. Chem.* **2010**, *82*, 5290−5295. (c) Zong, S.; Wang, Z.; Zhang, R.; Wang, C.; Xu, S.; Cui, Y. *Biosens. Bioelectron.* **2013**, *41*, 745−751. (d) Yoon, J.; Choi, N.; Ko, J.; Kim, K.; Lee, S.; Choo, J. *Biosens. Bioelectron.* **2013**, *47*, 62−67. (e) Baniukevic, J.; Hakki Boyaci, I.; Goktug Bozkurt, A.; Tamer, U.; Ramanavicius, A.; Ramanaviciene, A. *Biosens. Bioelectron.* **2013**, *43*, 281−288. (f) Guven, B.; Basaran-Akgul, N.; Temur, E.; Tamer, U.; Boyaci, I. H. *Analyst* **2011**, *136*, 740−748. (g) Kim, I.; Junejo, I.-R.; Lee, M.; Lee, S.; Lee, E. K.; Chang, S.-I.; Choo, J. *J. Mol. Struct.* **2012**, *1023*, 197−203. (h) Shin, M. H.; Hong, W.; Sa, Y.; Chen, L.; Jung, Y.-J.; Wang, X.; Zhao, B.; Jung, Y. M. *Vib. Spectrosc.* **2014**, *72*, 44−49.
(20) Markova, Z.; Siskova, K.; Filip, J.; Safarova, K.; Prucek, R.; Panacek, A.; Kolar, M.; Zboril, R. *Green Chem.* **2012**, *14*, 2550−2558.
(21) Reen, D. J.; Murphy, M. B.; Oconnor, A.; Fitzgerald, M. X. *Irish J. Med. Sci.* **1981**, *150*, 265−269.

analytical chemistry

Article

pubs.acs.org/ac

Detection of Prosthetic Joint Infection Based on Magnetically Assisted Surface Enhanced Raman Spectroscopy

Ariana Fargašová,[†] Anna Balzerová,[†] Robert Prucek,[†] Miroslava Htoutou Sedláková,[‡] Kateřina Bogdanová,[‡] Jiří Gallo,[§] Milan Kolář,[‡] Václav Ranc,*[,†] and Radek Zbořil*[,†]

[†]Regional Centre of Advanced Technologies and Materials, Department of Physical Chemistry, Faculty of Science, Palacký University Olomouc, Šlechtitelů 27, 783 71 Olomouc, Czech Republic

[‡]Department of Microbiology, Faculty of Medicine and Dentistry, Palacký University Olomouc, Hněvotínská 3, 775 15 Olomouc, Czech Republic

[§]Department of Orthopaedics, Faculty of Medicine and Dentistry, Palacký University Olomouc, I. P. Pavlova 6, 77520 Olomouc, Czech Republic

Supporting Information

ABSTRACT: Accurate and rapid diagnosis of prosthetic joint infection (PJI) is vital for rational and effective therapeutic management of this condition. Several diagnostic strategies have been developed for discriminating between infected and noninfected cases. However, none of them can reliably diagnose the whole spectrum of clinical presentations of PJI. Here, we report a new method for PJI detection based on magnetically assisted surface enhanced Raman spectroscopy (MA-SERS) using streptavidin-modified magnetic nanoparticles (MNP@Strep) whose surface is functionalized with suitable biotinylated antibodies and then coated with silver nanoparticles by self-assembly. The high efficiency of this approach is demonstrated by the diagnosis of infections caused by two bacterial species commonly associated with PJI, namely, *Staphylococcus aureus* and *Streptococcus pyogenes*. The method's performance was verified with model samples of bacterial lysates and with four real-matrix samples of knee joint fluid spiked with live pathogenic bacterial cells. This procedure is operationally simple, versatile, inexpensive, and quick to perform, making it a potentially attractive alternative to established diagnostic techniques based on Koch's culturing or colony counting methods.

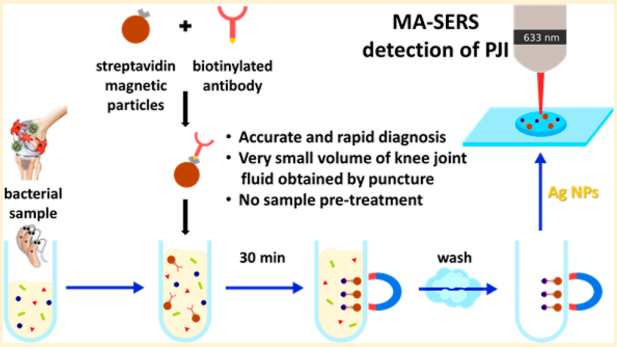

Prosthetic joint infection (PJI) is a feared complication of total joint arthroplasty that substantially increases morbidity and mortality following total joint arthroplasty. Current estimates suggest that PJI complications occur in up to 3% of primary hip and knee arthroplasties and up to 15.4% and 25% of revision hip and knee arthroplasties, respectively.[1,2] The pathogenesis of PJI is related to the presence of biofilm-forming microorganisms, most commonly *Staphylococci* and *Streptococci*.[3,4]

Most current methods for diagnosing PJI are rather time-consuming, involving several pre- and intraoperative steps. This is especially true for low-grade infections that are difficult to distinguish from aseptic failure.[5] The condition is typically diagnosed on the basis of four generally accepted criteria: (i) the presence of a cutaneous sinus tract communicating with the prosthesis, (ii) histopathological evidence of acute inflammation, (iii) increased counts or differentials of leukocytes or neutrophils in the synovial fluid, and (iv) the development of a positive culture from samples of synovial fluid, intraoperative periprosthetic tissue, or sonication fluid.[3,5−8] In recent years, there has also been considerable interest in diagnosing PJI by detecting antibacterial molecules. These methods achieve excellent sensitivity and specificity in around 95% of all enrolled cases.[9] However, they provide no information about the causative bacteria in any given infection.

Most of the gold standard microbial methods for diagnosing PJI are based on Koch's culturing and colony counting methods[10] and only deliver results after several days.[11] Additionally, culture-based methods are susceptible to contamination, which can lead to false positive diagnoses, and yield false negative diagnoses in up to 30% of all cases.[12] More advanced alternative techniques have been proposed to shorten the analysis time and increase the accuracy of the identification of PJI. One such alternative is based on the polymerase chain reaction (PCR), which can be used to detect and identify diverse pathogens.[11,13−15] PCR is considerably less time-consuming and more sensitive than many other techniques, including the culturing and plating methods discussed above.[11,16] However, highly trained professionals are needed

Received: March 1, 2017
Accepted: May 22, 2017
Published: May 22, 2017

DOI: 10.1021/acs.analchem.7b00759
Anal. Chem. 2017, 89, 6598−6607

to perform PCR analyses and interpret their results.[16,17] Other techniques capable of bacterial identification are based on pulsed-field gel electrophoresis (PFGE).[18−20] Despite their sensitivity, methods based on PFGE are very time-consuming, which limits their practical utility. Thus, there is still a need for a rapid and highly sensitive typing tool that would enable the accurate diagnosis of PJI and the identification of the causative agent within a few minutes.

Procedures based on Raman spectroscopy represent interesting alternatives to culture- or PCR-based methods for PJI diagnosis. It was recently shown that surface enhanced Raman spectroscopy (SERS) can be used to rapidly identify selected microorganisms.[21,22] Additionally, Khan et al. showed that a SERS assay using antibody-conjugated popcorn-shaped gold nanoparticles can detect *Salmonella typhimurium* in water samples.[23] SERS was also used by Sivanesan et al. to selectively identify the pathogenic bacterium *S. epidermidis* in blood samples on a bare Ag−Au bimetallic surface.[24] More recently, a composite of nanoaggregates of gold particles was used with a high specificity single domain antibody to identify *Staphylococcus aureus* bacteria by SERS.[25] Another innovative approach based on immunomagnetic isolation, membrane filtration, and silver intensification was used to measure the SERS signals of pathogenic *Escherichia coli* bacteria in ground beef.[26,27] Unfortunately, all these nanoparticle-based techniques require precultivation periods of several hours to generate sufficient biomass and a silver intensification step to permit SERS measurements. Here, we present a fast new method for diagnosing PJI based on magnetically assisted surface enhanced Raman spectroscopy (MA-SERS), which was previously used by our group for fast, selective, and highly sensitive detection of various molecules including dopamine[28] and immunoglobulins.[29] It is worth mentioning that, despite Ag NPs being frequently used for their synergistic antibacterial and antibiofilm activity to inhibit the growth of bacteria,[30,31] Ag NPs at low concentrations effective for Raman signal enhancement do not have any inhibitory impact on the analyzed pathogens.

The method uses a new highly efficient biosensor based on streptavidin-modified carboxy-functionalized magnetic nanoparticles (henceforth referred to as MNP@Strep) for efficient target isolation. After isolation, the biosensor is coated with silver nanoparticles to enable MA-SERS detection of PJI. The nanomaterial used for MA-SERS detection has two beneficial effects. First, its magnetic properties enable effective and quantitative isolation of selected chemical targets from a complex matrix. Second, the SERS effect of the silver nanoparticles on adsorbed molecules gives the method ultralow limits of detection. We show that this method can be used to isolate and identify two bacterial strains, *Staphylococcus aureus* and *Streptococcus pyogenes*. Moreover, the method was successfully used to diagnose PJI in real-matrix samples of knee joint fluid in a few minutes, without any need for sample pretreatment. It could thus be an attractive alternative to established procedures for clinical diagnosis of PJI.

EXPERIMENTAL SECTION

Reagents and Chemicals. Carboxy-functionalized magnetic microparticles, *N*-hydroxysulfosuccinimide sodium salt (≥98% (HPLC); NHS), 1-[3-(dimethylamino)propyl]-3-ethylcarbodiimide methiodide (EDC), streptavidin from *Streptomyces avidinii* (essentially salt-free, lyophilized powder, ≥13 units/mg protein), biotin-conjugated mouse antiprotein A monoclonal antibody, ethylamine (purum, 70% in H_2O), and phosphate-buffered saline solution (PBS) were purchased from Sigma-Aldrich. Biotin-conjugated rabbit anti-*Streptococcus* group A polyclonal antibody was obtained from Abcam plc. (Cambridge, UK). Silver nitrate ($AgNO_3$, p.a., Tamda), ammonia (NH_4, aqueous solution 28% w/w, p.a., Sigma-Aldrich), sodium hydroxide (NaOH, p.a., Lach-Ner), and D(+)-maltose monohydrate ($C_{12}H_{22}O_{11} \times H_2O$, p.a., Sigma-Aldrich) were used to prepare primary silver nanoparticles. Sodium chloride (NaCl, p.a., Sigma-Aldrich) was used to treat the primary silver nanoparticles. All chemicals were used as received without any additional purification steps.

Preparation of Silver Nanoparticles. Maltose-reduced silver nanoparticles for use as SERS substrates were prepared by reducing the silver ammonia complex cation $[Ag(NH_3)_2]^+$ with D-maltose as described by Panacek and co-workers.[32] Briefly, silver nitrate and the reducing sugar (maltose) were dissolved in distilled water to initial concentrations of 10^{-3} and 10^{-2} M, respectively. The initial concentration of ammonia was 5×10^{-3} M. After the silver, sugar, and ammonia had been added, the reaction system's pH was adjusted to 11.5 ± 0.1 by adding sodium hydroxide. The reaction was deemed complete after 4 min, yielding a nearly monodispersed suspension of maltose-reduced silver nanoparticles with an average particle size of about 28 nm.

Preparation of Bacterial Samples. *Preparation of Model Samples.* The method was initially tested using model bacterial lysate samples without knee joint fluid. Testing samples were prepared using the bacterial species *Staphylococcus aureus* CCM 3953 and *Streptococcus pyogenes* (Strain No. SP12, from the culture collection of the Department of Microbiology, Faculty of Medicine and Dentistry, Palacký University Olomouc). Lysates were prepared from 24 h cultures of *S. aureus* and *S. pyogenes*. Well-isolated colonies were transferred into 5 mL of Mueller-Hinton broth so that the resulting turbidity was equivalent to a McFarland standard of 1.0 (approximate cell density of 3×10^8 CFU/mL). The inoculum density was determined by measuring the samples' optical density with a densitometer (Densi-La-Meter; LACHEMA, Czech Republic), and the bacterial suspensions were then cultured at 37 °C for 24 h. After incubation, the broth was centrifuged at 2000 rpm for 10 min. The supernatant was then removed, and 10 mL of distilled water was added to the pellet. Finally, the mixed suspension was repeatedly (10 times) frozen at −72 °C for 10 min and then thawed in a 37 °C water bath. The repeated freeze−thaw cycles cause lysis of bacterial cells in suspension.

Preparation of Real-Matrix Samples. After being validated against model samples, the method was tested using real-matrix samples prepared from sterile knee joint fluid obtained by puncture from patients with osteoarthritis. To verify the sterility of the initial joint fluid, it was inoculated onto blood agar (Trios, Ltd.) and into Mueller-Hinton broth (HiMedia) and cultivated. Real-matrix samples for testing were then prepared by spiking samples of the joint fluid in a 1:1 ratio with live cells of one of the two bacterial lysates. In these experiments, the spiking samples of the joint fluid and the sterile joint fluid were used as positive and negative controls, respectively. All joint fluid samples were obtained under standard conditions with written informed patient consent, and the study was approved by the local Ethics Committee.

Immobilization of Streptavidin onto Carboxy-Functionalized Magnetic Nanoparticles (MNP@Strep). To immobilize streptavidin on the surface of the carboxy-functionalized magnetic nanoparticles (MNP), 0.5 mL of the

DOI: 10.1021/acs.analchem.7b00759
Anal. Chem. 2017, 89, 6598−6607

stock dispersion of MNP was separated from the mixture solution using a magnet and then washed with deionized water. The carboxylic groups of these MNP were then activated with a 1 mL solution of EDC and NHS (the final concentrations of both reagents were 10 mM) and stirred for 45 min. The MNP were collected using an external magnetic field and washed three times with 10 mM PBS buffer. The MNP with activated carboxylic groups were then mixed with streptavidin (1 mg/L) and stirred for 2 h to form covalent bonds between the free amino ($-NH_2$) groups of streptavidin and the activated carboxylic groups of the MNP. After the addition of streptavidin, the MNP were collected using a permanent magnet and subsequently washed three times with 10 mM PBS buffer to remove free streptavidin.

MNP@Strep Nanoparticles and Antibody Binding Procedure. Two different biotinylated antibodies were used to prepare antibody-labeled MNP: mouse monoclonal antibody to protein A (anti-IgA) (a surface protein from the *S. aureus* cell wall) or rabbit polyclonal antibody to group-A streptococci polysaccharide (anti-APS). To prepare MNP with antibodies immobilized on their surfaces, MNP@Strep nanoparticles were mixed with 1 mL of the appropriate antibody solution (at a final concentration of 10 mg/L) and stirred for 1 h to enable noncovalent bond formation between the streptavidin and the antibody's biotin tag. After rinsing three times with 10 mM PBS buffer to physically remove residual unbound antibody molecules, ethylamine at a final concentration of 3.5% wt. was added to block the remaining active carboxylic groups. The resulting MNP@Strep@anti-IgA or MNP@Strep@anti-APS nanoparticles were stable over a period of 2 months.

Material Characterization Methods. The ζ potentials of the starting material, intermediates, and final products were measured using a Zetasizer NanoZS (Malvern, UK). A transmission electron microscope (TEM) (Jeol 2100) equipped with a LaB_6 cathode operated at an accelerating voltage of 200 kV with a point-to-point resolution of 0.194 nm was used to obtain an image of the commercial starting material, i.e., the carboxy-functionalized MNP. A drop of MNP dispersion was placed onto a holey carbon film supported on a copper-mesh TEM grid and left to air-dry at room temperature. Structural analysis of the starting MNP was performed with an X-ray powder diffractometer with programmable divergence (XRD, PANalytical X'Pert PRO) in the Bragg−Brentano geometry, equipped with an iron-filtered Co Kα radiation source, an X'Celerator detector, and diffracted beam antiscatter slits. 200 μL of liquid sample was dropped on a zero-background Si slide, dried under vacuum at room temperature, and scanned across 2θ values ranging from 10° to 105° under ambient conditions. HRTEM images of the final product were obtained using a high resolution transmission electron microscope (HR-TEM FEI Titan G2 60−300) with an X-FEG type emission gun, operating at 80 kV. This microscope was equipped with a Cs image corrector and a STEM high-angle annular dark-field detector (HAADF). Its point resolution was 0.08 nm in TEM mode. Elemental mapping was performed by STEM-Energy Dispersive X-ray Spectroscopy (EDS; Bruker SuperX) with an acquisition time of 20 min. Fourier transform infrared (FT-IR) absorption spectra were collected using a Nicolet iS5 infrared spectrometer (Thermo Scientific, U.S.A.) to identify the functional groups of the treated MNP and the nature of their bonding. FT-IR spectra were acquired by attenuated total reflectance (ATR) in a ZnSe crystal. A drop of sample was placed onto a ZnSe crystal and left to air-dry at room temperature. Then, a total of 64 scans with a resolution of 2 cm^{-1} were recorded and averaged for each sample. The FT-IR absorption spectra were processed using ATR correction.

Sample Preparation for SERS Detection. Bacterial lysates and live bacterial cells of *S. aureus* and *S. pyogenes* were prepared as described above. Prior to the analysis of real-matrix samples of joint fluid spiked with live bacterial cells, samples were diluted 10-fold with deionized water to modify their consistency. Both model bacterial lysate samples and real-matrix samples of knee joint fluid spiked with live bacterial cells were then analyzed using the following SERS protocol. A sample volume of 10 μL was mixed with a 10 μL solution of the MNP@Strep nanoparticles conjugated with a biotinylated antibody to either protein A or the group-A streptococci polysaccharide, and the resulting mixture was stirred for 30 min. A 20 μL aliquot of the stirred solution was then dropped onto a glass slide and magnetically separated from the excess sample matrix. Next, 8 μL of a silver nanoparticle (Ag NPs) suspension was pipetted onto the separated magnetic solid portion on the glass slide. Finally, 2 μL of a 1 M solution of NaCl was pipetted onto the magnetic biosensor and the resulting suspension was mixed in the pipet tip. A precipitate of the magnetic biosensor formed on the edge of the drop, from where it was captured with a magnet and analyzed immediately before it could dry.

SERS Instrumentation and Data Processing. SERS spectra were recorded using a DXR Raman Microscope (Thermo Scientific) equipped with a thermoelectrically cooled (−50 °C) charge-coupled device (CCD) camera and a 10× objective. All spectra were measured at room temperature on a glass slide. SERS spectra were measured with an excitation line at 633 nm (He−Ne gas laser) and were acquired over a wavenumber range of 400 to 1800 cm^{-1}. Spectral acquisition was repeated 16 times per sample, with an accumulation time of 0.5 s per repetition. The laser light power incident on the samples was adjusted to 5.0 mW, and the slit length was set to 50 mm.

All spectra were baseline corrected and unit-vector normalized to enable visualization of spectral dissimilarities. Spectra of experimental samples were evaluated by comparing their protein band ratios to those in the spectra of blank samples. The results were expressed as the mean of the standard deviation of values obtained from five independent experiments with ten measurements in the case of biosensor stability and four independent experiments with ten measurements in the case of the influence of concentration effects on bacterial recognition. The differences between blank sample and bacteria treated biosensors were analyzed by a two-tailed Student's t test using Microsoft Excel and were considered statistically significant ($p < 0.05$). The Nicolet TQ Analyst chemometric software package was used to construct and perform discriminant analysis of the bacteria related to prosthetic joint infection. Additionally, the TQ Analyst software package was used to perform a clustering analysis based on average intra- and intercluster distances in order to evaluate the MA-SERS method's ability to discriminate between bacteria. The capacity of the MA-SERS biosensor to detect PJI was evaluated using both infected and noninfected real-matrix samples. A set of 30 samples including ten sterile joint fluid replicates and spectra of sterile joint fluid spiked with live bacterial cells were used for this purpose. The three principal components needed to describe the spectral variation in the standards using the discriminant analysis method were chosen

DOI: 10.1021/acs.analchem.7b00759
Anal. Chem. 2017, 89, 6598−6607

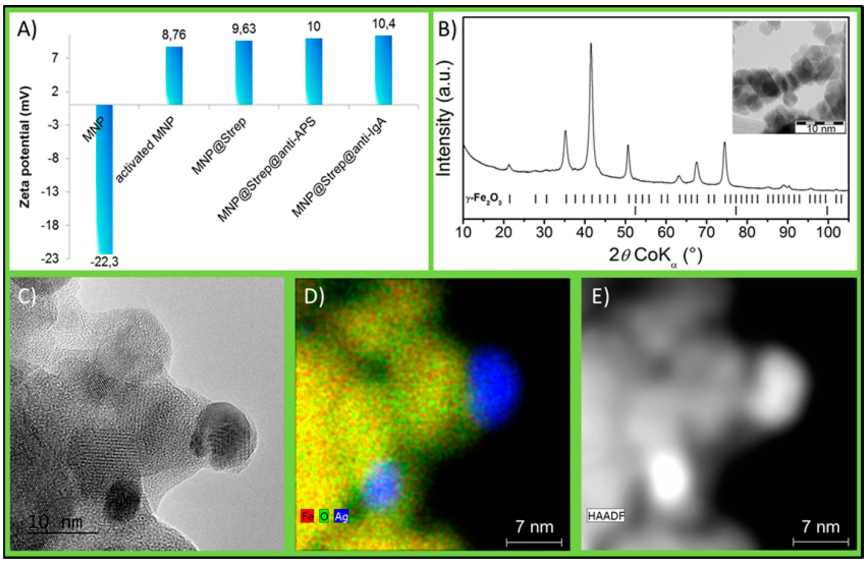

Figure 1. Material characterization of the MA-SERS biosensor: (A) Measured ζ potentials of the prepared biosensor after each modification step. (B) XRD pattern of MNP (inset: TEM image of the MNP). The theoretical position of the maghemite diffraction line is also shown. (C) Representative HRTEM image of MNP@Strep/Ag. (D) STEM-EDS chemical mapping (Fe, O, and Ag) of MNP@Strep/Ag. (E) HAADF image of MNP@Strep/Ag.

on the basis of an Eigenanalysis; the resulting decomposition converted the data into a principal component space with axes in the directions of maximal orthogonal variation inherent in the data. The chemometric models were constructed using data for the 400−1600 cm^{-1} region of the Raman spectra, where the full spectrum contribution was above 99.5%.

RESULTS AND DISCUSSION

In this work, MNP@Strep biosensors were used as SERS platforms for the determination of two bacterial strains, *Staphylococcus aureus* and *Streptococcus pyogenes*, in knee joint fluid samples. The presence of covalently bound streptavidin on the surface of these magnetic biosensors allows their selectivity to be tuned by simple functionalization using biotinylated antibodies. Two antibodies were employed in this work: an antibody to protein A[33] was used to achieve selectivity for *Staphylococcus aureus*, and an antibody to the group-A streptococci polysaccharide[34] was used to achieve selectivity for *Streptococcus pyogenes*.

The surface composition of the as-synthesized biosensors was monitored by measuring their ζ potential after each modification step, i.e., after the activation of functional groups and bond-forming steps. ζ potentials measured after each surface modification are shown in Figure 1A. The measured ζ potential of the pristine carboxy-functionalized magnetic nanoparticles (MNP) corresponded to a charge of −22.3 mV. This relatively high negative surface charge is attributed to the acidity of the free carboxyl groups. These pristine MNP were also characterized by XRD with Co Kα radiation (Figure 1B). The only crystalline phase can be identified from the diffraction pattern: cubic slightly nonstoichiometric maghemite phase (γ-Fe_2O_3; cell parameter a = 0.8360 nm) with partially ordered vacancies (space group *P*4332). The crystallite size derived from Rietveld refinement analysis of the X-ray powder diffraction pattern is 13 nm. A TEM image of the starting MNP is shown in the inset of Figure 1B. These pristine magnetic nanoparticles were selected because of the presence of free carboxylic groups, which increased the long-term stability of the as-prepared biosensor by enhancing its dispersibility in aqueous environments. The subsequent activation of the surface carboxyl groups using an aqueous mixture of EDC and NHS was accompanied by a substantial increase in the material's zeta potential (to 8.76 mV), reflecting the successful conversion of the carboxyl groups on the MNP surface into reactive *N*-hydroxysulfosuccinimide esters. In the next step, streptavidin was immobilized on the surface of the magnetic nanoparticles via the reaction of its terminal amino group ($-NH_2$) with the activated carboxyl groups on the MNP surfaces. This increased the particles' zeta potential further, to 9.63 mV. Streptavidin functionalization was required to enable binding of the biotinylated antibodies, which occurred in the next step of the synthesis. The formation of a noncovalent bond between streptavidin and the biotinylated antibodies and the final blockage of residual activated carboxylic groups caused a small further increase in the surface charge, to 10 mV for the nanoparticles bearing the anti-APS antibody and 10.4 mV for those bearing the anti-IgA antibody. The morphology of the final biosensors was characterized by HRTEM, STEM-EDS, and STEM-HAADF imaging. Figure 1C shows a HRTEM image of MNP@Strep/Ag which reveals that the overall diameter of the as-synthesized Fe_2O_3 (maghemite) and Ag nanoparticles is in the range of 10−20 nm. Moreover, the STEM-EDS chemical mapping (Figure 1D) of the biosensors clearly indicates the presence of both Fe and Ag species. As shown in Figure 1E, silver nanoparticles are distributed on the surface of maghemite; this is further confirmed by the presence of particles with different contrast in the STEM-HAADF image.

To better understand the surface composition of the functionalized MNP@Strep biosensors, they were analyzed by infrared spectroscopy (IR). IR absorption spectra collected after streptavidin decoration and the attachment of biotinylated antibodies to the MNP are shown in Figure 2. The IR spectrum of the pristine MNP features the characteristic vibrational modes (e.g., 1726 cm^{-1}), which are due to carbonyl stretching,

DOI: 10.1021/acs.analchem.7b00759
Anal. Chem. 2017, 89, 6598−6607

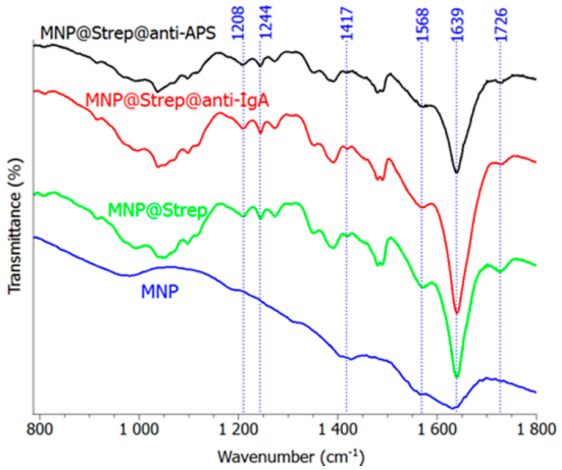

Figure 2. IR spectra of pure MNP, modified MNP@Strep, and MNP@Strep functionalized with biotinylated antibody to protein A (labeled as MNP@Strep@anti-IgA) and with biotinylated antibody to group-A streptococci polysaccharide (labeled as MNP@Strep@anti-APS).

yet contains no protein vibrations that will be featured in IR spectra after subsequent modification steps of MNP. The IR spectrum of the nanoparticles after streptavidin immobilization (i.e., MNP@Strep) features two amide bands: band I at 1639 cm^{-1}, corresponding to a β-pleated sheet structure (C═O stretch), and band II at 1568 cm^{-1} (N−H bend with C−N stretch). These bands can be attributed to the amide functionalities of streptavidin's peptide groups and thus indicate the presence of the streptavidin on MNP.[21,35,36] A peak corresponding to the carboxylate vibrational mode at 1417 cm^{-1} (COO^- stretch) is also identifiable in the spectrum of MNP@Strep.[37] The presence of streptavidin on MNP was confirmed by the presence of bands of weak-to-medium intensity at 1208 and 1247 cm^{-1}, both of which were assigned to amide III vibrations.[21] As can be seen in Figure 2, there are no new vibrational modes between the IR spectra of the biosensors prepared with antibodies (labeled MNP@Strep@anti-IgA and MNP@Strep@anti-APS, respectively) and that of the streptavidin-coated nanoparticles except for a slight red shift of a weak spectral band located at 1726 cm^{-1} arising from carbonyl stretching, which may be attributed to the formation of a lock-and-key type interaction between the nanoparticle-bound streptavidin and the biotin tag on the antibodies.[38]

The biosensors were initially tested against model samples consisting of a *Staphylococcus aureus* (henceforth referred to as STAU) bacterial lysate. The resulting SERS spectra are shown in the Figure 3, together with spectra for a pure MNP sample, a modified sample consisting of the MNP@Strep nanoparticles in aqueous solution, and a blank sample consisting of the MNP@Strep@anti-IgA biosensor in aqueous solution with no added lysate. The spectrum of the pure MNP sample features none of the strong vibrational modes observed in the spectra of the modified MNP@Strep, blank, or model samples. Conversely, the SERS spectra of the MNP@Strep and MNP@Strep@anti-IgA (blank) samples are very similar. Both feature spectral bands characteristic of proteins, including the amide II and III bands. The spectral bands located at 1558 and 1450 cm^{-1} were assigned to the amide II mode, which arises mostly from NH bending, and to (δ-CH_2) scissoring vibrations modes, respectively.[39] The amide III mode, which is associated with

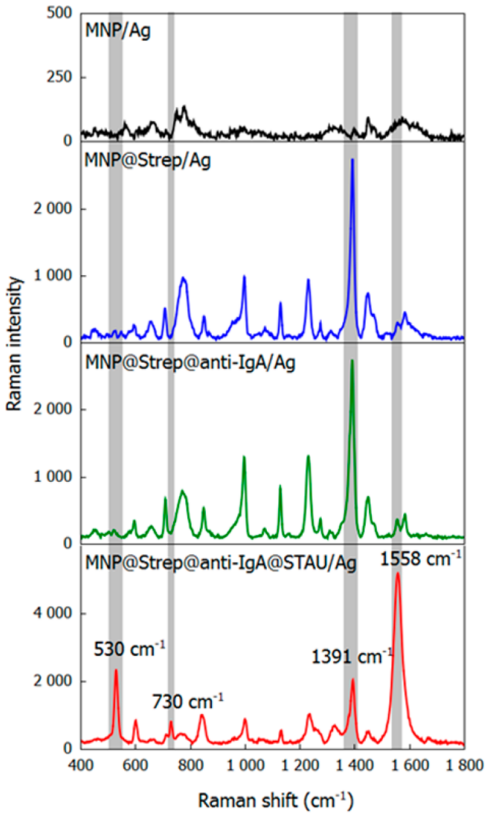

Figure 3. SERS spectra of the pure MNP/Ag, modified MNP@Strep/Ag, MNP@Strep modified with biotinylated antibody to protein A (labeled as MNP@Strep@anti-IgA/Ag), and bacterial lysate of *Staphylococcus aureus* CCM 3953 (labeled as MNP@Strep@anti-IgA@STAU/Ag).

α-helices and is primarily due to ν(CN) stretching and NH in-plane bending vibrations of the peptide bond, is represented by the bands at 1391 and 1231 cm^{-1}.[40,41] Functionalization of the MNP@Strep biosensor using either of the biotinylated antibodies increased the intensity of the amide III band at 1231 cm^{-1}, which is consistent with an increase in the prevalence of α-helical conformations and thus successful noncovalent binding between streptavidin and the biotinylated antibody. A representative SERS spectrum of an antibody-decorated MNP sample is shown in Figure 3 with the label MNP@Strep@anti-IgA/Ag. Finally, treatment of anti-IgA-decorated MNP with the STAU lysate yielded a sample referred to as MNP@Strep@anti-IgA@STAU/Ag. SERS analysis of this material revealed pronounced changes in the relative intensities of the bands at 1391 and 1558 cm^{-1} when compared to the modified MNP@Strep and blank sample. The ratio of intensities (I_{1391}/I_{1558}, henceforth referred to as the protein band ratio, PBR) changed from 13.31 in the blank sample to 0.36 with the difference statistically significant (p value = 1.035×10^{-5}), which is consistent with a successful interaction between a functionalized composite and protein A, which is a characteristic protein of STAU.

The SERS spectrum of the lysate-treated MNP (MNP@Strep@anti-IgA@STAU/Ag) also features new well-resolved bands at 530, 602, and 730 cm^{-1} that were not present in the spectra of the modified MNP@Strep and blank samples. The strong Raman mode at 530 cm^{-1} could be assigned to S−S

DOI: 10.1021/acs.analchem.7b00759
Anal. Chem. 2017, 89, 6598−6607

stretches of the L-cysteine-rich polypeptide toxin produced by STAU.[21,42,43] The SERS spectrum also features a significant band at 602 cm^{-1} which might be due to a vibrational mode of phenylalanine, which is also produced by STAU.[44,45] Another important peak at 730 cm^{-1} may correspond to a glycosidic ring mode of the bacterium's peptidoglycan cell wall building blocks, poly-*N*-acetylglucosamine (NAG) and *N*-acetylmuramic acid (NAM).[46−49] On the other hand, Ankamwar et al.[50] attributed the 730 cm^{-1} peak to the purine ring breathing mode and the C−N stretching mode of the adenine part of the lipid layer components of the bacterial cell wall.

Our method offers a high degree of versatility because the selectivity of the nanoparticle biosensors can be altered simply by changing the antibody that is added in the final step of the synthesis. This was demonstrated by analyzing a lysate of *Streptococcus pyogenes* (henceforth, STPY), which is frequently associated with PJI. Figure 4 compares the SERS spectra of the

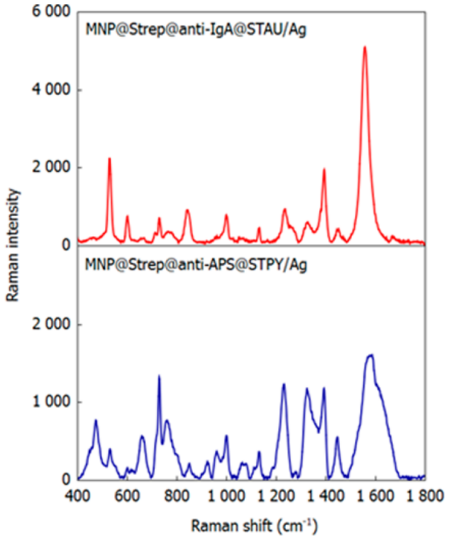

Figure 4. SERS spectra of model samples of bacterial lysates of *Staphylococcus aureus* CCM 3953 (labeled as MNP@Strep@anti-IgA@STAU/Ag) and *Streptococcus pyogenes* (labeled as MNP@Strep@anti-APS@STPY/Ag).

STPY biosensor after treatment with the corresponding bacterial lysate (labeled MNP@Strep@anti-APS@STPY/Ag) to that of the previously discussed STAU sensor (MNP@Strep@anti-IgA@STAU/Ag) after treatment with the STAU lysate. As might be expected given that both of these bacteria are Gram-positive facultative anaerobic species, the two spectra are quite similar, although there are some noteworthy differences. The PBR for the peaks at 1391 and 1558 cm^{-1} in the SERS spectrum of the MNP@Strep@anti-APS nanoparticles changed substantially upon treatment with the STPY lysate, from 19.71 falling to 0.48 with a statistically significant difference (p value = 2.522×10^{-6}). This is clearly indicative of an interaction between the lysate and the functionalized biosensor. The largest differences between the SERS spectra of the lysate-treated STAU MNP (MNP@Strep@anti-IgA@STAU/Ag) and STPY MNP (MNP@Strep@anti-APS@STPY/Ag) relate to the bands at 475, 924, and 962 cm^{-1}. All of these could be due to vibrations of D-mannose, which is the main sugar component in the matrix of STPY.[51] The MNP@Strep@anti-APS@STPY/Ag spectrum also features a striking and intense peak at 660 cm^{-1}, corresponding to the C−S stretch of the methionine-containing STPY toxin.[47,52] Moreover, the important band at 530 cm^{-1} (corresponding to cysteine S−S stretches) is less intense in the spectrum of the STPY MNP than in the STAU MNP, which could be used to further differentiate these bacterial species. Moreover, the PBR values for the STAU and STPY lysates were statistically significantly different (0.36 vs 0.48, p value = 0.021). This direct comparison of the SERS spectra of two different bacterial lysates with tailored MA-SERS biosensors clearly shows that our new MA-SERS assay can distinguish between *Staphylococcus aureus* and *Streptococcus pyogenes*.

Because knee joint fluid samples are typically information-rich and contain a wide range of different molecules, interpreting the spectra of bacterial pathogens in a knee joint fluid matrix is usually very difficult and often requires the use of complex data analysis techniques. Despite this, SERS microscopy is a promising clinical analytical technique for detecting pathogenic bacteria. Because of the samples' biochemical complexity, they are likely to contain a diverse mix of SERS-active vibrational modes arising from pathogen cell envelope components and native components of the matrix. While the system presented here relies on a priori knowledge of the biochemistry of the pathogen of interest and the host, the technique offers some flexibility in that the SERS spectrum of a lysate-treated biosensor is likely to contain multiple peaks that could be used for diagnosis and detection. Although this flexibility is attractive, an ideal system would not permit any band to be assigned tentatively. In practice, tentative assignment is likely to be unavoidable for the time being because of the lack of SERS spectral databases that could be used to identify peaks due to bacterial components; this makes the analytical process more time-consuming than it would be otherwise. Although database resources for basic Raman spectra of biological materials are gradually becoming more accessible and comprehensive, it is not certain that the vibrational bands seen in Raman spectra will also appear in the SERS spectra of the corresponding bacteria.

We tested the stability of our fabricated SERS biosensor by storing it for various periods of time under atmospheric conditions and then repeating the SERS analysis. The SERS signal stability was evaluated using a batch of the MNP@Strep@anti-IgA that was prepared (on day 0) and stored in a refrigerator for a period of 60 days. Aliquots of this stored material were removed and treated with an STAU lysate on days 1, 15, 30, 45, and 60, and the SERS spectra of the resulting MNP@Strep@anti-IgA@STAU nanoparticles were acquired. Figure S1A shows these spectra. All the spectra contain the same bands as those for the fresh material, although their absolute intensities decrease appreciably over time. However, the calculated PBR values are rather stable, with an average value of 0.36 and a relative standard deviation of less than 5% between PBR values. Consequently, we have plotted additional line charts of the main peak intensity at 1558 cm^{-1}/PBR value as y axis and time as x axis. Both values were monitored for a 2 month period as can be seen in Figure S1B,C. The SERS biosensor thus appears to be quite stable when stored under ambient atmospheric conditions even after two months.

To further evaluate the viability of the proposed cultivation-free approach for detecting and identifying STAU and STPY in a real matrix, samples of a sterile knee joint fluid spiked with live bacterial cells were examined. The Raman spectra obtained in these experiments are shown in Figure 5. The signals in both

DOI: 10.1021/acs.analchem.7b00759
Anal. Chem. 2017, 89, 6598−6607

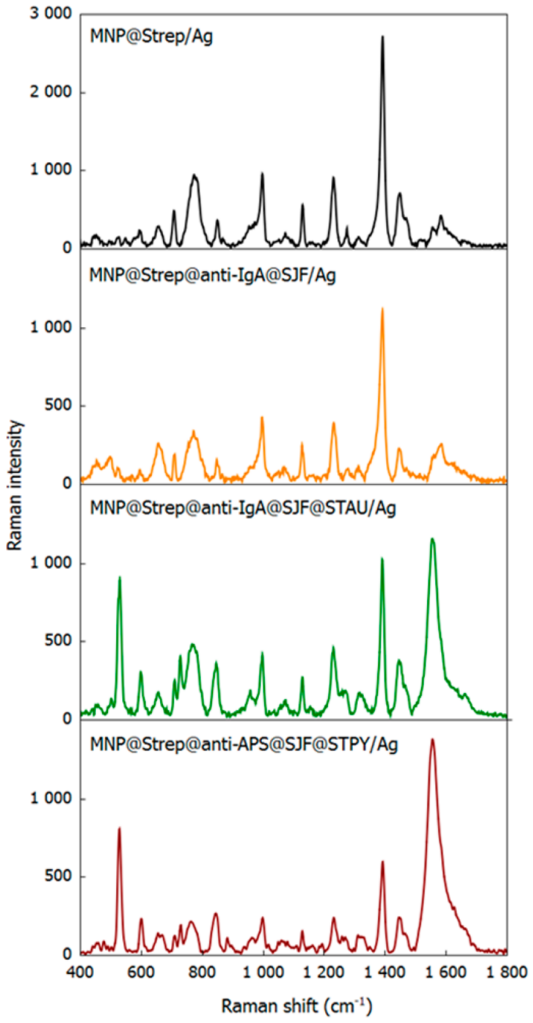

Figure 5. SERS spectra of the modified MNP@Strep/Ag nanoparticles, sterile joint fluid (labeled as MNP@Strep@anti-IgA@SJF/Ag), joint fluid with *Staphylococcus aureus* CCM 3953 (labeled as MNP@Strep@anti-IgA@SJF@STAU/Ag), and joint fluid with *Streptococcus pyogenes* (labeled as MNP@Strep@anti-APS@SJF@STPY/Ag).

spectra agree well with those for the corresponding model samples; while the peaks' absolute intensities changed because of concentration effects, both the model samples and the real matrix samples yielded the same trend in the PBR, which decreased from 13.31 to 0.80 (p value = 1.010×10^{-5}) in the case of *S. aureus* and from 19.71 to 0.65 (p value = 2.817×10^{-5}) for STPY. We then investigated the influence of concentration effects and nonspecific interactions on bacterial recognition. The influence of nonspecific interactions was studied using the MNP@Strep@anti-IgA biosensor with real-matrix samples of knee joint fluid from four patients (labeled A–D) spiked with live STAU bacteria prepared at different times. Figure S2 shows the spectral data for these measurements. All the spectra contain the previously identified bands, although their absolute abundances vary appreciably. However, the calculated PBR values are stable (averaging around 0.80), and the relative standard deviation of the PBR between batches is only 10%. The spectra shown in Figures 5 and S2 contain minor bands originating from nonspecific interactions of the remaining free surface of the silver nanoparticles with small organic molecules and salts. These interactions have no appreciable effect on the calculated PBR values, as demonstrated by the low RSD and steady PBR.

The performance of the new method was then tested using real-matrix samples from the same four patients (A, B, C, and D). Briefly, ten technical replicate analyses were performed for each sample, and the resulting spectral data were subjected to statistical analysis to further evaluate the method's ability to distinguish between the two studied bacterial strains. The chosen analytical technique was discriminant analysis (DA), which is used to determine the classes of known materials that have similar spectra by calculating the distance between each class center in Mahalanobis distance units. When working with data derived from multiple sources, DA can be used to map the observations into a coordinate space that maximizes source separation. As applied in this work, DA facilitates the detection of spectral similarities and differences and can also be used to screen incoming materials to determine how they should be classified. If the SERS spectra of the biological samples have obvious, repeatable similarities, data points from each species should group together within the transformed space, indicating successful discrimination of a species-specific SERS signature. After the material was successfully classified by DA, the Statistical Spectra software tool supplied with the spectrometer was used to compute a mean spectrum for each class. Due to the rich informational content of the spectra in the region between 400 and 1600 cm^{-1}, the DA was performed based on this region. The study was performed on a set of 30 samples from the four patients, including replicate spectra of the sterile joint fluid and sterile joint fluid spiked with live bacterial cells. The results obtained are summarized in Figure 7A–D, which

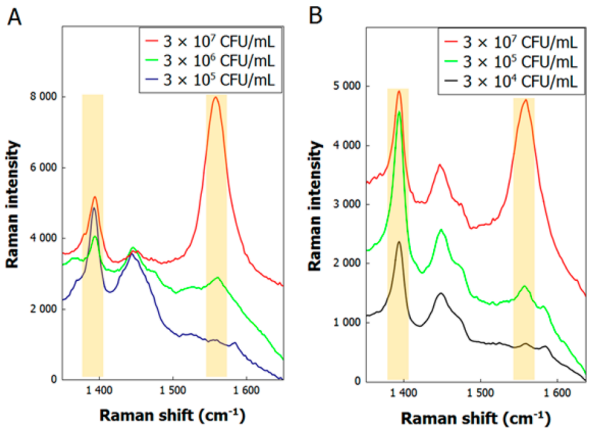

Figure 6. Close up of the 1391 and 1558 cm^{-1} peaks of real matrix sample with different concentrations of (A) *S. aureus* and (B) *S. pyogenes*. The spectra were shifted by a hundred units of Raman intensity in order to increase the transparency.

show the results of a DA and the associated mean SERS spectra (Figure S3A–D). The classes identified by the DA are clearly visible and distinct, with the sterile joint fluid cluster shown in red, the sterile joint fluid with added *Staphylococcus aureus* CCM 3953 cluster shown in blue, and the sterile joint fluid with added *Streptococcus pyogenes* cluster shown in green. DA data based on the SERS spectra obtained for each individual patient indicate that the method can differentiate between pathogenic samples and sterile sample (SJF, red cluster) as well as between

DOI: 10.1021/acs.analchem.7b00759
Anal. Chem. 2017, 89, 6598–6607

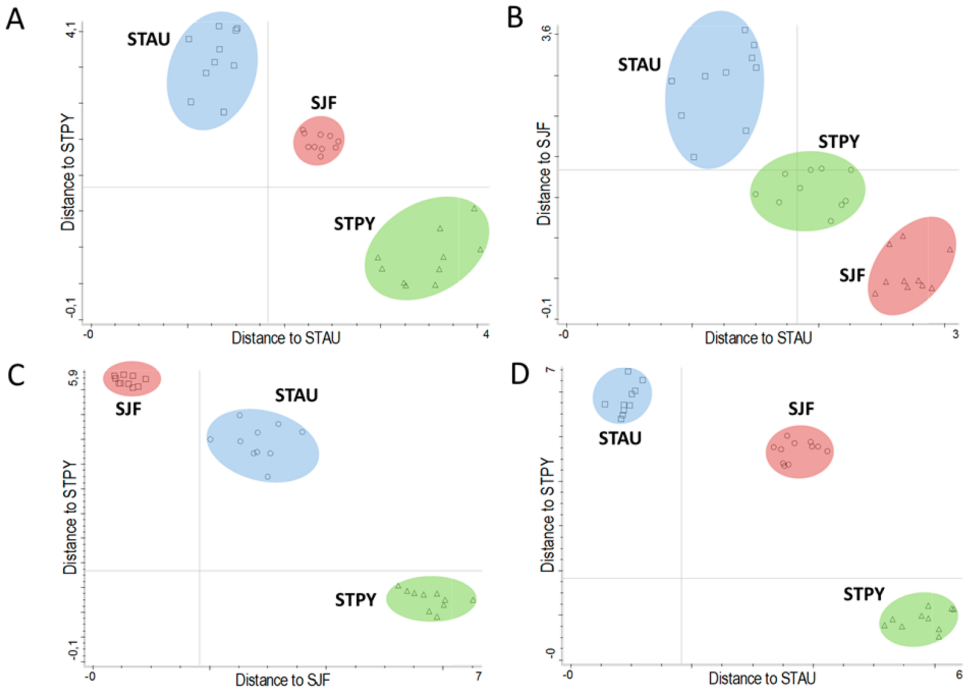

Figure 7. Discriminant analysis of knee joint fluid samples from four real patients (A, B, C, and D). Clusters defined training sets: sterile joint fluid (SJF; red), joint fluid with *Staphylococcus aureus* CCM 3953 (STAU; blue), and joint fluid with *Streptococcus pyogenes* (STPY; green).

the *S. aureus* (blue cluster) and *S. pyogenes* (green cluster) samples because the experimental data points are centered in clusters that are separated by appreciable distances. The DA accurately classified all the tested samples as belonging to one of the sterile fluid, *S. aureus*, or *S. pyogenes* classes. For all patients (Figure 7A–D), the signals corresponding to *S. aureus* and *S. pyogenes* are located in two distinct clusters and can be clearly distinguished from the sterile knee joint fluid. The calculated average intracluster distances for patients A, B, C, and D are 0.37, 0.57, 0.59, and 0.94, respectively, for sterile joint fluid; 1.31, 1.24, 0.80, and 0.92, respectively, for sterile joint fluid with added *S. aureus* CCM 3953; 0.84, 0.82, 1.27, and 0.91, respectively, for sterile joint fluid with added *S. pyogenes*. The average intercluster distances between the sterile joint fluid cluster and the *Staphylococcus aureus* CCM 3953 or *Streptococcus pyogenes* clusters are 2.37, 2.90, 2.83, and 3.72 and 2.46, 1.60, 5.69, and 4.69, respectively. The average intercluster distance between sterile joint fluid with added *Staphylococcus aureus* CCM 3953 and sterile joint fluid with added *Streptococcus pyogenes* is 3.62, 1.95, 4.45, and 5.83. These results show that MA-SERS combined with DA can reliably be used to differentiate the three analytes, a conclusion that was subsequently validated using standard cultivation methods with the same set of samples.

The sensitivity of the method was tested using the same MA-SERS detection protocol described in the Experimental Section. We have decreased the concentration of both bacteria down to a limit, where a statistically significant change in PBR value can still be observed between the blank and bacteria containing real samples. On the basis of the results, this approach gives a positive response for the common concentration of bacteria present (3×10^8 CFU/mL) in real samples accompanying prosthetic joint infection. Moreover, the purposed approach showed that the limit of detection of the MA-SERS method is two (STAU) or three (STPY) orders below a common value accompanying bacterial joint infections, which can be seen in Figure 6.

Finally, the ability of the purposed MA-SERS biosensor to selectively trap a target pathogen in real-matrix samples was briefly tested using the 1:1 mixture of biosensors (MNP@Strep@anti-IgA and MNP@Strep@anti-APS) treated with pure *S. aureus* or *S. pyogenes* as well as with the mixture of bacterial lysates in a 90:10 ratio for both bacteria. The mixed biosensors were treated with the above-mentioned bacterial samples with the same sampling protocol described in the Experimental Section. When differentiating between the sets with pure *S. aureus* or *S. pyogenes* against their respective bacterial mixtures, two different classes observed in DA were obtained (see Figures S4 and S5, respectively). The calculated average intracluster distances for STAU samples sets 90:10 and 100:0 are 1.11 and 0.68, respectively. On the other hand, these clusters are completely separated and the distance between the classes is 2.45. Then, the calculated average intracluster distances for STPY samples sets 90:10 and 100:0 are 1.06 and 0.79, respectively. On the other hand, these clusters are completely separated and the distance between the classes is 1.97. It has been estimated that the assay is selective for both pathogens despite the fact that one is present in a very small amount compared to the other one.

CONCLUSION

Aspiration of the knee joint is required before reoperation due to PJI and before the second stage of the two-stage surgery. Additionally, many orthopedic surgeons perform this simple examination routinely before any revision total joint arthroplasty. Joint fluid samples are regularly analyzed for the presence of cells and molecules associated with antibacterial host responses and for causative agents of PJI. However, cultures grown from joint fluid samples often yield false negative results even in cases with evident PJI. In addition, the

DOI: 10.1021/acs.analchem.7b00759
Anal. Chem. 2017, 89, 6598–6607

identification and characterization of bacteria using culture methods is time-consuming, laborious, and expensive. Our work demonstrates that characteristic proteins of pathogenic bacteria, protein A from *Staphylococcus aureus* and the group-A streptococci polysaccharide from *Streptococcus pyogenes*, can be detected in experimental settings and in clinical knee joint fluid samples using MA-SERS spectroscopy with antibody-functionalized magnetic nanoparticle biosensors. The analysis can be performed much more quickly than established methods for diagnosing PJI based on Koch's culturing protocols, colony counting, PCR, or PFGE and can be tailored to specific pathogens of interest by selecting an appropriate antibody when functionalizing the nanoparticles in the final step of their synthesis. As such, our new method could be clinically useful for rapidly diagnosing cases of PJI and identifying appropriate treatments. Additionally, the results presented herein clearly demonstrate the power of functionalized magnetic nanoparticles in biorecognition.

■ ASSOCIATED CONTENT

Supporting Information

The Supporting Information is available free of charge on the ACS Publications website at DOI: 10.1021/acs.analchem.7b00759.

SERS spectra of MNP@Strep@anti-IgA@STAU/Ag obtained with samples of different batches in a 2 month period after the preparation and SERS spectra obtained by analysis of real-matrix samples of knee joint fluid collected from four different patients spiked by live bacteria cells of STAU; mean SERS spectra for each class of discriminant analysis of knee joint fluid samples from four patients and graphical representation of the discriminant analysis of data obtained by evaluation of the mixture of biosensors treated with a mixture of bacterial lysates (PDF)

■ AUTHOR INFORMATION

Corresponding Authors

*E-mail: vaclav.ranc@upol.cz (V.R.).
*E-mail: radek.zboril@upol.cz (R.Z.).

ORCID

Radek Zbořil: 0000-0002-3147-2196

Author Contributions

The manuscript was written through contributions of all authors.

Notes

The authors declare no competing financial interest.

■ ACKNOWLEDGMENTS

The authors gratefully acknowledge support from the Ministry of Education, Youth and Sports of the Czech Republic (project LO1305), and Palacký University (Student Project IGA_PrF_2017_025). The authors also acknowledge the assistance provided by the Research Infrastructure NanoEnviCz, supported by the Ministry of Education, Youth and Sports of the Czech Republic under Project No. LM2015073. This work was further supported by the Ministry of Health of the Czech Republic (AZV VES 15-27726A) and Project IGA_LF_2017_009 of Palacký University. Mrs. Jana Stráská is thanked for TEM measurements, Mr. Josef Kašlík for XRD measurements and analysis, and Dr. Klára Čépe and Mr. Ondřej Tomanec for HRTEM measurements (all from the Regional Centre of Advanced Technologies and Materials, Faculty of Science, Palacký University in Olomouc, Czech Republic).

■ REFERENCES

(1) Voigt, J.; Mosier, M.; Darouiche, R. *Antimicrob. Agents Chemother.* **2015**, *59*, 6696−6707.
(2) Kamath, A. F.; Ong, K. L.; Lau, E.; Chan, V.; Vail, T. P.; Rubash, H. E.; Berry, D. J.; Bozic, K. J. *J. Arthroplast.* **2015**, *30*, 1492−1497.
(3) Corvec, S.; Portillo, M. E.; Pasticci, B. M.; Borens, O.; Trampuz, A. *Int. J. Artif. Organs* **2012**, *35*, 923−934.
(4) Zimmerli, W.; Trampuz, A.; Ochsner, P. E. *N. Engl. J. Med.* **2004**, *351*, 1645−1654.
(5) Trampuz, A.; Zimmerli, W. *Swiss Med. Wkly.* **2005**, *135*, 243−251.
(6) Portillo, M. E.; Salvadó, M.; Alier, A.; Martínez, S.; Sorli, L.; Horcajada, J. P.; Puig, L. *J. Infect.* **2014**, *69*, 35−41.
(7) The Workgroup Convened by the Musculoskeletal Infection Society. *J. Arthroplast.* **2011**, *26*, 1136−1138.
(8) Parvizi, J.; Zmistowski, B.; Berbari, E. F.; Bauer, T. W.; Springer, B. D.; Della Valle, C. J.; Garvin, K. L.; Mont, M. A.; Wongworawat, M. D.; Zalavras, C. G. *Clin. Orthop. Relat. Res.* **2011**, *469*, 2992−2994.
(9) Deirmengian, C.; Kardos, K.; Kilmartin, P.; Gulati, S.; Citrano, P.; Booth, R. E., Jr. *Clin. Orthop. Relat. Res.* **2015**, *473*, 2229−2235.
(10) Saeed, K.; Ahmad-Saeed, N. *Expert Rev. Mol. Diagn.* **2015**, *15*, 957−964.
(11) Lazcka, O.; Del Campo, F. J.; Muñoz, F. X. *Biosens. Bioelectron.* **2007**, *22*, 1205−1217.
(12) Berbari, E. F.; Marculescu, C.; Sia, I.; Lahr, B. D.; Hanssen, A. D.; Steckelberg, J. M.; Gullerud, R.; Osmon, D. R. *Clin. Infect. Dis.* **2007**, *45*, 1113−1119.
(13) Metso, L.; Mäki, M.; Tissari, P.; Remes, V.; Piiparinen, P.; Kirveskari, J.; Tarkka, E.; Anttila, V.-J.; Vaara, M.; Huotari, K. *Acta Orthop.* **2014**, *85*, 165−170.
(14) Qu, X.; Zhai, Z.; Li, H.; Li, H.; Liu, X.; Zhu, Z.; Wang, Y.; Liu, G.; Dai, K. *J. Clin. Microbiol.* **2013**, *51*, 2742−2746.
(15) Panousis, K.; Grigoris, P.; Butcher, I.; Rana, B.; Reilly, J. H.; Hamblen, D. L. *Acta Orthop.* **2005**, *76*, 341−346.
(16) Cazanave, C.; Greenwood-Quaintance, K. E.; Hanssen, A. D.; Karau, M. J.; Schmidt, S. M.; Gomez Urena, E. O.; Mandrekar, J. N.; Osmon, D. R.; Lough, L. E.; Pritt, B. S.; Steckelberg, J. M.; Patel, R. *J. Clin. Microbiol.* **2013**, *51*, 2280−2287.
(17) Hommelsheim, C. M.; Frantzeskakis, L.; Huang, M.; Ülker, B. *Sci. Rep.* **2015**, *4*, 5052.
(18) Weller, T. M. A. *J. Hosp. Infect.* **2000**, *44*, 160−172.
(19) Corvec, S.; Illiaquer, M.; Touchais, S.; Boutoille, D.; van der Mee-Marquet, N.; Quentin, R.; Reynaud, A.; Lepelletier, D.; Bémer, P. *J. Clin. Microbiol.* **2011**, *49*, 380−382.
(20) Kourbatova, E. V.; Halvosa, J. S.; King, M. D.; Ray, S. M.; White, N.; Blumberg, H. M. *Am. J. Infect. Control* **2005**, *33*, 385−391.
(21) Maquelin, K.; Kirschner, C.; Choo-Smith, L.-P.; van den Braak, N.; Endtz, H. P.; Naumann, D.; Puppels, G. J. *J. Microbiol. Methods* **2002**, *51*, 255−271.
(22) Prucek, R.; Ranc, V.; Kvítek, L.; Panáček, A.; Zbořil, R.; Kolář, M. *Analyst* **2012**, *137*, 2866−2870.
(23) Khan, S. A.; Singh, A. K.; Senapati, D.; Fan, Z.; Ray, P. C. *Chem. Commun.* **2011**, *47*, 9444−9446.
(24) Sivanesan, A.; Witkowska, E.; Adamkiewicz, W.; Dziewit, Ł.; Kamińska, A.; Waluk, J. *Analyst* **2014**, *139*, 1037−1043.
(25) Huang, P.-J.; Tay, L.-L.; Tanha, J.; Ryan, S.; Chau, L.-K. *Chem. - Eur. J.* **2009**, *15*, 9330−9334.
(26) Cho, I.-H.; Bhandari, P.; Patel, P.; Irudayaraj, J. *Biosens. Bioelectron.* **2015**, *64*, 171−176.
(27) Guven, B.; Basaran-Akgul, N.; Temur, E.; Tamer, U.; Boyacı, İ.H.B. *Analyst* **2011**, *136*, 740−748.
(28) Ranc, V.; Markova, Z.; Hajduch, M.; Prucek, R.; Kvitek, L.; Kaslik, J.; Safarova, K.; Zboril, R. *Anal. Chem.* **2014**, *86*, 2939−2946.

DOI: 10.1021/acs.analchem.7b00759
Anal. Chem. 2017, 89, 6598−6607

(29) Balzerova, A.; Fargasova, A.; Markova, Z.; Ranc, V.; Zboril, R. *Anal. Chem.* **2014**, *86*, 11107−11114.
(30) Gallo, J.; Panacek, A.; Prucek, R.; Kriegova, E.; Hradilova, S.; Hobza, M.; Holinka, M. *Materials* **2016**, *9*, 337.
(31) Habiba, K.; Bracho-Rincon, D. P.; Gonzalez-Feliciano, J. A.; Villalobos-Santos, J. C.; Makarov, V. I.; Ortiz, D.; Avalos, J. A.; Gonzalez, C. I.; Weiner, B. R.; Morell, G. *Appl. Mater. Today* **2015**, *1*, 80−87.
(32) Panáček, A.; Kvítek, L.; Prucek, R.; Kolář, M.; Večeřová, R.; Pizúrová, N.; Sharma, V. K.; Nevěčná, T.; Zbořil, R. *J. Phys. Chem. B* **2006**, *110*, 16248−16253.
(33) Kobayashi, S. D.; DeLeo, F. R. *mBio* **2013**, *4*, e00764-13.
(34) Poulsen, F. M.; Johansen, J. T.; Pedersen, J. A. *Carlsberg Res. Commun.* **1977**, *42*, 369−378.
(35) Pradier, C.-M.; Salmain, M.; Zheng, L.; Jaouen, G. *Surf. Sci.* **2002**, *502*−*503*, 193−202.
(36) Liu, Z.; Amiridis, M. D. *J. Phys. Chem. B* **2005**, *109*, 16866−16872.
(37) Barth, A. *Biochim. Biophys. Acta, Bioenerg.* **2007**, *1767*, 1073−1101.
(38) Haris, P. I. *Biochem. Soc. Trans.* **2010**, *38*, 940−946.
(39) Harz, M.; Rösch, P.; Peschke, K.-D.; Ronneberger, O.; Burkhardt, H.; Popp, J. *Analyst* **2005**, *130*, 1543−1550.
(40) Knauer, M.; Ivleva, N. P.; Niessner, R.; Haisch, C. *Anal. Sci.* **2010**, *26*, 761−766.
(41) Shao, J.-H.; Zou, Y.-F.; Xu, X.-L.; Wu, J.-Q.; Zhou, G.-H. *Food Res. Int.* **2011**, *44*, 2955−2961.
(42) Ton-That, H.; Mazmanian, S. K.; Alksne, L.; Schneewind, O. *J. Biol. Chem.* **2002**, *277*, 7447−7452.
(43) Chauhan, R. P.; Singh, G.; Singh, S.; Bag, N.; Patra, M.; Vadera, S. R.; Mishra, A. K.; Mathur, R. *Cancer Nanotechnol.* **2011**, *2*, 111−120.
(44) Puppels, G. J.; Garritsen, H. S.; Segers-Nolten, G. M.; de Mul, F. F.; Greve, J. *Biophys. J.* **1991**, *60*, 1046−1056.
(45) Halvorson, R. A.; Leng, W.; Vikesland, P. J. *Anal. Chem.* **2011**, *83*, 9273−9280.
(46) Jarvis, R. M.; Goodacre, R. *Anal. Chem.* **2004**, *76*, 40−47.
(47) Guicheteau, J.; Argue, L.; Emge, D.; Hyre, A.; Jacobson, M.; Christesen, S. *Appl. Spectrosc.* **2008**, *62*, 267−272.
(48) Liu, T.-T.; Lin, Y.-H.; Hung, C.-S.; Liu, T.-J.; Chen, Y.; Huang, Y.-C.; Tsai, T.-H.; Wang, H.-H.; Wang, D.-W.; Wang, J.-K.; Wang, Y.-L.; Lin, C.-H. *PLoS One* **2009**, *4*, e5470.
(49) Kropec, A.; Maira-Litran, T.; Jefferson, K. K.; Grout, M.; Cramton, S. E.; Götz, F.; Goldmann, D. A.; Pier, G. B. *Infect. Immun.* **2005**, *73*, 6868−6876.
(50) Ankamwar, B.; Sur, U. K.; Das, P. *Anal. Methods* **2016**, *8*, 2335−2340.
(51) Shafreen, R. M. B.; Srinivasan, S.; Manisankar, P.; Pandian, S. K. *J. Biosci. Bioeng.* **2011**, *112*, 345−350.
(52) Liu, M.; Prakash, C.; Nauta, A.; Siezen, R. J.; Francke, C. *J. Bacteriol.* **2012**, *194*, 3522−3533.

DOI: 10.1021/acs.analchem.7b00759
Anal. Chem. 2017, 89, 6598−6607

Analytica Chimica Acta 997 (2018) 44–51

Contents lists available at ScienceDirect

Analytica Chimica Acta

journal homepage: www.elsevier.com/locate/aca

Label-free determination of prostate specific membrane antigen in human whole blood at nanomolar levels by magnetically assisted surface enhanced Raman spectroscopy

Zuzana Chaloupková [a], Anna Balzerová [a], Jitka Bařinková [b], Zdenka Medříková [a], Pavel Šácha [d], Petr Beneš [c], Václav Ranc [a, *], Jan Konvalinka [b], Radek Zbořil [a]

[a] Regional Centre of Advanced Technologies and Materials, Department of Physical Chemistry, Faculty of Science, Palacky University in Olomouc, 17. Listopadu 12, CZ-77146 Olomouc, Czech Republic
[b] Department of Biochemistry, Faculty of Science, Charles University, Hlavova 2030/8, 128 40 Praha 2, Czech Republic
[c] Oncology Clinic, University Hospital in Olomouc, I. P. Pavlova 6, Olomouc, Czech Republic
[d] Institute of Organic Chemistry and Biochemistry, The Czech Academy of Sciences, Flemingovo n. 2, 16610, Prague 6, Czech Republic

HIGHLIGHTS

- A new method for a determination of prostate specific membrane antigen is proposed.
- The method utilizes magnetic; surface functionalized Fe_3O_4@Ag nanocomposite.
- A determination is based on magnetically assisted surface enhanced Raman spectroscopy.
- Method application potential is demonstrated by analysis of human whole blood.

GRAPHICAL ABSTRACT

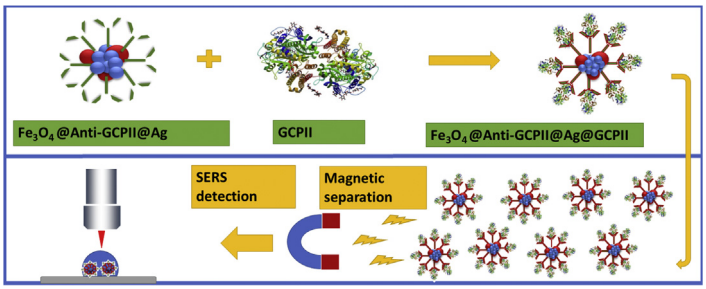

ARTICLE INFO

Article history:
Received 3 July 2017
Received in revised form
6 October 2017
Accepted 8 October 2017
Available online 17 October 2017

Keywords:
Raman spectroscopy
Nanocomposites
Prostate cancer
GCPII
MA-SERS

ABSTRACT

Prostate cancer is one of the most common cancers among men and can in its later stages cause serious medical problems. Due to the limited suitability of current diagnostic biochemical markers, new biomarkers for the detection of prostate cancer are highly sought after. An ideal biomarker should serve as a reliable prognostic marker, be applicable for early diagnosis, and be applicable for monitoring of therapeutic response. One potential candidate is glutamate carboxypeptidase II (GCPII), also known as prostate specific membrane antigen (PSMA), which has a promising role for direct imaging. GCPII is considerably over-expressed on cancerous prostatic epithelial cells; its analysis typically follows radiological or spectrophotometric principles. Its role as a biomarker present in blood has been recently investigated and potential correlation between a concentration of GCPII and prostate cancer has been proposed. The wider inclusion of GCPII detection in clinical praxis limits mainly the time and cost per analysis. Here, we present a novel analytical nanosensor applicable to quantification of GCPII in human whole blood consisted of Fe_3O_4@Ag magnetic nanocomposite surface-functionalized by an artificial antibody (low-molecular-weight GCPII synthetic inhibitor). The nanocomposite allows a simple magnetic isolation of GCPII using external magnetic force and its consecutive determination by magnetically assisted surface enhanced Raman spectroscopy (MA-SERS) with a limit of detection 6 pmol. L^{-1}. This

* Corresponding author.
E-mail address: vaclav.ranc@upol.cz (V. Ranc).

https://doi.org/10.1016/j.aca.2017.10.008

method enables a rapid determination of picomolar concentrations of GCPII in whole human blood of healthy individuals using a standard addition method without a complicated sample pre-treatment.

1. Introduction

Prostate cancer is among the most frequently diagnosed forms of cancer, and currently accounts for 12% of all cancer cases worldwide. The incidence rate in the global population has increased 155% since 1970, and nearly 500,000 new cases were diagnosed in 2012 [1,2]. The most common screening tests for early diagnosis of prostate cancer are based on determination of the blood level of prostate specific antigen (PSA) or a digital rectal exam (DRE) [3]. Elevated PSA levels indicate higher probability of prostate cancer; however, PSA elevations also can be caused by other health complications, including benign prostatic hyperplasia and nonspecific inflammation [4,5]. If PSA or DRE suggests prostate cancer, transrectal biopsy is typically used to confirm the diagnosis. Diagnostic information describing a tumor behavior can be alternatively obtained from a patient's genomic data, however, utilization of his procedure is still limited due a still required biopsy [6]. Therefore, new biomarkers and more reliable techniques for a prostate cancer diagnosis are being actively investigated. Prostate specific membrane antigen [PSMA, also known as folate hydrolase I and glutamate carboxypeptidase II (GCPII)], is one potential candidate. GCPII is a type II transmembrane zinc-metalloenzyme with glutamate carboxypeptidase activity [7]. It catalyzes the hydrolysis of N-acetylaspartylglutamate (NAAG) to glutamate and N-acetylaspartate (NAA) and is considerably over-expressed on prostate cancer cells [7,8]. Some studies have also indicated a correlation of GCPII expression with tumor stage and grade [9]. Reports also indicate its potential applicability in all stages of diagnostics and monitoring of disease treatment [10]. Clinical trials utilizing labeled antibody against GCPII for prostate cancer detection have shown promising results [11]; however, their usability is considerably limited by a long biological half-life [12]. Strategies to overcome this limitation include use of antibodies labeled with long-lived PET radionuclides, including ^{89}Zr and ^{64}Cu, and utilization of antiGCPII mini-bodies [13]. An alternative approach is utilization of small-molecule inhibitors that mimic the endogenous substrate NAAG. Development of inhibitors for visualization of GCPII led to introduction of various radiolabels, including ^{68}Ga, ^{123}I, ^{18}F, and ^{111}In, of which ^{68}Ga seems to offer the best results [14–20]. However, radiolabeled molecules were not very effective at detecting small metastatic deposits, leading researchers to design inhibitors with fluorescent labels. Inhibitors labeled with fluorescein dyes have been applied intraoperatively to identify brain tumors using photo-diagnosis (PDD) [21,22]. This approach was further improved using quantum dots [23] and advanced fluorescent labels, including indocyanine green (ICG) [24]. Detection of GCP-II as a potential biomarker in blood serum has been investigated e.g. by Rochon et al., where higher levels in prostate cancer patients were demonstrated, compared to healthy patients [25]. Similar results were obtained by Murphy *et.al*, where GPC-II shown a better prognostic value than PSA [26]. GCP-II levels in blood has been further evaluated by Beckett et al. [27], and Knedlik et al. [28], where a further potential has been proposed. Methods based on molecular spectroscopy are an interesting alternative to these more common label-based approaches. Surface-enhanced Raman spectroscopy (SERS) is considered a promising technique for analysis of molecular targets at ultra-low concentration levels. Since its introduction in 1979 by Fleischmann, the technique has undergone dramatic developments [29]. Development of novel substrates allowed detection of record-low concentrations of various targets, and introduction of magnetic nanocomposites allowed isolation of the chemical target before follow-up spectral analysis [30–33]. Here, we demonstrate the utilization of low-molecular-weight GCPII inhibitors in magnetically assisted (MA)-SERS. The suitability of this type of low-molecular-weight inhibitor in the analysis of GCPII has been demonstrated in previous analyses of human blood [28] using a radio-immunoanalytical approach (RIA) and of brain tissue [34], as well as in GCPII detection using DNA-linked inhibitor [35]. Sacha et al. described a more complex strategy employing synthetic polymer conjugates [36]. The MA-SERS approach described here utilizes Fe_3O_4@Ag magnetic nanocomposite functionalized with a low-molecular-weight inhibitor of GCPII. This novel approach enables magnetic isolation of GCPII and its follow up SERS detection in whole human blood in a very short time, with a limit of detections orders of magnitude lower than commonly used techniques.

2. Experimental section

2.1. Reagents and chemicals

Silver nitrate (p.a.), D-(+)-maltose monohydrate (p.a.), ammonia (25%) (p.a.), carboxymethyl cellulose sodium salt (low viscosity), iron(II) sulfate heptahydrate (>=99%), ammonium hydroxide solution, (28.0–30.0%), and N-(3-dimethylaminopropyl)-N′ ethylcarbodiimide hydrochloride (>=99.0%) were purchased from Sigma Aldrich (San Chose, U.S.A.) and used without further purification. Sodium hydroxide (p.a.) was purchased from Lach-Ner (Neratovice, Czech Republic).

2.2. Synthesis of low-molecular-weight GCPII inhibitor

All chemicals were purchased from Sigma-Aldrich unless stated otherwise. The final compound was purified using a preparative scale Jasco PU-986 HPLC (flow rate 10 mL/s), equipped with a YMC C18 Prep Column, 5 μm, 250 × 20 mm. Purity was tested on an analytical Jasco PU-1580 HPLC (flow rate 1 mL/s), equipped with a Watrex C18 Analytical Column, 5 μm, 250 × 5 mm. The final compound was of at least 99% purity. The structure was confirmed by HRMS at LTQ Orbitrap XL (Thermo Fisher Scientific).

Compound **1** was prepared as previously described [37]. Compound **2** was synthesized as shown in Scheme 1.

Compound **2**: 1-amino-39,47-dioxo-3,6,9,12,15,18,21,24,27,30,33,36-dodecaoxa-40,46,48-triazahenpentacontane-45,49,51-tricarboxylic acid. 511 mg (0.68 mmol, 1.1 eq) Z-PEG_{12}-COOH (IRIS Biotech) was dissolved in 1.5 mL DMF, and 297 mg (0.775 mmol, 1.25 eq) TBTU along with 150 μL DIEA (0.87 mmol, 1.4 eq) were added. The reaction mixture was left stirring for 30 min, and 307 mg (0.62 mmol, 1.0 eq) compound **1** along with 118 μL DIEA (0.68 mmol, 1.1 eq) dissolved in 1.5 mL of DMF, were added into the reaction mixture in one portion. The reaction was left overnight, and the mixture was rotary evaporated to dryness. The crude product was dissolved in MeOH, and the Cbz protective group was removed by hydrogenation (1.1 atm) with $Pd(OH)_2$ as catalyst (the

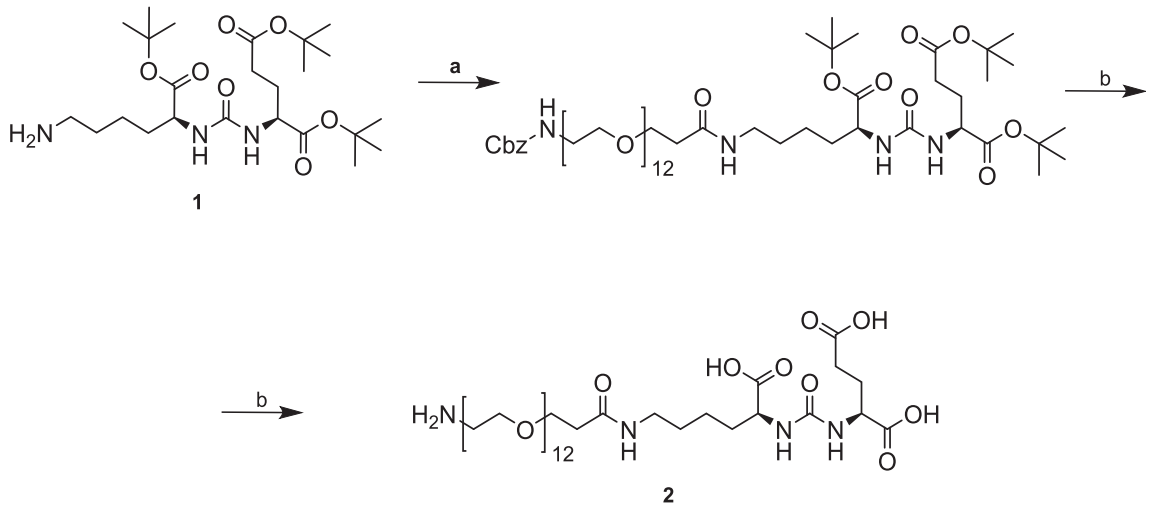

Scheme 1. Synthesis of Anti-GCPII (labeled as compound **2)**
a) Z-PEG12-COOH, TBTU, DIEA, DMF; b) 1) H_2, $Pd(OH)_2$, MeOH; 2) TFA.

course of the reaction was monitored with TLC; it completed in 3 h). The product was filtered and solvent removed on a rotary evaporator. To one-third of this product, 1 mL TFA was added and the reaction mixture was alternately sonicated and stirred for 15 min. TFA was removed by flow of nitrogen, and the product was purified using preparative scale HPLC (gradient 2–30% ACN in 60 min, ^tR = 38.1 min). 113 mg of product was obtained (isolated yield = 60%). Analytical HPLC (gradient 2–100% ACN in 30 min, ^tR = 14.8 min). HRMS (ESI-): calculated for $C_{39}H_{74}N_4O_{20}$ $[M]^-$ 917.48,236. Found 917.48,138. A stock solution of compound **2** was prepared by dissolving 40 μg of the inhibitor in 1 mL deionized water.

2.3. Preparation of a standard solution of GCPII

GCPII protein was prepared as previously described [38]. Briefly, the extracellular portion of GCPII (amino acids 44–750 with an AviTag at the N-terminus) was produced in insect S2 cells; purified on Streptavidin mutein matrix; dialyzed against 20 mM MOPS, 20 mM NaCl, pH 7.4; aliquoted; and stored at −80 °C. The purity was estimated to be >95% using sodium dodecyl sulfate - polyacrylamide gel electrophoresis (SDS-PAGE). The concentration of purified protein was 0.24 mg/mL, as determined by amino acid analysis after hydrolysis.

A solution containing 10 ng/mL of the isolated protein was prepared by diluting the stock solution with phosphate buffer (pH = 7.2). The sample was divided into 10 aliquots, which were kept at −20 °C. Aliquots were diluted to the concentration levels described in the Results section immediately before use.

2.4. Preparation of samples of whole human blood

Five healthy volunteers in ranging in age from 50 to 71 years (5 males, 0 females) agreed to participate in this study. Blood specimens were collected to 2 mL Eppendorf tubes with citrate as anticoagulating agent. Samples were kept at −80 °C and analyzed within 24 h. Blood samples were prepared by dilution 200 μL whole blood with 800 μL water (total volume of blood samples was 1 mL). No additional sample pre-treatment was performed. This step is necessary to reduce a total sample density and viscosity to further increase efficiency of consecutive magnetic isolation of GCPII from the sample.

2.5. Preparation of silver nanoparticles

Silver nanoparticles were prepared by a reduction of silver ammonia complex cation $[Ag(NH_3)_2]^+$ with D-maltose according to protocol previously described by Panacek et al. [39]. Briefly, silver nitrate and the maltose were dissolved in distilled water to initial concentrations of 1 mmol and 10 mmol, respectively. The concentration of ammonia was 5 mmol. After the silver, sugar, and ammonia had been added, the reaction system's pH was adjusted to 11.5 ± 0.1 by adding sodium hydroxide, initiating the reduction process. The reaction was considered complete after four minutes, yielding a nearly monodispersed suspension of maltose-reduced silver nanoparticles with an average particle size of about 28 nm.

2.6. Synthesis of Fe_3O_4@Anti-GCPII@Ag nanocomposite

First, magnetite nanoparticles stabilized using carboxymethyl cellulose ($cmcFe_3O_4$) were prepared according to the protocol described by Bakandritsos et al. [40]. Briefly, CMC and $FeSO_4 \cdot 7H_2O$ form a complex in aqueous solution. When NH_4OH (28%) is added to the mixture and the suspension is heated to 50 °C, a magnetic colloid form. The sample was centrifuged, and the supernatant containing residual chemicals from the reaction was removed and replaced with water, and the sample was sonicated. Subsequent functionalization of the nanomaterial is schematically described in Fig. 1. A 75-μL aliquot of carboxymethyl $cmcFe_3O_4$ (containing 250 μg of nanomaterial) was activated by 5 μL of EDC (activation of carboxyl groups). After 15 min, 10 μg of compound **2** was added, and the total volume was adjusted to 250 μL. Immobilization of the inhibitor was performed overnight. The cMNPs loaded with compound **2** was washed using centrifugation (20,000 rpm) to remove free inhibitor. Finally, 10 μL of silver nanoparticles was added to the mixture to add silver onto the surface of Fe_3O_4@Anti-GCPII nanoparticles, and nanoparticles were stirred 10–15 min at room temperature.

2.7. Preparation of samples containing GCPII

Analysis of GCPII using Fe_3O_4@Anti-GCPII@Ag nanoparticles was performed according to the following protocol: first, 10 μL of Fe_3O_4@Anti-GCPII@Ag nanocomposite was mixed with 10 μL of a standard solution of GCPII (c = 10 ng/mL), and the mixture was left

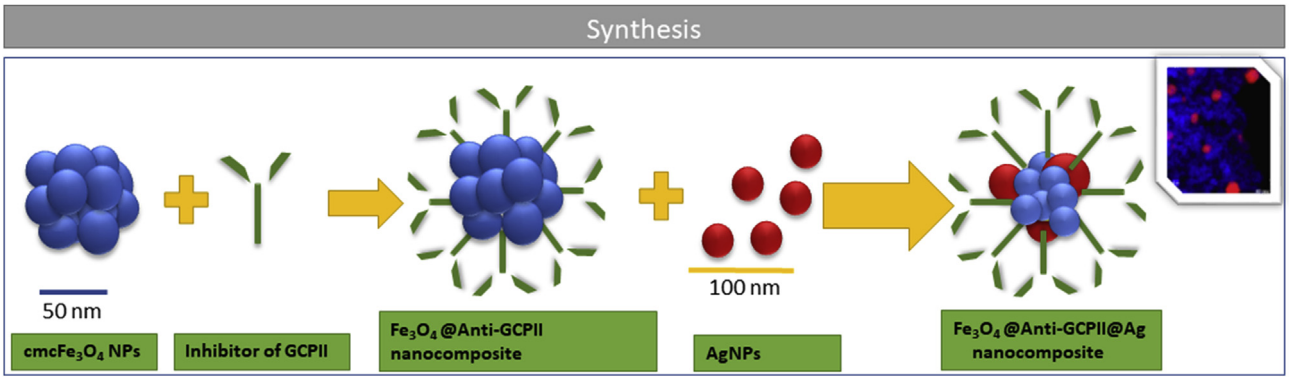

Fig. 1. General scheme describing the preparation and follow up functionalization of the nanomaterial.

for 30 min at room temperature. The dispersion was carefully mixed prior to use. Product was magnetically separated, washed three times with deionized water, and analyzed using our MA-SERS approach. The droplet containing sample and sensor was deposited on a glass platform, sensor was magnetically shifted closer to the droplet edge and measured immediately. Spectra were collected on nine representative spots and averaged.

2.8. Apparatus

The ζ potentials of the starting material and final products were measured using a Zetasizer NanoZS (Malvern, UK). Raman spectra were measured on a DXR Raman spectroscope (Thermo Scientific, U.S.A) equipped with a red excitation laser operating at 633 nm. Stokes Raman spectra were collected in the 400-1800 cm^{-1} range with a spectral resolution of 1.0 cm^{-1}. The Raman spectrometer was operated with the following experimental parameters: exposure time 32 s, laser power on sample 8 mW, 32 microscans were averaged to obtain one experimental point. Spectral background was corrected using subtraction of polynomic functions (n = 3) to remove interference caused by fluorescence. The measured spectra are presented in terms of their Raman scattered photon count. Elemental mapping was conducted using a high-resolution transmission electron microscope (HR-TEM TITAN 60–300 kV) operating at 80 kV. Protein quantification was performed using the TQ-Analyst software package (Omnic version 8, Thermo Scientific, USA).

2.9. Analysis of samples

Our analytical method utilizes Fe_3O_4@Ag magnetic nanocomposite functionalized with a low-molecular-weight GCPII inhibitor (compound **2**). The final (Fe_3O_4@Anti-GCPII@Ag) nanocomposite serves as a biosensor with dual modality: magnetic separation of GCPII from a complex biological sample and follow-up detection using surface-enhanced Raman spectroscopy. Prepared samples containing Fe_3O_4@Anti-GCPII@Ag@GCPII were magnetically isolated and diluted with deionized water (V = 0.02 mL). The resulting drop was deposited on a glass substrate and analyzed by Raman spectroscopy at 9 representative spots. Resulting spectral data were averaged and utilized in the follow-up steps.

2.10. Analysis of real samples

Real blood samples were analyzed analogically to a protocol described in the Experimental section, paragraph 2.9, and concentration of GCPII was determined using a following procedure. First, approximate concentration of the GCPII in the sample was calculated from an external calibration constructed using standard solutions in a concertation range 5–200 ng mL^{-1}. Second, concentration of GCPII was determined using a standard addition method based on three consecutive additions of the standard solution of GCP II. Concentrations of the standard GCPII additions were based on an approximate concentration of GCPII from the first step, where concentrations of additions 1–3 were set to be 30–50% increments. Standard addition method was utilized to improve method accuracy and minimize possible matrix effects. Spectral band localized at 1335 cm^{-1} was employed in both steps for a quantification purposes.

3. Results and discussion

3.1. Characterization of the GCPII nanosensor

The GCPII nanosensor, prepared as described in the Experimental section, was characterized by transmission electron microscopy, Raman and infrared spectroscopy, and ζ-potential measurements. High-resolution TEM results are displayed in Fig. 2A–B. Silver nanoparticles with an average diameter of 30 nm are enclosed by considerably smaller magnetic nanoparticles with sizes around 10 nm, organized into dense superclusters. This observation is further supported by high-angle angular dark field image (HAADF, Fig. 2C) and energy dispersed spectroscopy (EDS, Fig. 2D–E). The ζ-potential of the final biosensor was −46 mV, indicating that the system is stable [41].

Acquired infrared spectral data are shown in Fig. 3A and B. The recorded FT-IR spectra of free carboxymethyl-cellulose (CMC) and functionalized $cmcFe_3O_4$ demonstrate successful immobilization of CMC on the surface of the magnetic nanoparticles (Fig. 3A). Spectra were interpreted in accordance with approaches defined by Barth [42]. Both spectra contain characteristic bands of pure CMC at 3400–3000 (O–H stretch), 2917 (C–H stretch), 1594 ($-COO^-$ asymmetric stretch), 1417 ($-COO^-$ symmetric stretch), 1338 (bridge–O–stretch), 1058 (C–O stretch), and 910 cm^{-1} (pyranose ring). Moreover, the characteristic band for magnetite at 590 cm^{-1} was found in $cmcFe_3O_4$ data. Anchoring of the Anti-GCPII is documented in the spectral data shown in Fig. 3B. The obtained FT-IR spectra of free Anti-GCPII and Fe_3O_4@Anti-GCPII contain spectral bands at 1626–1629 (Lys, NH_3^+ asymmetric stretch), 1404 (Glu, COO^- vib. stretch), 1650 (amide I C=O stretch) and 1400 cm^{-1} (amide III C-N stretch).

3.2. Analysis of GCPII in model samples

To evaluate use of the synthesized nanomaterial in the analysis of GCPII, we first tested the analytical probe functionalized with

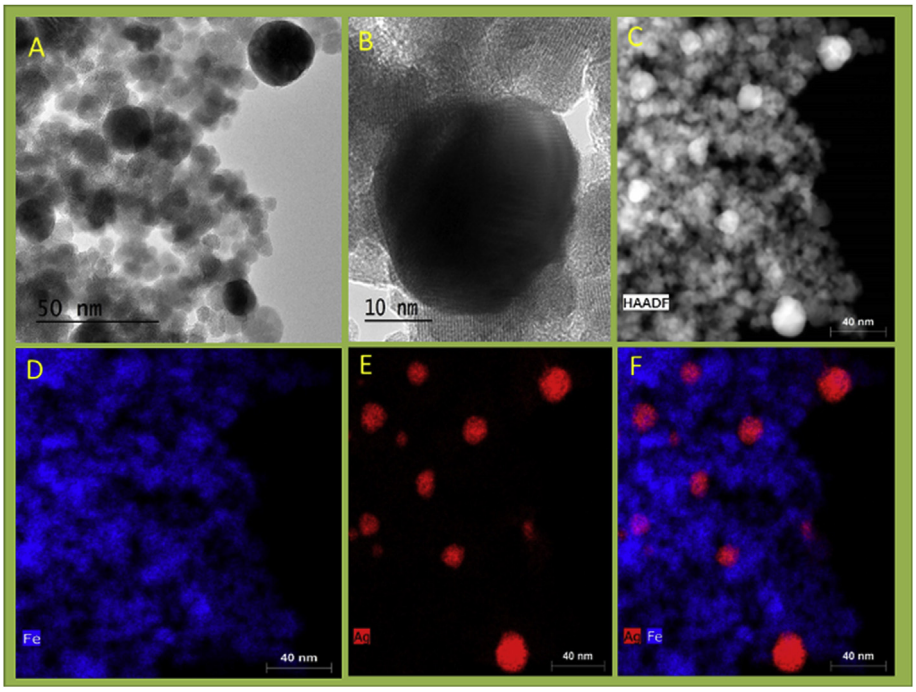

Fig. 2. High-resolution TEM images of colloidal Fe_3O_4@Ag stabilized by CMC. A: general overview of the sample, B: detailed view of a silver nanoparticle, C: HAADF image of the sample, D–F: EDS characterization focused on the presence of Ag and Fe elements.

Anti-GCPII using a standard solution of purified recombinant GCPII (c = 10 ng/mL). The resulting data are shown in Fig. 4. Raman spectra obtained from the analysis of the model sample of GCPII (label: Standard of GCPII) contain, compared to a blank sample (label: Blank sample) spectral bands characteristic of proteins. Distinctive vibrations of proteins include dominant spectral bands located at, 678 cm^{-1}, 728 cm^{-1}, 955 cm^{-1}, 1235 cm^{-1} (amide III), 1335 cm^{-1} (C-H deformation bands of proteins), 1450 cm^{-1}, 1577 cm^{-1}, 1670 (Amide I) cm^{-1}, and 1790 cm^{-1}.

We next measured calibration spectra for GCPII in the concentration range from 5 to 200 ng/mL, where seven calibration points with five technical replicates were evaluated. Spectral data of all seven calibration standards are shown in Fig. 5A and final calibration curve in Fig. 5B. These data illustrate that the Raman intensity of spectral bands of proteins and amino acids, characteristic for GCPII, change as the concentration varies. We designated the amide vibration of amide located at 1335 cm^{-1} as a quantification marker due to its higher absolute intensity and lower amount of interference compared to other intense spectral bands (Fig. 4). The normalized intensity of the band was used for construction of a calibration curve. The coefficient of determination (R [2]) of the linear regression was 0.985, and the limit of detection (LOD) was 0.48 ng/mL (calculated from the S/N ratio).

Next, the repeatability of the analytical procedure was evaluated on a set of five independent measurements (Fig. S1). All spectra are fully comparable; the statistical difference between the 3 most intensive bands in experimental data is lower than 7%. Furthermore, stability of the nanomaterial was evaluated using a set of periodic measurements performed over a 21-day interval. The results are shown in Fig. S2. A moderate decline in the total intensity of acquired spectral data due to a partial aggregation of the nanomaterial can be observed. Nevertheless, spectral data acquired 21 days after the synthesis of the nanomaterial contain a strong analytical signal of the measured chemical target.

3.3. Analysis of GCPII in samples of human whole blood

We next evaluated our functionalized nanocomposite for analysis of human whole blood samples containing various concentrations of GCPII. First, Raman spectrum obtained from the analysis of real sample and standard solution of GCPII (c = 10 ng mL^{-1}) are shown in Fig. 6. In-detail spectral analysis uncovered new bands located at 1415 cm^{-1}, and 1450 cm^{-1}, present in the spectrum of the real sample, indicating minor nonspecific interactions. Peak area of the newly formed spectral bands is lower than 5% of total peak area and does not interfere with a spectral band at 1335 cm^{-1} which minimizes its influence on a quantification of GCPII. Furthermore, total concertation of GCPII in real samples was performed using standard addition method to minimize effects of nonspecific interactions between matrix constituents and analytical sensor. Total five real samples of healthy adult individuals were evaluated. Spectral data of real samples and standard additions, accompanied by calibration data and calculated coefficients of determination are summarized in the Figure S-3. The GCPII concentrations in these samples was found to be in the range from 1 to 7.3 ng/mL, which is in a good correlation to previously reported values for a healthy population [28]. The relative errors of determination (RSD) were less than 10%. All values obtained, including calculated RSD and confidence intervals are further summarized in Tables S–1 with respective statistical values.

4. Conclusions

Tools to analyze the total amount of GCPII in biological samples present the potential opportunity for development of prostate cancer diagnostics. Working toward this goal, we developed a novel approach based on utilization of a low-molecular-weight GCPII ligand in MA-SERS analysis. The functionalization of raw Fe_3O_4@Ag nanocomposite was based on the anchoring of a GCPII inhibitor on its free surface. The resulting Fe_3O_4@Anti-GCPII@Ag functionalized

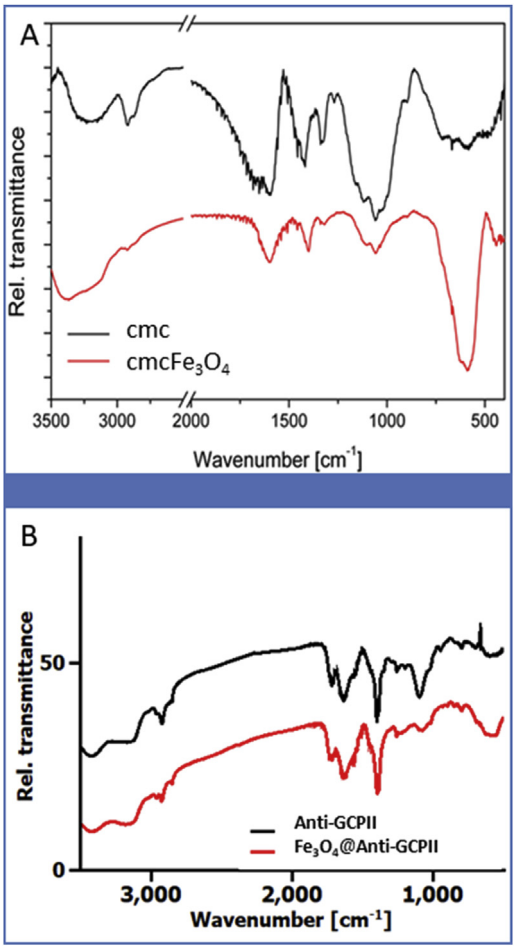

Fig. 3. A: FT-IR spectroscopy of cmcFe_3O_4. Black, FT-IR of raw CMC; red, FT-IR of nano Fe_3O_4 functionalized by CMC. B: FT-IR spectroscopy of functionalized Fe3O4@Anti-GCPII. Black trace, FT-IR of raw Anti-GCPII; red trace, FT-IR of cmcFe_3O_4 functionalized by Anti-GCPII forming Fe_3O_4@Anti-GCPII. (For interpretation of the references to colour in this figure legend, the reader is referred to the web version of this article.)

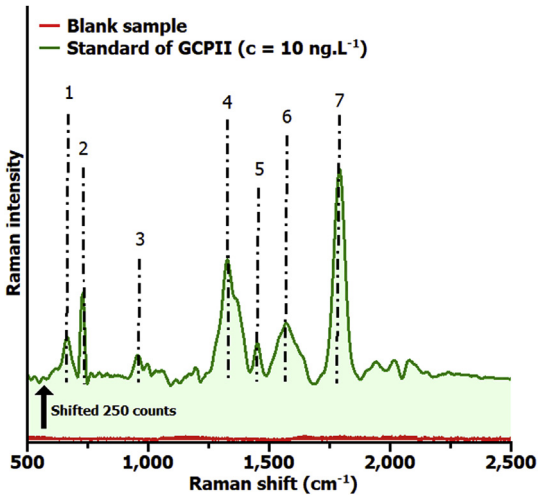

Fig. 4. Raman spectrum obtained by the analysis of Fe_3O_4@Anti-GCPII@Ag nanocomposite (label: Blank sample), and Raman spectrum obtained from the analysis of purified recombinant GCPII (c = 10 ng ml^{-1}) using Fe_3O_4@Anti-GCPII@Ag nanocomposite (label: Standard of GCPII). An interpretation of spectral data is given in Table S1. Data of Standard sample are shifted for 250 counts to make the figure readable. Spectral bands are labeled in a following order: 1: 678 cm^{-1}; 2: 728 cm^{-1}; 3: 955 cm^{-1} 4: 1335 cm^{-1}; 5: 1455 cm^{-1}; 6: 1577 cm^{-1} and 7: 1790 cm^{-1}.

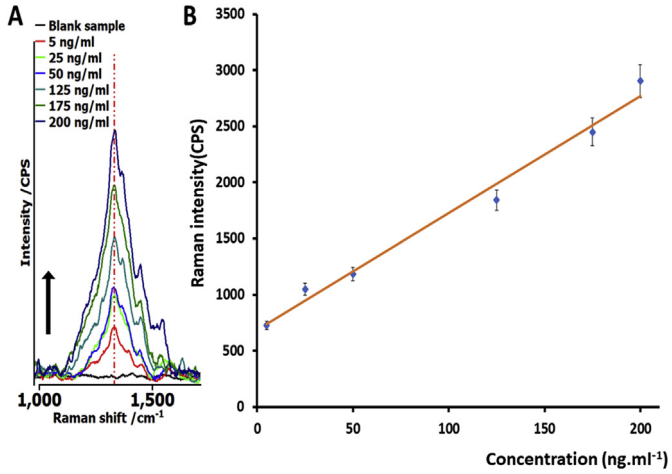

Fig. 5. A) Raman spectra obtained by analysis of GCPII at six different concentration levels: 5–200 ng/mL. B) Calibration curve for GCPII, obtained from the spectral analysis of standard samples.

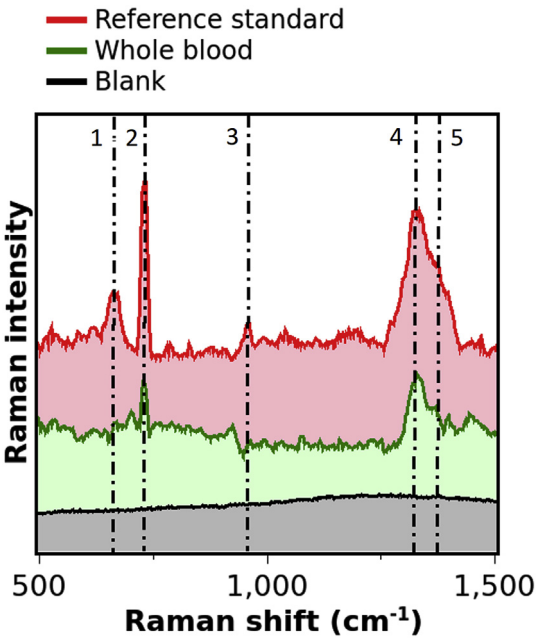

Fig. 6. Raman spectra obtained by analysis of a whole blood sample containing GCPII with nanocomposite functionalized by compound 2 (Whole blood) and reference spectrum of a standard solution of GCPII (c = 10 ng ml^{-1}), analyzed using Fe_3O_4@Anti-GCPII@Ag nanocomposite (Reference standard). Blank Raman spectrum represents an analysis of human blood using raw nanomaterial (Fe_3O_4@Ag). Spectral bands are labeled in a following order: Spectral bands are labeled in a following order: 1: 678 cm^{-1}; 2: 728 cm^{-1}; 3: 955 cm^{-1} 4: 1335 cm-1; 5: 1371 cm^{-1}.

nanocomposite was subsequently evaluated as a potential nanosensor for determination of the total amount of GCPII in whole human blood samples. The calculated limits of quantification are in the ng/mL range, and relative errors of determination, obtained from the analysis of blood samples, are lower than 7%. Furthermore, the method provides results with very good repeatability. The Fe_3O_4@Anti-GCPII@Ag nanocomposite remained stable for 21 days. The sensitivity of detection and simplicity of this method suggest its promise as a potential alternative to generally applied analytical procedures.

Author contributions

The manuscript was written through contributions of all authors.

Notes

The authors declare no competing financial interests.

Acknowledgements

The authors acknowledge Hillary Hoffman for language editing of the manuscript. The authors gratefully acknowledge support from projects NPU LO1305, NPU LO1302 and NPU LO1304 of the Ministry of Education, Youth and Sports of the Czech Republic; project IGA_UP_2017_025, CZ.1.07/2.3.00/30.0004 and Research Infrastructure NanoEnviCz, supported by the Ministry of Education, Youth and Sports of the Czech Republic under Project No. LM2015073; and project 16-02938S of the Grant Agency of the Czech Republic.

Appendix A. Supplementary data

Supplementary data related to this article can be found at https://doi.org/10.1016/j.aca.2017.10.008.

References

[1] S.H. Landis, T. Murray, S. Bolden, P.A. Wingo, Cancer statistics, 1999, Ca-Cancer J. Clin. 49 (1999) 8–31.
[2] P.A. Wingo, C.I. Cardinez, S.H. Landis, R.T. Greenlee, L.A.G. Ries, R.N. Anderson, M.J. Thun, Long-term trends in cancer mortality in the United States, 1930-1998, Cancer 97 (2003), 3133-+.
[3] A. Lorch, Systemic treatment of metastatic prostate cancer, Onkologe 23 (2017) 237–250.
[4] A.E. Ross, S. Loeb, P. Landis, A.W. Partin, J.I. Epstein, A. Kettermann, Z.Y. Feng, P.C. Walsh, H.B. Ctr, Prostate-specific antigen kinetics during follow-up are an unreliable trigger for intervention in a prostate cancer surveillance program, J. Clin. Oncol. 28 (2010) 2810–2816.
[5] K. Lees, M. Durve, C. Parker, Active surveillance in prostate cancer: patient selection and triggers for intervention, Curr. Opin. Urol. 22 (2012) 210–215.
[6] L. Klotz, Active surveillance: the Canadian experience, Curr. Opin. Urol. 22 (2012) 222–230.
[7] S. Perner, M.D. Hofer, R. Kim, R.B. Shah, H.J. Li, P. Moller, R.E. Hautmann, J.E. Gschwend, R. Kuefer, M.A. Rubin, Prostate-specific membrane antigen expression as a predictor of prostate cancer progression, Hum. Pathol. 38 (2007) 696–701.
[8] D.A. Silver, I. Pellicer, W.R. Fair, W.D.W. Heston, C. CordonCardo, Prostate-specific membrane antigen expression in normal and malignant human tissues, Clin. Cancer Res. 3 (1997) 81–85.
[9] J.C. Evans, M. Malhotra, J.F. Cryan, C.M. O'Driscoll, The therapeutic and diagnostic potential of the prostate specific membrane antigen/glutamate carboxypeptidase II (PSMA/GCPII) in cancer and neurological disease, Brit J. Pharmacol. 173 (2016), 3145–U3108.
[10] D.G. Bostwick, A. Pacelli, M. Blute, P. Roche, G.P. Murphy, Prostate specific membrane antigen expression in prostatic intraepithelial neoplasia and adenocarcinoma - a study of 184 cases, Cancer 82 (1998) 2256–2261.
[11] M.J. Evans, P.M. Smith-Jones, J. Wongvipat, V. Navarro, S. Kim, N.H. Bander, S.M. Larson, C.L. Sawyers, Noninvasive measurement of androgen receptor signaling with a positron-emitting radiopharmaceutical that targets prostate-specific membrane antigen, P Natl. Acad. Sci. U. S. A. 108 (2011) 9578–9582.
[12] M.J. Morris, C.R. Divgi, N. Pandit-Taskar, M. Batraki, N. Warren, A. Nacca, P. Smith-Jones, L. Schwartz, W.K. Kelly, S. Slovin, D. Solit, J. Halpern, A. Delacruz, T. Curley, R. Finn, J.A. O'Donoghue, P. Livingston, S. Larson, H.I. Scher, Pilot trial of unlabeled and indium-111-labeled anti-prostate-specific membrane antigen antibody J591 for castrate metastatic prostate cancer, Clin. Cancer Res. 11 (2005) 7454–7461.
[13] J.P. Holland, V. Divilov, N.H. Bander, P.M. Smith-Jones, S.M. Larson, J.S. Lewis, Zr-89-DFO-J591 for ImmunoPET of prostate-specific membrane antigen expression in vivo, J. Nucl. Med. 51 (2010) 1293–1300.
[14] K.P. Maresca, S.M. Hillier, F.J. Femia, D. Keith, C. Barone, J.L. Joyal, C.N. Zimmerman, A.P. Kozikowski, J.A. Barrett, W.C. Eckelman, J.W. Babich, A series of halogenated heterodimeric inhibitors of prostate specific membrane antigen (PSMA) as radiolabeled probes for targeting prostate cancer, J. Med. Chem. 52 (2009) 347–357.
[15] I. Rauscher, T. Maurer, W.P. Fendler, W.H. Sommer, M. Schwaiger, M. Eiber, Ga-68-PSMA ligand PET/CT in patients with prostate cancer: how we review and report, Cancer Imaging 16 (2016).
[16] S.M. Hillier, K.P. Maresca, F.J. Femia, J.C. Marquis, C.A. Foss, N. Nguyen, C.N. Zimmerman, J.A. Barrett, W.C. Eckelman, M.G. Pomper, J.L. Joyal, J.W. Babich, Preclinical evaluation of novel glutamate-urea-lysine analogues that target prostate-specific membrane antigen as molecular imaging pharmaceuticals for prostate cancer, Cancer Res. 69 (2009) 6932–6940.
[17] C.M. Zechmann, A. Afshar-Oromieh, T. Armor, J.B. Stubbs, W. Mier, B. Hadaschik, J. Joyal, K. Kopka, J. Debus, J.W. Babich, U. Haberkorn, Radiation dosimetry and first therapy results with a I-124/I-131-labeled small molecule (MIP-1095) targeting PSMA for prostate cancer therapy, Eur. J. Nucl. Med. Mol. I 41 (2014) 1280–1292.
[18] G.L. Lu, K.P. Maresca, S.M. Hillier, C.N. Zimmerman, W.C. Eckelman, J.L. Joyal, J.W. Babich, Synthesis and SAR of Tc-99m/Re-labeled small molecule prostate specific membrane antigen inhibitors with novel polar chelates, Bioorg Med. Chem. Lett. 23 (2013) 1557–1563.
[19] M. Eder, M. Schafer, U. Bauder-Wust, W.E. Hull, C. Wangler, W. Mier, U. Haberkorn, M. Eisenhut, Ga-68-Complex lipophilicity and the targeting property of a urea-based PSMA inhibitor for PET imaging, Bioconjugate Chem. 23 (2012) 688–697.
[20] S.Y. Cho, K.L. Gage, R.C. Mease, S. Senthamizhchelvan, D.P. Holt, A. Jeffrey-Kwanisai, C.J. Endres, R.F. Dannals, G. Sgouros, M. Lodge, M.A. Eisenberger, R. Rodriguez, M.A. Carducci, C. Rojas, B.S. Slusher, A.P. Kozikowski, M.G. Pomper, Biodistribution, tumor detection, and radiation dosimetry of F-18-DCFBC, a low-molecular-weight inhibitor of prostate-specific membrane antigen, in patients with metastatic prostate cancer, J. Nucl. Med. 53 (2012) 1883–1891.
[21] Z. Hollo, L. Homolya, T. Hegedus, M. Muller, G. Szakacs, K. Jakab, F. Antal, B. Sarkadi, Parallel functional and immunological detection of human multidrug resistance proteins, P-glycoprotein and MRP1, Anticancer Res. 18 (1998) 2981–2987.
[22] T. Okuda, K. Kataoka, M. Taneda, Metastatic brain tumor surgery using fluorescein sodium: technical note, Minim. Invas Neurosur 50 (2007) 382–384.
[23] D.J. Arndt-Jovin, S.R. Kantelhardt, W. Caarls, A.H.B. de Vries, A. Giese, T.M. Jovin, Tumor-targeted quantum dots can help surgeons find tumor boundaries, Ieee T Nanobiosci 8 (2009) 65–71.
[24] K. Gotoh, T. Yamada, O. Ishikawa, H. Takahashi, H. Eguchi, M. Yano, H. Ohigashi, Y. Tomita, Y. Miyamoto, S. Imaoka, How i do it a novel image-guided surgery of hepatocellular carcinoma by indocyanine green fluorescence imaging navigation, J. Surg. Oncol. 100 (2009) 75–79.
[25] Y.P. Rochon, J. Horeszewitz, A. Boynton, E. Holmes, R. Barren, S. Erickson, G. Kenny, G. Murphy, Western-blot assay for prostate specific membrane antigen in serum of prostate cancer patients, Prostate 25 (1994) 219–223.
[26] G. Murphy, H. Ragde, G. Kenny, R. Barren, S. Erickson, B. Tjoa, A. Boynton, E. Holmes, J. Gilbaugh, T. Douglas, Comparison of prostate specific membrane antigen, and prostate specific antigen levels in prostate cancer patients, Anticancer Res. 15 (1995) 1473–1479.
[27] M. Beckett, L. Cazares, A. Vlahou, P. Schellhammer, G. Wright, Prostate-specific membrane antigen levels in sera from healthy men and patients with benign prostate hyperplasia or prostate cancer, Clic. Cancer. Res. 5 (1999) 4034–4040.
[28] T. Knedlik, V. Navratil, V. Vik, D. Pacik, P. Sacha, J. Konvalinka, Detection and quantitation of glutamate carboxypeptidase II in human blood, Prostate 74 (2014) 768–780.
[29] M. Fleischmann, P.J. Hendra, A.J. Mcquillan, Raman-spectra of pyridine adsorbed at a silver electrode, Chem. Phys. Lett. 26 (1974) 163–166.
[30] Y.W.C. Cao, R.C. Jin, C.A. Mirkin, Nanoparticles with Raman spectroscopic fingerprints for DNA and RNA detection, Science 297 (2002) 1536–1540.
[31] J.J. Laserna, A.D. Campiglia, J.D. Winefordner, Mixture analysis and quantitative-determination of nitrogen-containing organic-molecules by surface-enhanced raman spectrometry, Anal. Chem. 61 (1989) 1697–1701.
[32] A. Balzerova, A. Fargasova, Z. Markova, V. Ranc, R. Zboril, Magnetically-assisted surface enhanced raman spectroscopy (MA-SERS) for label-free determination of human immunoglobulin g (IgG) in blood using Fe3O4@Ag nanocomposite, Anal. Chem. 86 (2014) 11107–11114.
[33] V. Ranc, Z. Markova, M. Hajduch, R. Prucek, L. Kvitek, J. Kaslik, K. Safarova, R. Zboril, Magnetically assisted surface-enhanced raman scattering selective determination of dopamine in an artificial cerebrospinal fluid and a mouse striatum using Fe3O4/Ag nanocomposite, Anal. Chem. 86 (2014) 2939–2946.
[34] P. Sacha, J. Zamecnik, C. Barinka, K. Hlouchova, A. Vicha, P. Mlcochova, I. Hilgert, T. Eckschlager, J. Konvalinka, Expression of glutamate carboxypeptidase II in human brain, Neuroscience 144 (2007) 1361–1372.
[35] V. Navratil, J. Schimer, J. Tykvart, T. Knedlik, V. Vik, P. Majer, J. Konvalinka, P. Sacha, DNA-linked Inhibitor Antibody Assay (DIANA) for sensitive and selective enzyme detection and inhibitor screening, Nucleic Acids Res. 45 (2017).
[36] P. Sacha, T. Knedlik, J. Schimer, J. Tykvart, J. Parolek, V. Navratil, P. Dvorakova, F. Sedlak, K. Ulbrich, J. Strohalm, P. Majer, V. Subr, J. Konvalinka, iBodies: modular synthetic antibody mimetics based on hydrophilic polymers decorated with functional moieties, Angew. Chem. Int. Ed. 55 (2016) 2356–2360.
[37] R.P. Murelli, A.X. Zhang, J. Michel, W.L. Jorgensen, D.A. Spiegel, Chemical control over immune recognition: a class of antibody-recruiting small molecules that target prostate cancer, J. Am. Chem. Soc. 131 (2009), 17090-+.
[38] J. Tykvart, P. Sacha, C. Barinka, T. Knedlik, J. Starkova, J. Lubkowski, J. Konvalinka, Efficient and versatile one-step affinity purification of in vivo

biotinylated proteins: expression, characterization and structure analysis of recombinant human glutamate carboxypeptidase II, Protein Expres Purif. 82 (2012) 106–115.
[39] A. Panacek, L. Kvitek, R. Prucek, M. Kolar, R. Vecerova, N. Pizurova, V.K. Sharma, T. Nevecna, R. Zboril, Silver colloid nanoparticles: synthesis, characterization, and their antibacterial activity, J. Phys. Chem. B 110 (2006) 16248–16253.
[40] A. Bakandritsos, G. Mattheolabakis, G. Chatzikyriakos, T. Szabo, V. Tzitzios, D. Kouzoudis, S. Couris, K. Avgoustakis, Doxorubicin nanocarriers based on magnetic colloids with a bio-polyelectrolyte corona and high non-linear optical response: synthesis, characterization, and properties, Adv. Funct. Mater 21 (2011) 1465–1475.
[41] B.J. Kirby, E.F. Hasselbrink, Zeta potential of microfluidic substrates: 1. Theory, experimental techniques, and effects on separations, Electrophoresis 25 (2004) 187–202.
[42] A. Barth, Infrared spectroscopy of proteins, Bba-Bioenergetics 1767 (2007) 1073–1101.

Applied Materials Today 13 (2018) 166–173

Contents lists available at ScienceDirect

Applied Materials Today

journal homepage: www.elsevier.com/locate/apmt

Multiplex competitive analysis of HER2 and EpCAM cancer markers in whole human blood using Fe_2O_3@Ag nanocomposite

Anna Balzerová, Ariana Opletalová, Václav Ranc*, Radek Zbořil*

Regional Centre of Advanced Technologies and Materials, Department of Physical Chemistry, Faculty of Science, Palacký University Olomouc, 17. listopadu 12, CZ-77146 Olomouc, Czech Republic

ARTICLE INFO

Article history:
Received 22 June 2018
Received in revised form 31 August 2018
Accepted 31 August 2018

Keywords:
Multiplex
Competitive analysis
Cancer markers
SERS
Magnetic

ABSTRACT

Sensitive, reliable, and selective detection of biochemical markers represents a challenging approach toward early diagnosis of cancer diseases. However, the complexity of the targeted physiological environments challenges currently available protocols. Therefore, new, reliable methodologies for the detection of cancer markers are highly demanded. Here, we describe a new method for parallel analysis of two essential cancer markers, HER2 (human epidermal growth factor receptor 2) and EpCAM (epithelial cell adhesion molecule). The method is based on a combination of a Fe_2O_3@Ag magnetic nanocomposite covalently functionalized with anti-EpCAM and anti-HER2, and surface-enhanced Raman spectroscopy. The detection of target molecules employs a competitive approach between reference compounds, labeled with Raman active tags, and their naturally accruing counterparts. The limit of detection was determined to be 5 ng L^{-1}, where both compounds are statistically distinguishable from a blank sample with $p = 0.0093$ (HER2) and 0.0016 (EpCAM). The developed methodology presents an exciting alternative to more common methods including immunological methods or PCR.

1. Introduction

Cancer, a disease caused by an uncontrolled division of abnormal cells, is one of the leading causes of death worldwide. In 2012, an estimated 14.1 million new cases were diagnosed, and 8.2 million people died [1]. Breast cancer, with an occurrence of 1.7 million cases, and with estimated 521 900 deaths, is the most frequent type of cancer among women [1]. These numbers strongly emphasize an urgent demand for novel methodologies that will be able to provide a reliable screening of tumor markers involved in its early diagnosis [2]. The available screening methods usually target tumor markers found in blood, urine, or saliva [3–5], and include nucleic acids, metabolites, isoenzymes, or hormones. Nonetheless, the most important part of the recognized markers represents proteins overexpressed by cancer cells [6]. Human epidermal growth factor receptor 2 (HER2), also known as receptor tyrosine-protein kinase erbB-2 or HER2/neu, is a member of the human epidermal growth factor receptor family and is associated with breast, lung, and ovarian cancer [7]. HER2 is overexpressed in 10–25% of cases [8] and is usually related to extremely aggressive forms [9]. Epithelial cell adhesion molecule (EpCAM) belongs to the family of the first discovered tumor-linked biomarkers [10]. It is often linked to a variety of human adenocarcinomas and squamous cell carcinomas or also breast, ovarian, and colon carcinomas [10]. Cancer screening techniques include cytology, histopathology, and immunochemistry [11–14] as well as tissue microarray techniques [15–19] or chips and paper-based electrochemical sensors [20–24]. Among potential candidates, surface-enhanced Raman spectroscopy (SERS) has proved to be an interesting alternative. Its potential has been demonstrated in the detection of many physiologically active compounds covering both large proteins and low molecular compounds [25–27], bacteria [28–30], viruses [31,32], neuro-hormones [33], and whole cells [34,35]. Moreover, a newly developed SERS approach, referred to as magnetically assisted surface-enhanced Raman spectroscopy (MA-SERS), further increases the potential of SERS by employing magnetic nanocomposites for highly efficient separation and preconcentration of target compounds by an external magnetic field [25]. The improved analytical performance of MA-SERS has been shown in cases covering a detection of cancer biomarkers and circulating tumor cells (CTCs) using sandwich-based approaches

* Corresponding authors.
E-mail addresses: vaclav.ranc@upol.cz (V. Ranc), radek.zboril@upol.cz (R. Zbořil).

https://doi.org/10.1016/j.apmt.2018.08.016
2352-9407/

[36–38], detection of non-small lung cancer cells with a limit of detection (LOD) approximately 10 cells per mL [34], detection of CEA with a resulting LOD = 0.1 ng mL^{-1} [39], or detection of a prostate-specific antigen by magnetic immunoassay technique utilizing surface-enhanced Raman-scattering-based micro-droplet sensor with an LOD = 0.1 ng mL^{-1} [40].

Nevertheless, a decision based on the detection of a single cancer-related biomarker does not often deliver suitable true positive or true negative rates. The demand for methods providing a multiplex detection of several biomarkers gives an opportunity to various types of highly advanced biosensors [41].

SERS-based methods for multiplex analyses usually introduce several Raman tags to distinguish the signals from targeted analytes [42]. Granger et al. [43] described a multiplex detection of pancreatic adenocarcinoma markers—serum carbohydrate antigen 19-9 and matrix metalloproteinase-7. The obtained results were subsequently compared to enzyme-linked immunosorption assay (ELISA) and eventually a good correlation was found [43]. Raman tags or reporters were also used for the simultaneous multiplex SERS detection of cancer markers, such as cancer antigen (CA) 15-3, CA 27-29, Glypican-3, α-fetoprotein, or cancer embryonic antigen (CEA) [5,44,45]. Maiti et al. [46] developed a biocompatible SERS nanotag with high stability by using sensitive triphenylmethine Raman reporters covalently attached to gold nanoparticles using lipoic acid (LA) as a linker. The prepared SERS nanotags were conjugated to selective antibodies recognizing HER2 and EGFR cancer proteins [46]. The above-mentioned experimental methods and approaches exhibit high selectivity and sensitivity in comparison with commonly used immunological methods like ELISA.

On the other hand, nonspecific interactions of the prepared materials with as complicated matrix as whole human blood cause interferences of signal and considerably limit such methods in clinical practice. Herein, we present a novel magnetic sensor for a competitive multiplexed detection of HER2 and EpCAM biomarkers using the SERS approach. The developed sensor employs Fe_2O_3@Ag nanocomposite functionalized by anti-HER2 and anti-EpCAM antibodies. The detection is based on the competition between naturally present biomarkers and their tagged (reference) counterparts. This approach allows for a simple magnetic separation of the sensor from human whole blood, minimizes the influence of nonspecific interactions through a competition-based approach and active surface functionalization of the nanocomposite, and increases the method reliability through a developed statistical evaluation.

2. Materials and methods

2.1. Chemicals

Silver nitrate (p.a.), D-(+)-maltose monohydrate (BioXtra, ≥99%), ammonium hydroxide solution (ACS reagent, 28.0–30.0% NH_3 basis), carboxy-functionalized magnetic particles (18–22 mg mL^{-1}), 1-[3-(dimethylamino)propyl]-3-ethylcarbodiimide methiodide (EDC), *N*-hydroxysulfosuccinimide sodium salt (≥98% (HPLC); NHS), sodium chloride (BioXtra, ≥99.5% (AT), anti-HER2 antibody produced in rabbit, anti-EpCAM antibody produced in rabbit, ethylamine (purum, 70% in H_2O), Cy®3 mAb Kit, Cy®5 mAb Kit were purchased from Sigma-Aldrich (USA) and used without further purification. Human HER2/ErbB2 Protein (Fc Tag) was purchased from Sino Biological, Inc. (China), recombinant human EpCAM protein was purchased from Abcam (United Kingdom), H_3PO_4 (p.a., 85%, w/w) and NaOH (p.a.) was bought from Lach-Ner (Czech Republic).

2.2. Functionalization of magnetic particles with antibodies (Fig. 1)

Magnetic particles with carboxylic groups were activated using EDC/NHS mixture (1:1, final concentration of 10 mM) and the reaction was stirred for 30 min; the particles were then magnetically separated and washed with 5 mL of PBS buffer. In the next step, the particles with the previously activated carboxylic groups were mixed with antibodies (c = 10 mg L^{-1}) and stirred overnight to form a covalent bond between free amino (–NH_2) groups present in the structure of the antibodies and the activated carboxylic groups of the magnetic particles. After the immobilization of antibodies, the magnetic particles were separated by a magnet and washed with 10 mM phosphate-buffered saline (PBS) buffer. After washing with the PBS buffer, the ethylamine with final concentration 3.5% wt. was added to block the rest of the active carboxylic groups to prevent any nonspecific interactions. In a final step, the functionalized nanoparticles were washed three times with PBS buffer (Fig. 1).

2.3. Labeling of proteins

Proteins (HER2, EpCAM) were labeled using a labeling kit containing reactive fluorescent dye Cy3 or Cy5 tags, coupling buffer (1 M sodium carbonate buffer, pH 9.3), and PBS buffer. HER2 protein was labeled with Cy3 tag (HER2_Cy3) in a ratio 1:10 and EpCAM protein with Cy5 tag (EpCAM_Cy5) in the same ratio as HER2 according to the recommended procedure. The labeled proteins were purified using centrifugal filter units (Amicon Ultra 0.5 mL, MWCO 3 kDa) at 10 000 rpm for 10 min to separate the excessive free compound. The concentration of the proteins after labeling with Cy3 and Cy5 was measured using a colorimetric method with Coomassie Brilliant Blue G-250 agent (Bradford assay) at 595 nm. According to the measured data, the concentration of the markers after labeling was the following: HER 0.009 mg mL^{-1} and EpCAM 0.01 mg mL^{-1}. The labeled marker HER2 (HER2_Cy3) was analyzed using HPLC-UV system to find out the yield of the labeling process. From the chromatogram, it was found that 70% of markers were successfully labeled (Fig. S1) and the sample did not contain a free Cy3 tag. The same yield of the labeling process was expected for EpCAM_Cy5. The optimal concentration for competitive analysis was set up experimentally as a breakpoint in a graph of the intensity–concentration dependence of the 1450 cm^{-1} spectral band of the labeled markers (Fig. S2). Two linear fits were used for the calculation, and the breakpoint was determined at the concentration 10 ng L^{-1}.

2.4. Apparatus

The ζ-potential was measured using a Zetasizer NanoZS (Malvern, UK). A high-resolution transmission electron microscope (HR-TEM FEI Titan G2 60–300) with an X-FEG type emission gun, operating at 80 kV, was used to obtain the images of the final products. This microscope is equipped with a Cs image corrector and an TEM high-angle annular dark field detector (HAADF). The point of resolution is 0.08 nm in the TEM mode. The elemental mapping was obtained by STEM-energy dispersive X-ray spectroscopy (EDS; Bruker SuperX) with acquisition time 20 min. The X-ray powder diffraction pattern was recorded on a PANalytical X'Pert PRO diffractometer in Bragg–Brentano geometry, equipped with an iron-filtered Co Kα radiation source, X'Celerator detector, programmable divergence, and diffracted beam anti-scatter slits. 200 μL of the liquid sample was dropped on a zero-background Si slide, dried under vacuum at RT, and scanned in the two θ range from 10° to 105° under ambient conditions. Samples of protein standard and Cy3-labeled protein were analyzed using HPLC-UV system (Dionex UltiMate 3000, Thermo Scientific, USA). The samples were separated on a C18 column (Nucleodur C18

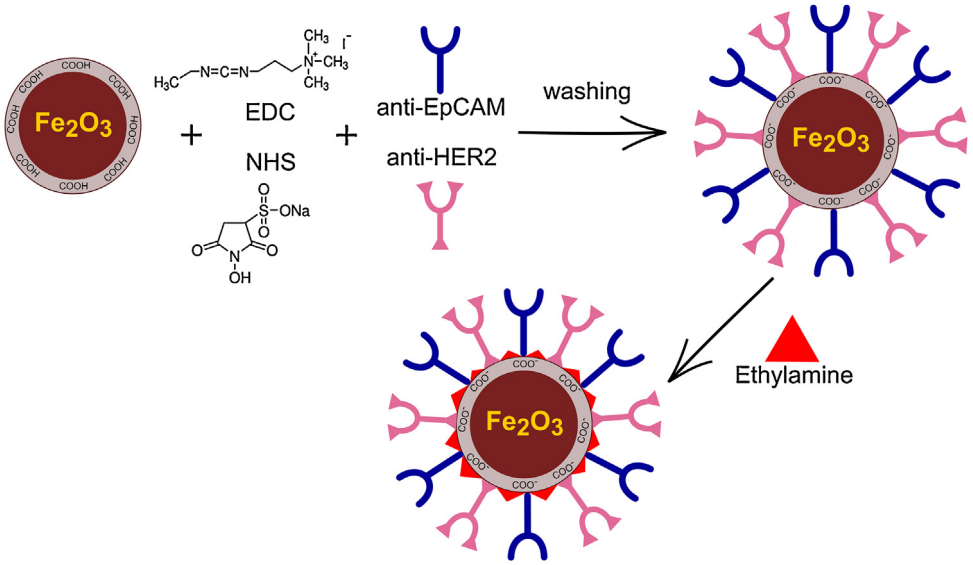

Fig. 1. Schema of sensor preparation (functionalization of MNPs with antibodies anti-HER2 and anti-EpCAM).

Gravity, 150 × 2 mm, 1.8 μm particles). The separation was performed under isocratic conditions with composition of mobile phase: water:acetonitrile:TFA (0.95:0.049:0.001, v/v/v). The separated peaks were detected using a UV detector operating at 274 nm. Raman spectra were collected using a DXR Raman spectroscopy (Thermo Scientific, USA) equipped with a laser operating at a wavelength of 633 nm. The laser power on the sample was set to 5 mW. Each measured Raman spectrum was an average of four experimental microscans. The acquisition time was set to 3 s. SERS experiments employing silver nanoparticles were performed according to the procedure previously described by Fargašová et al. [47]. Briefly, 1 μL of the sample was mixed with 7 μL of the prepared silver nanoparticles (108 mg L^{-1}, 30 nm), and then 2 μL of sodium chloride (c = 4 mol L^{-1}) was added to the mixture, mixed thoroughly, and analyzed using SERS. Infrared spectra were acquired using a Nicolet iS5 infrared spectrometer (Thermo Scientific, USA). A total of 32 scans were measured and averaged for each material. Raman and IR spectra were evaluated using instrument control software (Omnic, version 8, Thermo Scientific, USA), and heights of the target spectral bands were statistically assessed using LibreOffice (version 4.3.0, The Document Foundation, Berlin, Germany). Discriminant analysis was performed using the TQ Analyst. It revealed significant differences between blank samples and model samples according to the intensity ratios of the selected spectral bands (660, 475, and 373 cm^{-1}).

2.5. Sample preparation

The blank sample composed of the PBS (c = 10 mM, pH 7.5). The model samples contained a HER2 and EpCAM biomarkers at concentration levels 5, 10, and 25 ng L^{-1} dissolved in the PBS (c = 10 mM, pH 7.5). The human whole blood samples (20 samples from two volunteers, V = 1 mL) were collected with the volunteers' permission for blood collection and subsequent experiments. Whole human blood was diluted 100 times with PBS (c = 10 mM, pH 7.5), and spiked with HER2 and EpCAM biomarkers at final concentrations 5 and 10 ng L^{-1}.

2.6. Sample analysis

The samples were analyzed using a procedure described in Fig. 2. First, 2 μL of the sample (blank, model, human whole blood) was mixed with 10 μL of the prepared MNPs@anti-HER2@anti-EpCAM sensor. After the sample was shaken for 1 h, the sensor was magnetically separated, washed with PBS (10 mM, pH 7.5), and dispensed in 10 μL PBS. Consecutively, 2 μL of the tagged HER2_Cy3 and EpCAM_Cy5 (final concentration 10 ng L^{-1}) was added and the mixture vortexed. After 1 h, the sample was magnetically separated from an excess of the tagged markers and washed with deionized water (20 μL) twice. Finally, the sample was analyzed using SERS according to a previously described procedure.

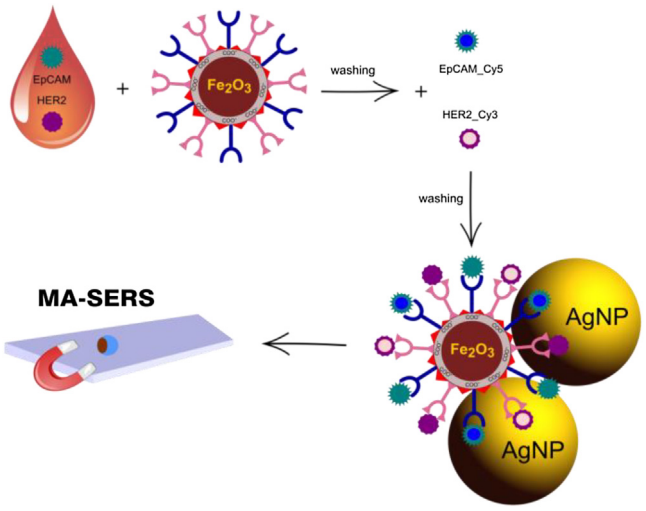

Fig. 2. Schema of competitive multiplex analysis of two different tumor markers in human whole blood.

3. Results and discussion

3.1. Characterization of magnetic nanoparticles and MNPs@Ag hybrid system

The chemical structure of the initial magnetic nanoparticles (Fig. 3A) and Fe_2O_3@Ag nanocomposite (Fig. S3) was investigated using X-ray powder diffraction (XRD). Maghemite (γ-Fe_2O_3) and silver were identified as the only crystalline phase in the sample (Fig. S3). The crystallite size of initial magnetic nanoparticles derived from Rietveld refinement was 13 nm. The HRTEM images

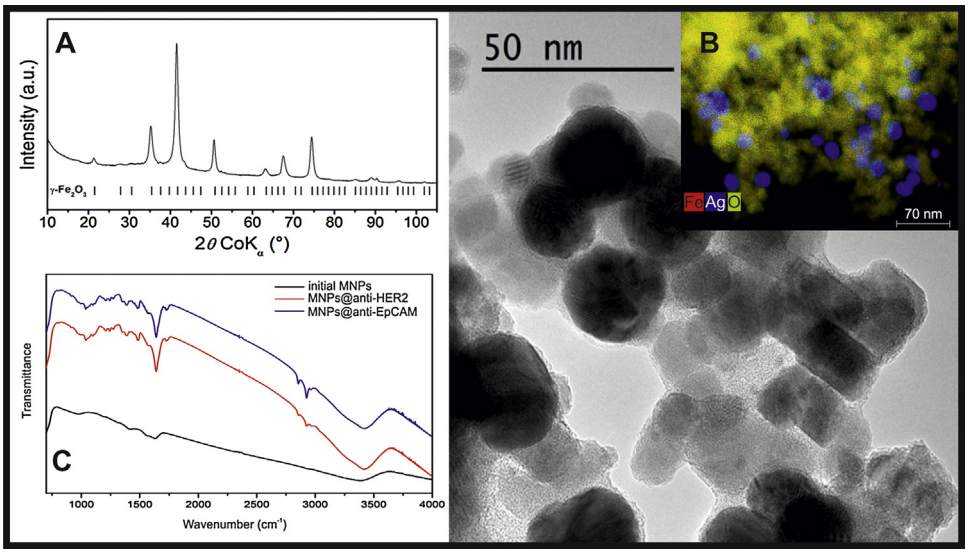

Fig. 3. (A) XRD spectrum of pristine MNPs; (B) HRTEM image of MNPs@Ag hybrid system including HAADF/EDS elemental mapping in the inset (scale bar 70 nm); (C) IR spectra of the initial MNPs and functionalized MNPs.

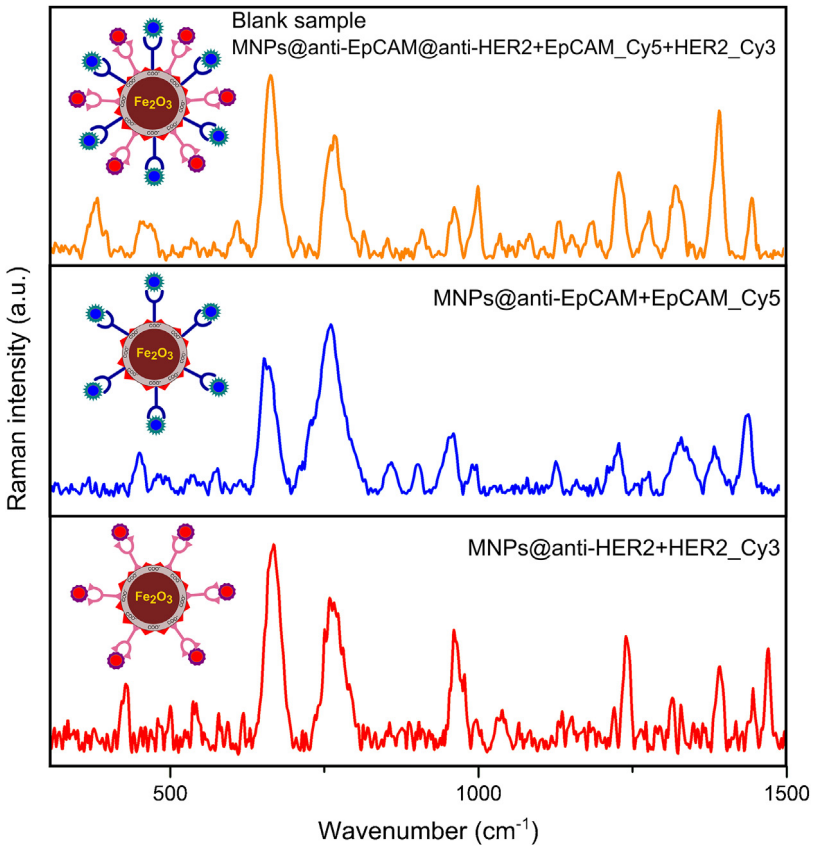

Fig. 4. Raman spectra of functionalized MNPs with anti-HER2 after addition of labeled tumor marker HER2 (HER2_Cy3), Raman spectra of functionalized MNPs with anti-EpCAM after addition of labeled tumor marker EpCAM (EpCAM_Cy5), multiplex Raman analysis with the sensor (MNPs@anti-HER2@anti-EpCAM) after addition of labeled tumor markers HER2 (HER2_Cy3) and EpCAM (EpCAM_Cy5).

accompanied by an elemental map with the distribution of Ag and MNPs are depicted in Fig. 3B. The brighter, smaller objects were identified as Fe_2O_3 particles having a size in the range 10–15 nm, in a good correspondence with XRD data. Larger objects on the image belong to the activated silver nanoparticles exhibiting an average size about 30 nm. This interpretation is further supported by an elemental map as depicted in the right corner of Fig. 3B. The smaller yellow parts of the image represent iron oxide particles, whereas the blue spots correspond to silver nanoparticles. Infrared spectroscopy and ζ-potential measurements were used to monitor changes in the surface characteristics of the functionalized MNPs during the surface functionalization process. The measured ζ-potential of unmodified initial magnetic nanoparticles was –22.3 mV. The strong negative charge of MNPs was

caused by carboxylic groups present on the surface of the magnetic nanoparticles. The activation of the carboxylic groups with an aqueous solution of EDC and NHS was accompanied by a considerable change of firstly negative charge to positive values of +7 mV ($\Delta\zeta$-potential = 29.3 mV). The final step related to immobilization of anti-HER2 and anti-EpCAM antibodies onto the MNPs surface. Consecutive anchoring of proteins changed the charge to more positive values of +9 mV for anti-HER2 and +8 mV in the case of anti-EpCAM. The successful immobilization of both antibodies was further confirmed by measured IR spectra, as shown in Fig. 3C. The spectrum contains bands located at 3430 cm^{-1} interpreted as a stretching vibration of O–H, and band at 1726 cm^{-1} interpreted as a C=O vibration of the carboxyl groups presented on the surface of magnetic particles [48,49]. The presence of the anchored proteins is supported by the presence of two strong protein bands of amide I (–CO–NH) and amide II (–CO–NH–) localized at 1570 and 1650 cm^{-1}, respectively [50,51].

The spectral band at 1385 cm^{-1} represents COO stretching, and it is caused by the presence of the remaining unmodified carboxylic groups on the Fe_2O_3 surface [52].

3.2. Raman characterization of the sensor

The sensor MNPs@anti-HER2@anti-EpCAM was designed for the competitive multiplex analysis of two different tumor markers, HER2 and EpCAM, in whole human blood by a competitive approach with tagged standards of HER2, HER2_Cy3, and EpCAM, EpCAM_Cy5. Firstly, Raman spectra of functionalized MNPs were obtained to confirm the successful immobilization of antibodies HER2 (orange trace) and EpCAM (green trace) onto the MNPs surface, as shown in Fig. S4. The spectra contain characteristic protein bands amide III (1240 cm^{-1}) and amide II (1554 cm^{-1}) representing successful anchoring of the proteins [50,51,53–55]. Secondly, labeling of reference compounds was evaluated. SERS spectra of the stock solutions of tags (Cy3, Cy5) and labeled markers were measured and are shown in Fig. S5. Raman spectra of the sensor and pure compounds, including Cy3, Cy5, HER2, and EpCAM, were compared to confirm the successful labeling of the proteins HER2 and EpCAM using respective Raman tags in the presence of spectral bands located at 373 cm^{-1} (Cy3) and 475 cm^{-1} (Cy5). Furthermore, to considerably improve the method reliability, a reference band located at 660 cm^{-1}, characteristic for tyrosine, was selected and used in the consecutive analytical steps. Raman spectra obtained by the analysis of tagged tumor markers HER2_Cy3 and EpCAM_Cy5 are shown in Fig. 4. The red trace represents a Raman spectrum obtained by the analysis of HER2 using MNPs@anti-HER2 sensor. The spectrum contains abundant spectral bands characteristic for Cy3 and reference band located at 660 cm^{-1}. The blue trace represents a Raman spectrum obtained by the analysis of EpCAM antigen using MNPs@anti-EpCAM sensor and contains strong spectral characteristic for Cy5 and reference band at 660 cm^{-1}. The orange trace shows a Raman spectrum obtained by the multiplex analysis of both proteins using MNPs@anti-HER2@anti-EpCAM sensor. The spectrum contains spectral bands of both tags, namely Cy3 at 373 cm^{-1} and Cy5 at 475 cm^{-1}.

3.3. Multiplex analysis with model samples

The multiplex analysis was based on a competition between unlabeled tumor markers HER2 and EpCAM; and labeled tumor markers HER2_Cy3 and EpCAM_Cy5. To test the sensor functionality, the spectra of the blank samples and the model samples were evaluated and used for further calculation. The analysis was done using 10 blank samples and 10 model samples. Each sample was measured five times. The average intensity of Cy3, Cy5, and

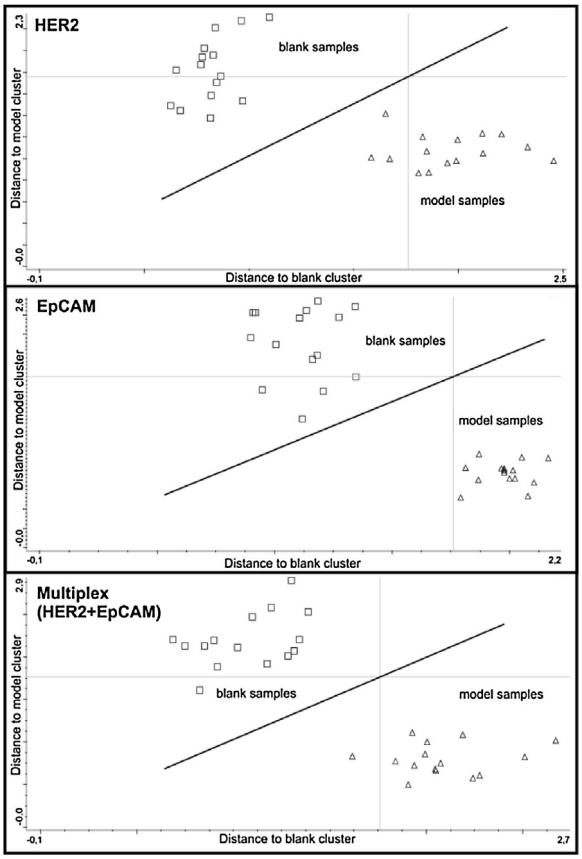

Fig. 5. Discriminant analysis of MNPs with single markers HER2, EpCAM, and sensor (MNPs@anti-HER2@anti-EpCAM) for multiplex analysis.

reference spectral bands, obtained for five independent measurements, was used for the calculation of the overall intensity ratio as

$$R_{\mathrm{Tag}} = \frac{I_{\mathrm{Tag}}}{I_{\mathrm{ref}}} \quad (1)$$

where I_{Tag} represents a spectral intensity of the respective Raman tag (Cy3 or Cy5), and I_{ref} represents a spectral intensity of the reference band present at 660 cm^{-1}. The ratios were calculated for the blank samples (PBS buffer, c = 10 nM, pH 7), and model samples containing natural HER2 and EpCAM compounds in ratios 1:1 and 1:2 (c/c, tagged:natural). The competition between the tagged and the natural antigens will be projected in the lowered intensity of spectral bands characteristic for the tags. This hypothesis was confirmed in the present Raman spectra of the blank sample and the model sample containing 10 ng L^{-1} HER2 and EpCAM (Fig. S6). The decrease in the signal intensities was determined for each tag separately. The intensity ratio ($I_{\mathrm{Tag}}/I_{\mathrm{ref}}$) changed from 0.15 (Cy3) and 0.12 (Cy5) in the blank samples that contained only labeled markers to 0.08 (Cy3) and 0.03 (Cy5) in the model samples that also contained unlabeled markers. Such changes refer to a successful interaction between sensor and natural HER2 and EpCAM compounds and occupation of binding sites by natural markers prior to labeled markers.

3.4. Statistical evaluation of the method

The method potential was further evaluated by a discriminant analysis, where spectral bands of the reference (tyrosine), Cy3, and Cy5 (660, 475, and 373 cm^{-1}) were included. Fig. 5 demonstrates the presence of significant differences between Raman spectra of blank samples (square mark) and model sample (triangle mark).

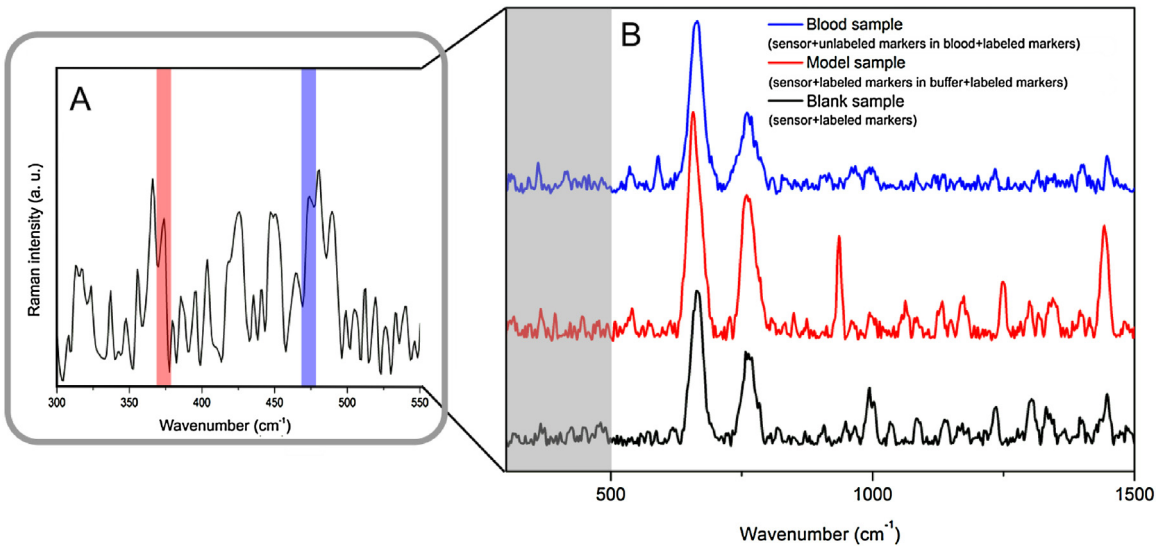

Fig. 6. (A) Detail of the spectral region from 300 to 550 cm^{-1} originated from the marked area in (B); (B) Raman spectra of multiplex analysis using a sensor with only labeled tumor markers HER2 (HER2_Cy3) and EpCAM (EpCAM_Cy5) (black line), Raman spectra of multiplex analysis using a sensor with unlabeled tumor markers in a buffer solution and labeled tumor markers (model sample; red line), Raman spectra of competitive multiplex analysis of human whole blood containing tumor markers using sensor and labeled tumor markers (blue line). The shift between spectra is 200 units of Raman intensity to make the figure more transparent.

The differences were caused by a decrease in intensity due to the competition between the unlabeled markers and the labeled markers as described above. The calculated average Mahalanobis distance between clusters was the following: 1.9 for HER2, 2.0 for EpCAM, and 2.1 for the multiplex sample.

3.5. Stability and reproducibility

Signal and sensor stability were evaluated to test the method's reliability. The signal stability was tested with a blank sample to obtain the Raman spectra during the time interval from 2 to 12 min after the preparation. Fig. S7 shows that all the spectra contain the same spectral bands, although their absolute intensities decrease inappreciably over time. Also, the reproducibility of the system was tested. Raman spectra of six different drops of the sensor with the labeled markers are presented in Fig. S8. In both cases, the spectra are very similar without any considerable changes and it can be thus stated that the method produces repeatable results. The spectra were supported by calculating the relative standard deviation (RSD) separately for each tag. The calculated RSD values, defined as an I373/I660 ratio or I475/I660 ratio, were 5.6 and 2.2%, respectively. The LOD was determined according the 3 s/m criteria where 's' is the standard deviation of the low concentration of the analyte and 'm' is the slope of the calibration graph (Fig. S9). The calculated value of the LOD was 4.9 ng L^{-1}. Long-term stability was evaluated on the blank sample. The resulting spectra are presented in Fig. S10. Ten days after preparation, the activity of the system was 81%. After 40 days, the intensity of the band at 660 cm^{-1} was 57% lower due to sensor degradation, however it can be clearly seen that the spectrum of the 40-day-old sample contains the same spectral bands as the sample measured immediately after the preparation so the system is still fully operational.

3.6. Multiplex analysis of human whole blood samples

The application potential of the proposed method was further tested with the aim of using it for the competitive multiplex analysis of human whole blood samples (details are given in Section 2). Ten samples from two volunteers were collected and analyzed five times to perform a statistical evaluation. The process of the sensor synthesis was tuned to minimize nonspecific interactions of the functionalized MNPs with non-targeted compounds present in the complex matrix of human blood by addition of ethylamine in the last step of sensor preparation and careful multiple washing with deionized water. However, new spectral bands located at 560 and 1242 cm^{-1} in the spectrum of the blood sample indicate minor nonspecific interactions; nonetheless, their interference is minimized by a described post-processing procedure and they do not influence the detection. A SERS spectrum for the whole blood is presented in Fig. 6, showing that all the bands previously attributed to the model and blank samples (a) demonstrate an absence of interfering nonspecific interactions and (b) show a change in absolute intensities of the evaluated spectral bands with respect to a changing concentration of target compounds HER2 and EpCAM. The additional statistical evaluation was performed by Student's *t*-test for paired group. Student's *t*-tests were performed to determine the significance of differences of average intensity ratios for Cy3 and Cy5 (as described earlier) between blank and whole blood samples. The calculated *p*-values were 0.0093 for HER2 and 0.0016 for EpCAM. Such results show a statistically significant difference between the samples. The results of the *t*-test for competitive multiplex analysis are in Table S1.

4. Conclusions

Current screening methods for the detection of cancer markers in clinical samples are mostly based on the fluorescence analysis. Such methods can detect targets at low concentration levels but the high risk of autofluorescence and photobleaching makes these methods difficult to apply to all samples. Here we report a magnetic biosensor for the multiplex detection of tumor markers in the whole human blood. The designed sensor enables simultaneous detection of two different tumor markers in one step using SERS. Moreover, the magnetic properties allow a simple manipulation. The analysis is based on the competition between unlabeled (HER2, EpCAM) and tagged biomarkers (HER2_Cy3, EpCAM_Cy5) to minimize the influence of nonspecific interactions. Both biomarkers compete for the active sites on the respective antibodies, anchored on a surface of the prepared sensor. The benefit of such an approach lies mainly in the possible substitution of anti-HER2 and anti-EpCAM for other antibodies as well as for other small molecular

targets using specific compounds that can be employed in the analysis. An interesting alternative would be the application of the designed sensor for the screening of CTCs in blood, which is essential for the early detection of cancer and tracing metastasis in real time.

Acknowledgements

The authors would like to thank Ondřej Tomanec and Klára Čépe for providing HRTEM and EDX and also Josef Kašlík for XRD data. The authors gratefully acknowledge the support from project NPU LO1305 of the Ministry of Education, Youth and Sports of the Czech Republic.

Appendix A. Supplementary data

Supplementary data associated with this article can be found, in the online version, at doi:10.1016/j.apmt.2018.08.016.

References

[1] L.A. Torre, R.L. Siegel, E.M. Ward, A. Jemal, Global cancer incidence and mortality rates and trends—an update, Cancer Epidemiol. Biomarkers Prev. 25 (2016) 16–27.
[2] S. Feng, S. Huang, D. Lin, G. Chen, Y. Xu, Y. Li, Z. Huang, J. Pan, R. Chen, H. Zeng, Surface-enhanced Raman spectroscopy of saliva proteins for the noninvasive differentiation of benign and malignant breast tumors, Int. J. Nanomed. 10 (2015) 537–547.
[3] R. Nagler, G. Bahar, T. Shpitzer, R. Feinmesser, Concomitant analysis of salivary tumor markers—a new diagnostic tool for oral cancer, Clin. Cancer Res. 12 (2006) 3979–3984.
[4] N. Kosaka, H. Iguchi, T. Ochiya, Circulating microRNA in body fluid: a new potential biomarker for cancer diagnosis and prognosis, Cancer Sci. 101 (2010) 2087–2092.
[5] M. Li, J.W. Kang, S. Sukumar, R.R. Dasari, I. Barman, Multiplexed detection of serological cancer markers with plasmon-enhanced Raman spectro-immunoassay, Chem. Sci. 6 (2015) 3906–3914.
[6] S. Sharma, Tumor markers in clinical practice: general principles and guidelines, Indian J. Med. Paediatr. Oncol. 30 (2009) 1–8.
[7] J. Yang, Z. Wang, S. Zong, C. Song, R. Zhang, Y. Cui, Distinguishing breast cancer cells using surface-enhanced Raman scattering, Anal. Bioanal. Chem. 402 (2012) 1093–1100.
[8] P. Chandra, P. Suman, M. Mukherjee, P. Kumar, HER2 protein biomarker based sensor systems for breast cancer diagnosis, J. Mol. Biomarkers Diagn. 5 (2013) 1000e119.
[9] J.T. Gohring, P.S. Dale, X. Fan, Detection of HER2 breast cancer biomarker using the opto-fluidic ring resonator biosensor, Sens. Actuators B 146 (2010) 226–230.
[10] P.A. Baeuerle, O. Gires, EpCAM (CD326) finding its role in cancer, Br. J. Cancer 96 (2007) 417–423.
[11] V.S.P.K.S.A. Jayanthi, A.B. Das, U. Saxena, Recent advances in biosensor development for the detection of cancer biomarkers, Biosens. Bioelectron. 91 (2017) 15–23.
[12] D. Sidransky, Nucleic acid-based methods for the detection of cancer, Science 278 (1997) 1054–1058.
[13] E. Heyderman, Immunoperoxidase technique in histopathology: applications, methods, and controls, J. Clin. Pathol. 32 (1979) 971–978.
[14] H. Yaziji, L.C. Goldstein, T.S. Barry, R. Werling, H. Hwang, G.K. Ellis, J.R. Gralow, R.B. Livingston, A.M. Gown, HER-2 testing in breast cancer using parallel tissue-based methods, JAMA 291 (2004) 1972–1977.
[15] G. Mor, I. Visintin, Y. Lai, H. Zhao, P. Schwartz, T. Rutherford, L. Yue, P. Bray-Ward, D.C. Ward, Serum protein markers for early detection of ovarian cancer, Proc. Natl. Acad. Sci. USA 102 (2005) 7677–7682.
[16] R.L. Camp, L.A. Charette, D.L. Rimm, Validation of tissue microarray technology in breast carcinoma, Lab. Invest. 80 (2000) 1943–1949.
[17] L. Bubendorf, A. Nocito, H. Moch, G. Sauter, Tissue microarray (TMA) technology: miniaturized pathology archives for high-throughput *in situ* studies, J. Pathol. 195 (2001) 72–79.
[18] M.J. Lodes, M. Caraballo, D. Suciu, S. Munro, A. Kumar, B. Anderson, Detection of cancer with serum miRNAs on an oligonucleotide microarray, PLoS ONE 4 (2009) e6229.
[19] S. Sassen, E.A. Miska, C. Caldas, MicroRNA—implications for cancer, Virchows Arch. 452 (2008) 1–10.
[20] B. Mostert, S. Sleijfer, J.A. Foekens, J.W. Gratama, Circulating tumor cells (CTCs): detection methods and their clinical relevance in breast cancer, Cancer Treat. Rev. 35 (2009) 463–474.
[21] J. Zhou, Y. Zheng, J. Liu, X. Bing, J. Hua, H. Zhang, A paper-based detection method of cancer cells using the photo-thermal effect of nanocomposite, J. Pharm. Biomed. Anal. 117 (2016) 333–337.
[22] C. Gao, M. Su, Y. Wang, S. Ge, J. Yu, A disposable paper-based electrochemiluminescence device for ultrasensitive monitoring of CEA based on $Ru(bpy)_3^{2+}$@Au nanocages, RSC Adv. 5 (2015) 28324–28331.
[23] N. Radha Shanmugam, S. Muthukumar, S. Chaudhry, J. Anguiano, S. Prasad, Ultrasensitive nanostructure sensor arrays on flexible substrates for multiplexed and simultaneous electrochemical detection of a panel of cardiac biomarkers, Biosens. Bioelectron. 89 (2017) 764–772.
[24] J.S. Ross, E.A. Slodkowska, W.F. Symmans, L. Pusztai, P.M. Ravdin, G.N. Hortobagyi, The HER-2 receptor and breast cancer: ten years of targeted Anti–HER-2 therapy and personalized medicine, Oncologist 14 (2009) 320–368.
[25] A. Balzerova, A. Fargasova, Z. Markova, V. Ranc, R. Zboril, Magnetically-assisted surface enhanced Raman spectroscopy (MA-SERS) for label-free determination of human immunoglobulin G (IgG) in blood using Fe_3O_4@Ag nanocomposite, Anal. Chem. 86 (2014) 11107–11114.
[26] B.-H. Jun, M.S. Noh, G. Kim, H. Kang, J.-H. Kim, W.-J. Chung, M.-S. Kim, Y.-K. Kim, M.-H. Cho, D.H. Jeong, Y.-S. Lee, Protein separation and identification using magnetic beads encoded with surface-enhanced Raman spectroscopy, Anal. Biochem. 391 (2009) 24–30.
[27] L. Chen, W. Hong, Z. Guo, Y. Sa, X. Wang, Y.M. Jung, B. Zhao, Magnetic assistance highly sensitive protein assay based on surface-enhanced resonance Raman scattering, J. Colloid Interface Sci. 368 (2012) 282–286.
[28] C. Wang, J. Wang, M. Li, X. Qu, K. Zhang, Z. Rong, R. Xiao, S. Wang, A rapid SERS method for label-free bacteria detection using polyethylenimine-modified Au-coated magnetic microspheres and Au@Ag nanoparticles, Analyst 141 (2016) 6226–6238.
[29] J. Wang, X. Wu, C. Wang, Z. Rong, H. Ding, H. Li, S. Li, N. Shao, P. Dong, R. Xiao, S. Wang, Facile synthesis of Au-coated magnetic nanoparticles and their application in bacteria detection via a SERS method, ACS Appl. Mater. Interfaces 8 (2016) 19958–19967.
[30] J. Wang, X. Wu, C. Wang, N. Shao, P. Dong, R. Xiao, S. Wang, Magnetically assisted surface-enhanced Raman spectroscopy for the detection of *Staphylococcus aureus* based on aptamer recognition, ACS Appl. Mater. Interfaces 7 (2015) 20919–20929.
[31] J. Baniukevic, I. Hakki Boyaci, A. Goktug Bozkurt, U. Tamer, A. Ramanavicius, A. Ramanaviciene, Magnetic gold nanoparticles in SERS-based sandwich immunoassay for antigen detection by well oriented antibodies, Biosens. Bioelectron. 43 (2013) 281–288.
[32] Y. Sun, L. Xu, F. Zhang, Z. Song, Y. Hu, Y. Ji, J. Shen, B. Li, H. Lu, H. Yang, A promising magnetic SERS immunosensor for sensitive detection of avian influenza virus, Biosens. Bioelectron. 89 (2017) 906–912.
[33] V. Ranc, Z. Markova, M. Hajduch, R. Prucek, L. Kvitek, J. Kaslik, K. Safarova, R. Zboril, Magnetically assisted surface-enhanced Raman scattering selective determination of dopamine in an artificial cerebrospinal fluid and a mouse striatum using Fe_3O_4/Ag nanocomposite, Anal. Chem. 86 (2014) 2939–2946.
[34] Y. Qiu, D. Deng, Q. Deng, P. Wu, H. Zhang, C. Cai, Synthesis of magnetic Fe_3O_4–Au hybrids for sensitive SERS detection of cancer cells at low abundance, J. Mater. Chem. B 3 (2015) 4487–4495.
[35] M.S. Noh, B.-H. Jun, S. Kim, H. Kang, M.-A. Woo, A. Minai-Tehrani, J.-E. Kim, J. Kim, J. Park, H.-T. Lim, S.-C. Park, T. Hyeon, Y.-K. Kim, D.H. Jeong, Y.-S. Lee, M.-H. Cho, Magnetic surface-enhanced Raman spectroscopic (M-SERS) dots for the identification of bronchioalveolar stem cells in normal and lung cancer mice, Biomaterials 30 (2009) 3915–3925.
[36] C. Song, Y. Yang, B. Yang, L. Min, L. Wang, Combination assay of lung cancer associated serum markers using surface-enhanced Raman spectroscopy, J. Mater. Chem. B 4 (2016) 1811–1817.
[37] C. Sun, R. Zhang, M. Gao, X. Zhang, A rapid and simple method for efficient capture and accurate discrimination of circulating tumor cells using aptamer conjugated magnetic beads and surface-enhanced Raman scattering imaging, Anal. Bioanal. Chem. 407 (2015) 8883–8892.
[38] C. Song, L. Min, N. Zhou, Y. Yang, B. Yang, L. Zhang, S. Su, L. Wang, Ultrasensitive detection of carcino-embryonic antigen by using novel flower-like gold nanoparticle SERS tags and SERS-active magnetic nanoparticles, RSC Adv. 4 (2014) 41666–41669.
[39] Y. Lin, G. Xu, F. Wei, A. Zhang, J. Yang, Q. Hu, Detection of CEA in human serum using surface-enhanced Raman spectroscopy coupled with antibody-modified Au and γ-Fe_2O_3@Au nanoparticles, J. Pharm. Biomed. Anal. 121 (2016) 135–140.
[40] R. Gao, Z. Cheng, A.J. deMello, J. Choo, Wash-free magnetic immunoassay of the PSA cancer marker using SERS and droplet microfluidics, Lab Chip 16 (2016) 1022–1029.
[41] U.S. Dinish, G. Balasundaram, Y.-T. Chang, M. Olivo, Actively targeted in vivo multiplex detection of intrinsic cancer biomarkers using biocompatible SERS nanotags, Sci. Rep. 4 (2014) 4075.
[42] J. Li, S. Dong, J. Tong, P. Zhu, G. Diao, Z. Yang, 3D ordered silver nanoshells silica photonic crystal beads for multiplex encoded SERS bioassay, Chem. Commun. 52 (2016) 284–287.
[43] J.H. Granger, M.C. Granger, M.A. Firpo, S.J. Mulvihill, M.D. Porter, Toward development of a surface-enhanced Raman scattering (SERS)-based cancer diagnostic immunoassay panel, Analyst 138 (2013) 410–416.
[44] W. Lu, Y. Wang, X. Cao, L. Li, J. Dong, W. Qian, Multiplexing determination of lung cancer biomarkers using electrochemical and surface-enhanced Raman spectroscopic techniques, New J. Chem. 39 (2015) 5420–5430.
[45] B. Tang, J. Wang, J.A. Hutchison, L. Ma, N. Zhang, H. Guo, Z. Hu, M. Li, Y. Zhao, Ultrasensitive, multiplex Raman frequency shift immunoassay of liver cancer biomarkers in physiological media, ACS Nano 10 (2016) 871–879.

[46] K.K. Maiti, U.S. Dinish, C.Y. Fu, J.-J. Lee, K.-S. Soh, S.-W. Yun, R. Bhuvaneswari, M. Olivo, Y.-T. Chang, Development of biocompatible SERS nanotag with increased stability by chemisorption of reporter molecule for *in vivo* cancer detection, Biosens. Bioelectron. 26 (2010) 398–403.
[47] A. Fargašová, R. Prucek, V. Ranc, A. Panáček, L. Kvítek, R. Zbořil, Influence of various chloride ion concentrations on silver nanoparticle transformations and effectiveness in surface enhanced Raman scattering for different excitation wavelengths, RSC Adv. 5 (2015) 9737–9744.
[48] R. Li, R. Wu, L. Zhao, M. Wu, L. Yang, H. Zou, P-glycoprotein antibody functionalized carbon nanotube overcomes the multidrug resistance of human leukemia cells, ACS Nano 4 (2010) 1399–1408.
[49] K. Jiang, L.S. Schadler, R.W. Siegel, X. Zhang, H. Zhang, M. Terrones, Protein immobilization on carbon nanotubes *via* a two-step process of diimide-activated amidation, J. Mater. Chem. 14 (2004) 37–39.
[50] A. Barth, Infrared spectroscopy of proteins, Biochim. Biophys. Acta Bioenerg. 1767 (2007) 1073–1101.
[51] L.K. Tamm, S.A. Tatulian, Infrared spectroscopy of proteins and peptides in lipid bilayers, Q. Rev. Biophys. 30 (1997) 365–429.
[52] V. Kumar, G. Nath, R.K. Kotnala, P.S. Saxena, A. Srivastava, Biofunctional magnetic nanotube probe for recognition and separation of specific bacteria from a mixed culture, RSC Adv. 3 (2013) 14634–14641.
[53] A. Kasprzak, M. Poplawska, M. Bystrzejewski, I.P. Grudzinski, Sulfhydrylated graphene-encapsulated iron nanoparticles directly aminated with polyethylenimine: a novel magnetic nanoplatform for bioconjugation of gamma globulins and polyclonal antibodies, J. Mater. Chem. B 4 (2016) 5593–5607.
[54] R. Tuma, Raman spectroscopy of proteins: from peptides to large assemblies, J. Raman Spectrosc. 36 (2005) 307–319.
[55] S. Feng, R. Chen, J. Lin, J. Pan, G. Chen, Y. Li, M. Cheng, Z. Huang, J. Chen, H. Zeng, Nasopharyngeal cancer detection based on blood plasma surface-enhanced Raman spectroscopy and multivariate analysis, Biosens. Bioelectron. 25 (2010) 2414–2419.

Analytical and Bioanalytical Chemistry
https://doi.org/10.1007/s00216-018-1311-4

RESEARCH PAPER

Imaging of growth factors on a human tooth root canal by surface-enhanced Raman spectroscopy

Václav Ranc[1] · Radovan Žižka[2] · Zuzana Chaloupková[1] · Juraj Ševčík[3] · Radek Zbořil[1]

Received: 4 May 2018 / Revised: 30 July 2018 / Accepted: 6 August 2018

Abstract

Endodontic treatment of immature permanent teeth with necrotic pulp poses several clinical challenges and is one of the most demanding interventions in endodontics. Recently, with new discoveries in the field of tissue engineering, novel treatment protocols have been established. The most promising treatment modality is revascularization, whose integral part is the exposure of collagen matrix and embedded growth factors. However, optimization of the treatment protocol requires a development of analytical procedures able to analyze growth factors directly on the sample surface. In this work, method based on surface-enhanced Raman spectroscopy (SERS) was developed to investigate the influence of the time of the medical treatment using EDTA on exposure and accessibility of the growth factors, namely TGF-ß1, BMP-2, and bFGF on the dentine surface. The nanotags, which consist of magnetic Fe_3O_4@Ag nanocomposite covalently functionalized by tagged antibodies (anti-TGF-ß1-Cy3, anti-BMP-2-Cy5, and anti-bFGF-Cy7), were employed as a SERS substrate. Each antibody was coupled with a unique label allowing us to perform a parallel analysis of all three growth factors within one analytical run. Developed methodology presents an interesting alternative to a fluorescence microscopy and in contrary allows evaluating a chemical composition and thus minimizing possible false-positive results.

Keywords SERS · Nanocomposites · Growth factors · Imaging

Introduction

The endodontic treatment of immature permanent teeth with necrotic pulp remains one of the most challenging treatment options in endodontics. Root canal treatment is nowadays a standard modality for teeth with infected dental pulp [1]. However, this process is still a subject to several clinical challenges [2, 3]. Nowadays, the cell-free approach of regenerative treatment known as revascularization or revitalization belongs among the most applied approaches. It depends on the intracanal delivery of scaffold which is rich in growth factors and contains stem cells or can attract such cells residing in the periapical region [4, 5]. The growth factors of the extracellular dentinal matrix, with significant roles in pulp-dentin regeneration, are transforming growth factor-beta1 (TGF-ß1), bone morphogenetic protein-2 (BMP-2), and basic fibroblast growth factor (bFGF). One of the most considerable challenges of the newly developed protocols is efficient removal of the present smear layer [6]. Smear layer is an amorphous layer of dentin, pulp, and bacterial remnants which is produced during cavity preparation or root canal instrumentation. The content is composed of two distinct layers where a thin superficial layer 1–2 μm thick is overlying a densely packed layer that penetrated into the dentinal tubules which are subsequently occluded. The organic part is mostly composed of collagen residues and glycosaminoglycans [7]. Its presence is efficiently lowering the availability of the growth factors by an effective blocking of the surface for further interactions. Based on its structure, it cannot be removed by a water stream, and it is thus usually treated with acids [8] or chelators such as ethylenediaminetetraacetic acid (EDTA)

✉ Václav Ranc
vaclav.ranc@upol.cz

[1] Regional Centre of Advanced Technologies and Materials, Department of Physical Chemistry, Faculty of Science, Palacký University Olomouc, 17. listopadu 12, 771 46 Olomouc, Czech Republic

[2] Czech Educational and Dental Research Innovative Group, 602 00 Brno, Czech Republic

[3] Department of Analytical Chemistry, Faculty of Science, Palacký University Olomouc, 17. listopadu 12, 771 46 Olomouc, Czech Republic

Published online: 15 August 2018

[9–11]. The efficiency of each treatment approach is given by the number of the exposed growth factors available for further interactions with the introduced stem cells, and development of analytical protocols allowing us to study the distribution of the growth factors on the dentin surface is thus essential.

Majority of approaches is based on immunohistochemical localization of the growth factors, including recently published works by Hisamoto et al. [12], where selected growth factors and receptors in the tooth germ of murine fetuses and neonates were studied; Shubo et al. [13], where an expression of growth factors such as connective tissue growth factor and TGF-ß1 was studied during a mouse tooth development; and Niwa et al., who demonstrated a localization of TGF-ß in dental pulp, odotoblasts, and dentin [14]. However, the results obtained by an immunohistochemical analysis could be influenced by a presence of nonspecific interactions and thus false-positive results. Interestingly, only a limited number of works employs alternative approaches. One of few examples was demonstrated by Zhao et al., where a distribution of TGF-ß isoforms on dentinal cut surfaces of mature teeth was studied using an electron microscopy and functionalized gold substrate [15].

To our best knowledge, parallel imaging of growth factors directly on the dentin surface using molecular spectroscopy has not been reported yet. Raman spectroscopy has been previously exploited in this area only superficially, despite its considerable potential. It was applied in the analysis of carious lesions in enamel [16], analysis of enamel fluorosis at healthy and affected samples [17], study of dentine [18], or analysis of microorganism present in oral cavity [19, 20]. The potential of Raman spectroscopy was considerably increased with a discovery of surface-enhanced Raman scattering (SERS) by Fleishman [21]. Recent modification of SERS, The magnetically assisted surface-enhanced Raman spectroscopy (MA-SERS) presents an interesting alternative to a selective detection of single molecules, such as PSMA, dopamine, or IgG [22–24]. However, its application in surface imaging was limited. The aims of this present work are to enhance the original MA-SERS methodology and to apply it in a parallel imaging of growth factors, namely TGF-β1, BMP-2, and bFGF, on root dentin canals on four real samples. The developed methodology is based on magnetic Fe_3O_4@Ag nanosensors, functionalized using covalently anchored antibodies tagged with unique Raman tags.

Experimental section

Reagents and chemicals

Silver nitrate (p.a.), 1-[3-(dimethylamino)propyl]-3-ethylcarbodiimide methiodide (EDC), N-hydroxysulfosuccinimide sodium salt (98% (HPLC); NHS), Cy3 mAb kit, Cy5 mAb kit, and Cy7 mAb kit were purchased from Sigma-Aldrich (San Jose, USA). H_3PO_4 (p.a., 85% *w*/*w*) and NaOH (p.a.) were purchased from Lach-Ner. Acetic acid (99.8%) and methanol (p.a.) were obtained from P-LAB (Czech Republic). Antibodies, namely anti-TGF-ß1, anti-BMP-2, and anti-bFGF, were purchased from Abcam (UK).

Sample extraction

Five non-carious immature single-rooted human premolars were obtained from three patients in cases where extraction of these teeth had been indicated for orthodontic reasons and otherwise the teeth would have been disposed of. The parents were informed about further usage of the extracted premolars and a written informed consent was obtained. The approval of the ethic committee of the Faculty Hospital Olomouc and Medical Faculty of Palacký University for the study was obtained (NV-18-08-00328). After extraction, the teeth were washed with saline (0.9% NaCl, B. Braun Medical, Melsungen, Germany), stored in a solution of inorganic salts (1.5 mmol/L $CaCl_2$, 1.0 mmol/L KH_2PO_4, 50.0 mmol/L NaCl) and immediately transported for specimen preparation.

Sample treatment using EDTA

After radiological verification that only one root canal is present, the teeth were decoronated and the roots were sectioned in the middle of the longitudinal and horizontal dimension plane with a segmented diamond-edged blade cooled by water. Under this procedure, four specimens from one tooth with the intact surface of the root canal have been obtained and were randomly divided into four groups—negative control group, positive control group, and two experimental groups with different time exposures with 17% EDTA; five samples from different specimen were present in each group. In the negative control and experimental groups, the surface of the root canal was smoothened with a diamond burr (FGSL H.1.316.010, Komet USA, Rock Hill, USA) to obtain the smear layer. In the positive control group (labeled as physiological sample), the specimen was rinsed with saline (0.9% NaCl, B. Braun Medical, Melsungen, Germany). In the experimental groups, the surface of the root canal was rinsed with 17% EDTA (MD-Cleanser, Meta Biomed, Cheongju-Si, South Korea) for 5 and 20 min and subsequently rinsed with saline (0.9% NaCl, B. Braun Medical, Melsungen, Germany).

Tagging of antibodies

Antibodies, namely anti-TGF-ß1, anti-BMP-2, and anti-bFGF, were labeled using a labeling kit containing reactive fluorescent dye Cy3, Cy5, and Cy7 tags, coupling buffer (1 M sodium carbonate buffer, pH 9.3) and PBS buffer. Anti-TGF-B1 protein was labeled with a Cy3 tag, anti-

BMP-2 with a Cy5 tag, and anti-bFGF with a Cy7 tag according to the obtained standard protocol. Labeled proteins were purified by using centrifugal filter units (Amicon Ultra 0.5 mL, MWCO 3 kDa) at 10,000 rpm for 10 min to separate an excessive free compound.

Preparation of silver nanoparticles

Silver nanoparticles were prepared by a reduction of silver ammonia complex cation $[Ag(NH_3)^2]^+$ with D-maltose according to the protocol previously described by Panacek et al. [25]. Briefly, silver nitrate and maltose were dissolved in deionized water to achieve a concentration of 1 mmol and 10 mmol, respectively. The added concentration of ammonia was 5 mmol. After the silver, sugar, and ammonia were added, the reaction system's pH was adjusted to 11.5 by adding sodium hydroxide to initiate the reduction process. The reaction was complete after 4 min having yielded a suspension of silver nanoparticles with an average particle size of 30 nm, measured by a dynamic light scattering method.

Synthesis of Fe_3O_4@Ag nanocomposite

The magnetite nanoparticles stabilized by using carboxymethyl chitosan (CMC) were prepared according to the protocol described by Markova et al. [26]. Briefly, carboxymethyl chitosan and $FeSO_4.7H_2O$ form a complex in aqueous solution. When NH_4OH (28%) is added to the mixture and the suspension is heated to 50 °C, magnetic nanoparticles are formed. The sample was centrifuged and the supernatant containing residual chemicals was removed and replaced with water. Finally, 10 μL of dispersion containing previously prepared silver nanoparticles ("Preparation of silver nanoparticles" section) was mixed with 200 μL of dispersion containing prepared magnetic nanoparticles. The silver nanoparticles were immobilized on the present carboxymethyl chitosan shell via a bond between present nitrogen atoms and silver. The formed nanocomposite was stirred for 10–15 min at room temperature.

Functionalization of nanomaterials

The prepared nanomaterial was functionalized using antibodies, tagged with Raman labels. First, 75 μL of CMC magnetic nanocomposite was activated by using 15 μL EDC (1 mM) for 60 min. Next, 15 μL of NHS (1 mM) and respective Raman-tagged antibody (50 μM) were added and let react overnight. The magnetic properties of the nanocomposite allowed to quantitatively isolate the product from the reaction medium by a simple application of external magnetic field wash it three times with a distilled water. This step minimized a presence of nonspecific adsorption of free Raman tags and free antibodies on a surface of the nanosensor.

Sample pretreatment

Each sample was immersed in a 1 mL solution containing 100 μL of each functionalized nanomaterial, namely Fe_3O_4@Ag@anti-TGF-ß1@Cy3, Fe_3O_4Ag@anti-BMP-2@Cy5, and Fe_3O_4Ag@anti-bFGF@Cy7. The sample was let to interact for 20 min. When finished, it was washed in water three times to remove any unbonded nanomaterial.

Apparatus

Sample Raman spectra were acquired using a DXR Raman spectrometer (Thermo Scientific, USA) equipped with a red excitation laser operating at the wavelength of 633 nm. Stokes Raman spectra were collected at wavenumbers of 400–1800 cm^{-1} and a spectral resolution 1.0 cm^{-1}. The spectrometer operated under the following conditions: exposure time 32 s and laser power on sample 2 mW. In each case, an averaged Raman spectrum was obtained from a total of 32 micro scans. SERS spectra were measured using procedure described earlier by Prucek et al. [27]. Briefly, 200 μL of the prepared silver nanoparticles (described in the "Preparation of silver nanoparticles" section) was mixed with 100 μL of aqueous solution NaCl ($c = 4$ mol L^{-1}) and 690 μL of water. Consequently, 10 μL of analyte ($c = 10$ μmol L^{-1}) was added and sample was shaken. Resulting dispersion was measured in a quartz cuvette 3 min after its preparation using instrumental parameters described above. The acquired spectral data were evaluated using instrument control software (Omnic, version 8, Thermo Scientific, USA). The ζ potentials of nanocomposites and sizes of silver nanoparticles were measured using a Zetasizer NanoZS (Malvern, UK). A transmission electron microscope (TEM) (JEM 2010, Jeol, Japan) was used to obtain images and high-angle, annular dark field (HAADF) analysis of the final sensor. The TEM was operated at a voltage of 160 kV with a point-to-point resolution of 1.9 Å. Fluorescence microscopy was performed on an Olympus IX70 microscope with fluorescent mode. Samples of dentine treated using respective prepared nanosensors ("Sample pretreatment" section) were deposited on a microscopy glass and measured.

Raman imaging

Raman imaging was performed using a DXR micro-Raman spectrometer (Thermo Scientific, USA) with an excitation laser operating at 633 nm, spectral resolution 3 cm^{-1}, and spatial resolution 1 μm. The exposure time was set to 2 s, the spectra were averaged from 16 micro scans, and the laser power on the sample was set to 3 mW. The microscope was equipped with a × 50 objective, NA = 0.75, and estimated diameter of the irradiated spot was 1.6 μm. Spectral maps contain 100 × 100 Raman spectra, with a spacing 2 μm, giving a total number of 10.000 points.

Data processing

During this processing, the spectral background was corrected using an algorithm based on polynomial fitting with an order of 3. The measured spectra were plotted regarding Raman-scattered photon counts. Signal processing was performed using the TQ-Analyst software package (Omnic version 8, Thermo Scientific, USA) and QTI plot (version 0.9.9.1, Romania), respectively. Raman intensities of Cy3, Cy5, and Cy7 in the measured spectral maps were normalized to the intensity of the phosphate band at 960 cm^{-1} to minimize influences of the sample topography.

Results and discussion

Characterization of the nanosensor

Firstly, the functionalized nanocomposite was characterized by electron microscopy and EDX element mapping to evaluate its morphology, size distribution, and composition. Figure 1 shows TEM and EDX images of the functionalized nanocomposite with the average size of the spherical silver nanoparticles 30 nm and spherical maghemite nanocrystallite 10 nm (measured by TEM). It is worth mentioning that the magnetic nanoparticles are localized in clusters formed by the combination of the sample treatment required for a TEM imaging and magnetic forces among nanoparticles. Analysis of the bare Ag nanoparticles as well as Fe_3O_4@Ag nanocomposites using DLS is shown in Fig. 1d, where the size of Ag nanoparticles corresponds to previous findings based on TEM. Size of the magnetic nanocomposite was determined to 140 nm. The difference is caused by a formation of clusters due to a combination of electrostatic and magnetic interactions. The analysis of the ζ potential uncovered a considerable change from − 42 mV for a Fe_3O_4@Ag nanocomposite to + 2 mV for the material functionalized using the tagged antibodies. This considerable change is caused by anchoring the positively charged Raman-tagged protein on a surface of the negatively charged nanocomposite. The system is colloidally stable despite a low deviation of the value form zero due to electrostatic interactions between the anchored proteins.

To minimize possible interferences of the sample on the signal of nanosensor, the raw surface was first measured by Raman spectroscopy; obtained spectral data are shown in Fig. 2a. Signal contain characteristic bands for $\nu_1PO_4^{3-}$ (spectral band at 960 cm^{-1}) and $\nu_4PO_4^{3-}$ (spectral band at 588 cm^{-1}). It is shown that the spectrum does not contain any spectral bands characteristic for proteins, which indicates that their concertation is below the limit of detection of Raman spectroscopy, and surface-enhanced Raman scattering needs to be applied to visualize their distribution. Next, SERS spectra of Cy3, Cy5, and Cy7 were evaluated. Spectral data are shown in Fig. 2b and are in a full agreement with previously published results [28]. Next, antibodies, namely anti-TGF-β1, anti-BMP-2, and anti-bFGF, were measured using SERS, and resulting spectra are shown in Fig. 2c. Spectral data contain dominantly bands characteristic for proteins, including amide I and III, located at 1652 cm^{-1} and 1304 cm^{-1} However, the measured dentine contains a large set of proteins, including targeted growth factors. Moreover, measured spectra are frequently burdened with fluorescence (as shown in Fig. 2c, SERS spectrum of anti-bFGF). Selective detection of interaction between the anchored antibody and particular growth factor can be thus difficult and not reliable. Antibodies were thus labeled using Raman active spectral tags, namely Cy3, Cy5, and Cy7 to increase the selectivity of the analysis. Finally, functionalized antibodies together with respective antibodies were characterized using SERS, and resulting data are shown in Fig. 2d–f. SERS spectra contain bands characteristic for both Raman labels and proteins, although present with different intensities, caused by a spatial position of the adsorbed antibody on the surface of the silver nanoparticle. Larger distance of the labels from the

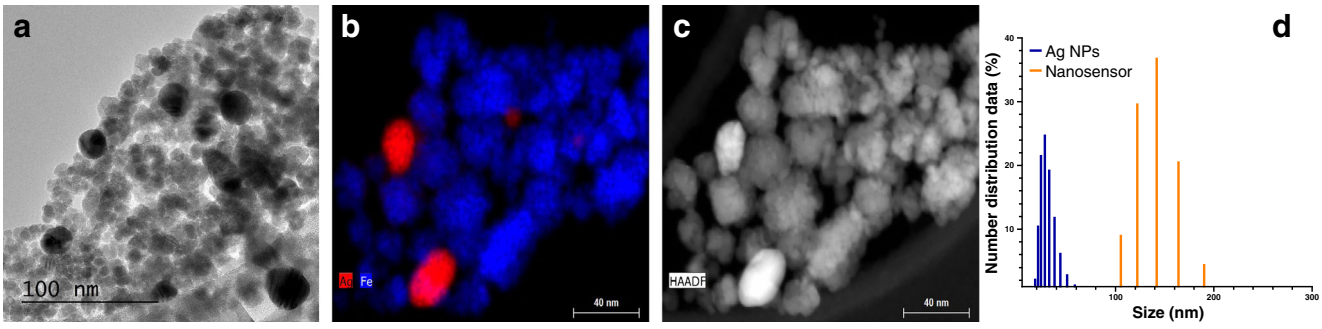

Fig. 1 **a** TEM image of the functionalized nanomaterial. **b** EDX element mapping of the nanocomposite with silver in red color and iron in blue color. **c** HAADF analysis of the nanocomposite, where silver is shown in bright and iron in darker shades. **d** Distribution of sizes of silver nanoparticles and nanosensor Fe_3O_4@Ag measured by DLS

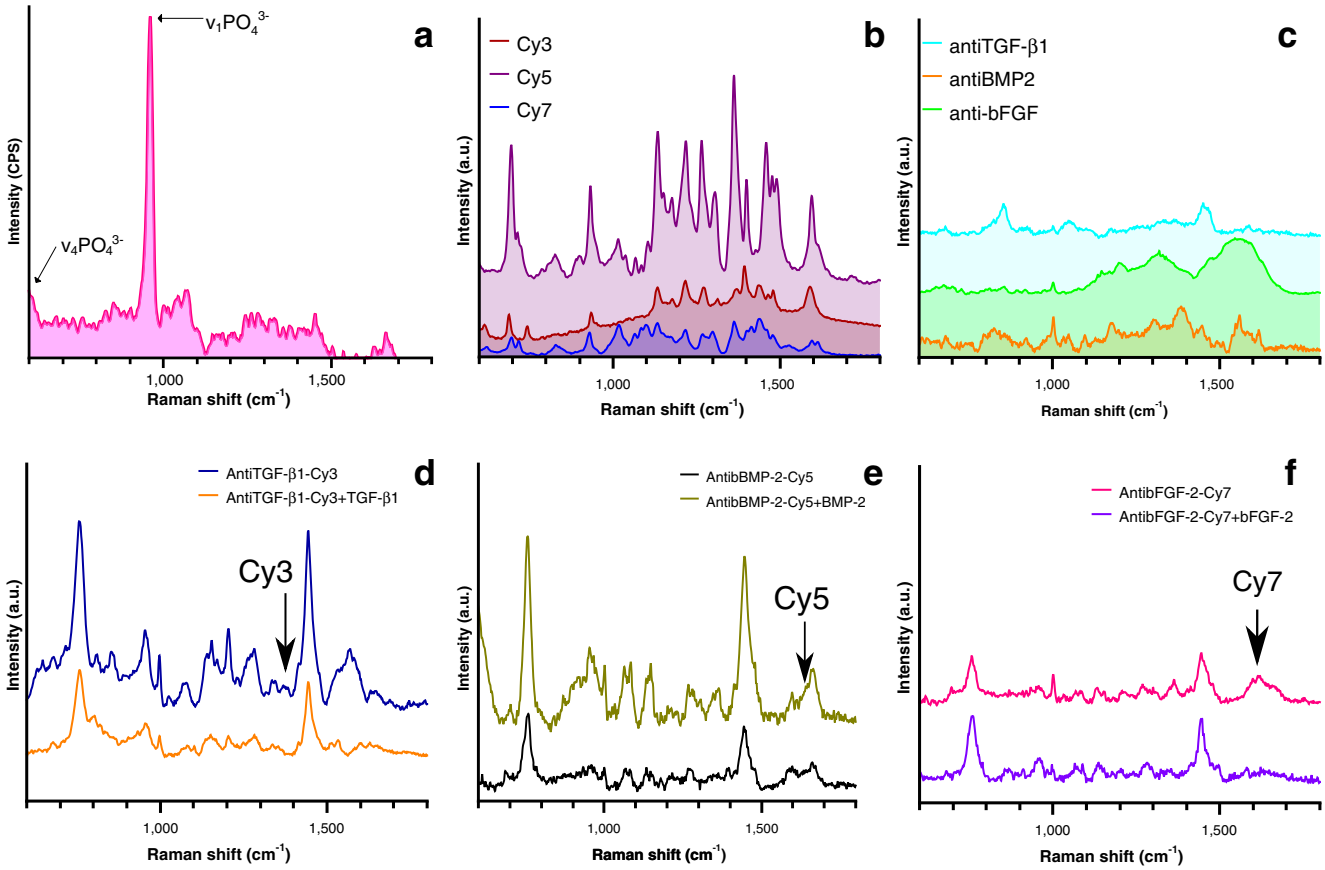

Fig. 2 **a** Raman spectrum of the root canal. **b** SERS spectra of Cy3, Cy5, and Cy7 Raman tags. **c** SERS spectra of antibodies anti-TGF-β1, anti-BMP-2, and anti-bFGF. SERS spectra of particular Raman-tagged antibodies and antibodies with bonded antigens, namely anti-TGF-β1-Cy3 (**d**), anti-BMP-2-Cy5 (**e**), and anti-bFGF-Cy7 (**f**)

nanoparticle surface is indicated by a relatively lower intensity of respective Raman bands, compared to the signal of proteins. Spectral analysis uncovered a presence of spectral bands, characteristic for each Raman tag, namely Raman band at 1395 cm^{-1} for anti-TGF-β1-Cy3, 1597 cm^{-1} for anti-BMP-2-Cy5, and 1621 cm^{-1} for anti-bFGF-Cy7, which were consequently selected for univariate analysis. Successful binding of antigens on the respective antibodies is indicated by a change of spectral intensities of bands characteristic for amino acids. Finally, SERS analysis of a sample containing the prepared nanosensor composed of the Fe_3O_4@Ag nanocomposite covalently functionalized by respective tagged antibodies uncovered a presence of bands characteristic for Raman tags, nanomaterial and anchored antibodies, as shown in Fig. 3a. The spectrum contains all previously identified bands, including bands characteristic for used Raman tags, which indicates a successful immobilization of the tagged antibodies on a surface of the nanocomposite. Spectrum of the prepared nanosensor anchored on a surface of dentine is shown in Fig. 3a (green spectrum). Spectral characteristics of the sensor are not considerably changed during the interaction and signals of particular Raman tags are measurable.

Repeatability and signal stability

The stability of the nanomaterial and the repeatability of the obtained results are considered as the essential factors for a consecutive analysis of real samples. First, the signal stability was analyzed. Six measurements of samples containing Fe_3O_4@Ag@anti-TGF-ß1-Cy3 sensor were performed in 21 days. The sensor was kept in the refrigerator at 7 °C in dark. The signal of the labels moderately decreased, as shown in Fig. 3b, and it is still significantly above a limit of detection (determined as $S/N = 3$) and thus fully utilizable. However, we have applied the sensor no longer than 1 day after the preparation. Based on the sensor nature, similar behavior can be hypothesized for BMP-2 and bFGF sensors. Further, signal repeatability was evaluated on a set of five samples containing Fe_3O_4@Ag@anti-TGF-ß1@Cy3. The measured data are shown in Fig. 3c. Raman spectra were first normalized according to the procedure described in the "Experimental section" and the intensities of the spectral bands characterizing particulate Raman tags, as described previously, were analyzed and subsequently relative standard deviations (RSDs) were calculated. RSD values for all the three tags did not exceed 5%.

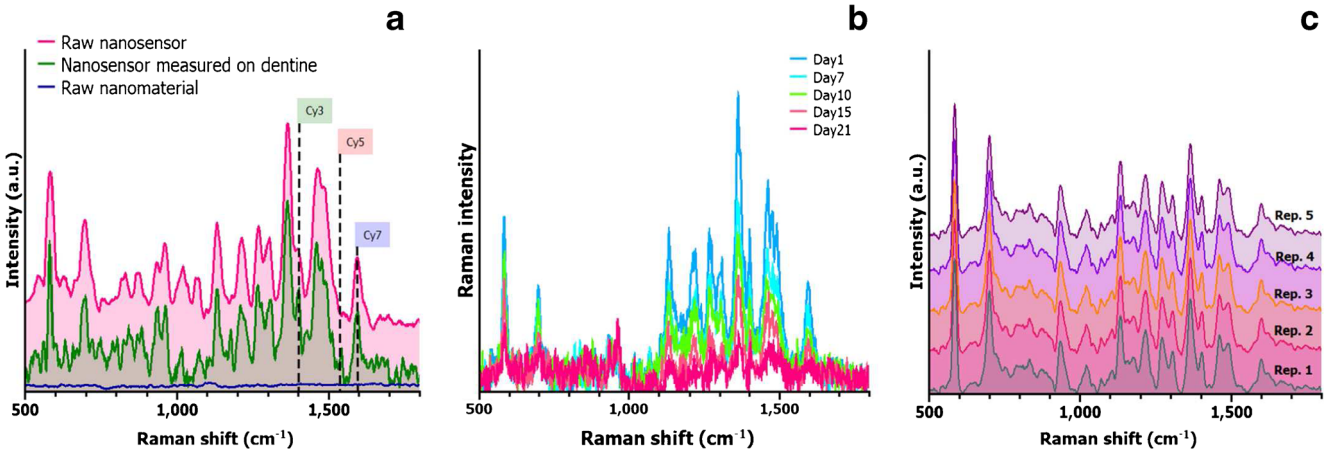

Fig. 3 **a** (blue) Raman spectrum of the pristine Fe_3O_4@Ag nanocomposite, (pink) Raman spectrum of the nanosensor with anchored Raman-tagged antibodies, and (green) average spectrum of the sensor measured on a surface of dentine. **b** Study of the signal stability and stability of the prepared Fe_3O_4@Ag@anti-TGF-ß1-Cy3 sensor. **c** Repeatability of the analytical signal of Fe_3O_4@Ag@anti-TGF-ß1-Cy3 sensor

Sample imaging of growth factors

This study aimed to develop a method for an analysis of selected growth factors on the dentinal surface. The next step involved treating the tooth samples for 5 and 20 min using EDTA in the role of a chelating agent, applied to remove the existing smear layer. The newly developed methodology was consequently utilized to study this process, mainly to evaluate the influence of the treatment time on the availability of growth factors on the sample surface. First, to test the method potential, the surface of a human tooth root canal without any pretreatment was measured. The sample was labeled using a mixture of all the three sensors according to the procedure described in the "Experimental section". First, samples were subjected to analysis using fluorescence microscopy to verify the presence of nanosensors on the sample surface. Obtained results are shown in Fig. 4, where presence of all the three sensors on the surface of the physiological sample is demonstrated.

Univariate analysis, utilizing characteristic spectral bands of each functionalized antibody, was applied in the analysis; particular spectral bands are described in the "Characterization of the nanosensor" section. The results of the univariate analysis performed for each Raman tag are shown in Fig. 5(a–l). The Raman intensities in all the obtained maps (four samples per group) were first normalized to allow a meaningful comparison between various measurements. The Raman maps obtained by the univariate analysis of physiological sample show the presence of each growth factor in varying abundances. The growth factor TGF-ß1 can be considered the most abundant, followed by bFGF and BMP-2. This agrees with previous studies, where TGF-ß1 was found to be more frequent than other growth factors [6, 10]. Second, a sample containing the smear layer covering the surface and thus disabling its interaction with sensors was selected as a negative control. The corresponding maps are shown in Fig. 5(d–f). The availability of all the three targeted growth factors on the root surface was considerably lowered. The spectral analysis shows a decrease of 70% for TGF-ß1, 50% for bFGF, and 82% for BMP-2. The lower number of active places indicates the absence of nonspecific interaction of the sensor with the sample surface and supports the role of the smear layer as a blockage between the

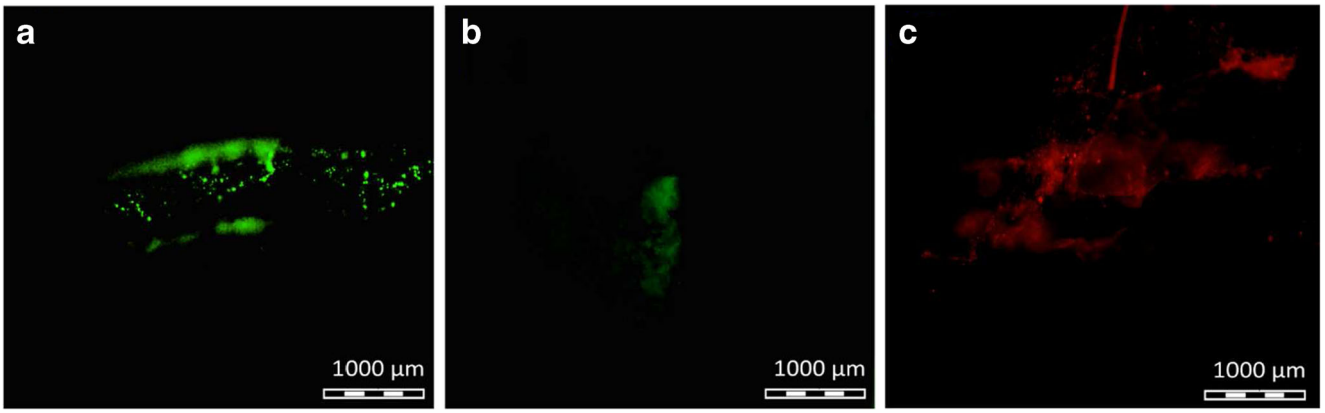

Fig. 4 Microscopy images of the nanosensors on a surface of the physiological tooth sample. **a** TGF-ß1 sensor, **b** BMP-2 sensor, and **c** bFGF sensor

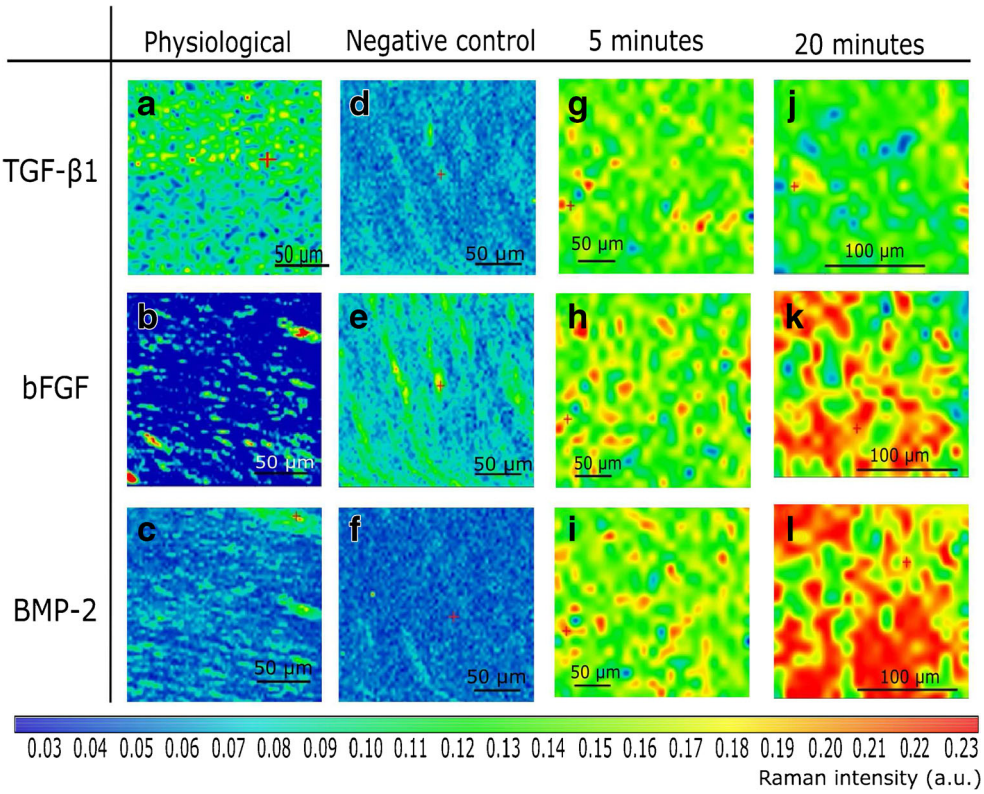

Fig. 5 (a–l) Raman spectral maps obtained by analysis of tooth sample. The rows represent individual growth factors (TGF-β1, BMP-2, and bFGF). Columns represent sample treatments, i.e., without sample treatment (labeled as physiological), negative control with a smear layer (labeled as negative control), treated by EDTA for 5 min (labeled as 5 minutes), and treated by EDTA for 20 min (labeled as 20 minutes). Relative Raman intensities of particular factors are shown as colors defined by the inserted color bar. For the Raman imaging, spectral bands localized at 1395 cm^{-1} for anti-TGF-β1-Cy3, 1597 cm^{-1} for anti-BMP-2-Cy5, and 1621 cm^{-1} for anti-bFGF-Cy7 were selected

growth factors present in dentin microchannels and the surface.

Next, the influence of the irrigation protocol on the availability of growth factors on the surface was evaluated. Namely, the duration of the treatment of the sample by EDTA was studied, while different periods of time 5 and 20 min were selected. Initially, the sample treated by EDTA for 5 min was measured. The results of the univariate analyses performed on the normalized and background corrected Raman data are shown in Fig. 5(g–i), where image (g) represents a distribution of TGF-ß1, (h) represents a distribution of bFGF, and (i) stands for distribution of BMP-2. Similar images (Fig. 5, labels (j)–(l)) were obtained from the samples treated for 20 min, albeit with intensities ranging at higher values. The abundance of the TGF-ß1 present in the sample treated for 20 min decreased by 10%, compared to the sample treated for 5 min, but it increased by 80% compared to the physiological sample, where a naturally according smear layer is present. Even better situation was observed in bFGF and BMP-2, where the treatment with EDTA for 20 min led to an increase in the growth factor abundances by more than 300% compared to the physiological sample.

Conclusions

Here, present methodology, providing a parallel analysis of growth factors, i.e., TGF-ß1, bFGF, and BMP-2 on the dentin surface, is based on the combination of surface-enhanced Raman spectroscopy and the new nanosensors based on Fe_3O_4@Ag nanocomposites functionalized by Raman-tagged antibodies, namely anti-TGF-ß1@Cy3, anti-bFGF@Cy7, and anti-BMP-2@Cy5. The methodology was studied on a set of samples of human teeth in which the distribution of all the three growth factors on the dentin surface was analyzed. Next, the influence of the time of treatment using EDTA was evaluated to study the possibility for the methodology to provide a semiquantitative analysis. It is shown that a 5-min treatment led to a considerable increase of the abundances of all the three studied proteins. It was also found out that longer periods of time could lead to washing some proteins out; therefore, the optimal time needs to be set carefully. Growth factor TGF-ß1 started to wash out relatively fast compared to bFGF and BMP-2, which is consistent with previous studies published by Galler [6]. The release of growth factors strongly depends on the applied solution. It is known that citric acids lead to a preferential release of bFGF and VEGF, compared to TGF-ß1, and TGF-ß1 is preferentially released by EDTA [11].

Author contributions The manuscript was written through contributions of all the authors.

Funding information The authors received financial support from project NPU LO1305 of the Ministry of Education, Youth and Sports of the Czech Republic; project IGA_PrF_2018_021, CZ.1.07/2.3.00/30.0004, and Research Infrastructure NanoEnviCz, supported by the Ministry of

Education, Youth and Sports of the Czech Republic under Project No. LM2015073; and project 16-02938S of the Grant Agency of the Czech Republic.

Compliance with ethical standards

The approval of the ethic committee of the Faculty Hospital Olomouc and Medical Faculty of Palacký University for the study was obtained (NV-18-08-00328).

Conflict of interest The authors declare that they have no conflict of interest.

References

1. Dhillon H, Kaushik M, Sharma R. Regenerative endodontics-creating new horizons: regenerative endodontics. J Biomed Mater Res B Appl Biomater. 2016;104:676–85. https://doi.org/10.1002/jbm.b.33587.
2. Wigler R, Kaufman AY, Lin S, Steinbock N, Hazan-Molina H, Torneck CD. Revascularization: a treatment for permanent teeth with necrotic pulp and incomplete root development. J Endod. 2013;39:319–26. https://doi.org/10.1016/j.joen.2012.11.014.
3. Nosrat A, Homayounfar N, Oloomi K. Drawbacks and unfavorable outcomes of regenerative endodontic treatments of necrotic immature teeth: a literature review and report of a case. J Endod. 2012;38:1428–34. https://doi.org/10.1016/j.joen.2012.06.025.
4. Žižka R, Šedý J. Paradigm shift from stem cells to cell-free regenerative endodontic procedures: a critical review. Stem Cells Dev. 2017;26:147–53. https://doi.org/10.1089/scd.2016.0264.
5. Smith AJ, Scheven BA, Takahashi Y, Ferracane JL, Shelton RM, Cooper PR. Dentine as a bioactive extracellular matrix. Arch Oral Biol. 2012;57:109–21. https://doi.org/10.1016/j.archoralbio.2011.07.008.
6. Galler KM, Buchalla W, Hiller K-A, Federlin M, Eidt A, Schiefersteiner M, et al. Influence of root canal disinfectants on growth factor release from dentin. J Endod. 2015;41:363–8. https://doi.org/10.1016/j.joen.2014.11.021.
7. Kakaboura A. Smear layer on prepared dentin. Odontostomatol Proodos. 1989;43:211–23.
8. Ferracane JL, Cooper PR, Smith AJ. Dentin matrix component solubilization by solutions at pH relevant to self-etching dental adhesives. J Adhes Dent. 2013;15:407–12. https://doi.org/10.3290/j.jad.a29536.
9. Galler KM, Widbiller M, Buchalla W, Eidt A, Hiller K-A, Hoffer PC, et al. EDTA conditioning of dentine promotes adhesion, migration and differentiation of dental pulp stem cells. Int Endod J. 2016;49:581–90. https://doi.org/10.1111/iej.12492.
10. Zeng Q, Nguyen S, Zhang H, Chebrolu HP, Alzebdeh D, Badi MA, et al. Release of growth factors into root canal by irrigations in regenerative endodontics. J Endod. 2016;42:1760–6. https://doi.org/10.1016/j.joen.2016.04.029.
11. Duncan HF, Smith AJ, Fleming GJP, Reid C, Smith G, Cooper PR. Release of bio-active dentine extracellular matrix components by histone deacetylase inhibitors (HDACi). Int Endod J. 2017;50:24–38. https://doi.org/10.1111/iej.12588.
12. Hisamoto M, Goto M, Muto M, Nio-Kobayashi J, Iwanaga T, Yokoyama A. A systematic analysis for localization of predominant growth factors and their receptors involved in murine tooth germ differentiation using in situ hybridization technique. Biomed Res. 2015;36:205–17. https://doi.org/10.2220/biomedres.36.205.
13. Li S, Pan Y. Differential expression of transforming growth factor-beta1, connective tissue growth factor, phosphorylated-SMAD2/3 and phosphorylated-ERK1/2 during mouse tooth development. J Mol Histol. 2017;48:347–55. https://doi.org/10.1007/s10735-017-9733-4.
14. Niwa T, Yamakoshi Y, Yamazaki H, Karakida T, Chiba R, Hu JC-C, et al. The dynamics of TGF-β in dental pulp, odontoblasts and dentin. Sci Rep. 2018;8:4450. https://doi.org/10.1038/s41598-018-22823-7.
15. Zhao S, Sloan AJ, Murray PE, Lumley PJ, Smith AJ. Ultrastructural localisation of TGF-β exposure in dentine by chemical treatment. Histochem J. 2000;32:489–94.
16. Ionita I. Diagnosis of tooth decay using polarized micro-Raman confocal spectroscopy. Rom Rep Phys. 2009;61:567–74.
17. Zavala-Alonso V, Loyola-Rodríguez JP, Terrones H, Patiño-Marín N, Martínez-Castañón GA, Anusavice K. Analysis of the molecular structure of human enamel with fluorosis using micro-Raman spectroscopy. J Oral Sci. 2012;54:93–8.
18. Wang Y, Yao X. Morphological/chemical imaging of demineralized dentin layer in its natural, wet state. Dent Mater. 2010;26:433–42. https://doi.org/10.1016/j.dental.2010.01.002.
19. Beier BD, Quivey RG, Berger AJ. Raman microspectroscopy for species identification and mapping within bacterial biofilms. AMB Express. 2012;2:35.
20. Cepeda-Pérez E, Moreno-Hernández C, López-Luke T, Monzón-Hernández D, de la Rosa E. Evaluation of bacterial presence in the root canal by Raman spectroscopy: a preliminary study. Biomed Phys Eng Express. 2016;2:065006. https://doi.org/10.1088/2057-1976/2/6/065006.
21. Fleischmann M, Hendra PJ, McQuillan AJ. Raman spectra of pyridine adsorbed at a silver electrode. Chem Phys Lett. 1974;26:4.
22. Balzerova A, Fargasova A, Markova Z, Ranc V, Zboril R. Magnetically-assisted surface enhanced Raman spectroscopy (MA-SERS) for label-free determination of human immunoglobulin G (IgG) in blood using Fe3O4@Ag nanocomposite. Anal Chem. 2014;86:11107–14. https://doi.org/10.1021/ac503347h.
23. Ranc V, Markova Z, Hajduch M, Prucek R, Kvitek L, Kaslik J, et al. Magnetically assisted surface-enhanced Raman scattering selective determination of dopamine in an artificial cerebrospinal fluid and a mouse striatum using Fe3O4/Ag nanocomposite. Anal Chem. 2014;86:2939–46. https://doi.org/10.1021/ac500394g.
24. Chaloupková Z, Balzerová A, Bařinková J, Medříková Z, Šácha P, Beneš P, et al. Label-free determination of prostate specific membrane antigen in human whole blood at nanomolar levels by magnetically assisted surface enhanced Raman spectroscopy. Anal Chim Acta. 2017; https://doi.org/10.1016/j.aca.2017.10.008.
25. Panacek A, Balzerova A, Prucek R, Ranc V, Vecerova R, Husickova V, et al. Preparation, characterization and antimicrobial efficiency of Ag/PDDA-diatomite nanocomposite. Colloids Surf B-Biointerfaces. 2013;110:191–8. https://doi.org/10.1016/j.colsurfb.2013.04.031.
26. Marková Z, Šišková K, Filip J, Šafářová K, Prucek R, Panáček A, et al. Chitosan-based synthesis of magnetically-driven nanocomposites with biogenic magnetite core, controlled silver size, and high antimicrobial activity. Green Chem. 2012;14:2550. https://doi.org/10.1039/c2gc35545k.
27. Prucek R, Panacek A, Fargasova A, Ranc V, Masek V, Kvitek L, et al. Re-crystallization of silver nanoparticles in a highly concentrated NaCl environment-a new substrate for surface enhanced IR-visible Raman spectroscopy. CrystEngComm. 2011;13:2242–8. https://doi.org/10.1039/c0ce00776e.
28. Wang Y, Schlücker S. Rational design and synthesis of SERS labels. Analyst. 2013;138:2224–38. https://doi.org/10.1039/C3AN36866A.